Electrodeposition of Semiconductors for Applications in Thin Film Solar Cells

Jayne Sara Wellings

A thesis submitted in partial fulfilment of the requirements of
Sheffield Hallam University
for the degree of Doctor of Philosophy

2009

Declaration

This thesis is original and no part of this work has been submitted in support of application for another degree of qualification in any other university, learning institute or industrial organisation.

Acknowledgements

I would like to acknowledge the UK Department of Trade and Industry (DTI) for providing the funding for this PhD. Thank you to Pilkington Group Ltd. and Ionotec Ltd. for supplying the substrates for the research. I would also like to gratefully thank my supervisor Prof. IM Dharmadasa and second supervisors Dr A Hassan and Dr S Heavens for their help. Dr A Samantilleke and Dr G Tolan are also gratefully acknowledged for their valuable discussion. Thanks also to the technical staff in the Materials Engineering Research Institute (MERI) at Sheffield Hallam University for their technical help. I would also like to thank my wonderful family and fiancée for their love and support.

Abstract

Electrodeposition was used to deposit thin film semiconductor materials for use in solar cell devices. Copper indium diselenide ($CuInSe_2$) was deposited from ethylene glycol at 150°C with the aim of improved material properties due to the elevated temperature. The broad nature of the X-ray diffraction (XRD) peaks before and after annealing indicated the layers were comprised of multiple phases identified as $CuInSe_2$ and Cu-Se binaries. Insufficient indium inclusion for device quality materials was incorporated into the layers over the explored growth range of -0.800 to -1.000 V vs Se reference electrode. The layers deposited at more positive deposition voltages were metallic and contained mainly Cu-Se binary phases. At more negative deposition voltages the formation of $CuInSe_2$ was confirmed although above -1.000 V vs Se the layers were often powdery and disintegrated on removal from the electrolyte. There were no noticeable improvements in the $CuInSe_2$ layers deposited from ethylene glycol compared to reports from aqueous media, which is less toxic and lower cost, therefore electrodeposition from aqueous solution is preferable.

Undoped zinc oxide (ZnO) and aluminium doped ZnO (ZnO:Al) were deposited from zinc nitrate solutions with the aim of using electrodeposition for the ZnO bilayer in $CuInSe_2$ devices to unify the production process. ZnO was deposited at a range of deposition voltages from -0.900 to -1.050 V vs silver/silver chloride reference electrode as identified using XRD. Various morphologies were observed using scanning electron microscopy (SEM) and the electrical resistivity was determined at 6.9×10^6 Ω cm and decreased to 3.4×10^5 Ω cm after Al doping. To make this method suitable for commercialisation more work would need to be carried out to address consistency issues mainly regarding the electrolyte conditions, including pH and oxygen concentration as a function of growth time.

A comparison was made between electrodeposited and sputtered ZnO and ZnO:Al. Some differences in the material properties were found; all layers were identified as hexagonal wurtzite ZnO. A considerable change in morphology was observed by SEM between the electrodeposited and sputtered materials. Little change in the electrical resistivity was observed between electrodeposited and sputtered undoped ZnO, having 6.9×10^6 and 6.2×10^7 Ω cm. The electrical resistivity of ZnO:Al was 3.4×10^5 and 2.3×10^5 Ω cm for electrodeposited and sputtered materials respectively. Further work would need to be carried out to quantify the concentration of Al dopant in the electrodeposition solution as a function of growth time if this method were to be used for commercialisation.

Cadmium telluride (CdTe) was electrodeposited from aqueous solution onto glass/fluorine doped tin oxide/cadmium sulphide substrates. Little improvement in XRD spectra was observed for annealed layers compared to the as-deposited material and the CdTe was identified exhibited cubic phase having (111) preferential orientation. Working solar cell devices were fabricated over a range of growth voltages with superior performance being observed for materials deposited between -0.620 to -0.650 V vs saturated calomel electrode (SCE). Furthermore high uniformity over a 2 cm^2 area completed with an array of 2 mm diameter contacts was observed for devices deposited in this growth voltage range. All devices fabricated using CdTe grown at -0.610 to -0.690 V vs SCE indicated photovoltaic activity although layers deposited between -0.630 and -0.650 V vs SCE indicated the highest performance, with device parameters of open circuit voltage = 420-540 mV, short circuit current density = 3.2-19.1 mA cm^{-2} and fill factor = 0.48.

Table of Contents

Chapter 1 Introduction to Solar Energy Materials and Solar Cells

1.1 Introduction

At present the world's population is estimated at seven billion with a drastic rise expected over the coming years. This large population puts a strain on the energy infrastructure, and subsequently sustainable energy supplies for long-term energy solutions are under investigation. Fossil fuels remain market leaders for electricity production, providing a reliable source of power at a cost effective price. The major drawback to burning fossil fuels is the emission of carbon dioxide (CO_2) and other greenhouse gases into the atmosphere, which are thought to contribute to climate change. Greenhouse gases are undesirable as they cause an un-natural warming effect by absorbing infra-red radiation that should leave the earth. The CO_2 emissions increased considerably during the industrial revolution [Hammond 2007].

It is predicted that fuel for electricity generation will become increasingly scarce and expensive over the coming years as fossil fuels deplete. Taking these factors of increasing population, climate change and depleting fuel supplies into account, the question of where the energy for electricity production will be sourced in the future is still under debate. A variety of existing technologies can be used in the near future for example nuclear power, fossil fuels and renewable energy. Renewable energy has the advantage of being constantly replenished and therefore provides a sustainable energy supply without CO_2 emission. Renewable energy consists of solar, wind, tidal/wave, biomass, hydroelectric and geothermal energy [Boyle 2004].

Solar power is an ideal energy solution, which theoretically has the capacity to provide the entire world's energy. It has been estimated that only a fraction of the earth's desert land would be required to supply the world energy needs [Kemell *et al.* 2005]. Energy from the sun can be converted into usable energy by using solar cells, which are available in two forms, active photovoltaic, (PV) and passive (thermal) cells [Markvart 2000, Kreith & Goswami 2007]. The varying size of solar modules provides the possibility of both individual cells for local use and large solar power stations supplying the national grid. Any surplus energy from home generation may be stored in batteries for later use or exported to the national grid.

Passive solar cells are mainly used for water heating purposes. Piped water is heated by radiation from the sun, which is connected to a storage tank. The system is comprised of two concentric glass tubes separated by a vacuum gap. The internal surface of the inner tube is coated with black aluminium-nitride/aluminium (Al-N/Al) to absorb the sunlight. The heat absorbed by the coating is transferred to the water inside the inner tube and the vacuum provides insulation to prevent heat loss. Solar heating systems provide free hot water and are effective for around 30 years [Boyle 2004].

Active PV solar cells convert photons of light into electricity. First Solar, Inc have boosted the market recently with the production of their photovoltaic cadmium telluride (CdTe) modules having 10.7% efficiency [First Solar 2009]. In order to make this technology more accessible it is important that the manufacturing costs are reduced and the efficiency is improved. One way to reduce the underlying production cost is to use cheaper growth methods such as electrodeposition [Lincot 2005]. Secondly, if the efficiency of a module is doubled, the cost would effectively be halved. Electrodeposition is a low-cost technique used to grow semiconductor materials. This technique also has the benefit of being scalable enabling various substrate shapes and sizes to be deposited [Lincot 2005, Dharmadasa & Haigh 2006].

Currently commercially available solar cells are mainly fabricated using single crystal or polycrystalline silicon, referred to as first generation PV. Other solar cell absorber materials include polycrystalline thin films of copper indium gallium diselenide ($CuInGaSe_2$ or CIGS) and CdTe, referred to as second generation PV. Currently the industry is researching novel thin film designs with the aim of improving the efficiency; these are referred to as third generation PV [Green 2001].

This research programme involved the development of semiconductor materials for use in solar cell devices. Copper indium diselenide ($CuInSe_2$ or CIS) absorber and zinc oxide (ZnO) buffer layers were developed using electrodeposition although devices were not fabricated. CdTe absorber layers were also developed using electrodeposition and working devices were produced. The remaining sections of this chapter introduce background information regarding semiconductors, solar cell principles, and device configurations and a brief description of first, second and third generation solar cells.

1.2 Theory of Semiconductors

1.2.1 Intrinsic Semiconductors

Intrinsic semiconductors are pure, undoped materials; the valence band (E_V) is full of electrons and the conduction band (E_C) is empty. The electrons are unable to move to the conduction band and therefore the intrinsic semiconductor exhibits the same properties as an insulator. The Fermi level (E_F) is situated in the middle of the bandgap, resulting in poor electrical conductivity. The bandgap energy (E_g) of a semiconductor is the minimum energy required to break the atomic bonds and promote an electron from the valence band to the conduction band. Figure 1.1 illustrates the energy band diagram of an intrinsic semiconductor [Tyagi 1991, Sze & Ng 2007, Rockett 2008].

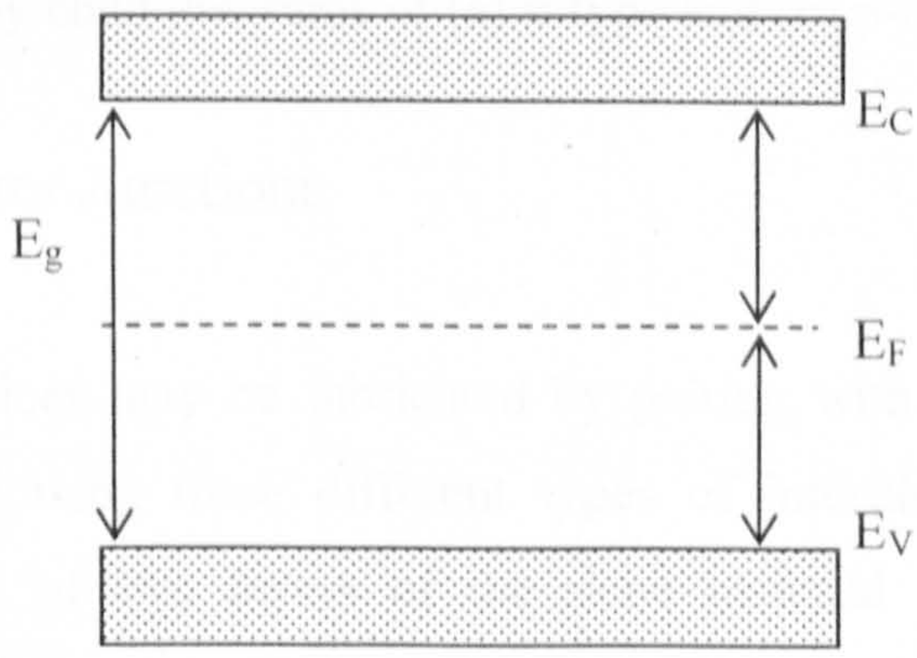

Figure 1.1. Energy band diagram of an intrinsic semiconductor.

1.2.2 Extrinsic Semiconductors

The electrical conductivity of a semiconductor may be increased by doping with suitable dopant atoms forming an extrinsic material. The electrical conductivity type of the extrinsic semiconductor is either n-type or p-type depending on whether electrons or holes are the majority charge carriers. An n-type material has extra loosely bound electrons donated by the dopant atom forming a donor level. As a result the Fermi level moves closer to the conduction band as shown in Figure 1.2 (a). For n-type electrical conductivity the electrons are the majority and holes are the minority charge carriers.

Holes are electron vacancies left behind when an electron is released from its host atom. To form p-type semiconductors dopant atoms with one electron short for completion of bonding in the host crystal is added to create an acceptor level close to the valence band as shown in Figure 1.2 (b). In this case the majority charge carriers are holes and the minority charge carriers are electrons.

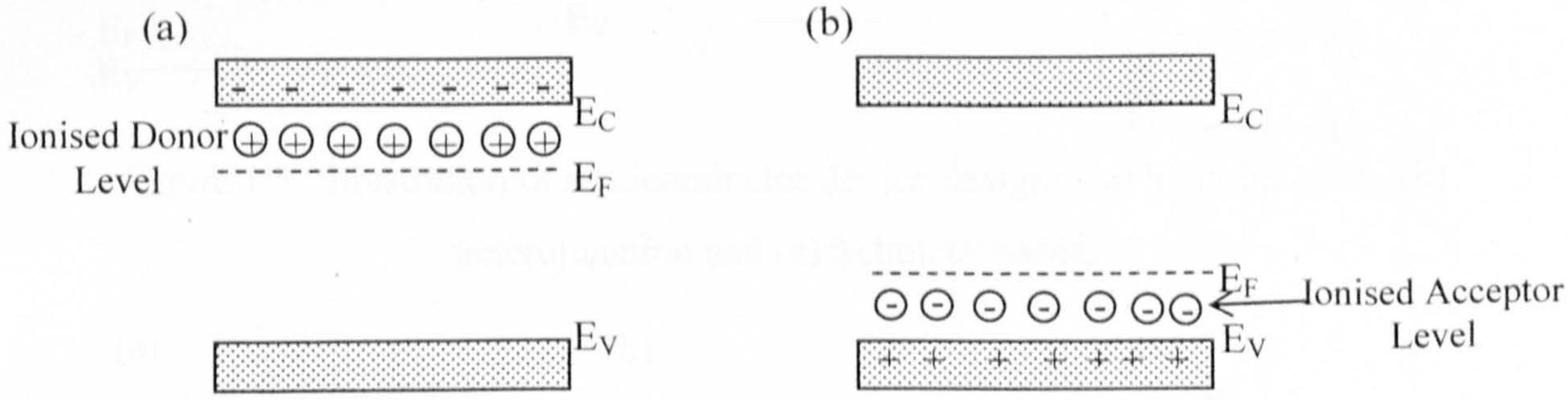

Figure 1.2. Energy band diagrams of (a) n-type and (b) p-type semiconductors.

1.2.3 Semiconductor Junctions

Semiconductor devices may be fabricated by pairing with another semiconductor, insulator or metal allowing three different types of interface to be formed. The homojunction consists of two layers of the same material with opposite electrical conductivity type as indicated in Figure 1.3 (a) for CIS. The heterojunction consists of a p-n junction fabricated using two different semiconductor materials. Figure 1.3 (b) illustrates a CdTe and cadmium sulphide (CdS) heterojunction. Thirdly, the metal/semiconductor junction or Schottky barrier design is illustrated in Figure 1.3 (c). The corresponding band diagrams for each semiconductor device are shown in Figure 1.4 (a-c). The band bending associated with the p-n junction metal/semiconductor interface is the basis for the production of an internal electric field, permitting the flow of charge carriers [Tyagi 1991, Sze & Ng 2007, Rockett 2008].

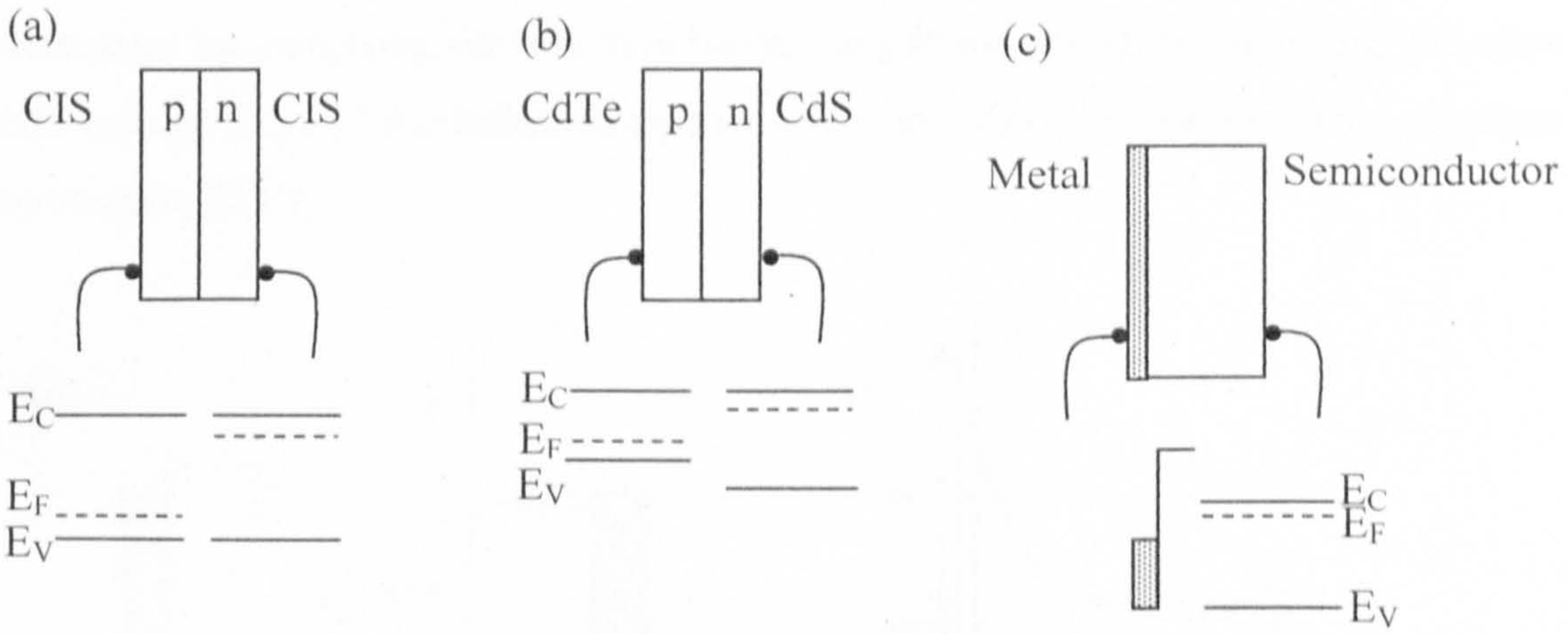

Figure 1.3. Illustration of semiconductor device designs, (a) homojunction, (b) heterojunction and (c) Schottky barrier.

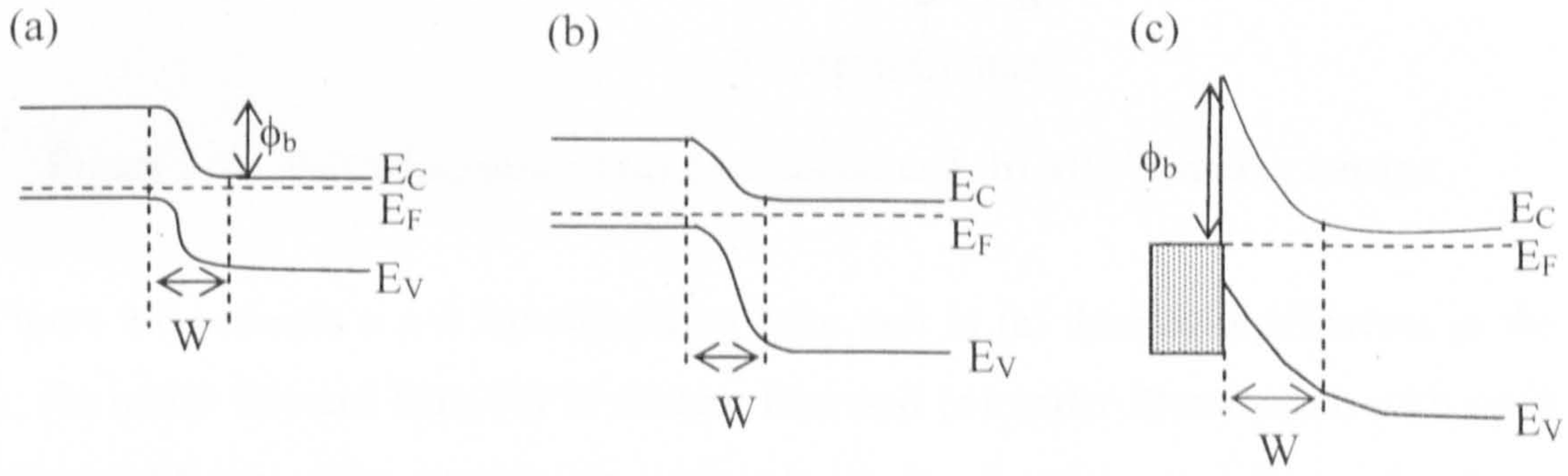

Figure 1.4. Band diagrams for (a) homojunction, (b) heterojunction and (c) Schottky barrier, ϕ_b = barrier height and W = depletion region at equilibrium.

Formation of a potential barrier occurs when an n-type and p-type semiconductor are in contact. The Fermi levels equalises when charge carriers diffuse across the interface leaving behind ionised states. The positively charged holes in the p-type region and negatively charged electrons in the n-type regions diffuse to form a depletion region. The degree of diffusion depends on the doping concentration of the semiconductors (N_d or N_a) which defines the size of the depletion width (W). Negatively or positively charged ions are left on the p-side and n-side respectively forming the internal electric field. The depletion region is the active area of the solar cell [Tyagi 1991, Sze & Ng 2007, Rockett 2008].

Metal-semiconductor (MS) and p-n junctions may be further modified to improve the performance of the device by addition of an insulating layer. The modified device structures form p-i-n diodes or metal-insulator-semiconductor (MIS) devices. Formation of p-i-n solar cells (Figure 1.5 a) with graded bandgap energy improves the PV conversion. Similarly the MIS diode indicated in Figure 1.5 (b) improves the device

performance by increasing the effective barrier height and therefore improving the open circuit voltage (V_{oc}) of the device compared to a conventional Schottky barrier structure [Dharmadasa 2005].

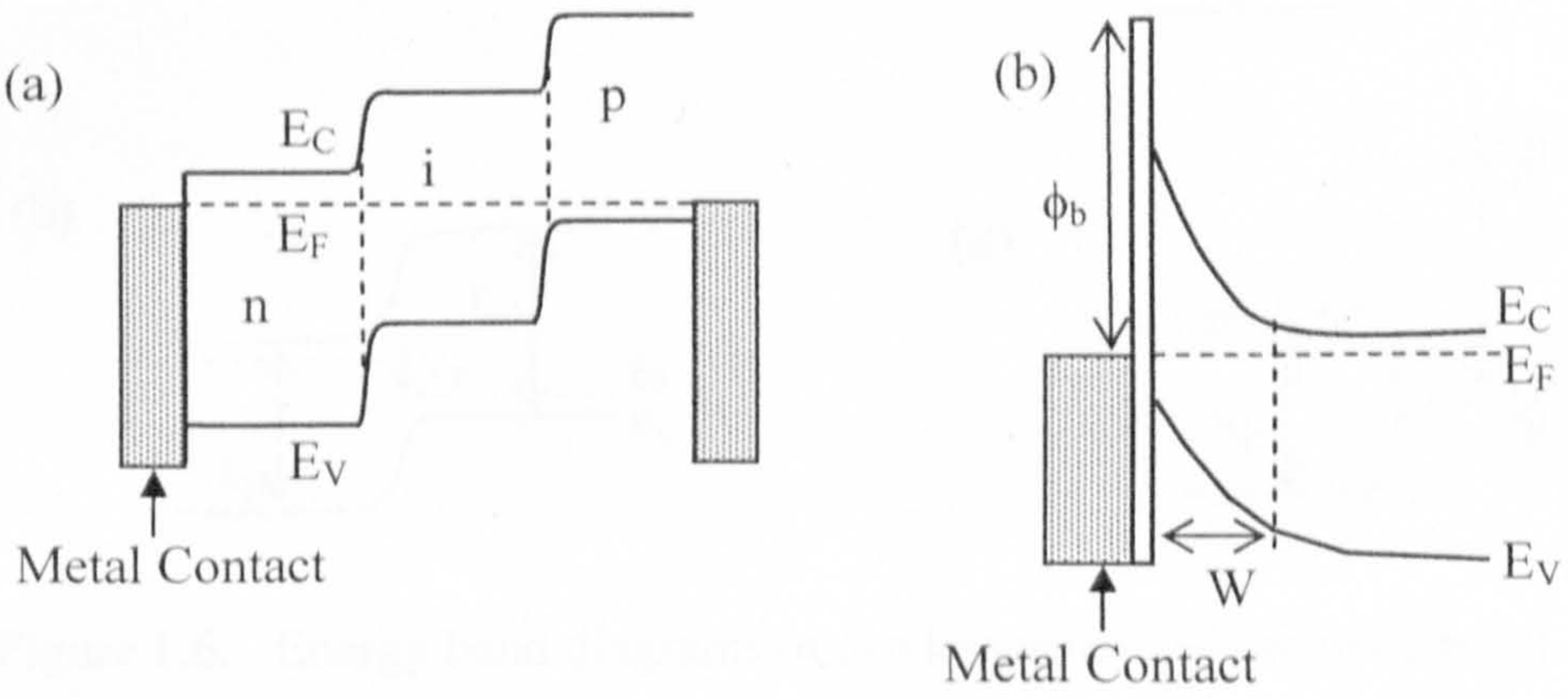

Figure 1.5. Band diagrams of (a) p-i-n diode and (b) MIS Schottky barrier.

Figure 1.6 presents a p-n heterojunction solar cell in (a) thermal equilibrium in the dark, (b) under forward bias, (c) in reverse bias and (d) under illumination with open circuit conditions. The conduction and valence bands edges and Fermi level are labelled as E_C, E_V and E_F respectively. The Fermi levels are equal and no current flows under zero bias conditions (a). Under forward bias (V_F) conditions (b) electrons flow into the n-type material and holes flow into the p-type region; the potential barrier is lowered as a result of the movement of the Fermi level in the respective materials, thus assisting current flow. In reverse bias (V_R) (c), electrons flow into the p-type material and holes flow into the n-type material moving the Fermi level in each material, increasing the potential barrier and thus inhibiting the current flow. Under illumination conditions, photons of light are absorbed by the semiconductor and electron-hole pairs are generated, this alters the Fermi level and creates photovoltage across the junction [Kemell *et al*. 2005].

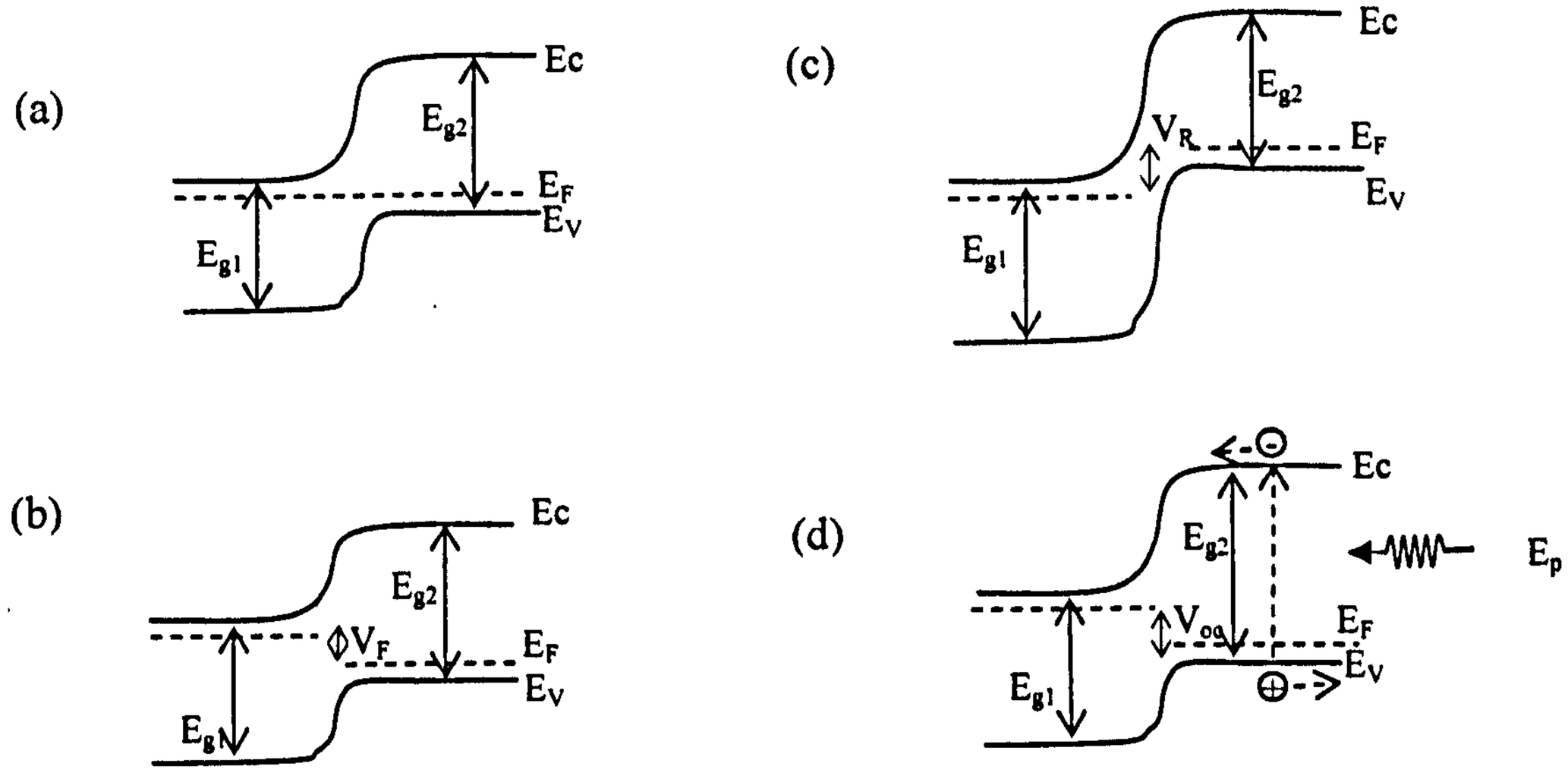

Figure 1.6. Energy band diagrams of p-n heterojunction solar cells (a) at thermal equilibrium in the dark, (b) with forward bias, (c) with reverse bias and (d) under illumination with the circuit in open conditions.

1.3 Photovoltaic Principles

1.3.1 Solar Energy

The word photovoltaic is derived from the words photon and voltage. Photovoltaics is the mechanism used to convert light energy (photons) into an electrical signal (voltage) and PV solar cell devices are used for this conversion. The electromagnetic spectrum consists of different wavelengths of electromagnetic radiation generated by the sun, which continuously travel to the earth. Each wavelength has a different energy associated with it as expressed by equation 1.1.

$$E_p = \frac{hc}{\lambda} \tag{1.1}$$

where E_p = photon energy (eV), h = Planck's constant (6.626×10^{-34} m^2 kg s^{-1})
λ = wavelength (m) and c = speed of light (3.0×10^{8} ms^{-1}).

The ultra violet (UV) part of the spectrum has wavelength in the range 10 to 400 nm, visible between 400 to 700 nm and near infra-red (IR) from 750 to 2500 nm. The visible region of the electromagnetic spectrum has the most suitable wavelengths for

absorption by solar cells, although depending on the bandgap energy of the semiconductor part of the UV and IR regions may also be useful for production of electricity. Figure 1.7 illustrates the photon flux of the electromagnetic radiation generated by the sun, which travels to the earth every second. The spectrum represents air mass 1.5 (AM 1.5) which is the typical solar spectrum falling on the earth's surface on a clear day. The undulation of the spectrum is due to absorption or scattering by air molecules, clouds and particulates such as aerosols [Markvart 2000].

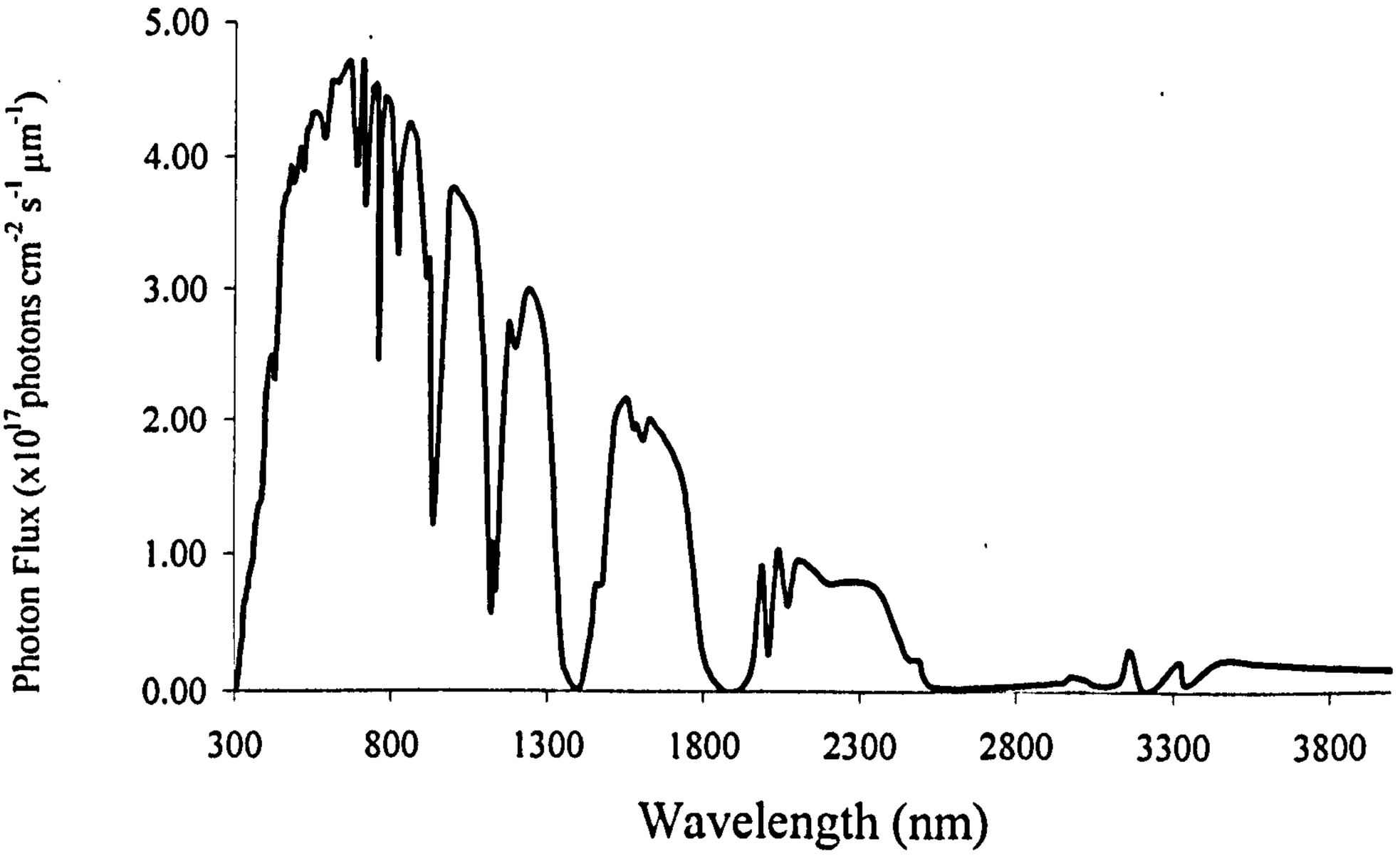

Figure 1.7. Photon flux of the electromagnetic radiation generated by the sun which travels to earth every second [Markvart 2000].

1.3.2 Solar Cells

Photons of light with energy E_p from the sun are absorbed by semiconductor materials and are converted to an electrical signal. If the photon energy is greater than or equal to the bandgap energy ($E_p \geq E_g$), the photons are absorbed and electrons are promoted to the conduction band of the semiconductor, leaving a hole in the valence band. The potential barrier within the device structure enables electrons to flow in the conduction band and be collected by an external circuit [Green 2002]. Photons with less energy than the bandgap energy ($E_p < E_g$) are not absorbed and therefore do not take part in PV conversion [Sze & Ng 2007].

The three main parameters used to determine the performance of solar cell devices are the V_{oc}, short circuit current (I_{sc}) and fill factor (FF). The V_{oc} is the maximum voltage across the cell under illumination at zero current. The I_{sc} is the maximum current flowing through cell when no load or resistance is applied. The current density (J_{sc} expressed in mA cm^{-2}) is a measure of the current flow per unit area. The FF is defined by equation 1.2 as the ratio of maximum power to actual power. These parameters may be used in equation 1.3 to determine the efficiency of the device.

$$FF = \frac{V_m I_m}{V_{oc} I_{sc}} \tag{1.2}$$

$$\eta = \frac{V_m I_m}{P_{in}} = \frac{V_{oc} \cdot FF \cdot I_{sc}}{P_{in}} \tag{1.3}$$

where FF = fill factor, V_m = maximum voltage, I_m = maximum current, V_{oc} = open circuit voltage, I_{sc} = short circuit current, η = efficiency and P_{in} = input power (100 mW cm^{-2}).

The dark (a) and illuminated (b) current-voltage (I-V) curves are illustrated by Figure 1.8. The series resistance (R_s) arises from the bulk of the semiconductor, depletion region, electrical contacts and connecting wires and should ideally be as low as possible. The shunt resistance (R_{sh}) is due to pin-holes in the device resulting in conductive paths and recombination centres, this parameter should ideally be infinite. The effect of the series and shunt electrical resistances on the electrical characteristics of solar cells is indicated in Figure 1.9 [Markvart 2000].

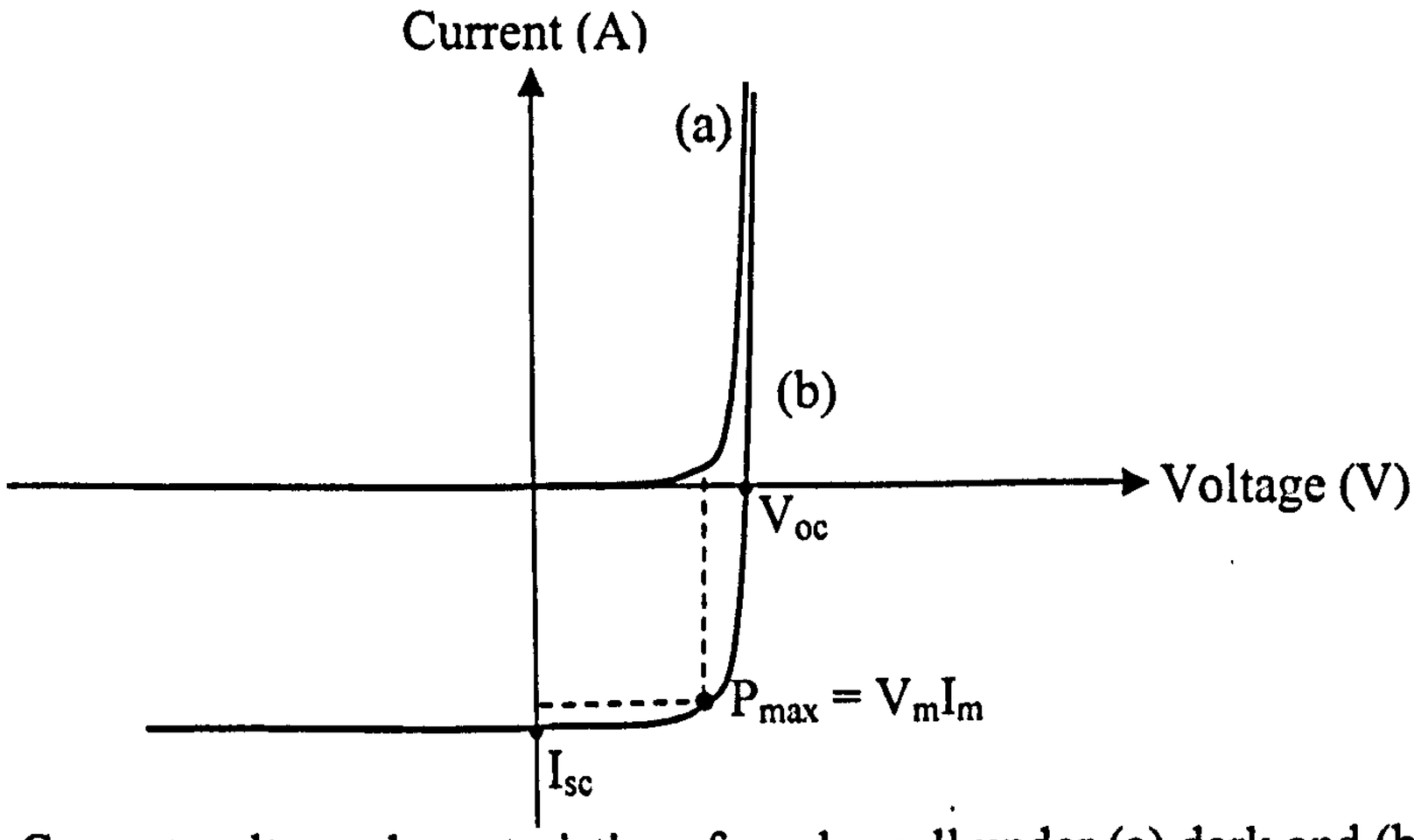

Figure 1.8. Current-voltage characteristics of a solar cell under (a) dark and (b) illuminated conditions.

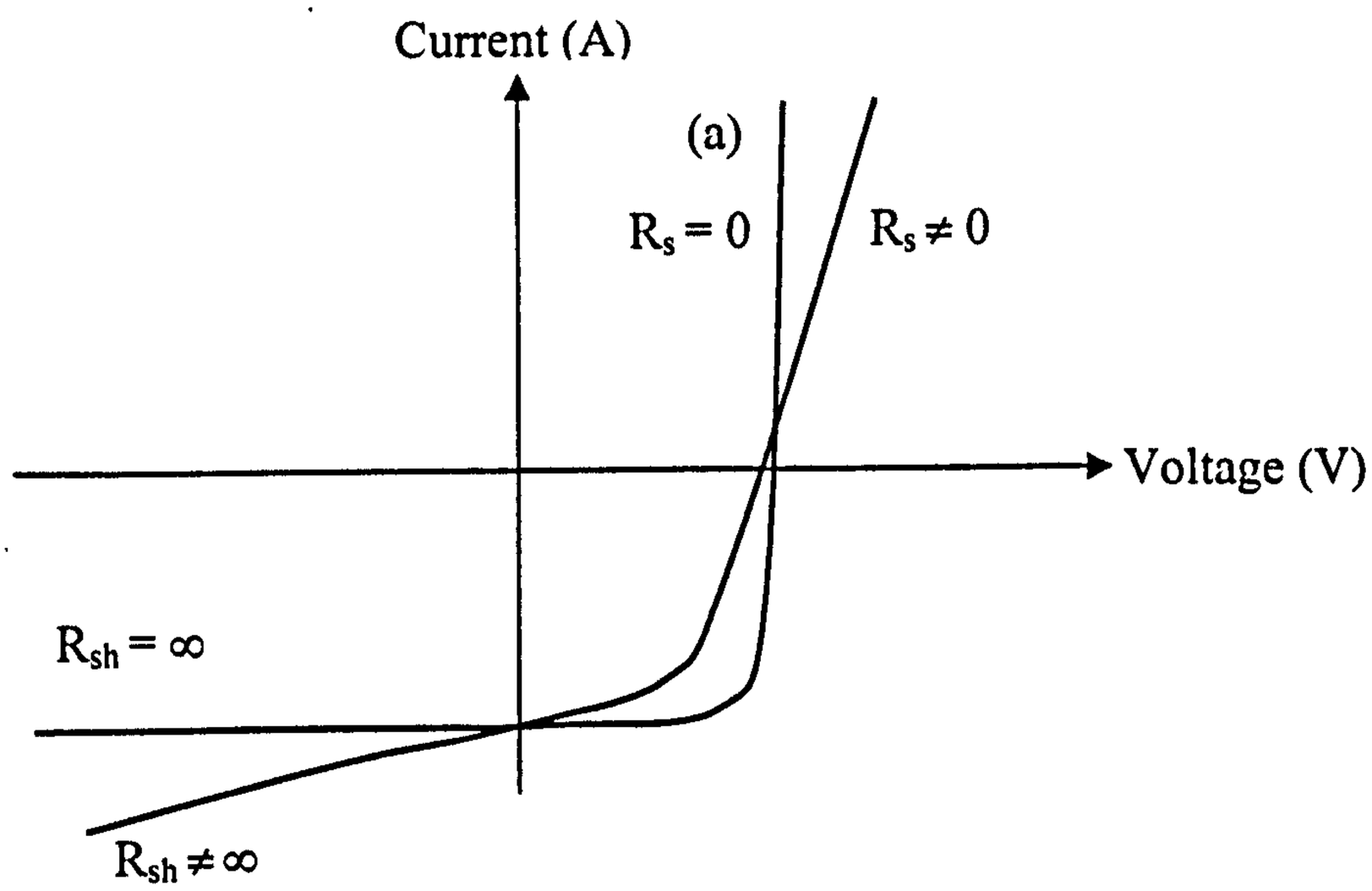

Figure 1.9. Current-voltage characteristics for (a) ideal and (b) non-ideal conditions indicating the effect of high series and low shunt electrical resistances.

1.3.3 Solar Cell Device Configurations

1.3.3.1 Substrate Configuration

Solar cell devices contain several layers, each with a specific function which improves the device performance. The majority of commercially available solar cells are fabricated using the substrate configuration as illustrated by Figure 1.10. This involves depositing each layer sequentially starting from the back, and depositing towards the front metal contact. The photons of light enter the cell via the front and travel towards the back metal contact. In the case of CIGS solar cells the back contact is a molybdenum (Mo) layer deposited onto a glass sheet. The CIGS absorber material is around 2 μm thick, has bandgap energy of 1.10 to 1.20 eV and is directly deposited onto the glass/Mo substrate. Most CIGS solar cells contain a thin (80 nm) CdS window or buffer layer, having bandgap energy of 2.42 eV and deposited using chemical bath deposition (CBD). The final layers are an intrinsic zinc oxide (i-ZnO) and aluminium doped ZnO (ZnO:Al) bilayer having bandgap energy of 3.40 eV and typical thicknesses of 50 nm and 350 nm respectively [Kemell *et al.* 2005].

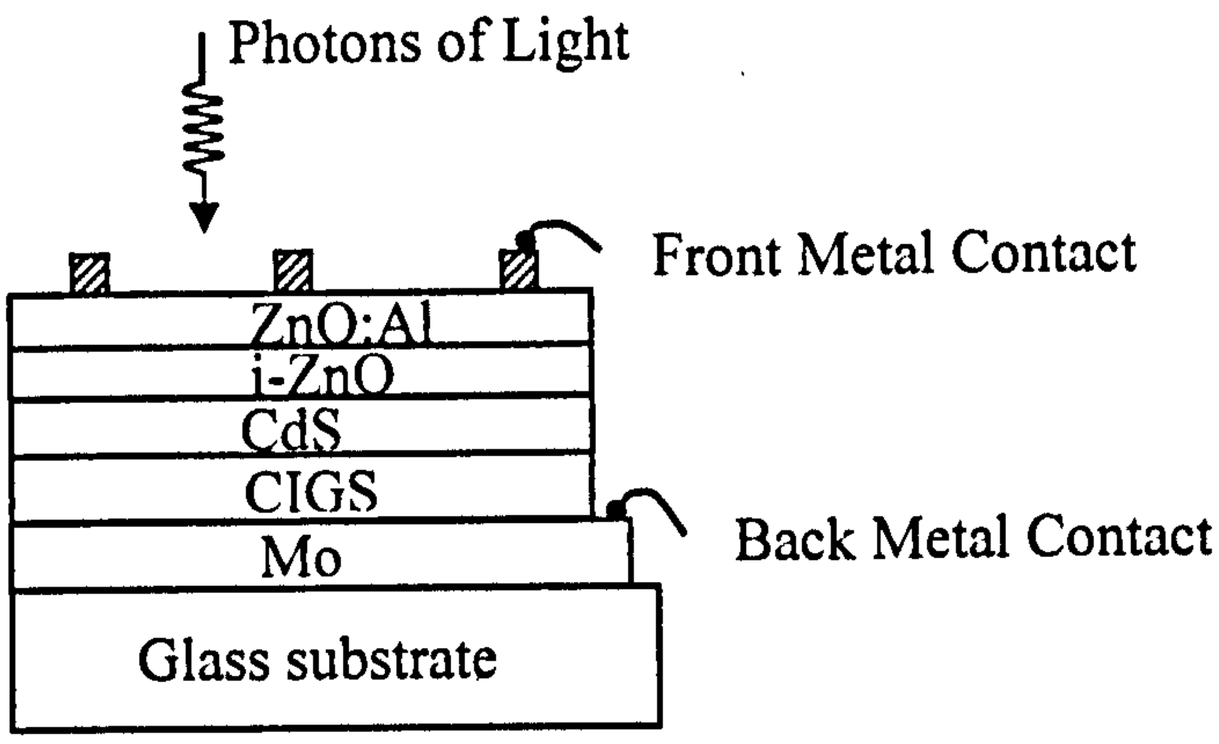

Figure 1.10. Substrate solar cell device configuration, fabricated from the back to the front metal contact.

There have been conflicting opinions in the PV community over the years about role of the CdS buffer layer within the CIS device structure and the origins of the electric field. Initially the CIGS device was considered as a simple n-p heterojunction with n-CdS and p-CIGS [Wagner *et al.* 1974]. Later it was argued that the thin CdS (80 nm) layer was insufficient to form a well defined crystal lattice and establish an n-p junction with the 2 μm thick CIGS. One suggestion is the CdS forms a surface passivation layer and also protects the absorber material from chemical or mechanical degradation during the ZnO sputtering [Markvart & Castaner 2003]. It has also been proposed the ammonia present in the CBD solution during CdS growth treats the CIGS surface, eliminating oxides [Schock & Noufi 2000, Canava *et al.* 2002].

An alternative suggestion is the formation of a buried homojunction within the CIGS layer which forms the internal electric field. This proposal is based on the naturally occurring phase segregation within the p-CIGS, forming an n-type layer at the surface with the CdS known as the ordered defect compound (ODC) layer. The ODC layer has been theoretically evaluated to consist of a copper deficient, indium rich layer and is discussed in more detail in section 3.2.8 of Chapter 3. The ODC concept has not been experimentally proven to date and the specifics of the device physics is still ongoing [Markvart & Castaner 2003].

Together the CdS/i-ZnO improves the electrical properties of the device by widening the depletion layer. Cd is also thought to improve the electrical properties by modifying the CIGS surface by filling Cu vacancies [Wei *et al.* 1999]. The thickness of the CdS affects the device performance as low wavelength photons are absorbed, decreasing the J_{sc}.

The thickness of the i-ZnO is also an important factor in achieving high efficiency as this layer is insulating and therefore if too thick increases the resistance of the device [Cooray *et al.* 1997]. The use of i-ZnO has been found by trial and error method in order to produce a high efficiency device. However the use of an insulating layer to form a good ohmic contact is questionable and the physics behind these devices needs improved understanding.

The purpose of the ZnO:Al is to form a transparent conductive front contact. The key factors to consider for this material are sufficient electrical conductivity of the layer to transport photogenerated current to the external circuit without high resistive losses. Substrate configuration cells have a metal grid deposited onto the top of the ZnO:Al to reduce resistive losses associated with photogenerated current collection, usually nickel-aluminium (Ni-Al). The disadvantages associated with this substrate configuration is the shading effect caused by the front metal contact, reducing the available area for photon absorption. The number of deposition techniques required complicates the growth process and makes the device structure expensive.

1.3.3.2 Superstrate Configuration

The superstrate configuration is an alternative growth arrangement and has undergone much less research than the substrate configuration for CIGS devices. Superstrate solar cells are deposited starting at the front metal contact which is a transparent conductive oxide (TCO) coated glass substrate. The substrate is used as a window for illumination and to support the device structure. CdTe solar cells are fabricated in the superstrate configuration. The CdS window layer, is deposited onto the glass/TCO substrate, followed by the absorber material, CdTe. Finally the back metal contact is deposited, usually copper (Cu) or gold (Au). A CdTe superstrate solar cell is illustrated in Figure 1.11. The advantage of this approach is the TCO front contact prevents any shading and simplifies the device structure [Goetzberger *et al.* 2003].

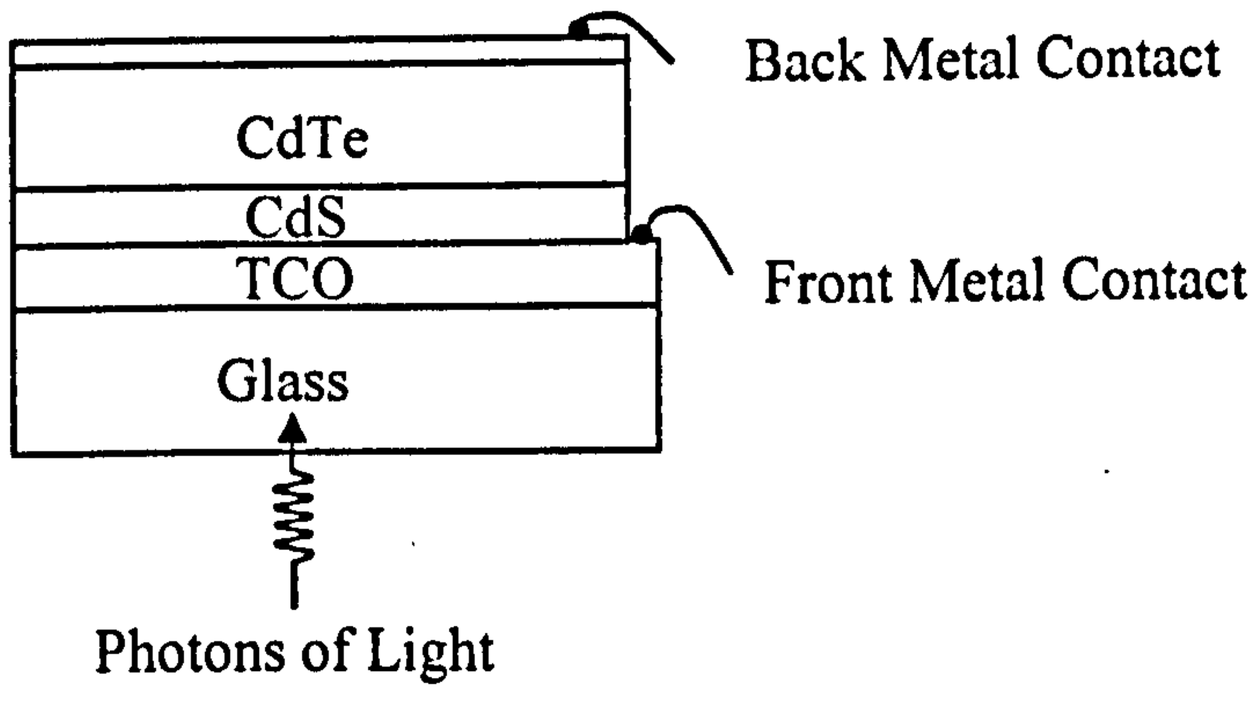

Figure 1.11. Superstrate configuration solar cell, grown from the front to the back metal contact.

1.3.4 First Generation Solar Cells

Silicon (Si) is a group IV element with atomic number 14 and atomic weight 28. First generation solar cells were based on single crystal and polycrystalline Si wafers having thicknesses of 0.2 to 0.9 mm. Silicon solar cells have been used in space applications since the 1950's and still dominate market sales for terrestrial use today [Green 2001, 2004].

The Czochralski method is used to grow single crystals [Goetzberger *et al.* 2003]. Using this method a single Si seed is slowly dipped into molten Si and pulled out with a rotational motion, producing a cylindrical ingot or boule. Intrinsic Si is insulating and therefore doping using suitable dopant atoms is required to increase the electrical conductivity for electronic applications. Doping Si with group V elements such as phosphorus (P) introduces a donor level just below the conduction band adding extra electrons, resulting in n-type electrical conductivity. Doping with group III elements such as boron (B) introduces an acceptor level just above the valence band resulting in p-type electrical conductivity. Wafers are sliced from the ingot and polished before device production. Estimates have suggested the raw material cost for first generation solar cells is as high as 70% of the total module cost. The continued increase in costs of raw materials and saturated efficiency of ~24.7% and 20.3% for crystalline and polycrystalline Si respectively limits the progress of first generation technology [Green 2007].

1.3.5 Second Generation Solar Cells

Second generation solar cells offer a potentially cheaper alternative to single crystal Si devices. Second generation solar cells utilise thin film technology with typical thicknesses of 2 μm. Thin film solar cells are fabricated in either the substrate or superstrate configuration as described in section 1.3.3. The main absorber material used in thin film technology is CdTe, CIGS and amorphous Si. Second generation solar cells also offer the advantage of production of larger area devices [Green 2001]. The highest reported efficiency for laboratory based CIGS cells is currently 19.9% and 16.5% for CdTe devices [Wu *et al.* 2001, Repins *et al.* 2008]. Thin film amorphous Si devices currently have efficiencies of 9.8% [Green 2007].

1.3.6 Third Generation Solar Cells

Third generation solar cells are based on utilisation of novel approaches for improved efficiency, such as quantum dots, and desensitized solar cells. Past efforts to improve the efficiency of solar cell devices have focused on stacking numerous absorber layers having varying bandgap energy to absorb a major part of the solar spectrum. Such tandem solar cells are fabricated with the wide bandgap at the front of the cell to absorb high energy photons and subsequent bandgaps are gradually reduced and graded for absorption of lower energy photons [Green 2001]. This approach is widely used and absorber materials are connected forming tunnel junctions. In this arrangement the conduction band of one device is connected to the valence band of the other. The tunnel junction was first discovered by Esaki in 1958 [Esaki 1958].

Recently it has been proposed that there is a severe disadvantage to using this method of connection. The thin neck at the tunnel junction increases recombination of photo-generated charge carriers at the interface. If the photo-generated charge carriers recombine, only the electrons from the back cell and holes from the front cell are collected in the external circuit. Therefore addition of a number of cells would not improve device performance although the cost would increase. The recombination and generation of electron-hole pairs in tandem solar cells connected in series is shown in Figure 1.12 [Dharmadasa 2005].

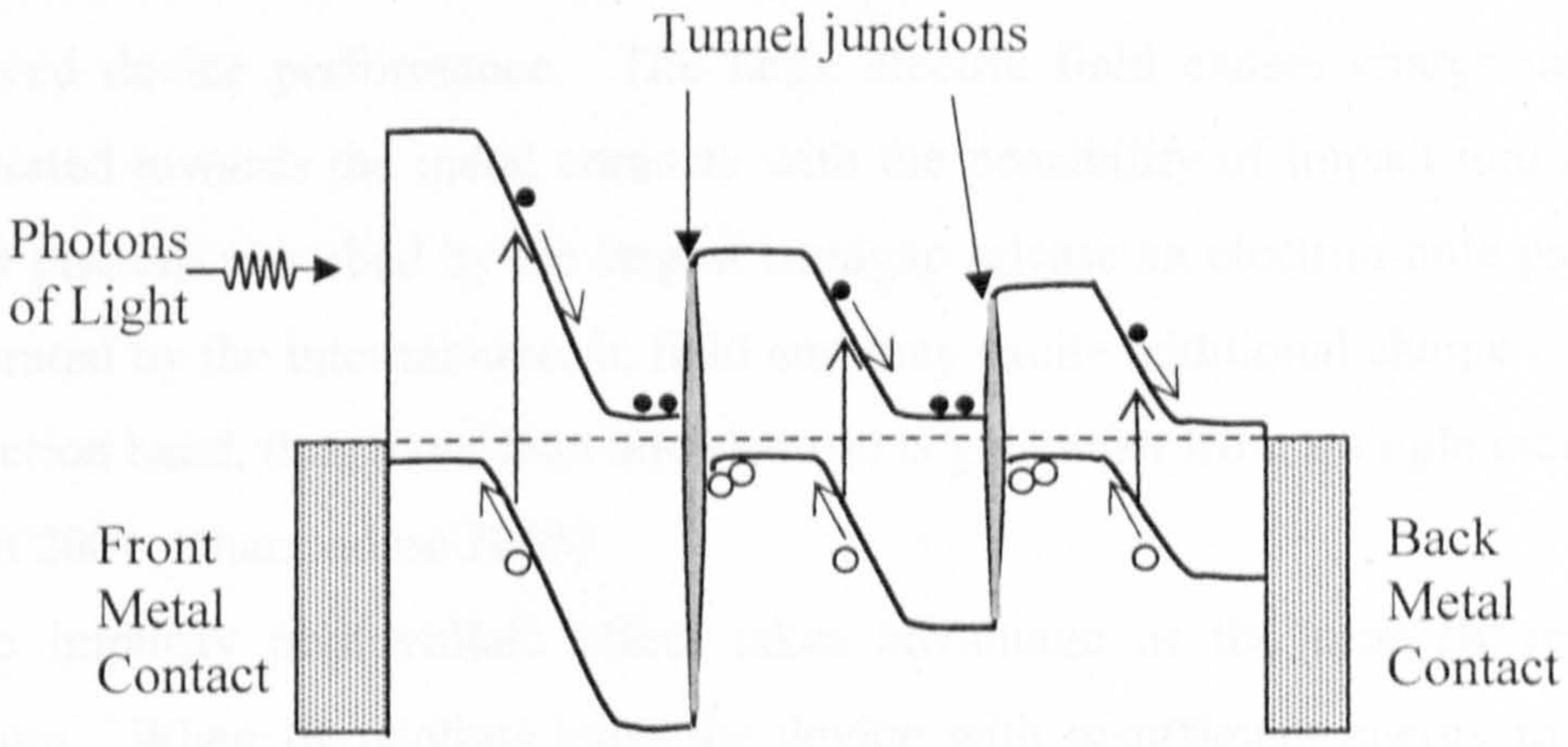

Figure 1.12. Tandem solar cells connected using tunnel junctions, with varying bandgap energy.

An alternative approach is to connect the conduction bands and valence bands of each material in parallel. Again the bandgap energy is varied to collect photons of different energy. In this approach the high bandgap energy at the front of the cell prevents hot-carrier production by blue wavelength photons and recombination of charge-carriers is reduced by the high electric field. Bandgap engineering ensures each layer is suited to the absorption of a certain wavelength range to absorb all available photons. Figure 1.13 illustrates the parallel connection of solar cell design [Dharmadasa 2005].

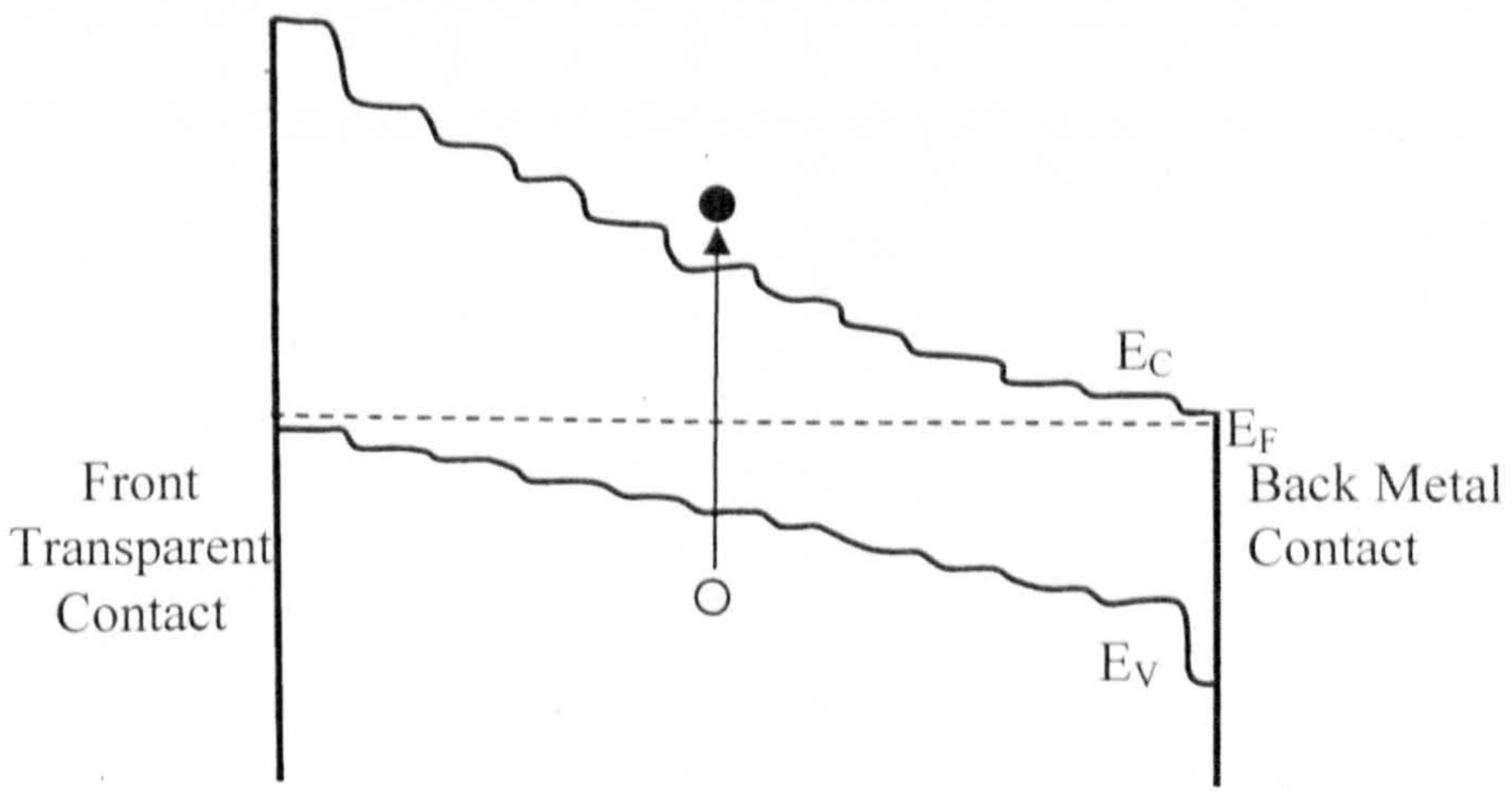

Figure 1.13. Alternative approach for tandem solar cell connection in parallel with graded bandgap structure.

Additional features of this design give the possibility of other mechanisms for improved device performance. The large electric field causes charge carriers to be accelerated towards the metal contacts with the possibility of impact ionisation. High energy photons absorbed by the largest bandgap release an electron-hole pair which are accelerated by the internal electric field and may excite additional charge carriers to the conduction band, thus more than one electron is generated from a single incident photon [Green 2001, Dharmadasa 2005].

The impurity photovoltaic effect takes advantage of the near IR region of the spectrum. When IR photons enter the device with insufficient energy to promote an electron to the conduction band, they may promote an electron to a defect level situated in the bandgap. This electron will be located on the defect site until another photon with sufficient energy promotes it to the conduction band [Green 2001, Dharmadasa 2005].

To date the work has been promising, this new approach has been tested with an already advanced material gallium arsenide/aluminium gallium arsenide ($GaAs/Al_xGa_{(1-x)}As$) forming a p-i-n diode. The world's highest reported V_{oc} was achieved of V_{oc} = 1175 mV and FF = 0.86 for devices with area 3x3 mm^2 [Dharmadasa 2005, 2006, 2008]. Work is progressing using these new ideas to develop devices using electrodeposited absorber materials for improved efficiency and lower cost.

Chapter 2 Experimental Background

2.1 Thin Film Growth Techniques

Material growth techniques for deposition of thin film semiconductors can be divided into two distinct groups, physical and chemical reactions as described in sections 2.1.1 to 2.1.3. Some of these techniques rely on high vacuum (HV) or ultra high vacuum (UHV) systems at high temperature. Such conditions yield superior quality material although production costs are high due to the initial cost of the equipment and power required for vacuum production and growth. The growth techniques discussed in sections 2.1.1 to 2.1.3 are directly related to this research and despite the existence of numerous other thin film growth methods they will not be discussed here.

One of the main barriers for PV development is the associated production costs. To make PV more accessible in the future the cell efficiencies must be improved or the cost of the modules reduced [Birkmire 2001]. An alternative low cost growth technique is electrodeposition, which offers low temperature deposition under non-vacuum conditions. This research project used electrodeposition to develop thin film semiconductor materials for use in solar cell devices and is described in section 2.1.3.

2.1.1 Sputtering

Sputtered i-ZnO and ZnO:Al on glass/FTO substrates were obtained from Pilkington Group Ltd. during this research program to make a comparison with the electrodeposited materials. Sputtering is a form of physical vapour deposition (PVD) and takes place in a vacuum chamber evacuated to pressures of around 10^{-6} to 10^{-10} Torr. A gas, usually argon, is pumped into the chamber to produce a glow discharge to a pressure of around 1 to 100 mTorr. The target material is negatively biased between 0.5 to 5 kV and the substrate is grounded. The target has a dual function during sputtering deposition; it is the source of coating material and the cathode for sustaining the glow discharge. The target attracts positive gas ions from the glow discharge, which hit the surface and knocks out atoms in the vapour phase. These atoms diffuse towards the substrate under the high pressure of the chamber. The target is usually water-cooled to prevent over-heating [Stuart 1983, Bunshah 1994].

Direct current (DC) discharge methods are usually used to sputter metals and a radio frequency (r.f.) source must be used to sputter non-conductors to prevent charge accumulation at the target. However DC sputtering has been used to deposit ZnO and overcomes the slow deposition rate associated with r.f. sputtering. The drawback to DC sputtering is the high energy of ejected particles which can damage the underlying semiconductor layer, producing dislocations and defects at the interface [Lee *et al.* 2000]. The r.f. sputtering technique can be used to deposit conductive, semiconducting and insulating materials, usually operating at a frequency of 13.56 MHz. This frequency has been found to be sufficient to prevent significant charge accumulation when the target is negatively biased [Stuart 1983, Bunshah 1994].

2.1.2 Chemical Bath Deposition

When depositing using CBD the precursor materials are dissolved in a solvent to form a solution. The substrates are often glass slides or TCO glass, which are dipped into the solution. The reagents undergo a chemical reaction, depositing a thin layer on the surface of the glass. The thickness of the deposited layer is dependent on the amount of time the substrate is dipped in the solution and the rate and lifetime of the reaction. This technique has the advantage of being a low cost method of film growth producing large area, uniform and well adhered layers. Disadvantages of using this technique are significant chemical wastage and thickness limitation influenced by the chemical reaction lifetime [Ortega-Borges & Lincot 1993]. The as-deposited films are usually annealed to improve the structural, optical and electrical properties. CBD of CdS was carried out during this research program and more detailed discussion of the reaction mechanism and results are found in Chapter 4.

2.1.3 Electrodeposition

Potentiostatic electrodeposition was used for growth of CIGS and CdTe absorber materials and i-ZnO and ZnO:Al window layers during this research program. Electrodeposition of metals is a well established science and has been used for industrial purposes for approximately 150 years. The electrodeposition of semiconductors is a recent development, used in the production of electronic devices since the late 1970's

[Markvart 2000]. Electrodeposition has the advantage of being a non-vacuum, low-cost, scalable and manufacturable technique. Self purification of the electrolyte is a further advantage, enabling removal of impurities from the solution before growth of the layer [Bhattacharya *et al.* 2000, Lincot 2005, Dharmadasa & Haigh 2006]. Drawbacks to using this technique are the need for a conducting substrate and variation in sheet resistance as a function of deposition time causing the possibility of inconsistent film growth or limited thickness. The solution is usually acidic which may limit the film thickness.

A conventional three-electrode electrodeposition system consists of a cathode, anode and reference electrode as illustrated by Figure 2.1. The cathode is connected to the substrate; the counter electrode is positioned parallel to this at a suitable distance. The reference electrode is positioned at 45° to the cathode and is used to maintain a constant voltage at the cathode surface. The material properties are dependent on the several parameters, ionic concentration, pH, temperature, applied voltage and stirring rate. The highest purity chemicals are used to minimise contamination. Deposition from an aqueous medium enables solution temperatures of <85°C and non-aqueous electrolytes permit higher temperatures which may improve the properties of the layer. Although electrodeposited material is deposited at relatively low temperatures reducing cost, materials require post-deposition heat-treatment to improve the properties of the layer [Dharmadasa & Haigh 2006].

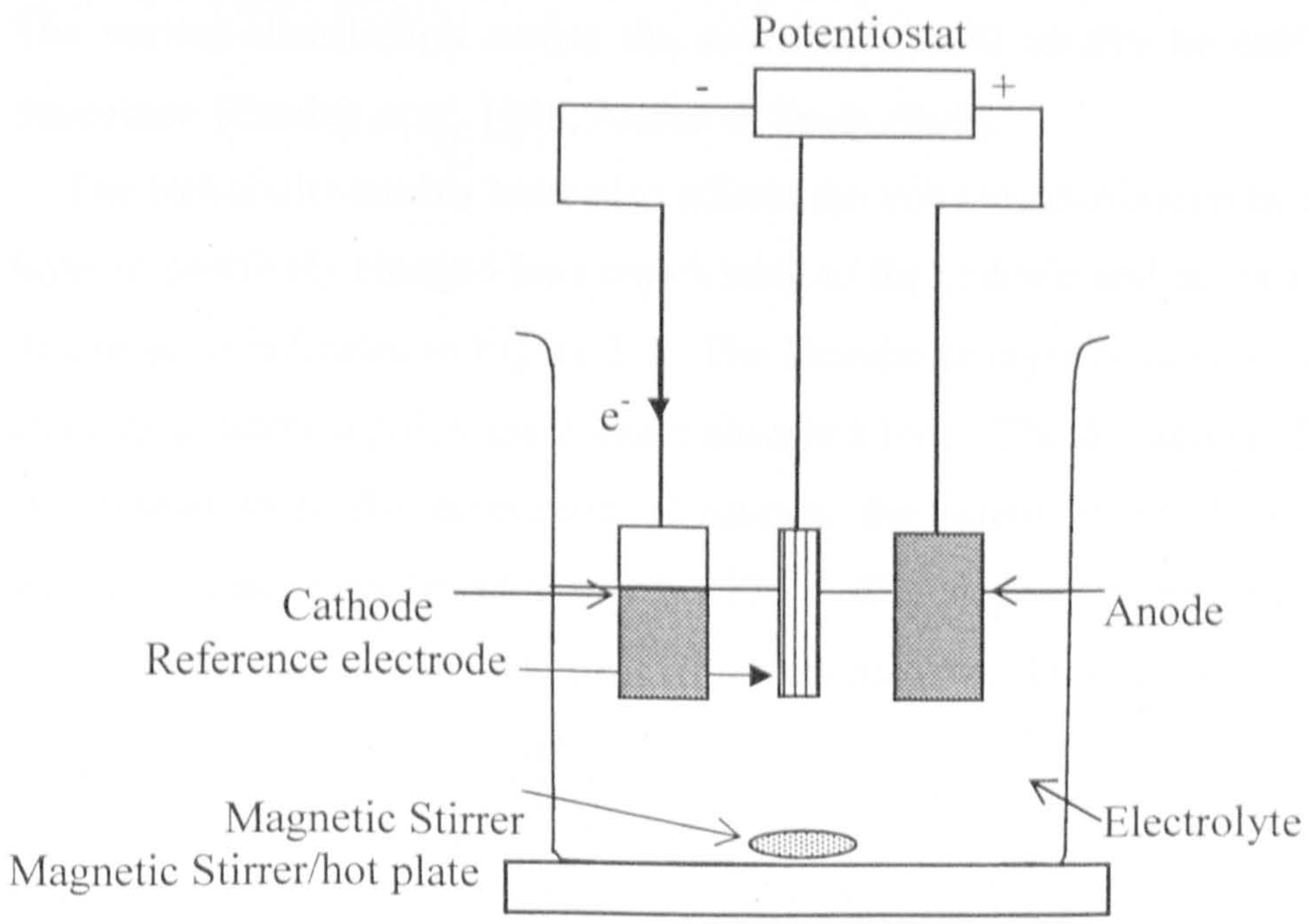

Figure 2.1. Typical three-electrode electrodeposition system.

When a voltage is applied between the cathode and anode, positive and negative ions are attracted towards each respectively. Cathodic electrodeposition is most common as ionic species are usually positive and anodic deposition has been shown to produce poor stoichiometry and adhesion to the substrate. The addition of additives to the electrolyte may increase the quality of the deposited layer, for example its uniformity and adhesion, but should not become part of the film [Pandey *et al.* 1996].

Potentiostatic deposition involves using a DC power supply and constant voltage. On application of the voltage, cations move towards the cathode, gain an electron and discharge as indicated by reaction 2.1.

$$A^+ + e^- \leftrightarrow A \tag{2.1}$$

If the electrolytic bath contains more than one species both types of ions may deposit simultaneously, forming a compound at the cathode as expressed by reaction 2.2.

$$A^+ + B^+ + 2e^- \leftrightarrow AB \tag{2.2}$$

Both reactions 2.1 and 2.2 are reversible reactions and under the right conditions the deposited layer may be oxidised releasing an ion and electron back into the solution. The range of cathodic voltages over which ions deposit depends on the specific element. The current distribution across the substrate should ideally be uniform for an even deposition [Pandey *et al.* 1996, Atkins & Paula 2005].

The Helmholtz double layer also affects the voltage distribution by attracting a dense layer of positively charged ions which stick to the cathode and act as a barrier for cation discharge as indicated in Figure 2.2. The Helmholtz layer is around 100 Å in width and consists of water dipoles and contact absorbed ions. The formation of this layer causes an obstruction to the deposition of cations; the extent of which may be reduced by stirring the solution [Pandey *et al.* 1996]. The deposition parameters may be used together with the Faraday relation (2.3) to estimate the thickness of the deposited layers.

$$T = \frac{itM}{nFA\rho} \tag{2.3}$$

where i = Current (A), t = time (s), M = Atomic Weight, n = Number of electrons transferred, F = Faraday's constant (96500 C mol^{-1}), A = Area of substrate (m^2) and ρ = density (Kg m^{-3}).

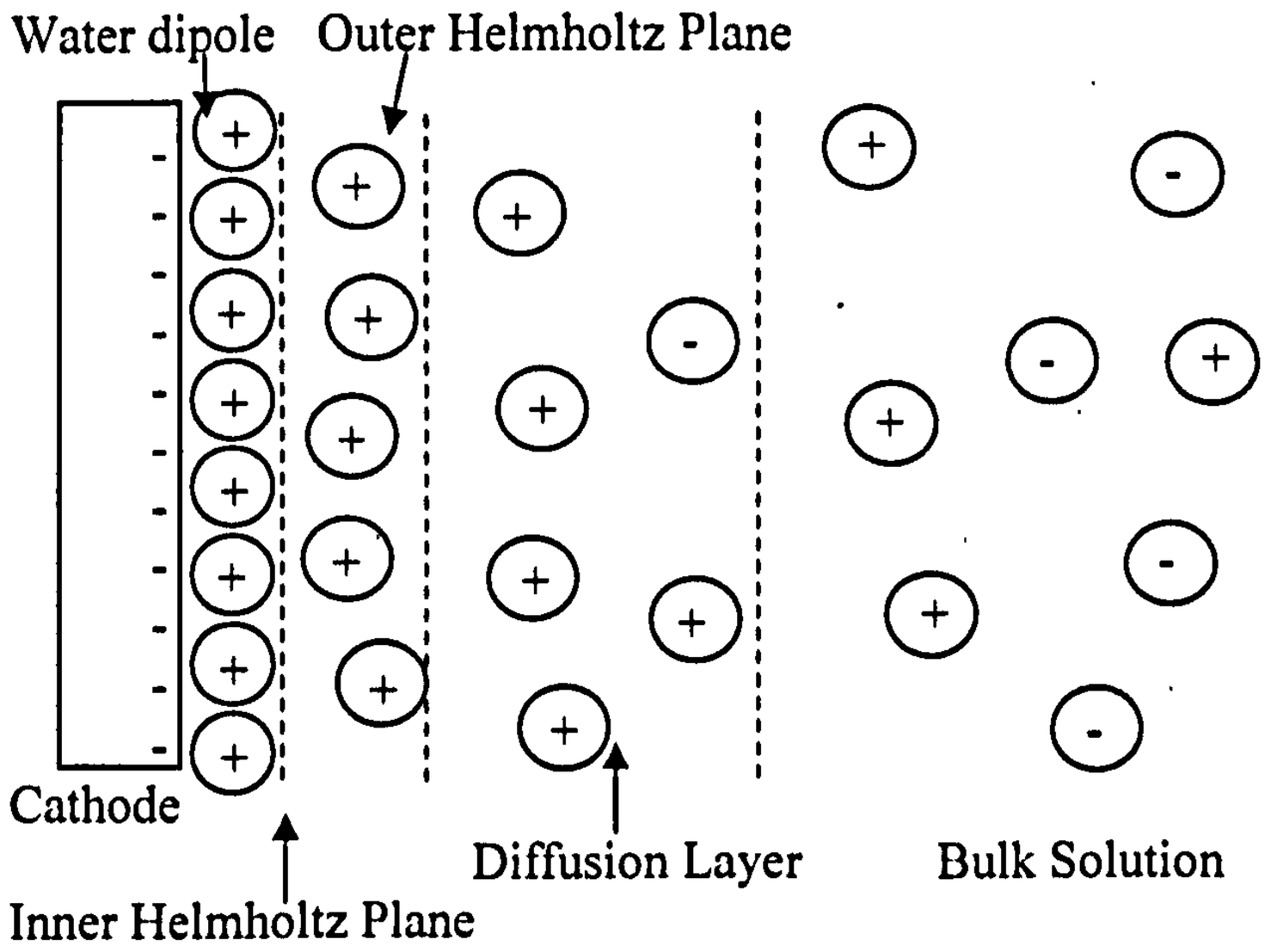

Figure 2.2. Illustration of the Helmholtz double layer formed at the cathode surface due to attraction of positively charged ions.

2.2 Material Characterisation Techniques

There are numerous characterisation techniques suitable for studying solar energy materials. In order to carry out a thorough investigation, structural, optical and electrical properties of the materials developed during this research were investigated, a brief summary of each is described in the following sections.

2.2.1 X-ray Diffraction

X-ray diffraction (XRD) is a non-destructive technique used for compound and phase identification and crystallographic analysis. A Philips X-Pert Pro-diffractometer was used to carry out XRD of layers during this research. The Miller indices (hkl), lattice spacing (a,b,c), grain size and degree of crystallinity were determined from the XRD data.

X-rays are short wavelength, high frequency electromagnetic waves with wavelength and energy in the range of $0.01<\lambda<100$ Å and $0.1<E<1000$ keV respectively. The wavelength of x-rays is comparable to atomic spacing making them suitable for probing materials on an atomic level. X-rays are generated in a sealed evacuated tube when

high energy electrons emitted from a tungsten target are accelerated by an anode, bombarding a target material such as Cu. The Cu atom emits characteristic photons having K_α wavelength of λ=0.15418 nm. X-rays are emitted in all directions and travel towards the sample under investigation. The x-rays penetrate the sample at an angle θ and either travel through or are diffracted by atoms, with an emission angle of 2θ, as indicated by Figure 2.3 [Bragg 1913].

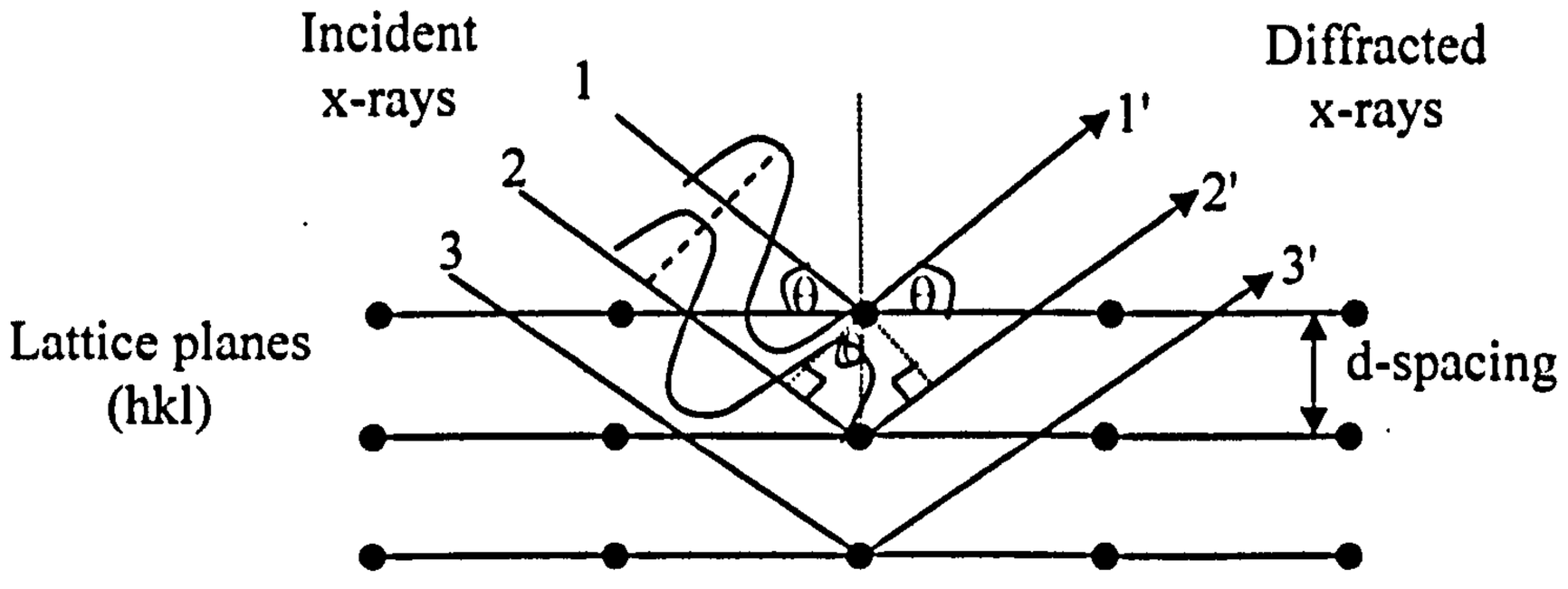

Figure 2.3. Illustration of x-rays scattered by the parallel atomic planes of a crystal.

Bragg's law describes the conditions which must be met for diffraction to occur. When x-rays are scattered by atoms arranged in parallel planes as illustrated by Figure 2.3, path length and phase differences may arise. When the summed amplitude of reflected waves from the first and second atomic planes are in phase the path difference is an integral number of wavelengths and XRD is observed. The intensity of the diffracted peaks is determined by the degree of crystallinity of the sample. Bragg's law is expressed by equation 2.4 [Bragg 1913].

$$n\lambda = 2d\sin\theta \qquad (2.4)$$

where n = integer, λ = wavelength (m), d = d-spacing (m) and θ = diffraction angle (°).

When the diffractometer is operating in θ-2θ mode the x-ray source is incident at an angle θ to the material surface, diffracts and is emitted at an angle θ. The detector rotates by an angle 2θ, allowing bulk material properties to be identified. In addition to this, a glancing angle mode enables a few nanometres of the surface layers of the sample to be probed. In this mode a fixed incident angle is selected, for example 0.5° whilst the detector scans over a chosen 2θ range. The obtained diffraction pattern is

almost unique for each material, giving reflection in the 2θ positions, which may be used to determine the d-spacing of the sample. The diffraction pattern is compared to standard Joint Committee on Power Diffraction Standards (JCPDS) files for phase identification. The orientation of a plane in a lattice is defined by its Miller indices. Miller indices are reciprocals of the fractional intercepts within the unit cell axes [Cullity & Stock 2001].

The Scherrer relation (2.5) is derived from Bragg's law and may be used to determine the grain size of the sample under investigation.

$$D = \frac{0.89\lambda}{b\cos\theta} \tag{2.5}$$

where D = grain size (m), λ = wavelength of incident radiation (m), b = full width at half maximum (FWHM) of the diffracted lines (radians) and θ = angle of diffraction (°).

The lattice parameters (a,b,c) may also be determined and compared with the standard values. Equations 2.6 to 2.8 indicate the lattice parameter equations for cubic, tetragonal and hexagonal unit cells which were used within this research [Cullity & Stock 2001].

Cubic a=b=c

$\alpha = \beta = \gamma = 90°$ $$\frac{1}{d^2} = \frac{h^2 + k^2 + l^2}{a^2} \tag{2.6}$$

Tetragonal a=b≠c

$\alpha = \beta = \gamma = 90°$ $$\frac{1}{d^2} = \frac{h^2 + k^2}{a^2} + \frac{l^2}{c^2} \tag{2.7}$$

Hexagonal a=b≠c

$\alpha = \beta = 90°\ \gamma = 120°$ $$\frac{1}{d^2} = \frac{4}{3}\left(\frac{h^2 + k^2 + hk}{a^2}\right) + \frac{l^2}{c^2} \tag{2.8}$$

where d = d-spacing (m), (hkl) = Miller Indices and a,c = lattice parameters (m).

2.2.2 X-ray Fluorescence

X-ray fluorescence is a non-destructive technique for compositional analysis of materials by identifying the concentrations of elements present in the layer. The sample is bombarded by high energy primary x-ray photons which knock out inner shell electrons from the atoms of the sample. The inner shells of the unstable atoms are filled by outer shell electrons which emit a secondary x-ray photon, known as fluorescence. The wavelength/energy of this x-ray photon is characteristic of the emitting atom and thus can be identified on detection [Jenkins 2001].

The x-rays produced by the sample have varying wavelengths, dependent upon the interacting element. They pass through a collimator and strike a crystal at an angle 0 where they diffract. According to Bragg's law (2.4), diffraction occurs when the emitted wavelengths from successive planes interfere constructively, therefore only these wavelengths reach the detector [Cullity & Stock 2001]. The intensity of the emitted photons is proportional to the concentration of the responsible element. Sequential measurement involves a number of elements being measured one after the other [Jenkins 2001].

The crystal rotates at an angle θ and the detector rotates through increments of 2θ and converts measured photon energies into voltage pulses. The number of voltage pulses is recorded as a function of amplitude. The peak intensities are compared with reference samples for identification. The instrument must be calibrated by measuring the peak intensities of reference samples of known composition. The instrument used for analysis of materials during this research was a Philips MagiX Pro instrument with rhodium target x-ray tube with 4 kW power for the sequential spectrometry measurement of elements [Jenkins 2001]..

2.2.3 Scanning Electron Microscopy

Scanning electron microscopy (SEM) is a useful technique to study the surface morphology of materials. A Philips FEI Nova NanoSEM was used for analysis of materials during this research program with an accelerating voltage of 20 kV. The

electrons have suitably short wavelengths of between 0.01 to 0.001 nm and are able to probe the surface of samples. The resolution limit of an SEM instrument is defined by the width of the excited electron beam and interaction volume of electrons in a solid. Electrons are strongly scattered by air molecules and therefore require a HV (10^{-6} to 10^{-8} Torr) system for operation. The basic layout of a scanning electron microscope is illustrated in Figure 2.4 [Goodhew *et al.* 2001].

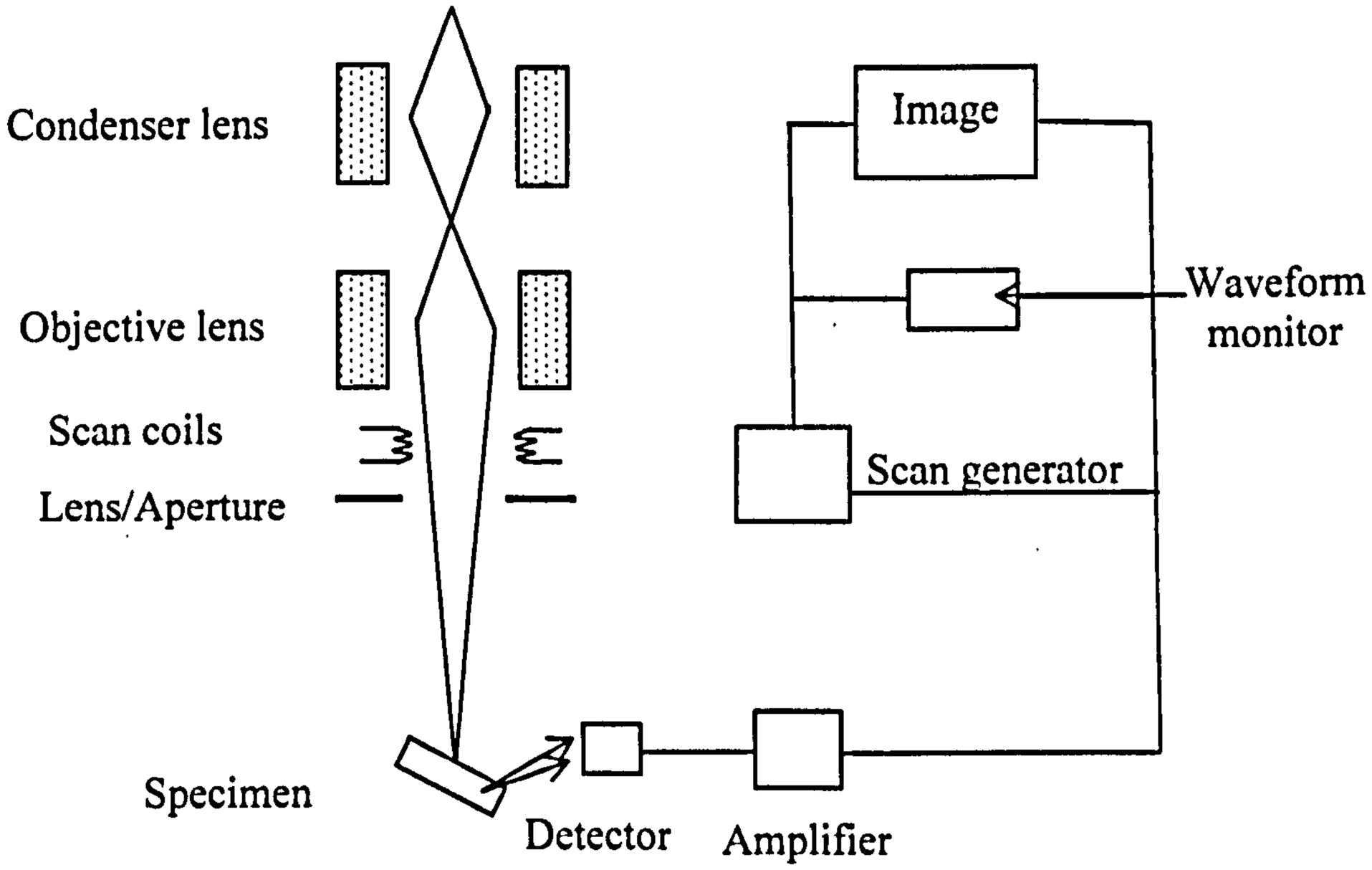

Figure 2.4. Schematic diagram illustrating the main components of the SEM instrument.

Samples are secured onto metal stubs using adhesive carbon foil, which are positioned on the sample holder within the focal range of the lenses. Conductive silver dag paint is used to ensure contact between the stub and the sample. Ensuring the sample is fully conductive is important due to the heavy influx of electrons that would lead to charging of insulating material. Charging results in image degradation such as blurring and over brightness.

The electron beam is emitted by the electron gun and is focused by magnetic condenser and objective lenses. The lenses are made of a soft iron core, around which wire is coiled. Current flows through the wire creating a magnetic field in the air gap of the iron core. When the current in the condenser and objective lenses changes, a proportional change occurs in the field strength (B), thus altering the focal length of the lenses. Magnetic scan coil lenses are used to deflect the electron beam to the desired

position on the sample. The scan generator is used to produce a varying current causing the scan coils to systematically scan the beam back and forth over the sample surface. Apertures are used to control the beam current and convergence angle. Two types of images may be obtained from SEM, secondary and backscattered. Secondary electrons have low energy typically <50 eV and escape from the first 20 nm of the sample surface. Backscatter electrons escape from the bulk of the sample (500 nm) and have energy >50 eV. Separate detectors are used for detecting secondary and backscattered electrons due to the nature of the radiation. Electrons pass through a grid and are accelerated by a potential of 10 keV towards a scintillator. Light is emitted on electron impact and is transmitted through a light tube into photomultiplier, which converts photons to electrons, multiplying the signal [Goodhew *et al.* 2001].

Other useful information which can be extracted from SEM is compositional analysis using energy dispersive x-ray analysis (EDX). The sample is bombarded by high energy electrons which interact differently depending on impact. Some incident electrons knock out a tightly bound inner shell electron leaving behind a hole. The hole is filled by an outer shell electron with additional emission of characteristic x-rays. The energy of emission is characteristic of the atoms involved, thus allowing elemental analysis. The EDX detector measures the number of x-rays as a function of energy [Goodhew *et al.* 2001].

2.2.4 Optical Spectroscopy

Optical absorption is a useful technique for determining the bandgap energy of semiconductors. A Unicam UV-2 UV-Visible spectrometer with wavelength ranging from 200 to 1100 nm was used for analysis of material during this research. When carrying out measurements a baseline was initially taken using a sample of the substrate which is automatically subtracted from all other readings. The experimental set-up is illustrated by Figure 2.5. The wavelength range of light may be specified and travels to the sample from the source, interacts and is detected. A graph of absorption as a function of wavelength may be plotted indicating the samples ability to absorb light in a given wavelength range.

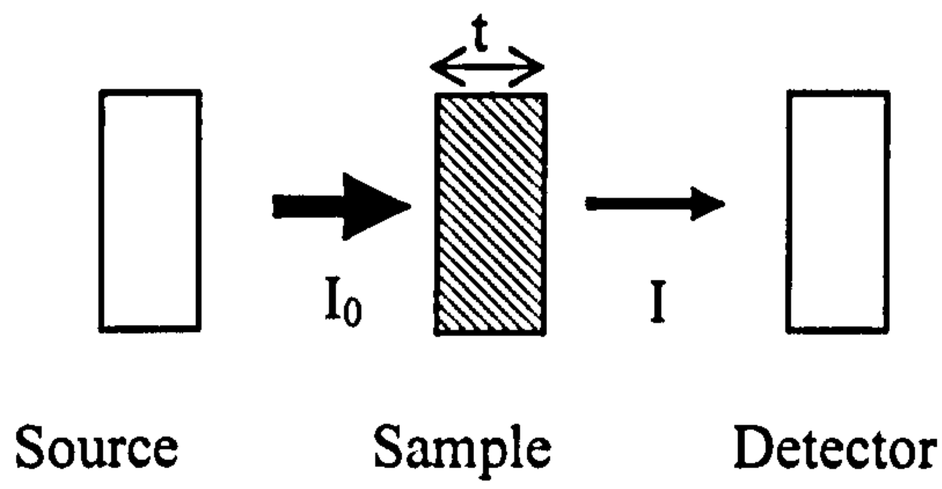

Figure 2.5. Illustration of the experimental set-up for optical spectroscopy.

Using equation 1.1 in Chapter 1 enables the photon energy of a given wavelength to be calculated. The absorption coefficient may be calculated using Beer's law and is a measure of the energy loss of an incident beam when passing through a material.

$$I(x) = I_0 \exp(-\alpha x) \tag{2.10}$$

$$\alpha = \frac{2.303 Abs}{x} \tag{2.11}$$

where I = light intensity at distance x in the sample, I_0 = intensity of the incident radiation, α = absorption coefficient (m^{-1}) and Abs = absorbance of radiation in the sample.

When calculated the absorption coefficient can be plotted as a function of photon energy to enable the determination of the bandgap energy of the semiconductor [Sundaram & Bhagavat 1981].

The transmission spectra may also be obtained using the same instrument as for optical absorption. The transmitted radiation is detected and may be plotted as a function of wavelength. The absorption edge indicates the wavelength at which the photon energy is equal to the bandgap energy of the semiconductor and at higher energies a percentage of incident photons are absorbed. The percentage transmission is dependent on the bandgap energy of the semiconductor; smaller bandgap energies transmit fewer wavelengths as a larger proportion of photons have energy greater than the bandgap and so are absorbed [Sundaram & Bhagavat 1981].

2.2.5 Photoelectrochemical Cell Studies

Photoelectrochemical (PEC) cell studies can be used to determine the electrical conductivity type of thin film semiconductor materials. The principle of PEC is based upon a liquid/solid junction, the V_{oc} of which is the difference between the dark and illuminated voltage. The experimental set-up is illustrated in Figure 2.6 indicating the semiconductor/electrolyte junction with a carbon rod counter electrode directly connected to a digital voltmeter. A reference electrode can also be used with a computerised potentiostat. All components are immersed in a suitable electrolyte, which must be sufficiently conducting, non-toxic and non-destructive to the thin film. The voltage of the system is measured under dark (V_{dark}) and illuminated (V_{light}) conditions. V_{dark} is subtracted from V_{light} to give the V_{oc}; the sign of which indicates the electrical conductivity type of the semiconductor, negative for n-type and positive for p-type. The system can be calibrated with a known sample such as an n-type CdS layer. It is important the sample is not immersed beyond the film edge as this would give a false reading [Grätzel 2001].

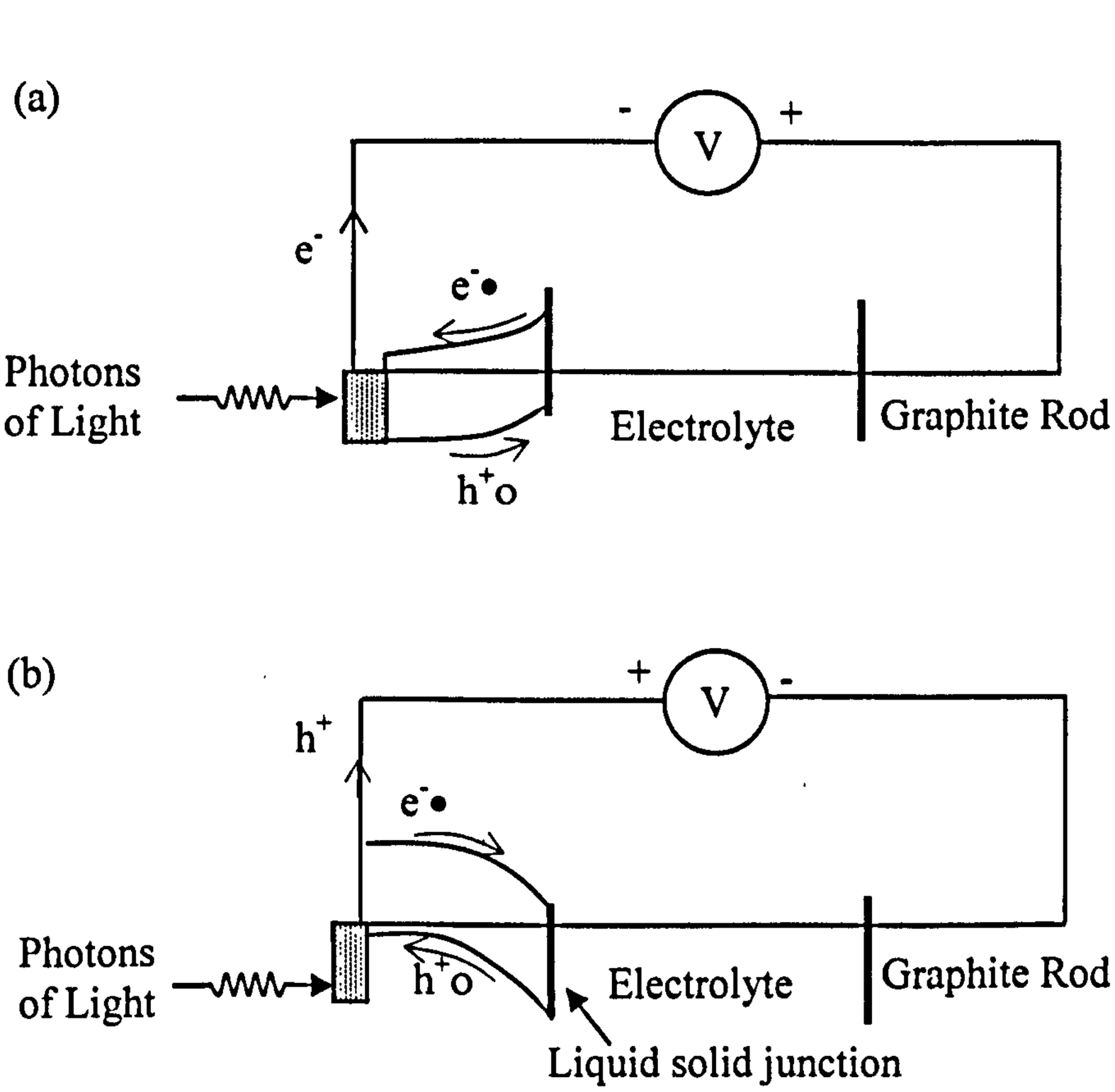

Figure 2.6. Liquid/semiconductor interface for (a) n-type and (b) p-type semiconductors.

The measured V_{dark} is a result of the potential difference between the liquid/solid junction and the carbon rod immersed in the ionic solution. Under illuminated conditions the photo-generated current flows in the directions shown in Figure 2.6 due to band bending. Photons excite electrons from the valence band to the conduction band of the semiconductor where they are free to flow and voltage changes can be measured by the voltmeter. [Lincot *et al.* 1990].

In an n-type semiconductor, electrons are generated and flow through the external circuit due to the band bending at the liquid/solid interface, holes flow in the opposite direction into the electrolyte. Opposite principles apply for a p-type semiconductor; photo-generated electrons are driven towards the electrode/electrolyte interface where they are transferred into the solution, reducing positively charged ions. A large PEC signal indicates the formation of a PV depletion region due to ideal doping of the semiconductor of 10^{14} - 10^{17} cm^{-3}. Heavily doped layers having p^+ and n^+ electrical conductivity (>10^{18} cm^{-3}) act in the same manner as a metal and therefore exhibit zero PEC signal due to a very thin or non-existent depletion region; insulating materials also give zero PEC signal. Figure 2.6 illustrates a simplified version of the liquid/semiconductor interface for both an n-type and p-type semiconductor [Grätzel 2001].

2.2.6 Electrical Measurements

2.2.6.1 Current-Voltage Measurements

Conventional current-voltage (I-V) measurements were conducted using a fully automated I-V system, on fully processed devices to determine the solar cell parameters; V_{oc}, I_{sc} and FF. The front and back electrical terminals of a solar cell are connected to a power supply and a voltage is applied, usually sweeping over a forward and reverse bias voltage range. Taking I-V measurements under dark conditions allows the rectification factor to be estimated, which is the ratio of the forward (I_F) and reverse bias (I_R) currents at a given voltage.

The diode equation defined as

$$I = I_0 \exp\frac{eV}{nkT} - 1 \tag{2.12}$$

and is an expression of the current through the diode as a function of voltage. The ideality factor (n) may be determined from the gradient of the forward bias log I vs V curve. The potential barrier height may be estimated using equation 2.14,

$$I_0 = SA^*T^2 \exp\left(\frac{-e\phi_b}{kT}\right) \tag{2.14}$$

where I_0 = Current intercept, S = Area of contact (m^2), A^* = Richardson constant (12×10^4 AKm^{-2}), T = Temperature (K), e = Electronic Charge (1.6×10^{-19} eV), k = Boltzmann constant (1.38×10^{-23} m^2 kg s^{-2} K^{-1}),

although this is only accurate when the ideality factor is close to unity. The series resistance may be determined from the high forward bias slope of the linear-linear I-V curve [Sze & Ng 2001].

2.2.6.2 Capacitance-Voltage Measurements

The capacitance of a device is a measure of its ability to hold electric charge. Capacitance of an n-p junction or Schottky barrier occurs at the depletion region due to a difference in charge on each side of the junction. Capacitance-voltage (C-V) measurements of p-n junctions or Schottky barriers may be carried out by probing the depletion region within the device. The depletion region does not contain charge carriers but does contain ionised donors or acceptors. A DC voltage is applied across the device which is often varied from forward to reverse bias; thus varying the depletion region width. An alternating current (AC) signal with a high frequency is applied for measurements of the capacitance due to the depletion region. The depletion region width varies as a function of applied DC voltage, altering the capacitance of the device which may be calculated using equation 2.15 [Sze & Ng 2001]. Capacitance-voltage measurements pose limitations when estimating the barrier heights due to the presence of defects in the depletion region.

$$C = \frac{\varepsilon_o \varepsilon_r A}{W} \tag{2.15}$$

where C = Capacitance (F), A = Contact Area (m^2), W = Depletion region width (m), ε_0 = permittivity of free space 8.85×10^{-12} A^2 s^4 kg^{-1} m^{-3} and ε_r = relative permittivity.

The free carrier concentration (N_a or N_d) may be determined from the slope of the $1/C^2$ vs V graph by using equation 2.16.

$$\frac{1}{C^2} = \frac{2}{\varepsilon_s A_2 e N_d}(V + V_d) \tag{2.16}$$

where $\varepsilon_s=\varepsilon_0\varepsilon_r$ permittivity of free space × relative permittivity, N_d = Free carrier concentration (m^{-3}), V = Voltage (V), V_d = Diffusion Voltage (V) and e = Electronic Charge (eV).

Chapter 3 Literature Review

The literature review is presented in three separate sections, describing key aspects of ZnO (3.1), CIS (3.2) and CdTe (3.3).

3.1 Zinc Oxide

3.1.1 Introduction

The ZnO literature review will introduce the subject in context of the research and will then discuss growth of ZnO using both sputtering and electrodeposition techniques followed by a discussion of the structural and electrical properties.

Zinc and oxygen are group II and VI elements with atomic numbers 30 and 8 and atomic weights 65.409 and 15.999 respectively. In stable form ZnO adopts a wurtzite phase and takes the mineral name of zincite. The other two forms of ZnO are zincblende and rock salt phases, which form under high pressure and revert back to wurtzite on decompression [Ozgur *et al.* 2005]. ZnO has wide direct bandgap energy of 3.20 to 3.40 eV and exhibits n-type electrical conductivity due to intrinsic defects such as oxygen vacancies and interstitial zinc atoms.

Recently ZnO has received considerable attention in the field of photovoltaics, due to its suitability as both an intrinsic n-type buffer layer (i-ZnO) and doped transparent top contact for CIGS solar cells. Substrate device structures usually consist of glass/Mo/CIGS/CdS/i-ZnO/ZnO:Al and the ZnO bi-layer is know to improve the device performance. Various reasons have been given in the literature as to why ZnO is beneficial although a conclusion is still to be agreed. Most commonly sputtering is used to deposit i-ZnO for PV applications. Growth of ZnO using electrodeposition has also emerged as a possible alternative [Gal *et al.* 2000]. The properties of ZnO are summarised in Table 3.1 [Pearton *et al.* 2005].

Table 3.1. Properties of ZnO.

Property	Value
Density	5.606 g cm^{-3}
Lattice Parameters	a=3.253 Å, c=5.120 Å
Stable Phase at 300 K	Hexagonal, Wurtzite
Melting Point	1975°C
Dielectric Constant	8.656
Refractive Index	2.008
Bandgap Energy	3.40 eV

3.1.2 Sputtered Zinc Oxide

The highest efficiency to date for CIGS solar cells is 19.9%, reported by the U.S. National Renewable Energy Laboratory (NREL) [Repins *et al.* 2008]. The structure contains an i-ZnO and ZnO:Al bi-layer deposited using r.f. sputtering. Showa Shell, Japan was one of the first groups to use a ZnO bi-layer with the aim of improving the device efficiency [Cooray *et al.* 1997]. Sputtering is now the standard deposition technique used for growth of the ZnO bi-layer for PV applications. Sputtering has advantages of being scalable and has controllability of film thickness and composition [Sittinger *et al.* 2006].

Kushiya *et al.* suggested the introduction of a thin, high resistivity transparent i-ZnO layer to prevent sputter damage to underlying layers by high energy particle bombardment during deposition of the ZnO:Al. Kushiya reported depositing i-ZnO using r.f. sputtering on to CIGS as lower power is required for this growth method compared to DC sputtering [Kushiya *et al.* 2001]. However DC and r.f. sputtering have been used to deposit both i-ZnO and ZnO:Al layers in various investigations, contradicting the purpose of the i-ZnO layer for sputter damage protection [Kushiya *et al.* 2001, Kemell *et al.* 2005]. The use of i:ZnO in CIGS solar cells is known to improve the efficiency but the reason behind this phenomenon is still under debate.

It has been suggested the i:ZnO layer provides an effective seed layer to enhance grain growth of the ZnO:Al layer [Lee *et al.* 2000]. Other suggestions have considered possibility of shunt path prevention between CIGS and the TCO. If the CdS has failed to form an even coating a thin resistive i-ZnO layer would fill in these shunt paths and prevent the device from shorting [Ishizuka *et al.* 2005]. A variety of precursors have

been used to sputter ZnO including fully or partially metallic (Zn/Al, ZnO/Al) or fully oxidised ($ZnO:Al_2O_3$) targets. In the case of metallic or partially oxidised targets a reactive oxygen gas is pumped into the chamber and in all cases an Ar ambient is utilised as an enhancing gas [Ozgur *et al.* 2005].

Optimisation of the i-ZnO thickness is essential for device fabrication; excessive thickness increases the series resistance and degrades device performance. Studies have been carried out to optimise the thickness and reports are often contradictory. Cooray *et al.* investigated the effect of i-ZnO thickness between 3 to 60 nm on device performance. The most notable improvement was observed for the thinnest layer (3 nm) and performance worsened with increasing thickness [Cooray *et al.* 1997]. This is in contrast with other reports of optimum thicknesses of 50 to 110 nm [Nagoya *et al.* 2003]. Ishizuka carried out a similar investigation varying the thickness of i-ZnO from 0 to 180 nm. Little change in efficiency and FF was observed for thicknesses between 0 and 70 nm (15.0 to 15.5% and FF = 0.70 to 0.75 respectively), although both parameters decreased when the i-ZnO layer was thicker than 110 nm [Ishizuka *et al.* 2005]. Lee *et al.* reported the series resistance of the CIGS device to increase with increasing i-ZnO layer thickness from 300 to 1200 nm [Lee *et al.* 2000].

It has also been suggested diffusion of Al from ZnO:Al into i-ZnO during heat-treatment may cause Al doping of i-ZnO. This effect was expected to be greatest when the i-ZnO layer was thinner than 70 nm and could potentially dope the entire layer. When the thickness was greater than 70 nm the Al would not penetrate through the entire i-ZnO layer and may be the cause of the increased series resistance [Ishizuka *et al.* 2005].

The properties of sputtered ZnO can be controlled by changing the deposition parameters such as r.f. power, gas atmosphere and pressure and substrate temperature [Chang *et al.* 2001, Dang *et al.* 2007]. In order to avoid diffusion of CdS into the CIGS layer the substrate temperature should be controlled to prevent overheating when depositing both ZnO layers. The resistivity has been shown to decrease with increasing substrate temperature, thought to be due to enhanced grain size and reduction of defects in the device structure [Lee *et al.* 2000].

Martinez *et al.* investigated the effect of substrate temperature on ZnO properties when depositing ZnO:Al using reactive sputtering from Zn/Al targets. It was found that temperatures >380°C were necessary to achieve the activation energy required to form ZnO:Al [Martinez *et al.* 1997]. Contrary to this report, Chang *et al.* observed a

minimum resistivity of 4.2×10^{-4} Ω cm with a substrate temperature of 250°C, which was attributed to improved crystallinity. Above this temperature the resistivity was found to increase ascribed to the segregation of Al_2O_3 at grain boundaries [Chang *et al.* 2001].

Low O_2 chamber pressure produces oxygen deficient ZnO films which are dark and metallic in appearance, although the resistivity is low. Increasing the O_2 pressure improves optical transparency although the electrical properties deteriorate as oxygen vacancies were filled. The resistivity of i-ZnO has been shown to be in the range of $10^{-4} < \rho < 10^{7}$ Ω cm and is controlled by either doping the material or controlling the oxygen partial pressure [Ellmer 2000]. Increasing the gas pressure increases the energy of atoms arriving at the substrate, which subsequently promotes the deposition rate [Dang *et al.* 2007].

3.1.3 Electrodeposited Zinc Oxide

Although vacuum deposition technologies produce high quality layers there is an interest in movement towards lower cost processing techniques with the possibility of large-scale deposition. Electrodeposition has emerged as a suitable growth technique with the possibility of controllability of film thickness, shape and low temperature growth [Pauporte *et al.* 2000]. The progress to date has been encouraging with highest reported efficiencies of 11.4% for electrodeposited ZnO in CIGS devices [Gal *et al.* 2000]. From the literature it is apparent that electrochemical growth of ZnO has been mainly developed using two separate precursors, namely zinc nitrate, $Zn(NO_3)_2$ and zinc chloride, $ZnCl_2$ and is discussed in the following sections.

3.1.3.1 Deposition from Zinc Chloride Precursors

The earliest reported study of electrodeposited ZnO from aqueous solution containing $ZnCl_2$ in the presence of oxygen was in 1996 [Peulon & Lincot 1996]. Two main mechanisms occur within this medium, one is precipitation and the other is electrochemical reactions at the cathode surface. Soluble and insoluble complexes with Zn^{2+} ions and various ligands such as hydroxychlorides and hydroxides form in aqueous solution. Formation of ZnO at the cathode by reaction with molecular

oxygen occurs via reactions 3.1 and 3.2. The reaction of Zn^{2+} with water and oxygen molecules forms $Zn(OH)_2$ indicated by reaction 3.3 [Goux *et al.* 2005].

$$ZnCl^+ + 2OH^- \rightarrow ZnO + H_2O + Cl^- \tag{3.1}$$

$$Zn^{2+} + \frac{1}{2}O_2 + 2e^- \rightarrow ZnO \tag{3.2}$$

$$Zn^{2+} + \frac{1}{2}O_2 + H_2O + 2e^- \rightarrow Zn(OH)_2 \tag{3.3}$$

According to the Pourbaix diagram (Figure 3.1) the solubility of ZnO is limited below pH=6. Above pH=12 insoluble zinc hydroxide, $Zn(OH)_2$ colloids precipitate in the solution. The diagram indicates that theoretically ZnO forms over a wide voltage range and at more negative voltages than -1.00 V vs normal hydrogen electrode (NHE) metallic Zn deposition is predominant [Goux *et al.* 2005].

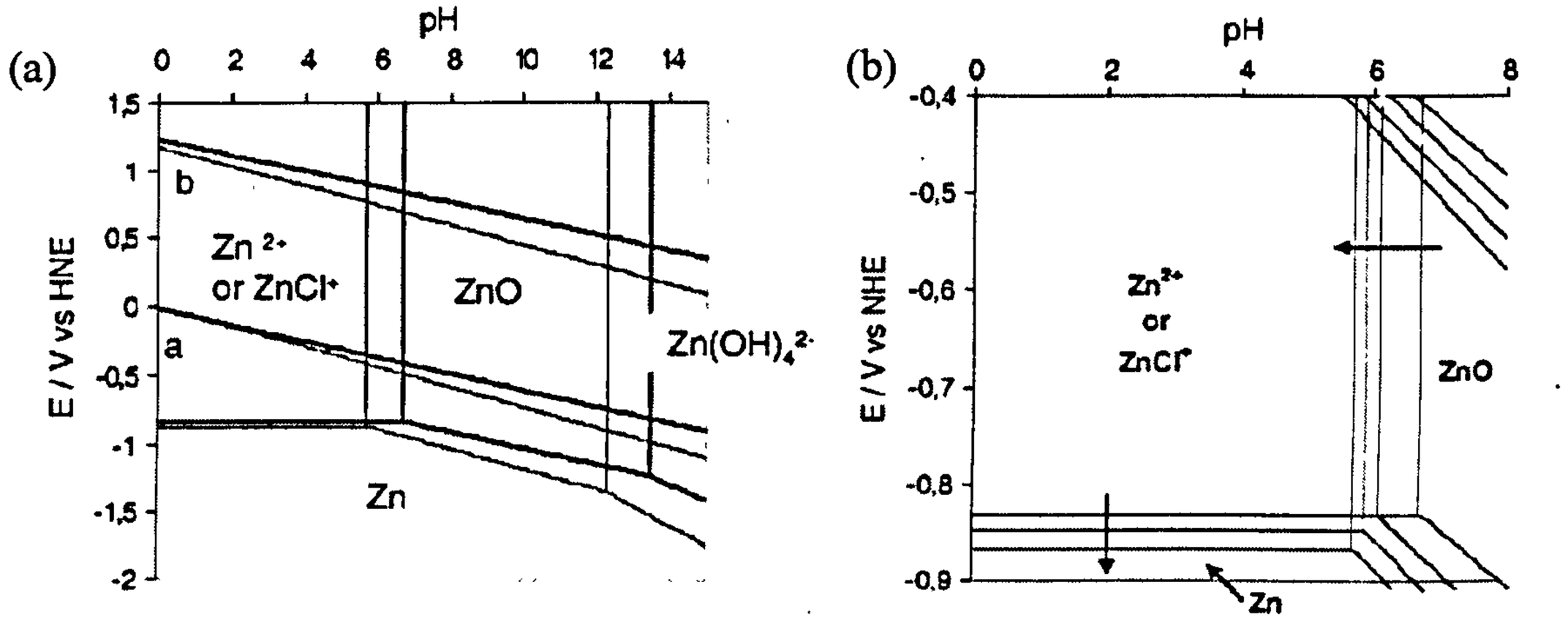

Figure 3.1. Pourbaix diagrams of ZnO, (a) the effect of temperature on the pH-potential of 5 mM $ZnCl_2$, thick line 25°C, thin line 90°C (b) ZnO deposition region is enlarged; the arrow represents increasing temperature of 25°C, 50°C, 70°C and 90°C [Goux *et al.* 2005].

Goux studied the effect of bath temperature on the deposition of ZnO and found between room temperature and 34°C, $Zn(OH)_2$ precipitation was predominant [Goux *et al.* 2005]. At low temperatures, nucleation is slow resulting in poorly crystalline, porous layers. Above 40°C the $Zn(OH)_2$ layer dehydrates via reaction 3.4 to form ZnO.

$$Zn(OH)_2 \rightarrow ZnO + H_2O \qquad (3.4)$$

Above 70°C the reaction rate increased forming ZnO crystallites. The concentration of dissolved oxygen in solution significantly decreases with increasing temperature from 1.5 mM at 20°C to 0.75 mM at 80°C [Goux *et al.* 2005].

Peulon *et al.* investigated the influence of temperature, oxygen concentration and zinc precursor concentration on the electrochemical deposition of ZnO. It was found the film growth increased linearly with temperature, with a rate of 1 μm h^{-1} at 85°C. At higher oxygen concentrations the ZnO layers were highly resistive. A linear relationship between the Zn^{2+} molarities of 5×10^{-4} and 3×10^{-2} M and growth rate was observed. The pH close to the electrode surface was found to increase to pH=10 from pH=6 due to the formation of hydroxide ions as a result of oxygen reduction via reaction 3.5 [Pauporte & Lincot 2001].

$$O_2 + 2H_2O + 4e^- \rightarrow 4OH^- \qquad E_o=0.4 \text{ V vs NHE} \qquad (3.5)$$

On the contrary, Yoshida *et al.* observed a reduction in pH during electrodeposition of ZnO. It was suggested the use of a Zn counter electrode maintained the pH by the oxidation of Zn to Zn^{2+}, although the specific mechanism was not described. Yoshida recommended that the area of this electrode should be restricted and placed in solution just before deposition to avoid an increase in pH pre-deposition [Yoshida *et al.* 2003]. Goux *et al.* and Pauporte *et al.* have also both employed Zn counter electrodes for this purpose in separate investigations [Pauporte *et al.* 2001, Goux *et al.* 2005].

3.1.3.2 Deposition from Zinc Nitrate Precursors

The earliest reported investigation devoted to the electrodeposition of ZnO from $Zn(NO_3)_2$ precursors was by Izaki & Omi in 1996. Deposition rates were explored as a

function of zinc nitrate concentration obtaining maximum deposition rates of 0.15 μm min^{-1} for a zinc nitrate concentration of 0.1 M [Izaki & Omi 1996, 1997]. The voltage range investigated was -0.7 to -1.4 V vs Ag/AgCl. Lower voltages produced porous layers, whilst at more negative voltages (-0.9 V) the crystallites rotated by 90° having (101) preferential orientation. The highest transmission of 70% was observed for layers deposited at this voltage.

Various substrate activation steps have been reported by different groups, attempting to increase the density of nucleation sites and promote compact film growth. Izaki claimed the SnO_2 substrates required anodic polarisation in 1 M NaOH solution followed by rinsing in deionised water [Izaki *et al.* 1996]. Goux *et al.* also employed this method by applying 0.65 V vs NHE for 1 hour in a similar solution [Goux *et al.* 2005].

Yoshida *et al.* and Pauporte *et al.* have both reported etching the substrate in nitric acid prior to deposition was an essential step in order to achieve oxygen reduction and nucleation at the substrate [Pauporte *et al.* 2001, Yoshida *et al.* 2003]. Canava and Lincot subjected the substrate to a galvanostatic activation step; holding the substrate at a certain current density for 15 seconds performs a redox process, which was claimed to promote the formation of a ZnO seed layer [Canava & Lincot 2000]. SEM indicated that subsequent deposition increased the density of crystallite formation, increasing compact growth and coalescence.

In the case of $Zn(NO_3)_2$ precursors; on release of the Zn^{2+} ion (dissociation 3.6) the nitrate molecule functions as a oxidising agent.

$$Zn(NO_3)_2 \rightarrow Zn^{2+} + 2NO_3^- \tag{3.6}$$

The reduction of nitrate (NO_3^-) to nitrite (NO_2^-) ions forms hydroxide ions at the surface of the cathode via reaction 3.7.

$$NO_3^- + H_2O + 2e^- \rightarrow NO_2^- + 2OH^- \tag{3.7}$$

This local increase in pH causes the formation of $Zn(OH)_2$ via reaction 3.8.

$$Zn^{2+} + 2OH^- \rightarrow Zn(OH)_2 \rightarrow ZnO + H_2O \tag{3.8}$$

The $Zn(OH)_2$ may decompose to form ZnO (reaction 3.4) during deposition or this step will occur during post deposition annealing.

Various authors have commented that the nucleation and growth mechanism of ZnO is not well understood, resulting in a varying film morphology [Ingham *et al.* 2008, Pauporte *et al.* 2000, Yoshida *et al.* 2004]. The growth characteristics such as size, orientation and morphology are influenced by the first few moments after application of the voltage [Canava & Lincot 2000].

The nucleation at the cathode is apparent from the current transient curve, by the increase in current density immediately after the application of voltage. The current density decreases and plateaus with time. Goux *et al.* reported the magnitude of the current density peak to increase with electrolyte temperature [Goux *et al.* 2005]. The density of nucleation centres may be increased by raising the oxygen concentration, leading to smaller grains [Pauporte *et al.* 2000].

The use of $Zn(NO_3)_2$ has the advantage of being highly soluble in aqueous solution. However the reduction of nitrate to nitrite on application of the voltage (reaction 3.7) renders the solution unusable after a few days storage. This limits the use of this precursor especially for commercialisation and scale-up [Yoshida *et al.* 1999].

3.1.3.3 Structural Properties

ZnO adopts a hexagonal wurtzite crystal structure having lattice parameters a=b=3.253 Å and c=5.120 Å, where ($a=b\neq c$), $\alpha=\beta=90°$ and $\gamma=120°$ [Rousseau 1998, Hammond 1997]. Each cation is surrounded by four anions at the corner of a tetrahedron and visa versa.

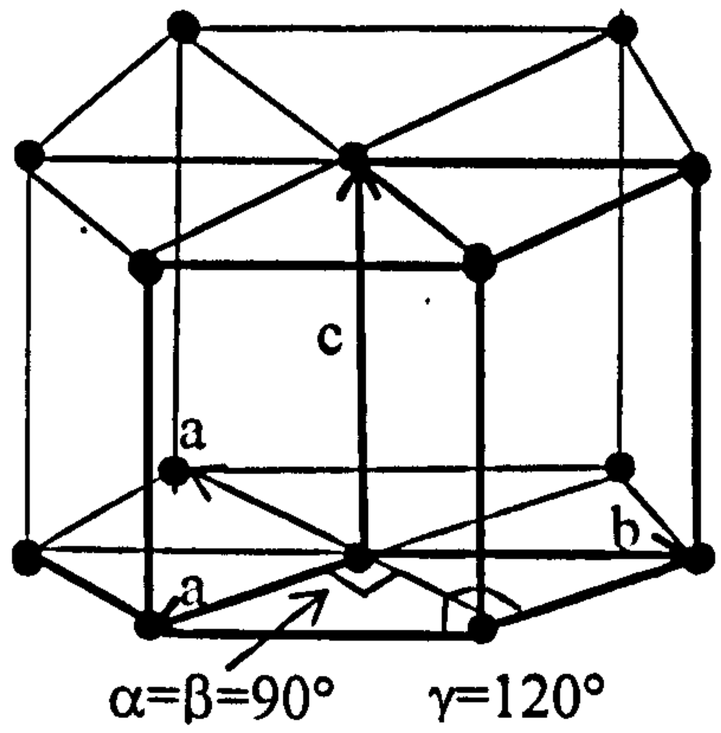

Figure 3.2. Illustration of a hexagonal Bravais unit cell, where $a=b\neq c$ and $\alpha=\beta=90°$ $\gamma=120°$ [Jawson & Rose 1983].

The hexagonal system has Miller-Bravais indices, referring to four axes (h k i l). The Miller indices (hkl) have their usual meanings and the index i is the reciprocal of fractional intercept on the a axis. Often only the (hkl) indices are used to describe crystal planes for a hexagonal structure [Cullity & Stock 2001]. Figure 3.3 illustrates the hexagonal wurtzite crystal structure of ZnO [Sowa & Ahsbahs 2006].

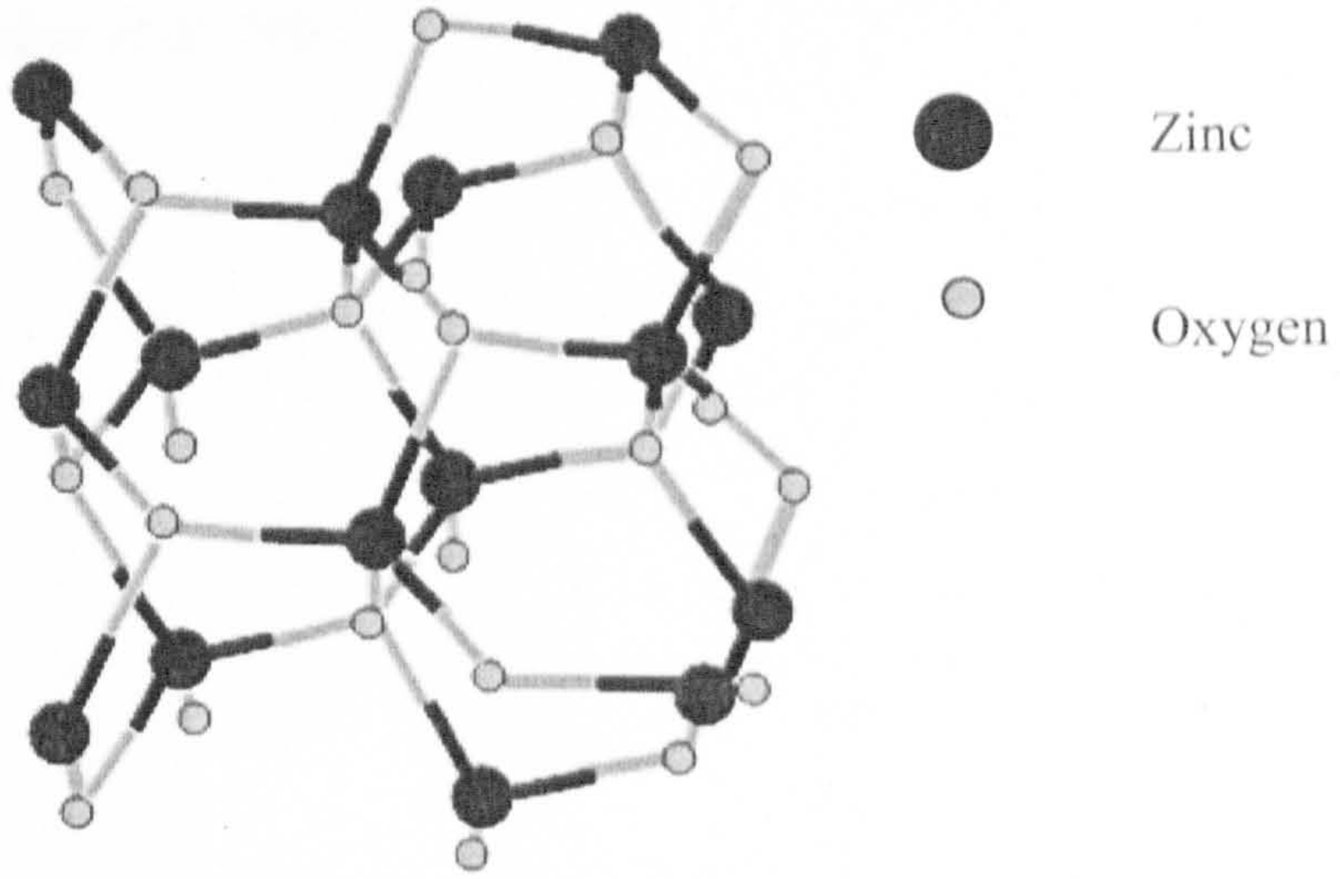

Figure 3.3. Illustration of the hexagonal, wurtzite crystal structure of ZnO [Sowa & Ahsbahs 2006].

3.1.3.4 Electrical Properties

Intrinsic ZnO exhibits n-type electrical conductivity due to deviation in stoichiometry due to the presence of native defects, Zn interstitial atoms (Zn_i) and oxygen vacancies (V_o). In both cases defect energy levels are introduced in the bandgap approximately 10 to 50 meV below the conduction band minimum forming donor levels [Pearton *et al.* 2004, Ozgur *et al.* 2005].

Extrinsic doping of ZnO to increase the electrical conductivity can be accomplished using group III elements, aluminium (Al), gallium (Ga) and indium (In) to replace Zn or group VII elements such as fluorine (F), chlorine (Cl), iodine (I) and bromine (Br) to replace oxygen [Kemell *et al.* 2003, Ozgur *et al.* 2005, Machado *et al.* 2005].

Bipolar semiconductors are often difficult to fabricate when dealing with materials with high bandgap energy. There are several reasons for this, self compensation of native defects, Zn_i, V_o or background impurities and low solubility of

dopant atoms in the host material. Prospective p-type dopant atoms for ZnO are group I atoms such as copper (Cu) and silver (Ag) substituting for Zn sites or group V elements, phosphorus (P), arsenic (As) or nitrogen (N) for substitution on the oxygen sites. According to Ozgur *et al.* group I elements tend to occupy interstitial sites rather than substitution sites and therefore act as donors instead of acceptors [Ozgur *et al.* 2005, Pearton *et al.* 2005]. The reproducibility of ZnO having p-type electrical conductivity has yet to be realised [Ozgur *et al.* 2005].

3.2 Copper Indium Diselenide

3.2.1 Introduction

The CIS literature review will discuss growth using electrodeposition from aqueous and non-aqueous media followed by an overview of the present status of commercially available solar cells and progress of laboratory scale work. Key aspects regarding device characteristics including the buffer and ODC layers and doping using Na, S and Ga will be described.

Group I-III-VI_2 materials such as CIS, CIGS and copper indium gallium sulphur selenide ($CuInGa(SSe)_2$ or CIGSS) are often referred to as chalcopyrite compounds due to their crystal structure. The atomic numbers and atomic weights of Cu, In and Se are presented in Table 3.2.

Table 3.2. Atomic numbers and weights for Cu, In and Se.

Element	Atomic Number	Atomic Weight
Cu	29	63.546
In	49	114.818
Se	34	78.960

CIS most commonly exhibits tetragonal phase having lattice parameters a=b=5.851 Å and c=11.726 Å. Figure 3.4 illustrates the structure of CIS [Schorr & Geandier 2006]. The bandgap energy of CIS is 1.04 eV and can be increased by the partial replacement of In with Ga and thus depends on the ratio of Ga/[In+Ga]. CIGS has been found to exhibit both n and p-type electrical conductivity [Kemell *et al.* 2005, Chaure *et al.* 2005].

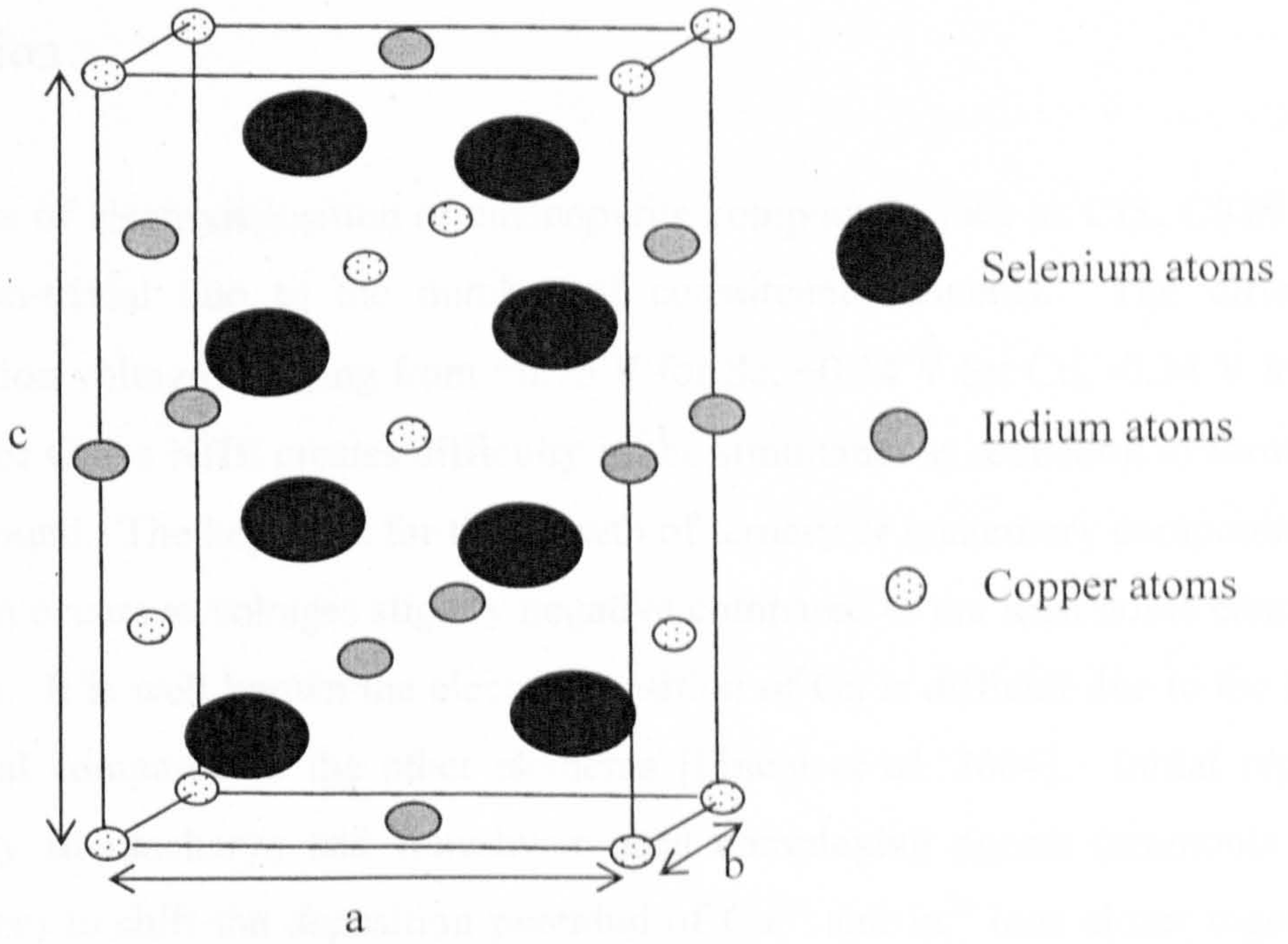

Figure 3.4. Illustration of CIS having tetragonal phase [Schorr & Geandier 2006].

The key function of the absorber material is to convert incoming photons of light into electron-hole pairs. In order for the cell to achieve optimum performance the bandgap energy of the material should match the spectral region as closely as possible. Bandgap energies in the range of 1.40 to 1.50 eV are required to achieve absorption of a major fraction of incoming photons with wavelengths in the visible range. Partial replacement of selenium with sulphur increases the bandgap energy of CIS; complete substitution forms $CuInS_2$ with a bandgap energy of 1.50 eV. Alternatively, fully replacing indium with gallium forming $CuGaSe_2$ increases the bandgap energy to 1.70 eV [Konovalov 2004].

Crystal defects and impurities should be minimised to maximise the life time of photogenerated charge carriers. Sufficient charge carrier life time is essential for their effective collection by the external circuit. Impurities form additional energy levels or traps in the bandgap which increases the recombination of charge carriers. Recombination of charge carriers is one of the major factors limiting device performance. Ideally the diffusion length of minority charge carriers should be greater than the thickness of the material to achieve maximum current collection. If the thickness of the layer exceeds the diffusion length of charge carriers the electric field within the device is weakened and the J_{sc} decreases. If the layer is too thin the J_{sc} will also decrease as fewer photons are absorbed [Konovalov 2004].

3.2.2 Electrodeposition of Copper Indium Diselenide from Aqueous Solution

The process of electrodeposition of chalcopyrite compounds such as CIS, CIGS and CIGSS is non-trivial due to the number of constituent elements. The different electrodeposition voltages ranging from +0.75 V for Se, +0.34 V for Cu, -0.34 V for In and -0.53 V for Ga vs NHE creates difficulty in the simultaneous reduction to form the desired compound. The key tenet for the growth of ternary or quaternary compounds is that deposition occurs at voltages slightly negative compared to the least noble element, in this case In. It is well known the electrodeposition of Ga is difficult due to the high redox potential compared to the other elements [Lincot *et al.* 2004]. Initial reports carried out by Bhattacharya and Rajeshwar used complexing agents (ammonia and treithanolamine) to shift the deposition potential of Cu^{2+} and In^{3+} ions closer together, also preventing precipitation of metal hydroxides over a wider pH range [Bhattacharya & Rajeshwar 1986].

In addition to complexing agents, experimentation using buffer solutions consisting of sulphamic acid and potassium biphtalate have been carried out by Fernandez and Bhattacharya. The use of pH=3 buffer solutions maintained the pH of the solution and reduce precipitation of hydroxides, which interfere with deposition [Fernandez & Bhattacharya 2003, 2005]. Sene *et al.* and Calixto *et al.* have since investigated the effect of pH=3 buffer solutions on the electrodeposition of CIS. The presence of the pH buffer did not alter the composition of the layers although the morphology varied. Layers deposited from buffered solutions had rougher surface morphology compared to those grown from non-buffered solution. It was suggested deposition of some species may be slowed in buffered solutions producing a less dense layer. It was found the cell characteristics were improved for layers deposited from non-buffered solutions [Calixto *et al.* 2006, Sene *et al.* 2008].

3.2.3 Electrodeposition of Copper Indium Diselenide from Non-Aqueous Solution

Electrodeposition from aqueous media does have disadvantages, such as hydrogen evolution which may cause pinholes and formation of metal hydroxides at the cathode.

There have been very few reports of the use of non-aqueous media for the electrodeposition of CIS to date. The use of dimethyl sulfoxide (DMSO), which is a toxic organic solvent has been used for elevated temperature deposition with the aim of improved crystallinity of the as-deposited material [Hodes & Cahen 1986]. This offers the possibility of allowing a higher voltage to be applied without the same level of oxide and hydroxide formation at the cathode. Thin film growth from non-aqueous solvents has other advantages over aqueous such as the possibility of deposition at temperatures >85°C, which is expected to promote improved crystallinity during deposition [Bhattacharya *et al.* 1998]. Although Hodes & Cahen reported little improvement in morphology of CIS when depositing from DMSO at 135°C [Hodes & Cahen 1986]. Electrodeposition from non-toxic ionic liquid ([BMP]Tf_2N) has previously been carried out by Zein El Abedin *et al.*, reporting the grain size to be nanocrystalline despite the elevated deposition temperature of 100°C [Zein El Abedin *et al.* 2007].

3.2.4 Commercially Available Copper Indium Diselenide Solar Cells

At present there are generally two methods used for the production of CIGS on a commercial scale. Both utilise vacuum technology, Würth Solar opting for the coevaporation of elements, where an in-line system has been developed for 120×60 cm^2 CIGS solar panels achieving 8% efficiency [Powalla & Dimmler 2003]. The other utilised by Siemens Solar uses DC-magnetron sputtering to evaporate Cu, Ga and In sequentially at room temperature followed by a post-deposition selenisation step at 550°C. CIGS modules ranging from 5 to 40 W having 9.6 to 11% efficiency are commercially available where-as smaller laboratory modules have achieved 14.7% efficiency [Karg 2001]. The modules are completed by laser scribing followed by deposition of ZnO before being covered with a protective glass sheet [Karg 2001]. Showa Shell, Japan has achieved efficiencies of 13.4% for 30×30 cm^2 CIGS devices deposited using metal organic chemical vapour deposition (MOCVD) [Kushiya 2004, Sang *et al.* 2003].

3.2.5 Laboratory Based Devices

A three-stage coevaporation method has been developed by NREL for production of CIGS solar cells. Devices with structure glass/Mo/CIGS/CdS/i-ZnO/ZnO:Al have produced the highest reported efficiency to date for CIGS solar cell devices of 19.9% [Repin *et al.* 2008]. This method deposited $(In,Ga)_2Se_3$ at 300°C followed by the evaporation of Cu and Se at 550°C and finally the material is made slightly Cu-deficient by evaporation of $(In,Ga)_2Se_3$. Drawbacks to using coevaporation are the composition gradient which depends on the substrate location and scale-up is non-trivial [Bhattacharya *et al.* 2005].

The maximum efficiency of CIGS solar cell devices has crept forward over the past decade or so from 17.7% in 1998 to 19.5% reported by NREL in 2005 and 19.9% in 2008 [Tuttle *et al.* 1996, Contreras *et al.* 2005, Repins *et al.* 2008]. Generally the improved efficiency has been attributed to optimisation of the ZnO window layer, enhanced diffusion of minority charge carriers and reduced recombination in the space-charge region [Contreras *et al.* 1999]. Suggestions for the latest improvement in efficiency were the absence of Ga during the last 10 seconds of growth and the post-deposition annealing step carried out at 600°C in a Se atmosphere, lead to a decrease in recombination of charge carriers. The device parameters of cells having area of 0.419 cm^2 were impressive having V_{oc}=0.690 V, J_{sc}=35.5 mA cm^{-2} and FF=0.81.

The maximum efficiency of 8.8% for 0.06 cm^2 CIS solar cells grown using electrodeposition was reported by the Copper Indium Selenide Electrodeposition (CISEL) project in 2002 [Guimard *et al.* 2002]. Layers deposited using low-cost, low temperature processes require a two stage device fabrication route. The first stage carried out using one-step electrodeposition does not produce a layer with adequate electronic properties and therefore a second annealing stage is required. One of the complexities of electrodeposition is the possibility of forming either elemental layers, or binary or ternary phases. The precursor films are thus often a mixture of multiple phases. The annealing stage promotes the intermixing of these compounds.

It is accepted that the composition of the film is controlled by the ratio of selenium to copper fluxes to the electrode which are diffusion controlled mechanisms [Lincot *et al.* 2004]. Electrodeposition is a competitive alternative to vacuum technology for the production of thin films and is ideally suited to large-scale industrial production. This

has already been realised with the highest reported efficiency of 7% for 15×15 cm^2 and 30×30 cm^2 modules by the CISEL project [Taunier *et al.* 2005].

A hybrid approach has been adopted by Bhattacharya *et al.* with the aim of development of a fast and lower-cost process. CIGS precursor layers were electrodeposited and the final composition was re-adjusted using PVD at a substrate temperature of 560°C. The layers were exposed to Se vapour during cooling to maintain stoichiometry. Devices fabricated using this process did not show deterioration in performance, achieving 15.4% efficiency [Bhattacharya *et al.* 1999].

3.2.6 Heat-Treatment

Post-deposition heat-treatment of electrodeposited layers is an essential step to achieve the necessary material properties for device fabrication. Annealing trials have previously been carried out to establish the effect of Se vapour pressure in the annealing chamber. It was found higher Se vapour pressures lead to improved morphology and electrical properties compared to a neutral atmosphere [Lincot *et al.* 2004]. For CIGS materials it is essential to perform this step under controlled conditions to maintain stoichiometry and prevent loss of Se. It has previously been observed annealing with insufficient Se atmospheres causes the development of pores degrading device performance, mainly due to sublimation of Se from the layer [Taunier *et al.* 2005].

The recrystallisation of grains is a mechanism which reduces grain boundaries and alleviates defects. It is thought that an exothermic reaction between Cu-In and melted selenium are the main phase transitions forming selenides followed by their peritectic decomposition [Karg 2001]. In addition to increasing the grain size, annealing may also alter the stoichiometry if some elements of the layer sublime leaving behind pin-holes. On the contrary pin-holes may be eliminated due to grain growth. Layers are generally annealed at temperatures of 450 to 650°C for a period of between a few minutes to an hour. The possibility of laser annealing of CIGS layers in an inert gas atmosphere has been investigated by Jost *et al.* Similar structural properties were obtained to those for furnace annealing with no significant loss of Se [Jost *et al.* 2008]. A surface oxide layer may form during annealing which may be removed by chemical etching before device fabrication.

Rapid thermal annealing (RTA) has been investigated by various groups with the attempt of lowering the processing costs, minimising impurity diffusion and reducing the layer damage compared to conventional furnaces. Wang *et al.* used NREL samples to study the effect of RTA and found little change to the XRD spectra or morphology using SEM. However the electrical properties markedly improved after RTA at 300°C, with reduced resistivity and increased carrier density [Wang *et al.* 2006]. It is also noteworthy that RTA has been exploited on a commercial basis by Shell Solar producing devices having 13.1% efficiency for 0.54 m^2 modules [Palm *et al.* 2004].

3.2.7 Buffer Layers for Copper Indium Diselenide

The buffer layer must have large bandgap energies for transmission of a high proportion of the solar spectrum to the space-charge region. CIS has a high absorption coefficient of 10^5 cm^{-1} and it has been reported a 2 μm thick layer is sufficient to absorb the useful part of the spectrum [Romeo *et al.* 2004]. The charge carrier diffusion length also dominates the performance of CIS devices and should therefore be greater than the distance from where light is absorbed to the space-charge region edge.

A large amount of work has been carried out to develop CIGS devices containing a CdS buffer layer. Indeed, this work has been successful over the years with the highest efficiency of 19.9% reported by NREL [Repin *et al.* 2008]. The CBD growth process is beneficial as it provides a complete coverage of rough absorber surfaces with the desired thickness of 80 nm. The CdS also protects the absorber layer from damage and chemical reactions during ZnO deposition. Although the use of the CdS buffer layer in CIGS devices has been extremely successful there are disadvantages to using this material. Short wavelengths are absorbed by CdS and therefore do not reach the absorber material, thus reducing the current collection [Ramanathan *et al.* 2003].

The subject of replacement of CdS with an alternative buffer layer has been investigated by various groups with the hope of reducing the loss of short wavelength photons. In order for this to be achieved materials such as Zn(O,S,OH) which are transparent in the wavelength range >360 nm and are electrically conductive have been investigated. NREL have investigated alternative buffer layers using CBD to deposit ZnS(O,OH) and Zn-Cd-S(O,OH) onto CIGS absorbers. The reported device parameters were comparable having efficiencies of 17.7% and 18% respectively compared to 17.5% for CdS buffer layers.

Kushiya *et al.* explored the replacement of CdS using Zn(O,S,OH) grown using CBD in the production of 30×30 cm^2 modules achieving an efficiency of 12.9% [Kushiya 2004]. Growth of ZnO using CBD involved the formation of $Zn(OH)_2$ in addition to ZnO which is converted to ZnO during annealing. The annealing temperature was limited to 300°C and therefore the conversion was not fully completed. Attempts to reduce the amount of OH^- in the structure were made to improve the quality of the junction. This was achieved by addition of thiosulphate to the deposition bath as the buffer layer grew on sulphur containing CIGSS layer. The concentration of $Zn(OH)_2$ in the layer reduced as a result of this modification and the buffer layer formed a mixed compound of ZnO, ZnS and $Zn(OH)_2$ [Kushiya 2004].

3.2.8 Ordered Defect Compound

There are unresolved fundamental issues surrounding the exact interface between the CIGS/CdS junction. The CdS is only weakly n-type and therefore is not thought to be responsible for the band bending. It is widely accepted that there is a large amount of band bending in the CIGS layer; the bulk of the material is p-type and becomes n-type at the interface with CdS. The origin of this naturally occurring property is thought to be manifested by a copper deficient, indium rich surface layer, which exists before the deposition of CdS and has different stoichiometry to the bulk CIGS. The Cu-poor second phase is known as the ODC layer and is associated with a Cu:In:Se ratio of 1:3:5 [Niemegeers *et al.* 1998, Liao & Rockett 2003].

The Cu-poor ODC layer has different electrical properties to the bulk absorber, which has a large defect density and larger bandgap energy of 1.45 eV [Niemegeers *et al.* 1998]. The junction between CIGS and the ODC layer is a homojunction [Contreras *et al.* 1999]. Cd atoms are thought to occupy Cu vacancy sites post-deposition contributing a large number of free electrons at the surface. It has been theoretically evaluated that the ODC layer forms due to its favourable low energy of formation of indium on copper sites and two copper vacancies, $In_{Cu} + 2V_{Cu}$ [Wei *et al.* 1998, 1999].

3.2.9 Sodium Incorporation

The incorporation of Na in CIGS solar cells has previously been shown to improve the device performance although the exact mechanism for this improvement is still under debate. Wei *et al.* suggested the most likely effects are the increase in hole density and film conductivity and suppression of the ODC layer [Wei *et al.* 1999]. Theoretical calculations to estimate the formation of secondary phases such as $NaInSe_2$ where Na is situated on a Cu-site have been carried out. It was predicted that $NaInSe_2$ formation increases the bandgap energy by 0.11 eV enhancing the V_{oc}. The formation of Na_{Cu} was found to be electrically inactive where-as Na_{In} was electrically active and is expected to increase the hole concentration in $CuInSe_2$ [Wei *et al.* 1999].

The most common unintentional source of Na in CIGS devices is from the glass substrate, diffusing through the MoO_2 grain boundaries. The diffusion occurs as a result of the elevated temperatures during deposition or annealing. For commercial interest Na from the back contact has insufficient reliability and therefore other methods of addition have been investigated. The Na precursor layer can be placed at various positions within the device structure; on top of the CIGS layer, beneath it or an addition during deposition [Romeo *et al.* 2004]. This includes the coevaporation of Na_2Se or Na_2S during the absorber deposition for vacuum growth techniques. Difficulties arise when attempting to incorporate Na using electrodeposition due to the high negative redox potential of -2.71 V vs NHE. However, Na which is a reactive ion may be incorporated into the film via other mechanisms such as absorption, adsorption and chemical reactions.

It is thought the Na improves the structural properties by increasing the grain size although contrary findings have also been reported [Birkmire 2001]. The presence of 0.1 at.% with doping concentration of 10^{20} cm^{-3} has been indicated as the optimum concentration, although this is beyond the ideal doping concentration for semiconductors. Contrary to this, layers have also been found to have doping concentrations of 10^{16} cm^{-3} [Schock & Noufi 2000].

The effect of Na on the electrical properties has been shown to decrease the resistivity by up to two orders of magnitude. This is likely to be due to Na segregation at grain boundaries which is likely to passivate charge carrier traps [Romeo *et al.* 2004]. It has also been suggested that Na becomes part of the lattice by replacing In and Ga atoms [Schock & Noufi 2000].

3.2.10 Sulphur Incorporation

The addition of sulphur is used to replace Se in $Cu(In,Ga)Se_2$ with S forming $Cu(In,Ga)(SSe)_2$. In principle there are four different options for incorporation of sulphur in $CuInGaSe_2$ for electrodeposited layers. Co-electrodeposition of sulphur simultaneously with the other elements (1); separate deposition of sulphur prior to heat-treatment (2) and annealing in a sulphur atmosphere (3) before or (4) after recrystallisation of the $CuInGaSe_2$ [Titus *et al.* 2006]. Typically the incorporation of sulphur is usually carried out using H_2S, which has been predicted to be via interdiffusion of S and Se, although the complete mechanism is still not fully understood [Titus *et al.* 2006]. Utilisation of this step has also achieved efficiencies of 11.5% with a bandgap energy of 1.47 eV [Kessler *et al.* 2005].

Although S incorporation is known to increase the bandgap energy it is at the expense of the crystallite size, which has been shown to decrease from 800 to 100 nm with 0 to 90% sulphur respectively. It has been reported that S-rich ($CuInS_2$) material exhibits p-type electrical conductivity and S-poor exhibit n-type electrical conductivity [Siebentritt 2002]. $CuInS_2$ solar cells do not perform as well as the selenide based counterparts. Suggestions for this discrepancy have been the apparent need for Cu-poor material, which is not feasible when depositing sulphide absorbers as Cu-richness improves S incorporation and crystallinity [Siebentritt 2002].

3.2.11 Gallium Incorporation

It is accepted that Ga incorporation in $CuInSe_2$ forming $CuIn_{1-x}Ga_xSe_2$ increases the bandgap energy from ~1.04 to 1.54 eV. The increase in bandgap energy is necessary to increase the V_{oc} of the device. Earlier work has established the optimal Ga concentration to have a Ga/(In+Ga) ratio of 0.3 [Romeo *et al.* 2004]. When the ratio is greater the device performance deteriorates. Suggestions to explain this finding include changes in the structural properties of the material resulting in an increase in the lattice mismatch, which leads to increased defect density and lattice strain [Wei *et al.* 1998, Contreras *et al.* 2005]. A large Ga ratio is also thought to alter the electrical conductivity type of the ODC layer from n to p which shifts the device junction from a p-n buried junction to an abrupt CIGS/CdS heterojunction [Schock & Noufi 2000]. Investigations to optimise the Ga content in CIGS layers have been carried out by

Ramdani *et al.* using electrodeposition [2006]. It was found that when the Ga/(Ga+In) ratio was 0.2 the layers were compact but had surface porosity. When the Ga/(Ga+In) ratio was increased to 0.7, although the layers were compact, post-deposition cracks made the layers unusable. It was also found that high Ga concentrations in aqueous solution encourages the prevalence of gallium oxide (Ga_2O_3) and hydroxide, $Ga(OH)_3$. Cell efficiencies of 7% were achieved with Ga/(Ga+In) content of 0.2 using electrodeposition.

Superstrate configuration CIGS devices have been prepared by Nakada *et al.* [2004]. Complications associated with this device structure are the need to establish a suitable buffer layer that can withstand the high temperature deposition and annealing of CIGS. CdS and Zn based layers have the disadvantage of undesirable inter-diffusion of Cd and Zn into the CIGS during deposition or annealing. Devices with similar performance as substrate configuration cells have been realised with structure glass/TCO/ZnO:Al/ZnO/CIGS/back contact. The CIGS was deposited by a three-stage evaporation process achieving maximum efficiency of 13.7% [Nakada *et al.* 2004].

3.3 Cadmium Telluride

3.3.1 Introduction

The CdTe literature review will discuss growth of CdTe using electrodeposition. The structural and electrical properties will be briefly described.

Cadmium and tellurium are group II and VI elements having atomic numbers 48 and 52 and atomic weight 114.211 and 127.600 respectively. CdTe forms a semiconductor having bandgap energy of ~1.45 eV, making it an ideal candidate as an absorber material for solar cell devices [Meulekamp & Peter 1996]. The suitability and scalability of this material deposited using electrodeposition has previously been proven by BP Solar Ltd, producing 0.94 m^2, 10.4% efficient solar cells [Cunningham 2002]. CdTe usually exhibits cubic structure and has been found to display both n-type and p-type electrical conductivity.

3.3.2 Electrodeposited Cadmium Telluride

CdTe layers are commonly electrodeposited from acidic aqueous solutions containing a high molarity of cadmium sulphate. BP Solar Ltd. studied the effect of concentration of Cd^{2+} ions on CdTe composition by varying the weight from 48 to 88 g L^{-1}. EDX indicated little deviation in the Cd content which was consistent between 49 and 50% [Cunningham 2002]. In contrast the required molarity of tellurium oxide (TeO_2) is extremely low and is pH dependent. One of the key factors in the electrodeposition of CdTe is the difficulty of controllability of TeO_2 which has low solubility in aqueous media. One method investigated by Basol used a Te anode which was switched periodically with an inert anode. When current passed through the Te anode, $HTeO_2^+$ was released into the solution thus replenishing the electrolyte [Basol 1988].

Sulphuric acid is often used to adjust the pH to around 1.5 to 2.0 to increase the solubility of TeO_2. A compromise must be met between pH for sufficient TeO_2 solubility without formation of pin-holes or dissolution of the CdS substrate. The lower pH limit for protection of CdS has been reported at pH=1.4, although at this pH the solubility of TeO_2 is still low at $<10^{-3}$ M. According to Duffy *et al.* the saturated

concentration of TeO_2 at pH=1.4 and 85°C is 6.5×10^{-4} mol dm^{-3} [Duffy *et al.* 2000]. The influence of pH has been studied by Meulenkamp and Peter, who reported the best quality layers to be deposited at relatively higher pH. It was suggested the pH should not be increased above 2.5 as this leads to impractically low deposition rates.

The use of non-aqueous electrolytes such as ethylene glycol have been investigated for CdTe deposition with the advantage of improved solubility of $TeCl_4$. The results were promising achieving efficiencies of 8.3% [Nair *et al.* 2001, Chaure *et al.* 2004], although this is not an improvement compared to layers produced from aqueous solutions, which have achieved 10.4% for large scale modules [Turner *et al.* 1994].

Panicker *et al.* were the first to propose the reaction mechanism of CdTe to proceed via a two stage process. The first step is the reduction of $HTeO_2^+$ to Te^{4+} via reaction 3.9.

$$HTeO_2^+ + 3H^+ + 4e^- \rightarrow Te^{4+} + 2H_2O \qquad +0.520 \text{ V vs NHE} \qquad (3.9)$$

The second reaction is the reduction of Cd^{2+} at Te surface sites via reaction 3.10.

$$Cd^{2+} + 2e^- \rightarrow Cd \qquad -0.403 \text{ V vs NHE} \qquad (3.10)$$

The overall simultaneous reaction is expressed by 3.11.

$$Cd^{2+} + HTeO_2^+ + 3H^+ + 6e^- \rightarrow CdTe + 2H_2O \qquad (3.11)$$

The rate of reactions 3.9 and 3.10 should be the same to produce stoichiometric CdTe and prevent elemental Te deposition [Meulenkamp & Peter 1996]. Based on the reactions it was proposed that CdTe is formed after Te has been deposited as the free energy gain is consumed by Cd, known as underpotential deposition [Panicker *et al.* 1978].

The rate of CdTe deposition is controlled by the availability and mass transport of soluble Te^{4+} ions and is unaltered by the applied voltage. Intrinsic defects determine the conductivity type of CdTe, which is determined by the growth voltage; both n and p-type CdTe have been reported [Panicker *et al.* 1978, Engelken & Van Doren 1985, Saraby-Reinjies *et al.* 1993, Romeo *et al.* 2004]. It is generally accepted that p-type CdTe is Te-rich and deposited at low voltages and n-type CdTe is Cd-rich and deposited at higher voltages. In the case of cadmium vacancies (V_{Cd}), or tellurium interstitials

(Te_i) the CdTe is p-type and cadmium interstitials (Cd_i) or tellurium vacancies (V_{Te}) yield n-type material [Basol 1988, Cowache *et al.* 1989, Kampmann *et al.* 1995]. Other possible intrinsic defects are Cd atoms on Te sites or Te atoms on a Cd site. Excess Te is readily removed during annealing due to its vapour pressure forming pin-holes, which degrades the uniformity of the layer [Lepiller *et al.* 2000].

A deposition rate of 1.7 μm over several hours has previously been reported [Sugimoto & Peter 1995]. Stirring the electrolyte is known to increase the deposition rate, although by no more than 0.1 μm h^{-1}. Figure 3.5 illustrates the influence of applied voltage and cathode rotation speed on the composition of CdTe as proposed by Lepiller *et al.* (the voltage has been adjusted with respect to SCE reference electrode). It is clear positive deposition voltages lead to a Te-rich deposit, forming a non-stoichiometric CdTe + Te compound. Increasing the deposition rate by raising the rotation speed of the cathode also has the same effect by increasing the range of applied voltage at which CdTe + Te is preferentially deposited. Increasing the voltage above -0.70 V yields elemental Cd.

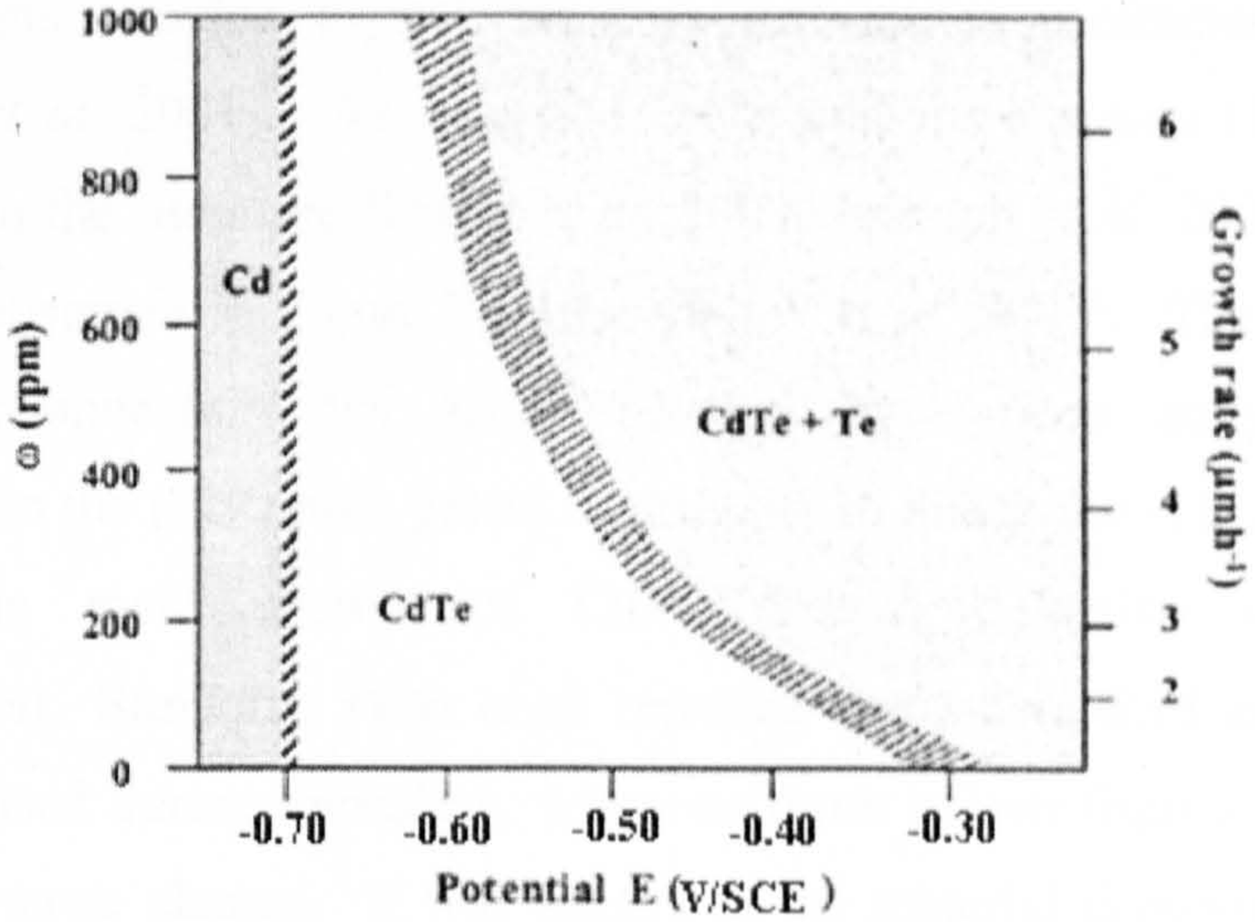

Figure 3.5. Illustration of the dependence of CdTe growth rate and composition on applied voltage and stirring rate [Lepiller *et al.* 2000].

Panicker *et al.* studied the effect of temperature on the electrodeposition of CdTe, finding at room temperature amorphous material was formed. The XRD spectra intensity improved as a function of growth temperatures of 35°C, 65°C, and 90°C [Panicker *et al.* 1978]. Cowache *et al.* reported a growth rate of 0.4 μm h^{-1} at 80°C and at temperatures above 90°C the growth rate increased although the layers had poor

adhesion [Cowache *et al.* 1989]. Thus the deposition current density is controlled by the temperature of the solution, the stirring rate and the concentration of Te [Basol 1988].

Although electrodeposition has the advantage of being low-cost the growth rate of CdTe is slow. For this technology to be commercially viable the rate of deposition must be increased. Various investigations have been carried out to decrease the deposition time, such as passing the solution through a channel flow cell over the substrate to control the mass transport of TeO_2. In this arrangement the CdS substrate was mounted in the side wall of the cell forming one side of the channel. The counter electrode was mounted in the opposite wall of the cell [Meulenkamp & Peter 1996]. Deposition times of 15 minutes for a 1.5 μm layer have been achieved using this set-up although the layers were Te-rich [Duffy *et al.* 2000, Peter *et al.* 1999].

3.3.3 Structural Properties

CdTe adopts a cubic crystal structure and lattice parameters a=b=c=6.482 Å [Rabadanov *et al.* 2001]. As-deposited CdTe exhibits a strong (111) orientation, as documented in the literature [Duffy *et al.* 2000, Johnson *et al.* 2000]; the cubic CdTe structure is illustrated in Figure 3.6 [Rabadanov *et al.* 2001]. The recrystallisation of CdTe during annealing has been observed by various authors. During the recrystallisation the (220) peak grows in intensity to match the (111) peak. Duffy *et al.* suggested the rapid growth of CdTe created defective crystals, favouring recrystallisation. Similarly, Peter *et al.* reported layers deposited using a channel flow cell recrystallised during annealing, where-as those grown from a stirred solution did not show the same change. It was suggested the material deposited by channel flow method has excess Te, which favours recrystallisation [Peter *et al.* 1999]. It has also been suggested the recrystallisation releases lattice strain from the as-deposited material promoting grain growth and passivation of grain boundaries [Duffy *et al.* 2000, Johnson *et al.* 2000, Peter *et al.* 1999].

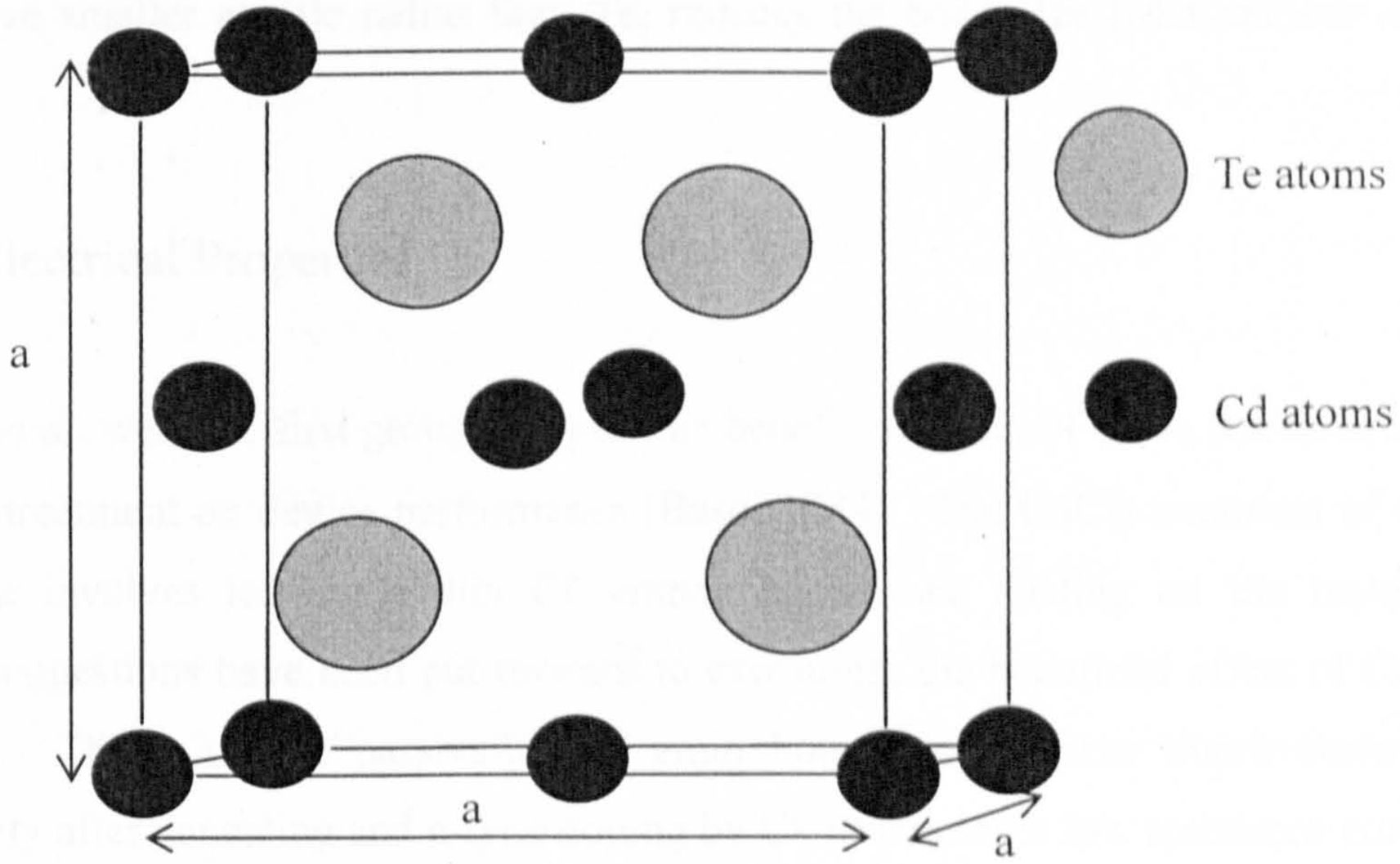

Figure 3.6. Cubic crystal structure of CdTe [Rabadanov *et al.* 2001].

Johnson reported the (111):(220) ratio is influenced by three main factors; the voltage drop at the substrate away from the contact, the substrate morphology and recrystallisation due to increasing temperature and time. If the applied voltage is more positive the layers are Te-rich, which encourages recrystallisation [Johnson 2000].

Inter-diffusion between the CdS/CdTe during annealing has been investigated by various groups. It was found the diffusion of sulphur from CdS into CdTe reduces the size of the window layer and forms $CdTe_{1-x}S_x$ close to the interface region; similarly diffusion of Te from CdTe into CdS forms $CdS_{1-y}Te_y$ [Lane *et al.* 1999]. Below a certain CdS thickness the device performance reduces and if the CdS is totally consumed a junction forms between TCO/$CdTe_{1-x}S_x$, encouraging shunting [McCandless *et al.* 1997, Romeo *et al.* 2004]. The diffusion of Te into CdS and S into CdTe alters the bandgap energies at the interface as observed by [Johnson *et al.* 2000, Duffy *et al.* 2002]. Another suggestion by the same authors was the heat-treatment stage increases the doping concentration of CdS forming n^+ material reducing the width of the space-charge region.

The lattice mismatch of 11% between cubic CdTe and CdS is a potential problem for bond formation, which results in lattice strain and dislocations [Rogers *et al.* 1999, Romeo *et al.* 2004]. McCandless *et al.* reported as-deposited material to have a 0.13% higher lattice parameter than expected for CdTe, suggesting a strained lattice attributed to lattice mismatch or impurities in the crystal matrix. Substitution of S onto Te sites,

which have smaller atomic radius than Te, reduces the bond size [McCandless *et al.* 1997].

3.3.4 Electrical Properties

Basol *et al.* were the first group to report the beneficial effect of Cl^- in the electrolyte or $CdCl_2$ treatment on device performance [Basol 1984]. The $CdCl_2$ treatment of CdS and CdTe involves leaving a thin Cl^- containing surface coating on the material. Various suggestions have been put forward to explaining the beneficial effect of $CdCl_2$ treatment. These include passivation of grain boundaries, further improvement of crystallinity after annealing and n-type doping by Cl^- producing a low resistance contact at the CdTe/metal interface [Johnson *et al.* 2000, Dharmadasa *et al.* 2002, Romeo *et al.* 2004].

The bandgap energy of CdS was found to change from 2.25 to 2.46 eV for $CdCl_2$ treated and non-treated layers [Johnson *et al.* 2000]. The device performance improved when the Cl^- concentration in the electrolyte were in the range of 50 to 300 ppm as indicated by Figure 3.7. Lines (a) and (b) represent CdS without and with Cl^-. The overall efficiency was increased from 3 to 10% with the addition of Cl^- to the CdS substrate. An increase in the I_{sc} and V_{oc} was observed for CdS containing Cl^-; the former was attributed to a decrease in bulk resistance and passivation of grain boundaries [Dennison 1994].

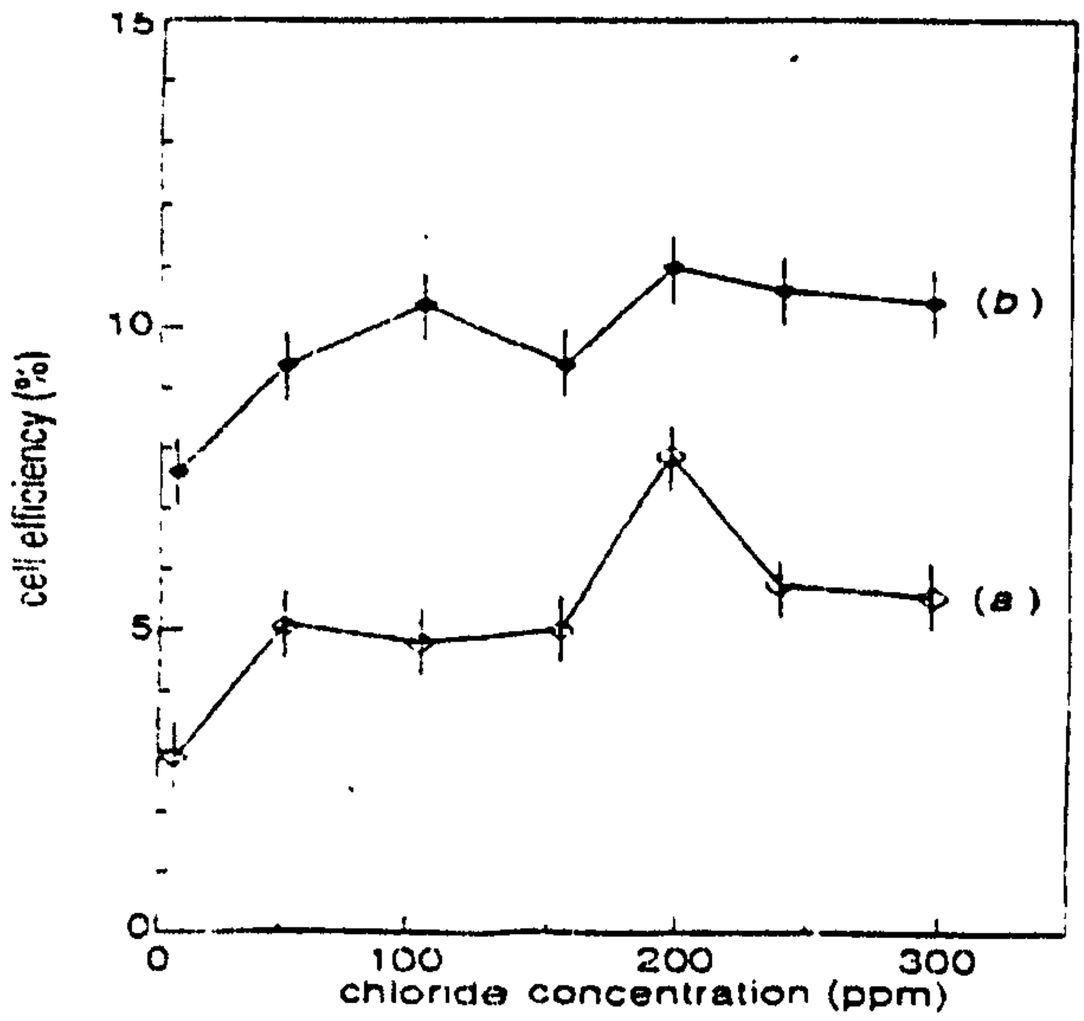

Figure 3.7. Cell performance of CdTe deposited from an electrolyte containing Cl^- (a) Cl^- free CdS and (b) CdS containing Cl^- [Dennison 1994].

Other methods used for $CdCl_2$ treatment involve coating the CdTe surface with $CdCl_2$ from an alcohol solution followed by evaporation and heat treatment. Alternatively $CdCl_2$ vapour has been used for post-deposition treatment of CdTe [McCandless *et al.* 1997]. McCandless noted the importance of the $CdCl_2$ treatment for improved device performance and grain growth and reorientation [McCandless *et al.* 2003]. The charge carrier diffusion length was found to increase after $CdCl_2$ treatment due to a reduction in recombination centres [Kampman & Lincot 1996].

The effect of addition of group I and XI elements to the electrolyte on the device performance has been investigated. It is understandable that Cu^{2+} may be deposited as due to its relatively positive redox potential compared to Cd^{2+} [Cunningham 2002]. The effect of Cu^{2+} on the performance of CdTe devices has also been studied by Dennison. It was found that 7 ppb background Cu^{2+} was present in the electrolyte. Following the deliberate addition of Cu^{2+} to the electrolyte a dramatic reduction in device performance paths was observed for concentrations above 30 ppb, with a reduction in V_{oc}, FF and increase in the R_{sh}. Figure 3.8 illustrates the effect of Cu^{2+} on device performance [Dennison 1994].

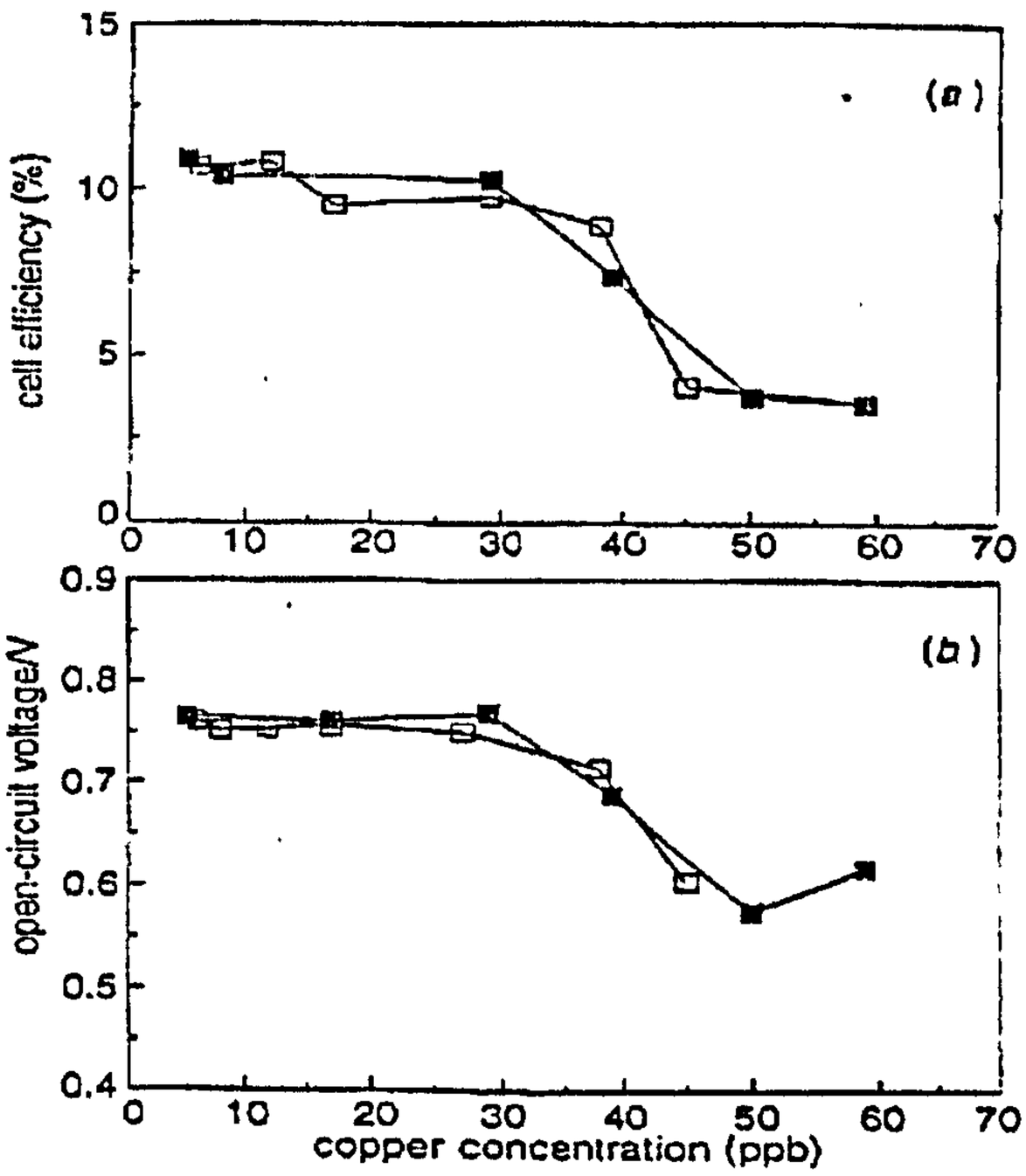

Figure 3.8. Device performance as a function of Cu^{2+} concentration in the electrolyte [Dennison 1994].

The addition of Ag^+ into the electrolyte has also been studied. A drastic decrease in efficiency from 11% to 0.7% for a concentration of 400 ppb of Ag^+ was observed. It is therefore particularly important to eliminate the use of Ag/AgCl reference electrodes for the electrodeposition of CdTe [Dennison 1994].

The performance of CdTe solar cells has been found to degrade over time, possibly due to diffusion of Cu from the metal contact into the bulk of the material. It is known that Cu diffuses rapidly from the back metal contact through the CdTe via grain boundaries, which act like channels, resulting in highly conductive areas although the bulk of grains remains unchanged [Dennison 1994, Moutinho *et al.* 2007].

According to the new model for CdTe proposed by Dharmadasa *et al.* [2002], suitable n-type dopants for n-CdTe are group III and VII elements for substitution on Cd site and Te sites respectively. To this end Chaure *et al.* investigated the effect of iodine (group VII) doping of CdTe. The resistivity was found to decrease from 3×10^5 to 0.1×10^5 Ω cm with iodine concentrations of 0 to 0.2M respectively [Chaure *et al.* 2003].

The BP Apollo project produced CdTe cells with 10.4% efficiency having glass/CdS/CdTe/Au device structures. The 12 cell 100×100 mm^2 module had cell parameters of V_{oc}=797 mV, J_{sc}=18.4 mA cm^{-2} and FF=0.69 [Turner *et al.* 1994]. BP Solar's Fairfield plant focused on increasing the plate size to 0.94 m^2. The primary objective was to scale-up the 80 W panels from a few mm^2 to 900 cm^2, 0.55 m^2 and 0.94 m^2 monolithic modules. High compositional uniformity was observed for all the panels, achieving 8% efficiency for the largest area cells [Cunningham 2002].

An important consideration when choosing a suitable conductive substrate is the need to minimise the voltage drop over the plate away from the contact. Such voltage drops result in a variation in stoichiometry of the layer. This problem can be reduced by employing substrates with low sheet resistance.

The thickness of the CdS is also an important consideration; if the layer is too thick the blue photon collection is reduced impacting the J_{sc} due to losses in the 400 nm to 512 nm wavelength range. Conversely if the CdS has insufficient thickness the device performance is degraded due to reduction in V_{oc} [Cunningham 2002]. Das and Morris reported a variation in cell efficiency from 9.5% to 11.5% from top to bottom of the plate due to the voltage drop during growth [Das & Morris 1993].

Gibson *et al.* investigated the effect of the voltage drop during growth, on the cell performance. The laser-beam induced current (LBIC) diagram (Figure 3.9) reported by Gibson indicates the variation in CdTe film thickness with distance along the plate. The

cathode was connected along the two vertical edges of the substrate. There is a distinct reduction in film thickness at each edge and this was indentified to produce lower cell efficiency. An annealing experiment was carried out as a function of time (8, 16 & 30 minutes). Recrystallisation of the material from the centre of the plate was first noted after 16 minutes whilst the edge did not show recrystallisation, suggesting varying composition [Gibson *et al.* 2001].

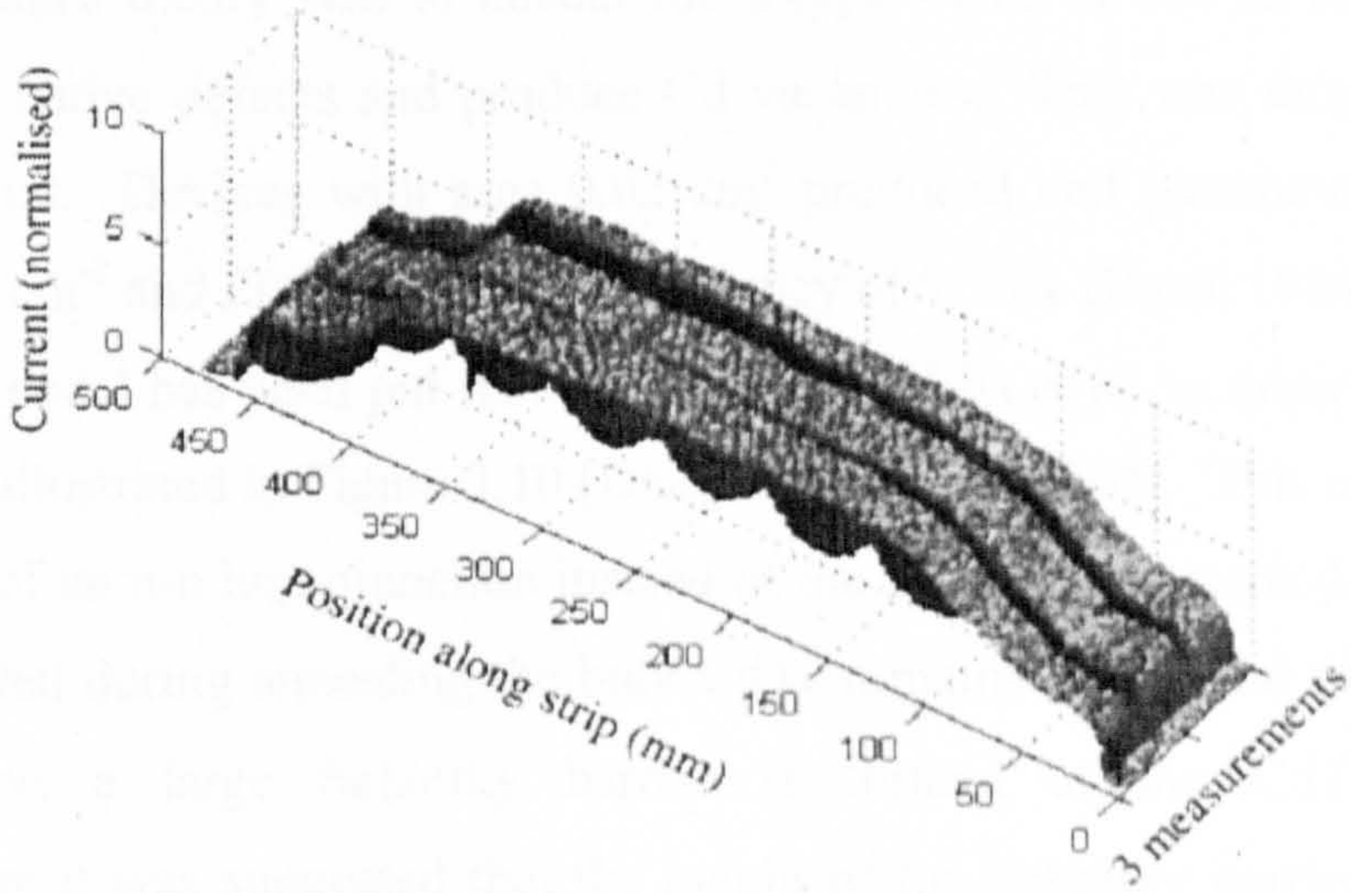

Figure 3.9. LBIC scans of CdTe/CdS layer, the edges of the cell exhibited poor performance [Gibson *et al.* 2001].

Post-annealing wet chemical surface treatments have been shown to drastically improve device performance. The interface between the CdTe and metal are improved when CdO is removed and a Te-rich surface is formed. Various surface modification steps have been investigated for etching CdTe. Etching CdTe in acidic solution, for example sulphuric acid (H_2SO_4), has been found to produce a Te-rich surface as the Cd is dissolved. Alternatively etching in a basic solution, potassium hydroxide (KOH), produces a Cd-rich surface [Sobiesierski *et al.* 1988, Dharmadasa *et al.* 1989]. Effects of potassium dichromate ($K_2Cr_2O_7$) and H_2SO_4 have been investigated to remove CdO leaving a Te-rich surface, found to promote a better quality interface for the metal contact [Savadogo 1998].

Chemical etching of CdTe has been investigated by Dharmadasa using 1% bromine in methanol and 1 g $K_2Cr_2O_7$ in 10 ml H_2SO_4 + 20 ml water for oxidising etches [Dharmadasa *et al.* 1989]. It has been reported Te-rich surfaces were achieved using this etch with the addition of TeO_2 and Cd-rich surfaces were formed by etching in an alkaline etch of 0.5 g of NaOH, 0.5 g $Na_2S_2O_3$ in 100 ml water. Other authors have also

reported the use of bromine in methanol for the production of Te-rich surfaces [Moutinho *et al.* 2007].

It is generally accepted that as-deposited CdTe is n-type and Basol was the first to report type conversion to p-type after heat-treatment forming an n-p heterojunction with CdS. The use of Au, Cu-Au, Cu-Ni or Ni metal contacts have been used to form an ohmic contact to p-type CdTe and also reduces the amount of Cu in contact with the CdTe. Basol's theory was to anneal the n-type CdTe at 450°C for 8-10 minutes to anneal out native defects and produce Cd vacancies. This was thought to produce p-type material. Devices with area 0.02 cm^2 produced cell parameters of V_{oc}=0.73 V, J_{sc}=20 mA cm^{-2} and FF=0.64 with an efficiency of 9.15% [Basol 1984].

A new model has been put forward by Dharmadasa *et al.* to describe the CdTe solar cell and is illustrated in Figure 3.10 [Dharmadasa *et al.* 2002]. This model describes the formation of an n-n homojunction instead of the previously accepted n-p junction. It is proposed that during annealing the bulk CdTe remains n-type and after processing and metallisation a large Schottky barrier is formed at the CdTe/metal interface. Furthermore it was suggested that the height of the Schottky barrier is determined by the Fermi level pinning position at this interface, where the pinning is due to defects at the surface of CdTe. For efficient devices doping concentrations should be of the order of 10^{14} to 10^{17} cm^{-3} and the Fermi level should be pinned at the defect level closest to the valence band maximum. The surface layer of the CdTe acts as a p-type layer and the bulk of the CdTe remains n-type. Dharmadasa has experimentally determined five defect levels of 0.40, 0.65, 0.73, 0.96, 1.18 eV below the conduction band minimum. Formation of the highest two barriers forms the most efficient devices, pinning at lower energy results in poor band bending [Dharmadasa *et al.* 1998, 2002 & 2005].

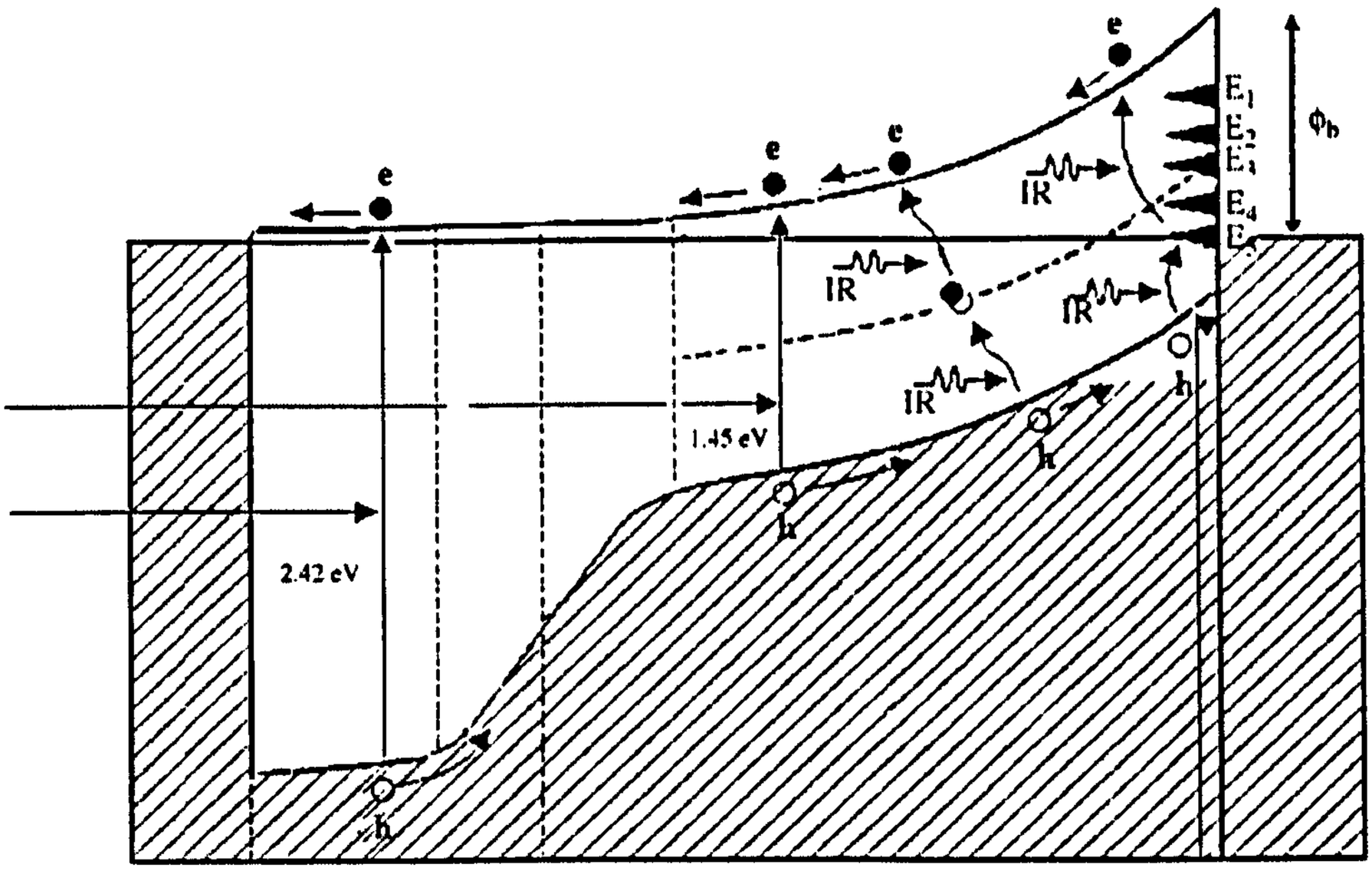

Figure 3.10. The new model proposed for glass/TCO/CdS/CdTe/Cu-Au thin film solar cells [Dharmadasa *et. al.* 2002].

It is believed the Cu contact dopes CdTe p-type and therefore decreases the resistivity at the interface [Dharmadasa *et al.* 1989, Moutinho *et al.* 2007]. However, according to the new model the metal contact produces a large Schottky barrier with the CdTe instead of an ohmic contact. The disadvantage of Cu diffusion into the bulk CdTe is deterioration of device performance by increasing resistance as a result of self-compensation [Gupta *et al.* 2001]. One way around this is to reduce the amount of Cu by producing a mixed metal contact (Au-Cu or Ni-Cu). An alternative method is to introduce a thin p-type layer having a larger bandgap energy than CdTe for example Sb forming a layer of Sb_2Te_3 to protect against Cu diffusion [Dharmadasa *et al.* 2002].

In 1994 the highest reported efficiency for CdTe solar cells was 15.8% reported by Ferekides *et al.* [1994]. A few years later NREL reported the record efficiency at 16.5% [Wu *et al.* 2001]. The improvement in efficiency of 0.7% may be considered to be within experimental error. The efficiency of CdTe solar cells has since stagnated with lack of progress to date.

Chapter 4 Substrate Investigations

4.1 Fluorine Doped Tin Oxide

4.1.1 Introduction

Pilkington Group Ltd. supplied all Fluorine doped Tin Oxide (FTO) coated glass substrates, which were used for the cathode in the electrodeposition set-up and during the CBD of CdS. Two grades of FTO were employed throughout the programme, initially "TEC-15", so named due to its sheet resistance of 15 Ω/□. Subsequently, in order to minimise the resistance of the electrolytic cell, "TEC-7" was supplied having a sheet resistance of 7 Ω/□. The FTO was sputtered onto ordinary soda-lime glass using r.f. sputtering.

The thickness of the FTO coatings for TEC-15 and TEC-7 was quoted by Pilkington Group Ltd. as 393 and 518 nm respectively. The structural, optical and electrical properties of both layers have been investigated and are presented in the following sections. The XRD spectra for TEC-15 and TEC-7 were used for identification of SnO_2 peaks arising from the substrate for all further measurements of semiconductor thin films within this thesis.

4.1.2 Results and Discussion

4.1.2.1 X-Ray Diffraction

The XRD spectrum of TEC-15 is shown in Figure 4.1, where all peaks were identified as tetragonal tin oxide (SnO_2) using the standard data files supplied by the online Daresbury Chemical Database Service [Gracia *et al.* 2007]. Table 4.1 presents the XRD data for TEC-15 compared to the standard data, indicating their similarity. The preferential reflection corresponds to the (200) plane followed closely by the (211) peak.

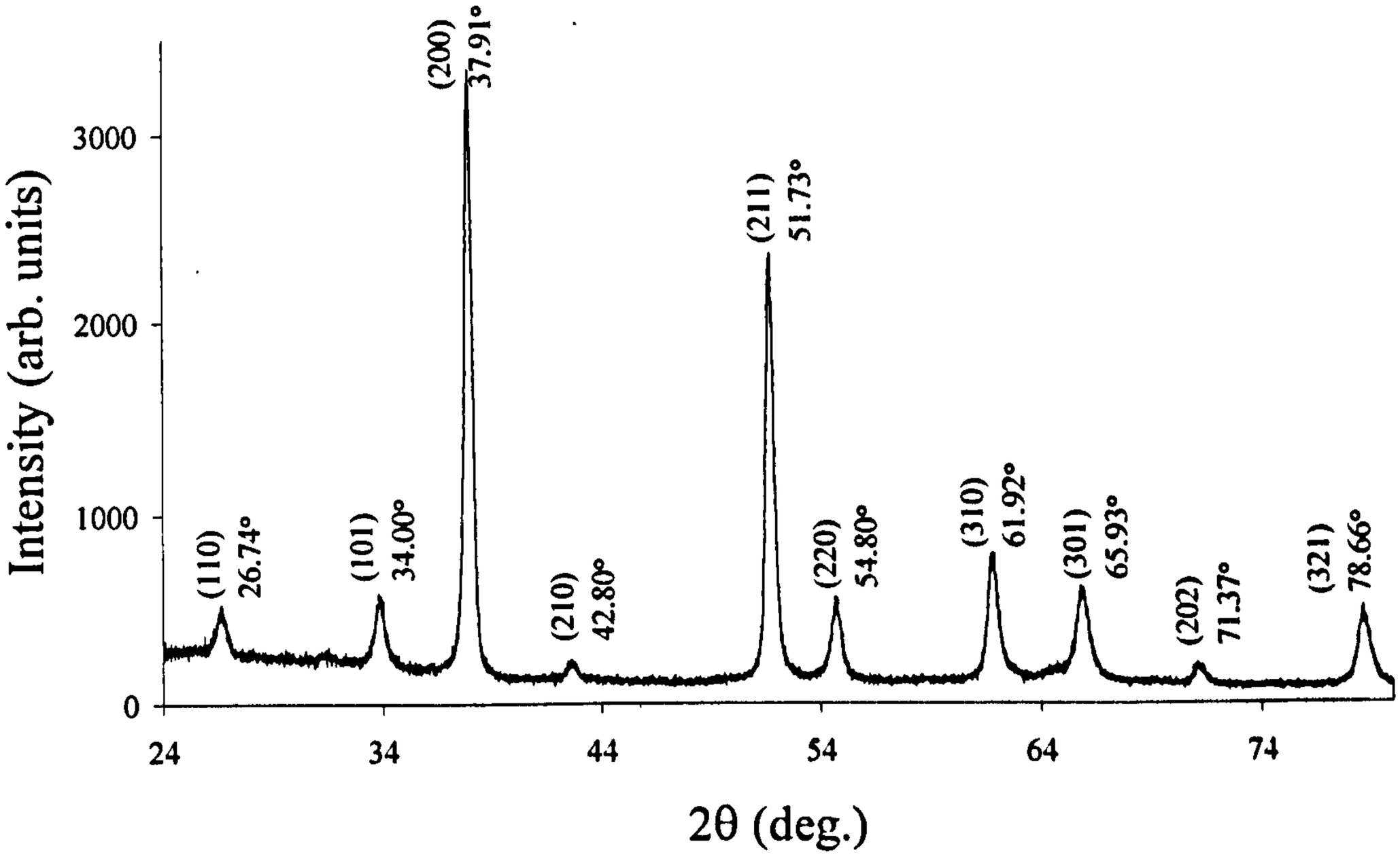

Figure 4.1. XRD spectra of TEC-15 FTO, all peaks were identified as SnO_2.

Table 4.1. XRD data obtained for TEC-15 FTO, identified as tetragonal SnO_2.

2θ (deg.)		d-Spacing (Å)		Miller Indices
Standard	Observed	Standard	Observed	(hkl)
26.74	26.74	3.334	3.335	(110)
33.90	34.00	2.644	2.649	(101)
38.17	37.91	2.357	2.368	(200)
42.89	42.80	2.109	2.120	(210)
51.96	51.73	1.760	1.768	(211)
55.09	54.80	1.667	1.675	(220)
62.27	61.92	1.491	1.502	(310)
66.28	65.93	1.410	1.415	(112)
71.33	71.37	1.322	1.325	(202)
79.14	78.66	1.210	1.219	(321)

The XRD spectrum of TEC-7 is presented in Figure 4.2, indicating the polycrystalline nature of the material. The preferential orientation is similar to TEC-15 although the (101) peak has increased markedly. The similarity of the standard and observed XRD data is found in Table 4.2. The increase in intensity of the TEC-7 spectra compared to TEC-15 is due to the increase in thickness.

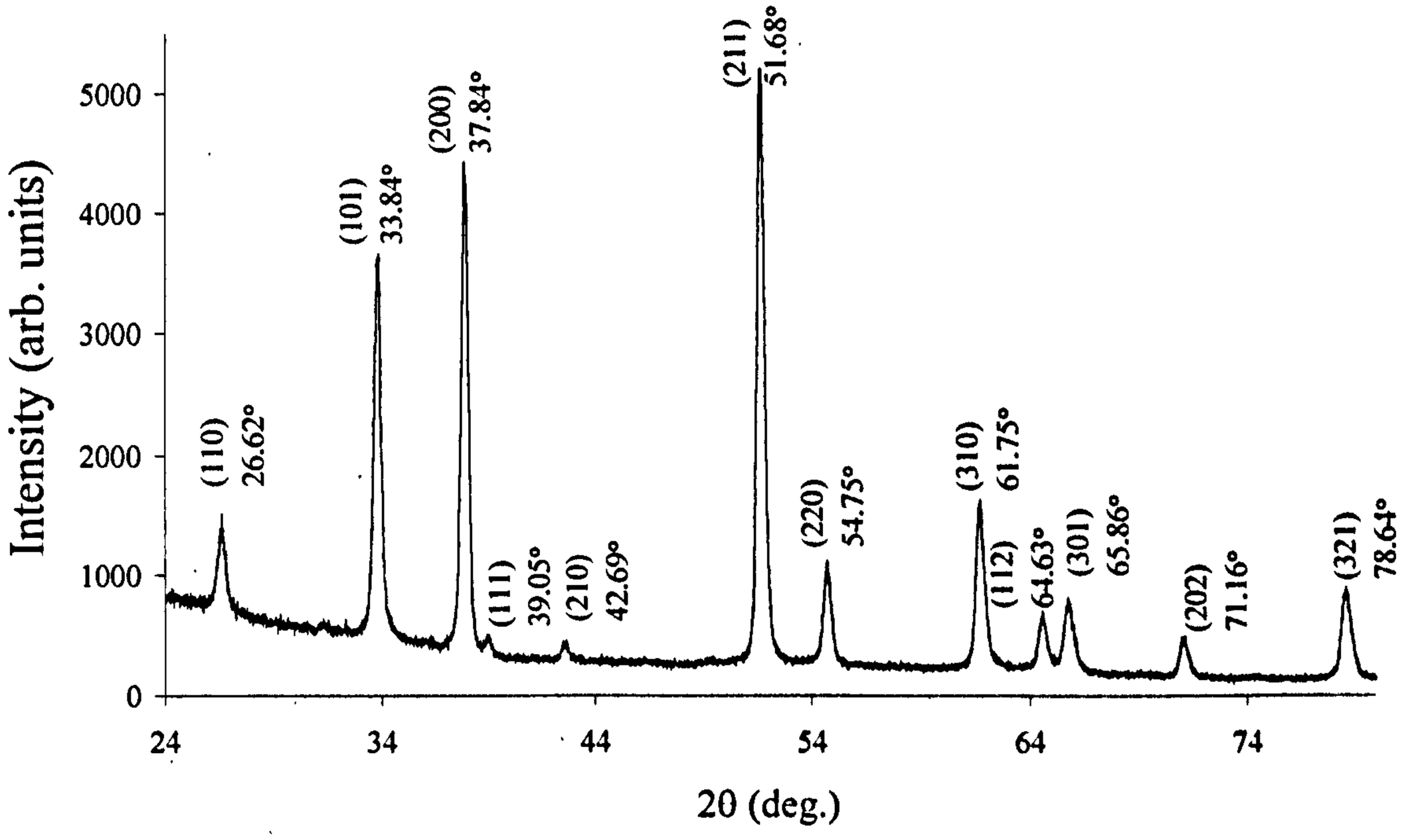

Figure 4.2. XRD spectra of TEC-7 FTO, all peaks were identified as SnO_2.

Table 4.2. XRD data obtained for TEC-7 identified as tetragonal SnO_2.

2θ (deg.)		d-Spacing (Å)		Miller Indices
Standard	Observed	Standard	Observed	(hkl)
26.74	26.62	3.334	3.357	(110)
33.90	33.84	2.644	2.645	(101)
38.17	37.84	2.357	2.368	(200)
39.05	39.11	2.306	2.305	(111)
42.89	42.69	2.109	2.116	(210)
51.96	51.68	1.760	1.768	(211)
55.09	54.75	1.667	1.672	(220)
62.27	61.75	1.491	1.499	(310)
64.72	64.63	1.440	1.437	(112)
66.28	65.86	1.410	1.414	(301)
71.33	71.16	1.322	1.322	(202)
79.14	78.64	1.210	1.214	(321)

The Scherrer relation (2.5), discussed in Chapter 2 was used to estimate the grain size of TEC-7 and TEC-15 which is presented in Table 4.3. The XRD data for the three main peaks for TEC-7 and TEC-15 were utilised for this calculation as

indicated in the table [Cullity & Stock 2001]. The sharpness of the peaks and the low FWHM indicate both TEC-15 and TEC-7 have a high degree of crystallinity. The preferential peaks for TEC-15 and TEC-7 located at 37.91° and 51.68° provides the most accurate estimation of grain size. The mean grain sizes of TEC-15 and TEC-7 were calculated as 17.6 and 17.3 nm respectively.

Table 4.3. Grain size calculated using the XRD data and the Scherrer relation for the three main peaks of TEC-15 and TEC-7.

TEC-15			
2θ (deg.)	**cos θ**	**b (deg)**	**D (nm)**
37.91	0.945	0.42	19.6
51.73	0.899	0.48	18.4
61.92	0.858	0.62	14.7
		Mean	17.6
TEC-7			
33.84	0.956	0.45	16.8
37.84	0.945	0.45	16.6
51.68	0.900	0.38	18.6
		Mean	17.3

The lattice parameters of TEC-15 and TEC-7 were calculated using the XRD data and the tetragonal d-spacing equation (2.7) discussed in Chapter 2 [Cullity & Stock 2001]. Table 4.4 compares the calculated values with standard values obtained from the online Daresbury Chemical Database Service [Gracia *et al.* 2007]. The Miller indices used in the calculation corresponding to the 2θ values for both XRD spectra are presented in the table.

Table 4.4. Lattice parameters calculated using the XRD data for TEC-15 and TEC-7 compared with standard data.

	2θ (deg.)	**d (Å)**	**(hkl)**	**a (Å)**	**c (Å)**
TEC-15	37.91	2.268	(200)	4.744	
	51.73	1.768	(211)		3.199
TEC-7	33.84	2.645	(101)		3.187
	37.84	2.368	(200)	4.758	
Standard				4.715	3.194

4.1.2.2 Scanning Electron Microscopy

The morphology of TEC-15 and TEC-7 was investigated using SEM. It is evident from the images presented in Figure 4.3 (a & b) there is a difference in the grain sizes between the two materials. TEC-15 has a smaller grains size of ~100 nm compared to 100 to 500 nm for TEC-7. The larger grain size of TEC-7 impacts on the electrical properties of the material, having a lower sheet resistance compared to TEC-15. The grain size does not agree with the values calculated using the Scherrer relation, which is one order of magnitude smaller. The Scherrer relation uses the FWHM which provides information on the coherence length of reflected x-rays. SEM detects the surface morphology and indicates the nodule size which is of greater magnitude than the information provided by XRD.

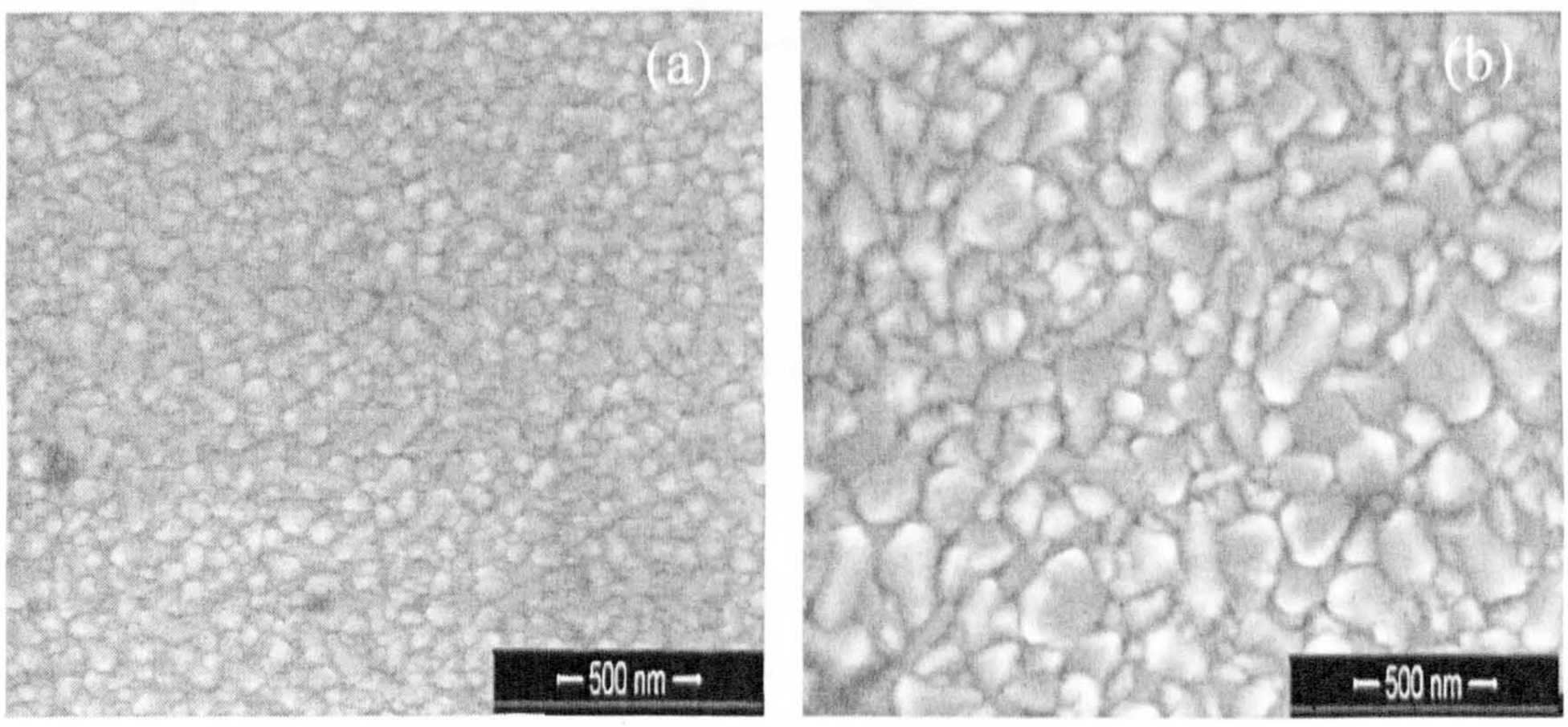

Figure 4.3. SEM images of (a) TEC-15 and (b) TEC-7 FTO, having grain sizes of 100 nm and 100 to 500 nm respectively.

4.1.2.3 Optical Properties

The optical absorption spectra of TEC-15 and TEC-7 are presented in Figure 4.4. It is evident to the naked eye the TEC-7 FTO is less transparent than the TEC-15, assumed to be due to the increase in thickness. The curves were extrapolated to estimate the bandgap energy, which was determined at 3.97 eV and 4.03 eV for

TEC-7 and TEC-15, agreeing with previously reported values [Sundaram & Bhagavat 1981]. For solar cells having superstrate configuration it is essential the bandgap energy of the conductive substrate is as high as possible to allow all useful wavelengths to pass to the space-charge region of the cell.

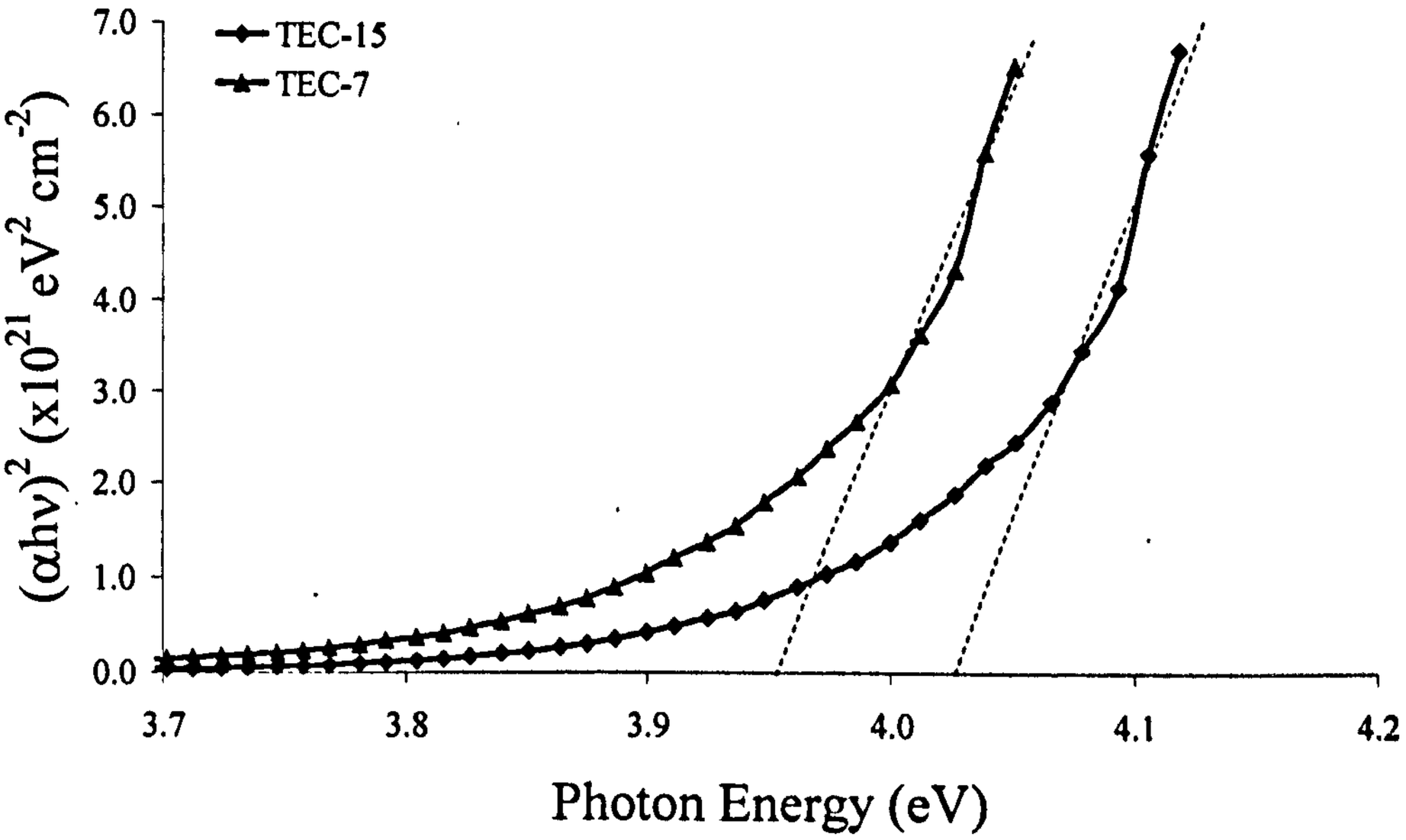

Figure 4.4. Optical absorption spectra of TEC-7 and TEC-15 FTO, having bandgap energy of 4.03 and 3.97 eV respectively; dashed lines are to guide the eye.

The transmission spectra for TEC-15 and TEC-7 were measured over the wavelength range 250 to 800 nm and are presented in Figures 4.5 and 4.6 respectively. The transmission spectra indicate a sharp absorption edge for both materials at ~300 nm. For TEC-15 80% of photons with wavelength longer than 400 nm were transmitted. The peak absorption edge of TEC-7 is less sharp; the transmission reaching 80% after 550 nm.

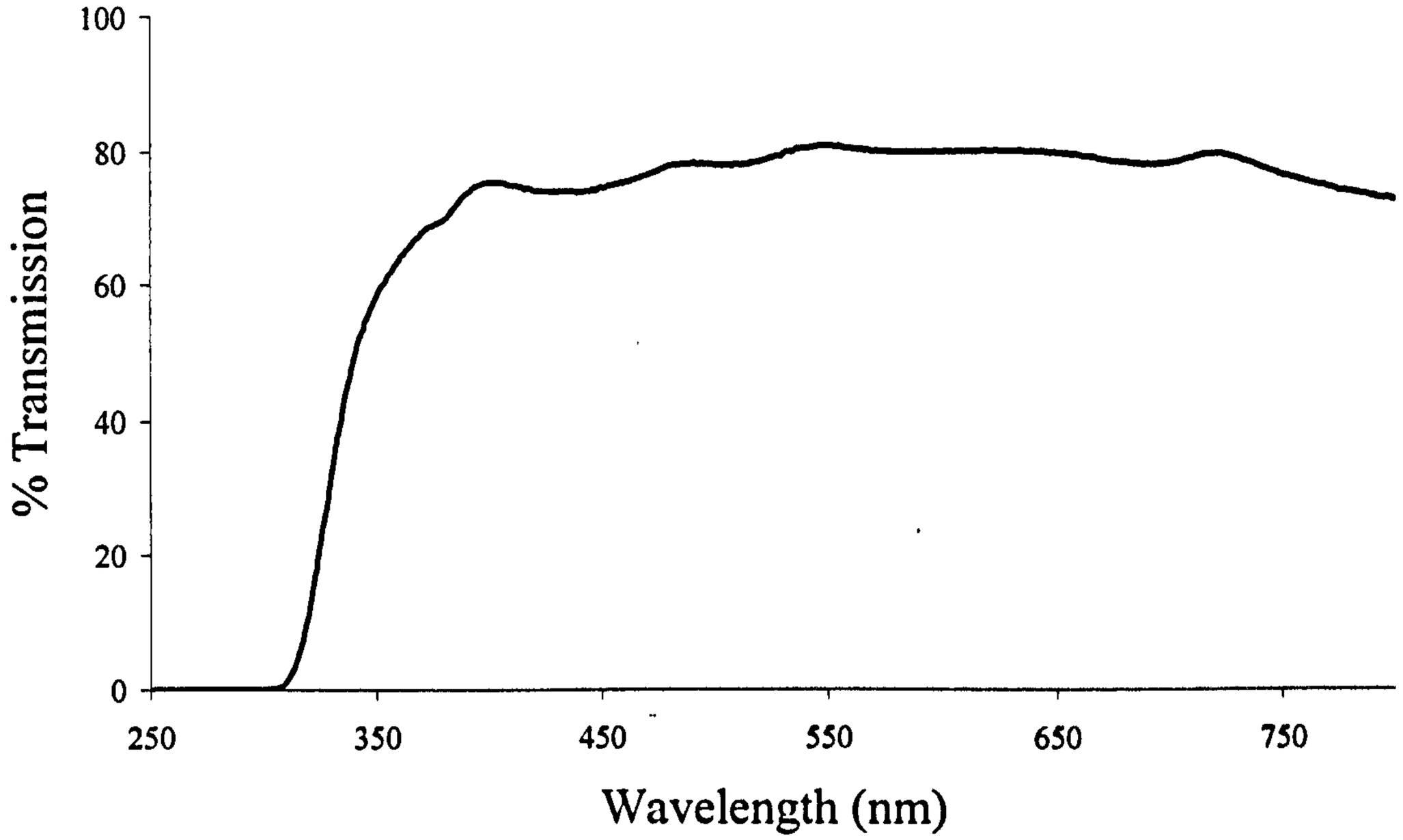

Figure 4.5. Transmission spectra of TEC-15 FTO conducting glass with absorption edge at 300 nm.

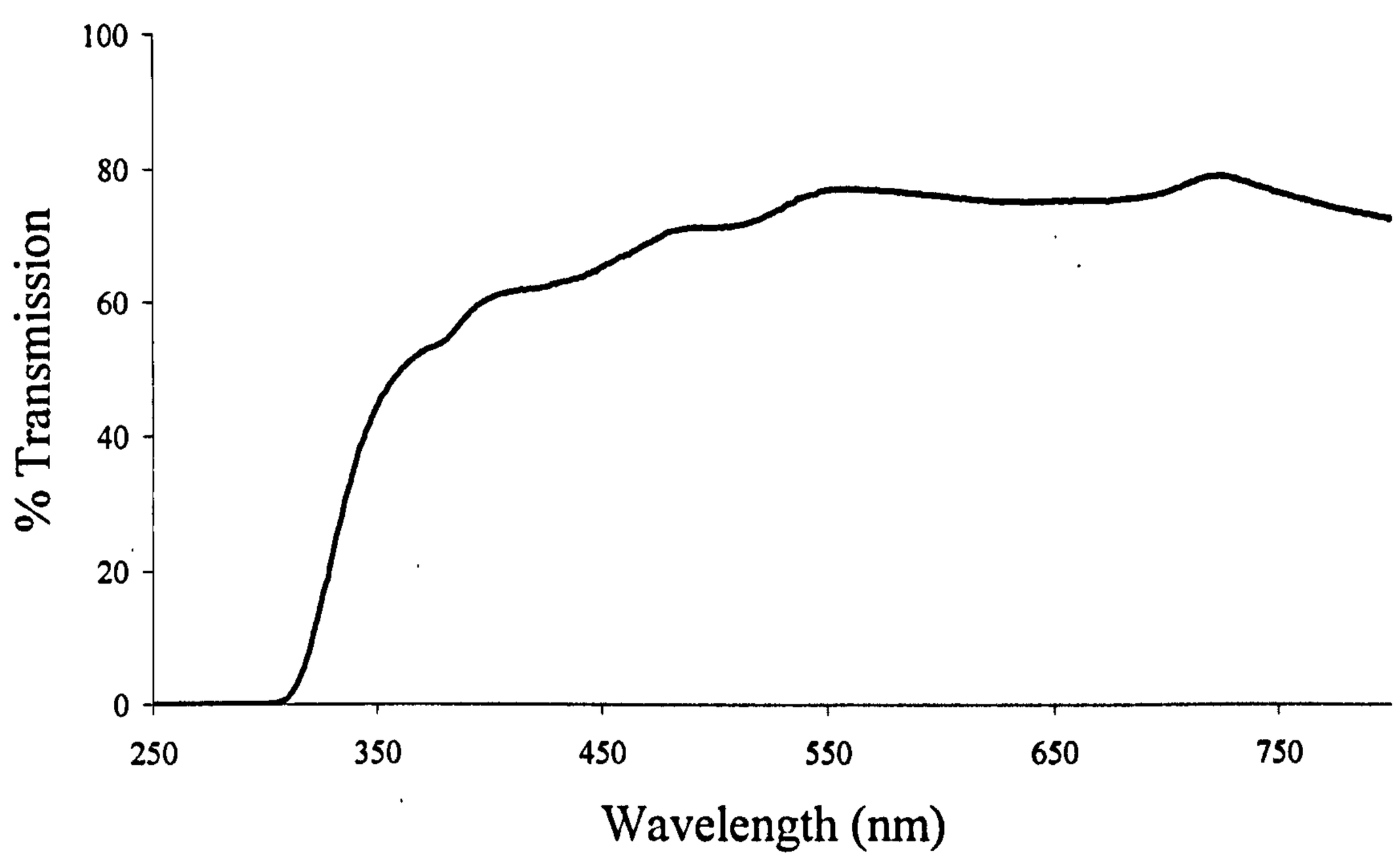

Figure 4.6. Transmission spectra of TEC-7 FTO having absorption edge at 300 nm.

4.1.2.4 Electrical Properties

Four-point probe measurements were carried out for TEC-15 and TEC-7 to confirm the values for sheet resistance quoted by Pilkington Group Ltd. Figures 4.7 and 4.8 present I-V characteristics of TEC-15 and TEC-7 obtained from the four-point probe measurements. Taking the inverse gradient of each I-V plot and using equation 4.1, the sheet resistances of TEC-15 and TEC-7 were calculated at 12.9 and 7.3 Ω/□ respectively. The bulk electrical resistivity was thus calculated using equation 4.2 at 3.3×10^6 and 1.4×10^6 Ω cm for TEC-15 and TEC-7 respectively.

$$R_s = 4.532\frac{V}{I} \tag{4.1}$$

$$R_s = \frac{\rho}{t} \tag{4.2}$$

where R_s = Sheet Resistance (Ω/□), V = Voltage (V), I = Current (A), ρ = Resistivity (Ω m) and t = Thickness (m).

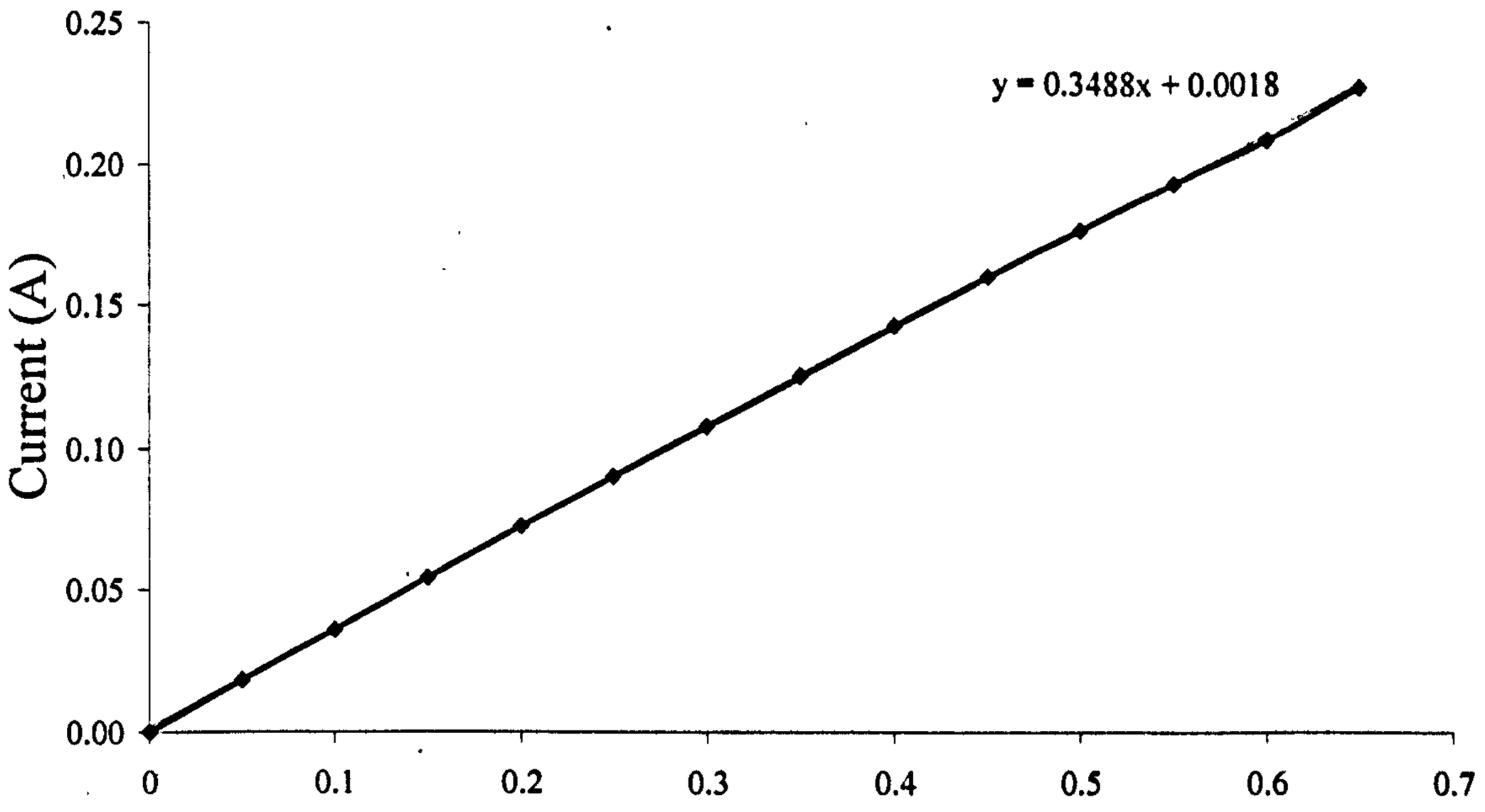

Figure 4.7. Four-point probe measurement of TEC-15 FTO having mean sheet resistance of 13 Ω/□.

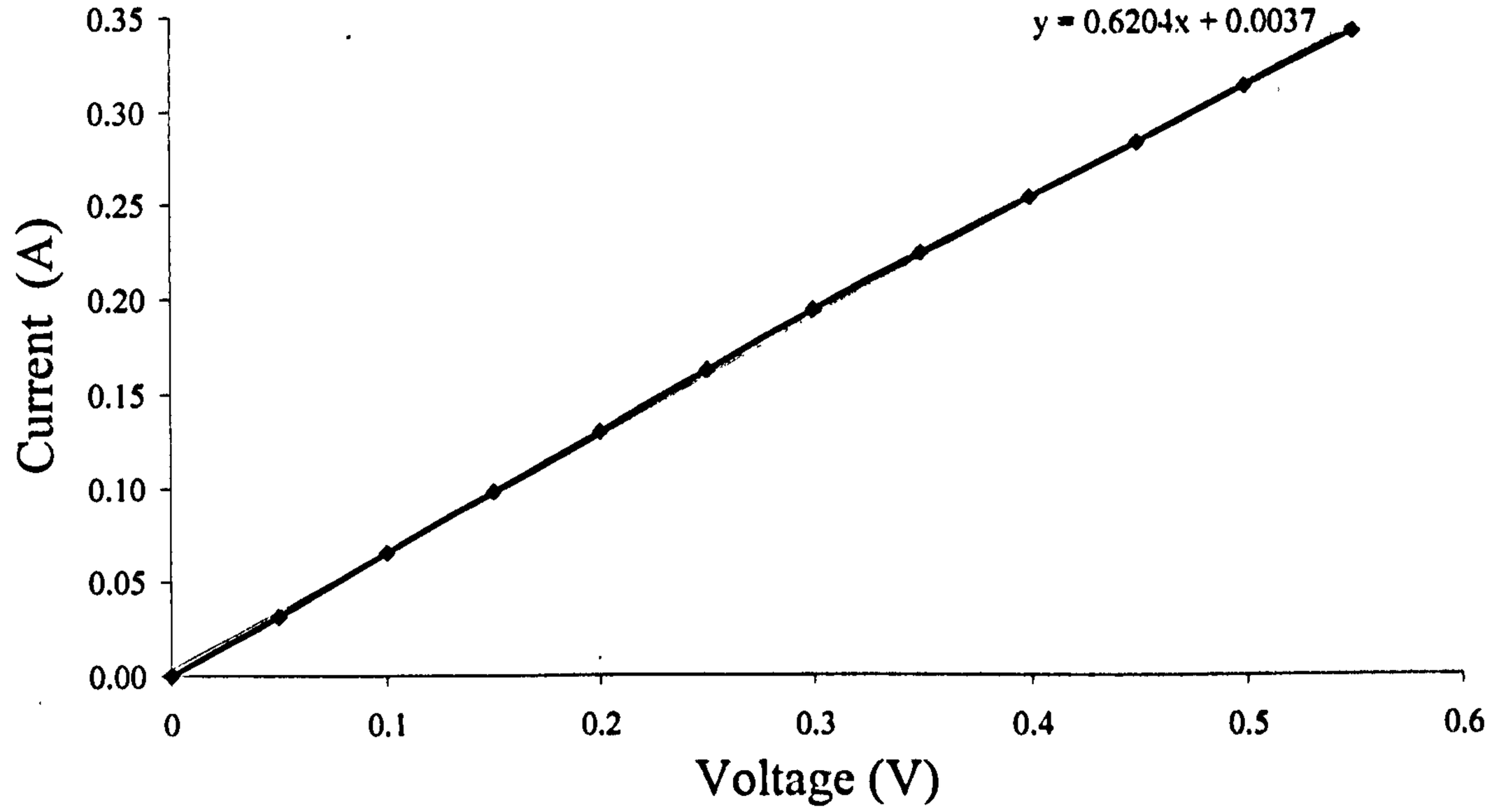

Figure 4.8. Four-point probe measurement of TEC-7 FTO having mean sheet resistance of 7.3 Ω/□.

4.2 Cadmium Sulphide

4.2.1 Introduction

CdS is a II-VI compound and is used as an n-type window material with CdTe and $CuInGaSe_2$ solar cells; most commonly having superstrate and substrate device structures respectively [Wagner *et al.* 1974, Mitchell *et al.* 1977]. The usual method of growth is via CBD, which has the advantage of requiring a short deposition time to obtain the desired thickness of ~80 nm. The reaction time may also be manipulated by varying the concentration of reagents. The CBD process is scalable, allowing multiple substrates to be deposited simultaneously; the size and shape of which are dependent upon the solution container.

CBD is a batch process with a significant amount of toxic chemical wastage, which presents disadvantages especially when considering scale-up. This issue was considered by Hariskos *et al.* who separated the CdS colloids from the waste solution by filtration and re-adjusted the cadmium salt, thiourea and ammonia concentrations. It was found subsequent usage of the recycled solution resulted in a decrease in the deposition rate from 9 nm min^{-1} to 2 nm min^{-1} [Hariskos *et al.* 2001].

The as-deposited layers require post-deposition annealing at a maximum temperature of 450°C to improve grain structure and to anneal out defects, improving the electrical quality of the material. For superstrate configuration devices this is carried out before the deposition of the absorber material. In the case of devices with substrate structure the CdS is deposited onto the absorber after its deposition. The following sections present the experimental details, followed by the reaction mechanism of CdS and finally the results and discussion of the investigation.

4.2.2 Experimental Procedure

Initially the deionised water bath was heated to ~65°C using a stirrer hot plate. The solution was agitated throughout deposition using a Teflon magnetic follower. Table 4.5 lists the precursors used together with their respective formula weights and molarities for the experiment.

Table 4.5. Precursors used for the CBD of CdS, including the formula weight (FW) of each chemical and the molarities used for the experiment.

Chemical	Formula	FW	Molarity
Cadmium Sulphate	$CdSO_4.8H_2O$	769.57	1.5mM
Ammonium Chloride	NH_4Cl	53.49	0.1M
Ammonium Hydroxide	NH_4OH	17.50	1.5M
Thiourea	$(NH_2)_2CS$	76.12	75mM

Initially the $CdSO_4.8H_2O$ and NH_4Cl were added to the water bath and stirred constantly to form a solution. The pH of the solution was adjusted to ~9-11 using NH_4OH. TEC-7 substrates were cleaned in iso-propanol and rinsed in deionised water. The pre-heated substrates were immersed in the solution immediately after the addition of $(NH_2)_2CS$. After the addition of $(NH_2)_2CS$ the duration of the useful part of the chemical reaction was ~14 minutes with this regent concentration. On removal from the deposition bath the layers were rinsed with deionised water and cleaned ultrasonically to remove loose CdS particles formed during the homogeneous reaction. The reaction mechanism is presented in Section 4.2.3 and Table 4.6 lists visual observations at 2 minute time intervals after $(NH_2)_2CS$ was added to the solution.

Post-deposition heat treatment was carried out in a Carbolite furnace in air atmosphere at 450°C for 20 minutes before the substrates were used for further deposition of CdTe. The layers were characterised using XRD, SEM, and optical spectroscopy. Electrical measurements were carried out on glass/FTO/CdS/Au structures, having a contact diameter of 2 mm.

4.2.3 Cadmium Sulphide Reaction Mechanism

The principles for the formation of ammine complexes in aqueous solution have been studied since the 1950's. Metal ions in the presence of aqueous ammonia form metal-ammonia complexes or ammines. The ammine complex decomposes at a slow rate releasing the metal ions into the solution where they can react with water forming water insoluble metal oxides and hydroxides. The growth mechanism proceeds via two processes; forming a suspension in the bulk of the solution known as homogeneous precipitation and adhering to the substrate surface or heterogeneous precipitation. In addition the particles formed via the homogeneous process stick loosely to the surface of the sample and can easily be rinsed away or ultrasonically removed.

The dissolution of ammonium hydroxide in aqueous solution occurs via reaction 4.1.

$$NH_4OH \rightarrow NH_4^+ + OH^- \qquad (4.1)$$

Formation of NH_3 occurs via the deprotonation reaction with water indicated by reaction 4.2.

$$NH_4^+ + OH^- \Leftrightarrow NH_3 + H_2O \qquad (4.2)$$

Few cations can form stable ammonia complexes in aqueous solutions, including Cd^{2+}, due to their relatively weak affinity with nitrogen [Mironov *et al.* 1992, Silver & Martin 1994]. Reaction 4.3 and 4.4 summarise the reactions between cadmium and ammonia (forming the ammine complex) and cadmium with hydroxide respectively. The concentration of dissolved Cd^{2+} in solution is limited by the onset of precipitation of $Cd(OH)_2$ complexes [Ortega-Borges & Lincot 1993].

$$Cd^{2+} + 4NH_3 \Leftrightarrow [Cd(NH_3)_4]^{2+} \quad (4.3)$$

$$Cd^{2+} + 2OH^- \Leftrightarrow Cd(OH)_2 \quad (4.4)$$

In the case of CdS CBD, following the addition of a sulphur containing reagent such as thiourea, sulphur is released into the solution when the conditions are favourable via reactions 4.5 and 4.6.

$$(NH_2)_2CS + OH^- \rightarrow HS^- + CH_2N_2 + H_2O \quad (4.5)$$

$$HS^- + OH^- \rightarrow S^{2-} + H_2O \quad (4.6)$$

The rate of release of S^{2-} is dependent on the temperature and pH of the solution. Increasing the temperature of the solution increases the rate of reaction. Ortega–Borges and Lincot [1993] investigated the effect of temperature on the growth rate and reported CdS formation was not observed for several hours. At 75°C the useful part of the reaction was completed within 3 minutes.

Increasing the concentration of ammonium hydroxide in the solution increases the pH which promotes the release of S^{2-}. This however also encourages the simultaneous formation of the $[Cd(NH_3)_4]^{2+}$ complex, reducing the rate of release of Cd^{2+} subsequently reduced the rate of CdS formation and is indicated by reaction 4.7.

$$Cd^{2+} + S^{2-} \rightarrow CdS \quad (4.7)$$

Additional ammonia may also be added to the solution using ammonium chloride, which helps to control the rate of reaction. The deposition of CdS occurs when the ionic product of Cd^{2+} and S^{2-} in solution exceeds the solubility product (K_p) of CdS (1.4×10^{-25}). Cd^{2+} release is high with high pH and therefore CdS forms easily, even with a low S content [Ortega-Borges & Lincot 1993].

The fast release of Cd^{2+} is detrimental as the homogeneous reaction can overtake the heterogeneous CdS formation reaction. The competition between the two reactions can be carefully controlled by adjusting the pH and temperature to encourage the heterogeneous reaction. NH_4Cl plays a key role in controlling the reaction by

complexing Cd^{2+} without increasing the pH [Chu *et al.* 1991]. Figure 4.1 is the schematic diagram of the homogeneous and heterogeneous CdS reactions [Ezema & Osuji 2007].

Table 4.6 list the visual observations of the CdS growth at 2 minute intervals after the addition of $(NH_2)_2CS$. Ortega-Borges and Lincot [1993] have previously reported the growth mechanism of CdS to consist of three different domains, which correspond to the observations in Table 4.6. The initial domain referred to as the induction period arises at short reaction times when nucleation takes place; this is denoted by the 1 to 2 minute reaction time (at 65°C) in Table 4.6. The second region (4 to 10 minutes in the table) corresponds to the growth of a compact and adhered layer which deposit linearly with time, saturating at ~100 nm. After longer reaction times (11 minutes and above) the sudden increase in growth rate corresponds to the deposition of a porous layer due to sticking of larger colloids which can be easily removed as described earlier [Ortega-Borges & Lincot 1993].

Table 4.6. Experimental observations noted during CBD of CdS over a 12 minute growth period.

Time (minutes)	Observation
2	Slight yellow tinge at edge of base of beaker
4	Solution turns partially cloudy, although remains transparent
6	Solution turns lemon in colour and remains transparent
8	Opaque and lemon in colour
10	Colloids large and clearly apparent
12	Deep yellow/orange colour
14	Useful part of reaction over

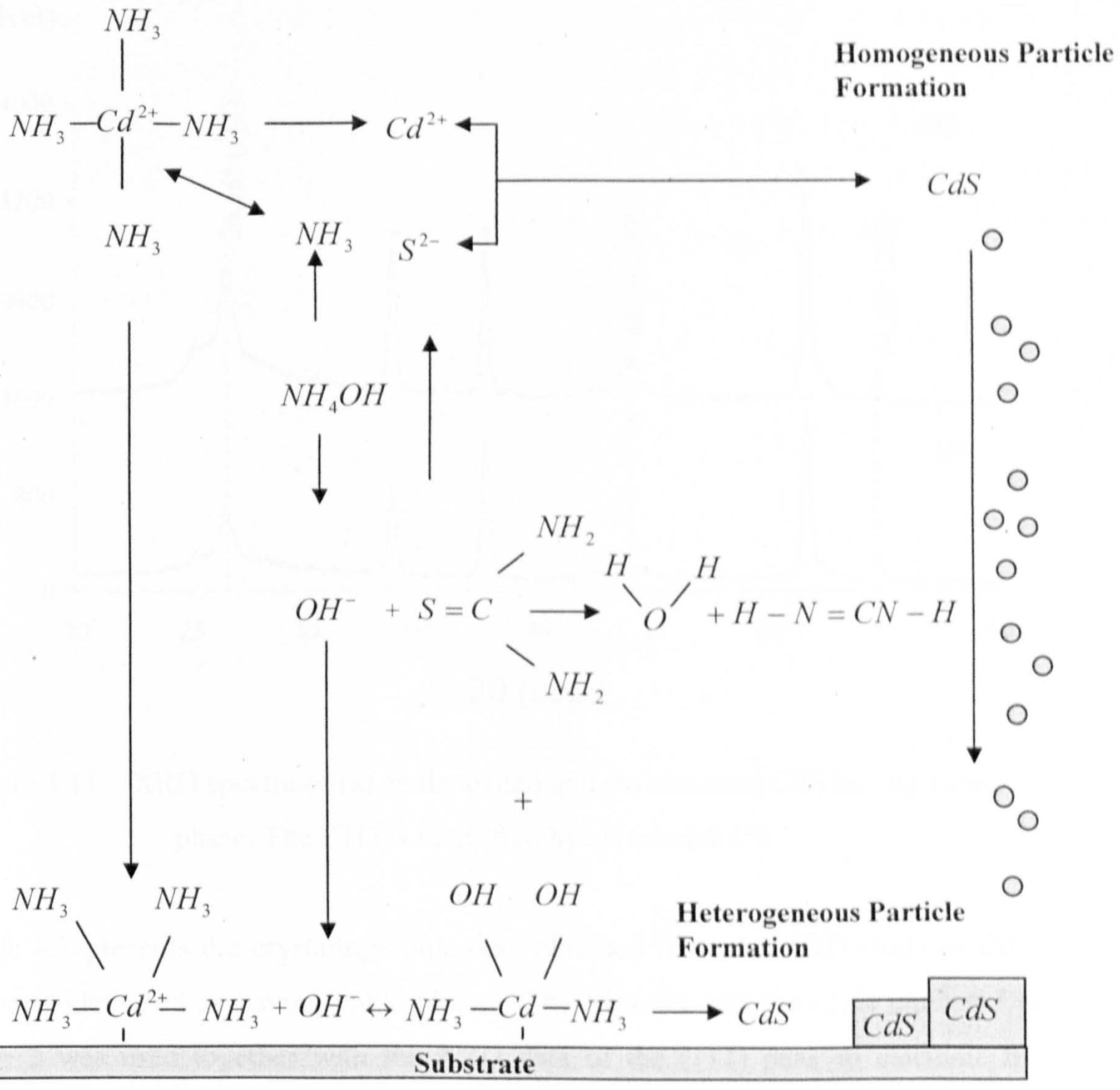

Figure 4.9. Schematic diagram of CBD CdS growth mechanism having homogeneous particle formation in the bulk of the solution and heterogeneous particle formation at the substrate surface.

4.2.4 Results and Discussion

4.2.4.1 X-Ray Diffraction

XRD studies were carried out on as-deposited and annealed CdS layers to determine the structural and crystallographic properties. Figure 4.11 presents the spectra obtained

for (a) as-deposited and (b) annealed (450°C for 20 minutes) glass/FTO/CdS layers respectively.

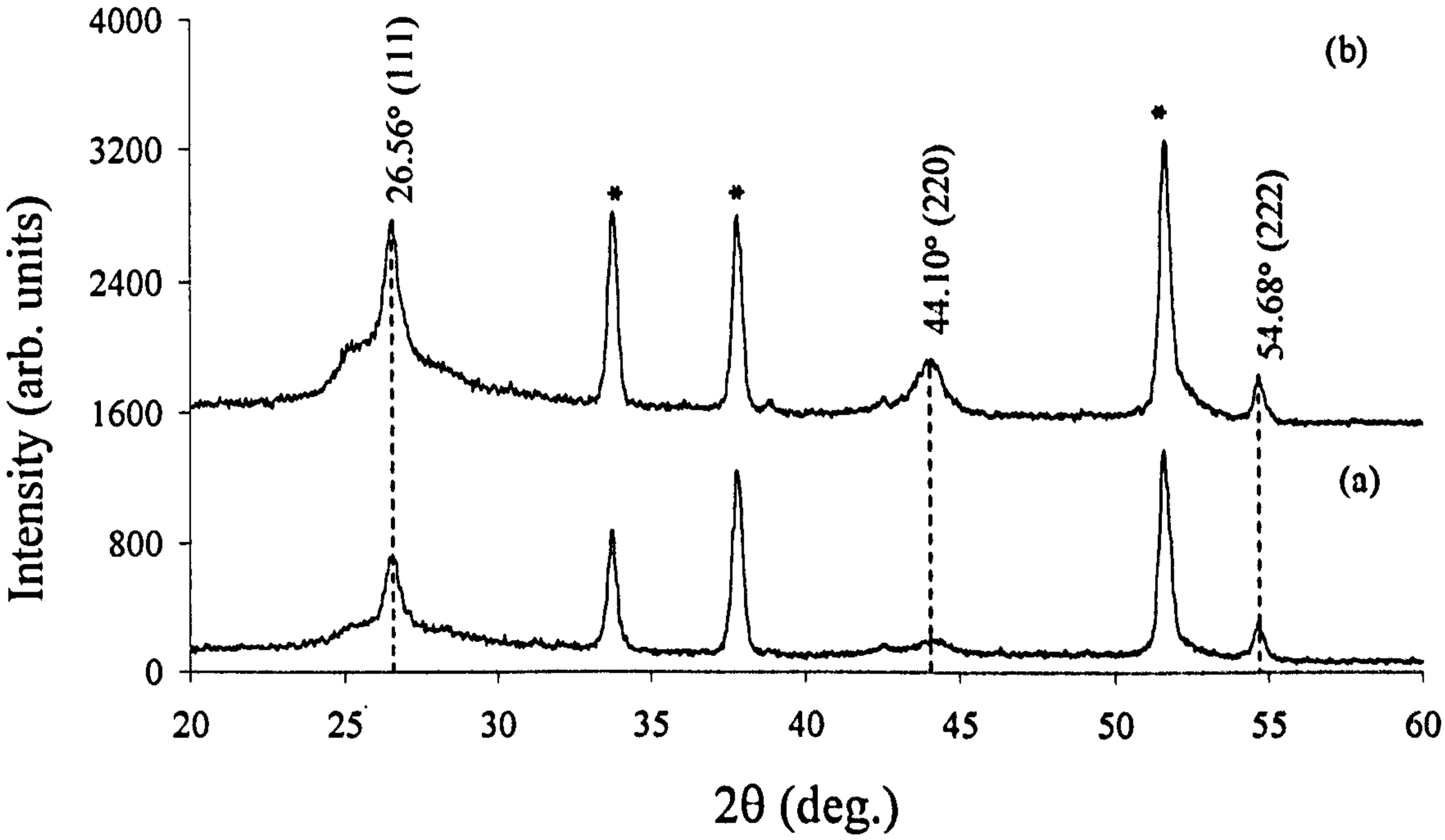

Figure 4.11. XRD spectra of (a) as-deposited and (b) annealed CdS having cubic phase. The FTO is identified by an asterisk (*).

Table 4.7 presents the crystallographic data obtained from the XRD study of CdS, which was identified as having cubic phase. The Scherrer relation (2.5) indicated in Chapter 2 was used together with the XRD data of the (111) peak to calculate the crystallite size. The grain size was calculated at 12.6 nm and did not change after annealing. Although the grain size did not change after heat-treatment the crystallographic transformation is evident from the increase in intensity of the (111), (220) and (222) peaks.

Table 4.7. XRD data representative of both as-deposited and annealed CdS having cubic phase.

2θ (deg.)		d-Spacing (Å)		Miller Indices	Compound
Standard	Observed	Standard	Observed	(hkl)	
26.48	26.56	3.366	3.356	(111)	CdS
33.84	33.76	2.644	2.656	(101)	SnO_2
37.84	37.80	2.357	2.380	(200)	SnO_2
43.92	44.10	2.061	2.048	(220)	CdS
51.68	51.60	1.760	1.771	(211)	SnO_2
54.52	54.76	1.683	1.679	(222)	CdS

The lattice parameter of the CdS was calculated using the XRD data for the (111) peak and the cubic d-spacing equation (2.6) described in Chapter 2. The lattice parameter was calculated at a=5.816 Å and compares well with the standard value of a=5.830 Å obtained from the online Daresbury Chemical Database Service [Rodic *et al.* 1996]. The dotted lines in Figure 4.11 indicate the peak positions are at the same 2θ values for as-deposited and annealed layers. The d-spacing values and lattice parameters are therefore the same.

4.2.4.2 Scanning Electron Microscopy

The surface morphology was investigated using SEM for both as-deposited and annealed CBD CdS as indicated by Figure 4.12 (a & b). The crystal structure of the as-deposited material (Figure 4.12a) appears to be uniform and nanocrystalline, having crystal size of around 100 nm. This is one order of magnitude larger than predicted by the Scherrer relation of 12 nm. This is likely to be due to the instrument capabilities as already discussed in Section 4.1.2.2. It is clear that after annealing the crystal structure changed, becoming less uniform with crystals of varying shape and size. The crystals have enlarged and are between 200 to 500 nm in size with varying orientation. Additionally, small nodules have developed ~20 nm in size.

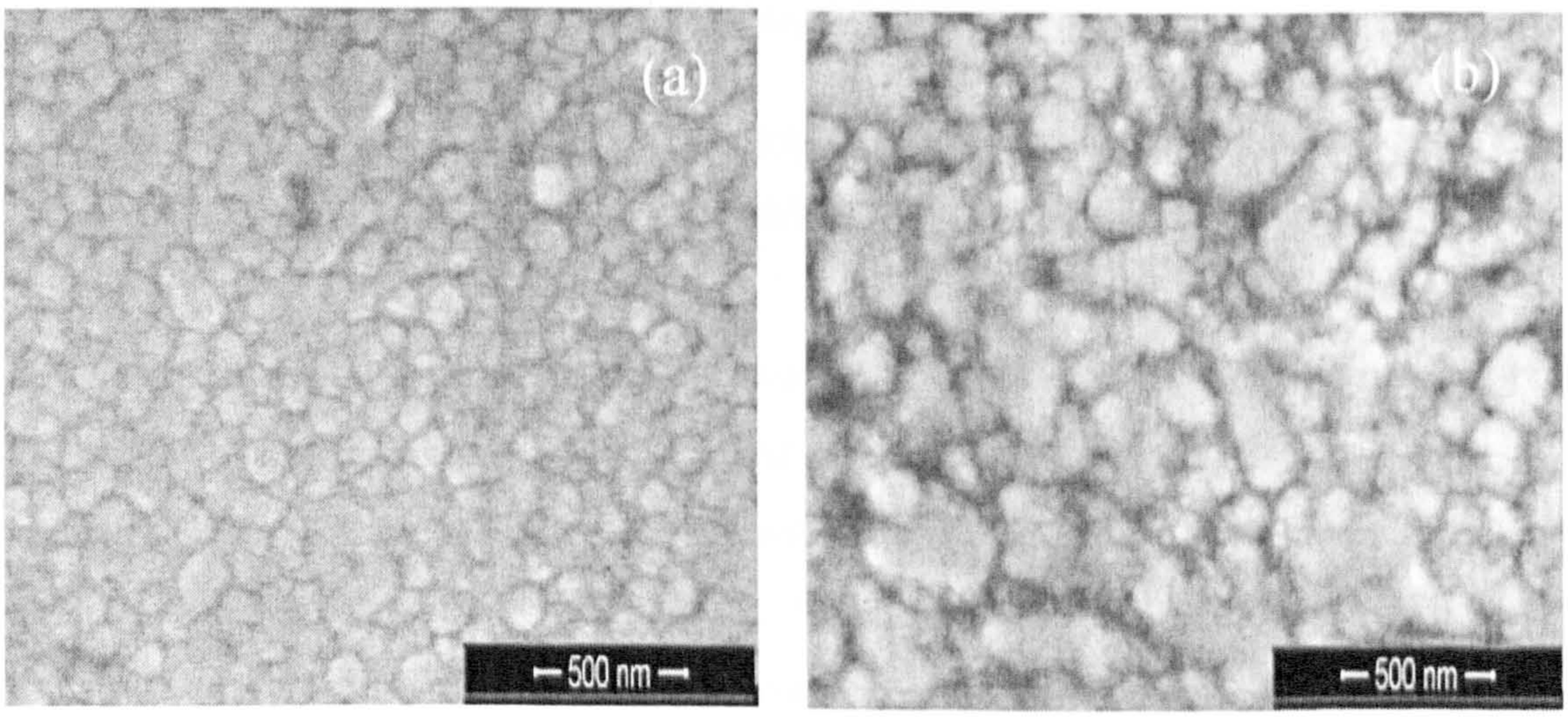

Figure 4.12. SEM images of (a) as-deposited CdS having crystal size of 200 nm and (b) annealed CdS indicating a less uniform crystal structure with varying grain size from 200 to 500 nm.

4.2.4.3 Optical Properties

The optical absorption spectra of as-deposited and annealed (450°C for 20 minutes) CdS on TEC-7 are presented in Figure 4.13. It is clear that the absorption profile and absorption edge changed after annealing. The bandgap energies were determined from this spectra at E_{g1} = 2.30 eV and E_{g2} = 2.45 eV for annealed and as-deposited CdS respectively. It is well known that CdO having bandgap energy of 2.30 eV forms on the surface of the CdS during annealing [Jayakrishnan & Hodes 2003]. This is observed by a visible change in colour from yellow to orange before and after heat-treatment. However no CdO peaks were observed during the XRD investigation.

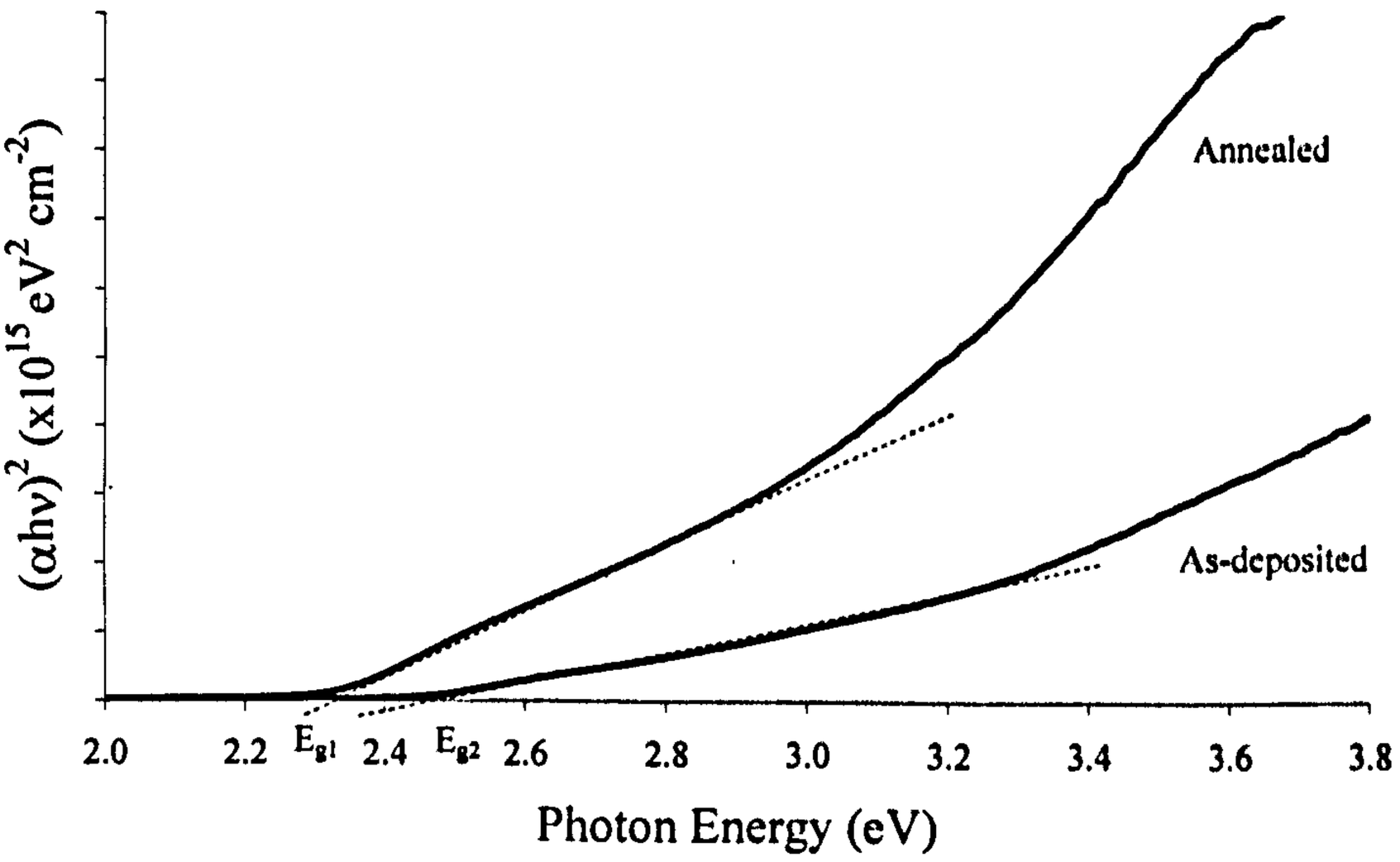

Figure 4.13. Optical absorption spectra of as-deposited and annealed CdS having bandgap energies of 2.45 and 2.30 eV respectively.

The transmission spectra of as-deposited and annealed CdS are presented in Figure 4.14. The absorption edge is sharper for the as-deposited material compared to the annealed CdS. The annealed material transmitted fewer photons at lower wavelengths compared to the as-deposited CdS due to the smaller bandgap energy. The percentage transmission of both materials is 80% at wavelengths above the absorption edge.

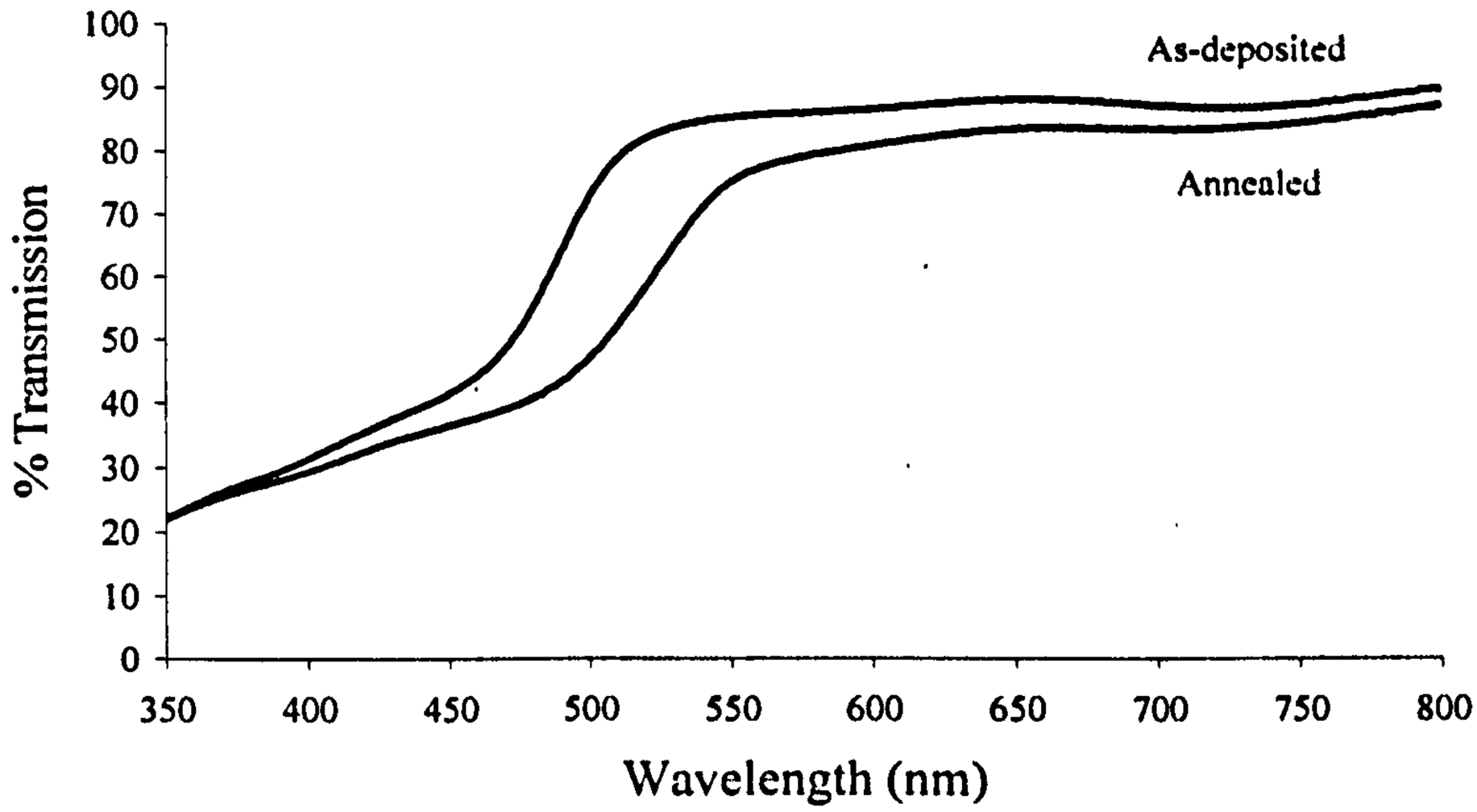

Figure 4.14. Transmission spectra of CdS deposited onto TEC-7; as-deposited and annealed at 450°C for 20 minutes.

The relationship between transmission and deposition time was investigated by studying the transmission spectra (Figure 4.15, a-f). The layers were sequentially removed from the deposition bath at 2 minute time intervals from 4 to 14 minutes. It is clear from the spectra that the transmission decreases as a function of deposition time and the absorption edge shifts to longer wavelengths. The thickness of the CdS increases with deposition time and this was apparent by the colour change of the layers from pale to dark yellow. On removal from the deposition bath after 4 minutes the layer was extremely thin and only just visible. Contreras reported initial nucleation to take place after 4 minutes and deposition of a continuous film at 6 minutes [Contreras *et al.* 2002]. Thus, transmission decreases with increasing thickness of CdS, which moves the absorption edge to higher wavelengths increasing the losses in low wavelength region.

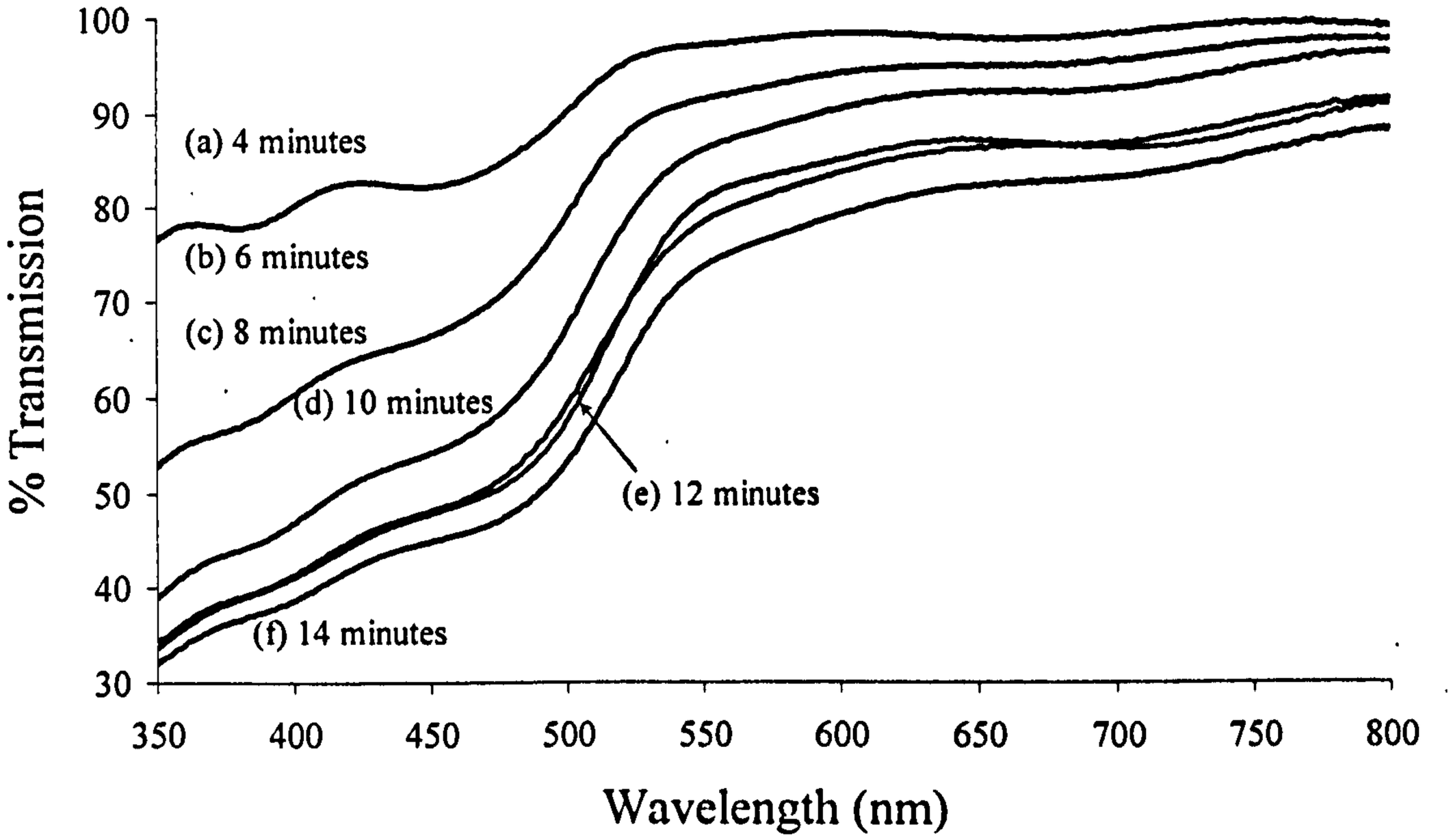

Figure 4.15. Transmission spectra of CdS deposited using CBD onto TEC-7 with a growth time of (a) 4, (b) 6, (c) 8, (d) 10, (e) 12, and (f) 14 minutes.

4.2.4.4 Electrical Properties

Schottky contacts were formed on annealed CdS using Au. The properties of the material improve after annealing due to the increase in grain size as determined by SEM and a reduction of defects is predicted. The electrical properties of the glass/FTO/CdS/Au were investigated under dark conditions. The Log I vs V and linear-linear I-V curves are presented in Figure 4.16 and 4.17 respectively. A rectification factor of 2.5 orders of magnitude at ~1.0 V was determined from the difference in forward and reverse bias curves of Figure 4.16. Using Figure 4.17 the series resistance was calculated at 1.1 Ω. Equations 2.15 and 2.16 were used to determine the ρ and σ at $4.4 \times 10^{5}\ \Omega$ cm and $2.3 \times 10^{-6}\ \Omega\ cm^{-1}$ respectively.

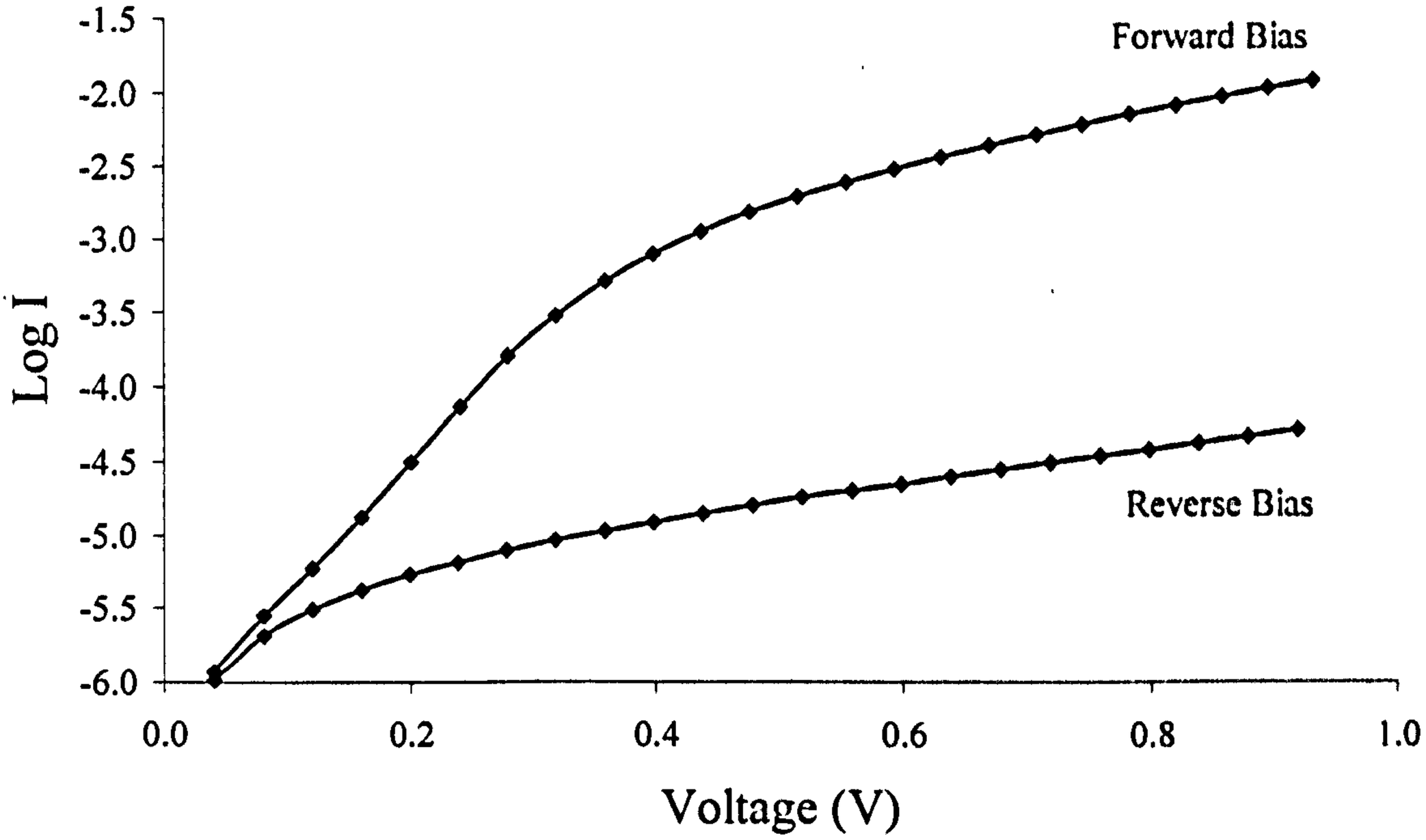

Figure 4.16. Log-linear curve of glass/FTO/CdS/Au under dark conditions having rectification factor of 2.5 orders of magnitude at ~1.0 V.

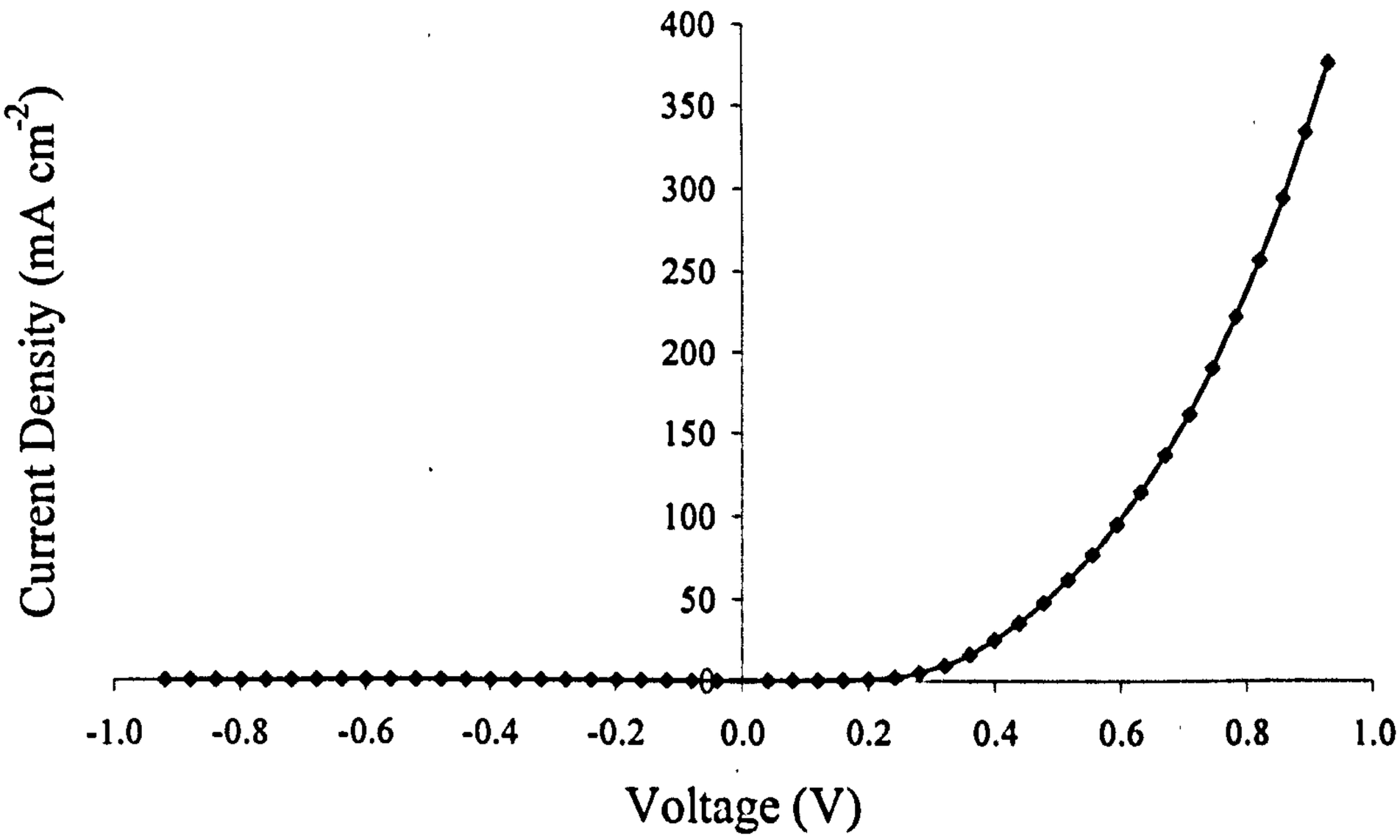

Figure 4.17. Linear current density-voltage curve of glass/FTO/CdS/Au in the dark.

Chapter 5 Electrodeposited Zinc Oxide

5.1 Introduction

The CIGS device structure includes an undoped and Al-doped ZnO layer with glass/Mo/CIGS/CdS/i-ZnO/ZnO:Al configuration for substrate devices. Currently sputtering is the most common technique used to deposit ZnO for CIGS solar cells; mainly due to controllability of layer thickness and composition but has the disadvantage of high equipment costs. The aim of the study was to evaluate the possibility of using electrodeposition for all layers as a unified production process for growth of the CIS layer and the ZnO bilayer. Electrodeposition has the advantage of being a low-cost technique and has already been proven scalable with the production of CIS and CdTe solar cells [Taunier *et al.* 2005, Turner *et al.* 1994].

Sections 5.2 to 5.3 give experimental details and the results and discussion for electrodeposited i-ZnO. Aluminium was added to the electrolyte in parts per million (ppm) concentration during a doping experiment to produce ZnO:Al; the results of which are presented in Section 5.4. The purpose of doping ZnO with Al is to increase the n-type electrical conductivity of the material to form an improved ohmic contact during device fabrication. There are very few reports in the literature about the use of electrodeposition to deposit ZnO:Al [Kemell *et al.* 2003].

A comparative study of sputtered i-ZnO and ZnO:Al supplied by Pilkington Group Ltd. and electrodeposited material was carried out. This study was undertaken to compare the characteristics of both ZnO materials to assess the feasibility of replacement of sputtering with electrodeposition for this application. The results and discussion of the comparative study are given in Section 5.5.

There are still reproducibility issues regarding the p-type doping of ZnO and several suggestions behind these challenges have been made. Electrodeposition has never been reported to be utilised for this purpose. Addition of group I (Ag) or VII elements (P and As) to the electrolyte was carried out to attempt p-type doping ZnO. Although p-type electrical conductivity was not observed the results are presented in Section 5.6. The conclusions to the ZnO studies are described in Section 5.7.

5.2 Experimental Procedure

Glass substrates coated with FTO (TEC-15) supplied by Pilkington Group Ltd., were used as the working electrode for the electrodeposition of ZnO. Prior to deposition the substrates were cleaned ultrasonically in iso-propanol and rinsed in deionised water. ZnO thin films were electrodeposited potentiostatically using a conventional three-electrode system and silver/silver chloride (Ag/AgCl) (+220 mV vs NHE). The aqueous solution contained 0.1M zinc nitrate, $Zn(NO_3)_2.6H_2O$ having pH=5 and was stirred using a magnetic stirrer throughout deposition at a temperature of 80°C (± 2°C). Annealing was carried out using a Carbolite furnace operating at a temperature of 550°C for 20 minutes in an air atmosphere.

Cyclic voltammetry was used to determine the suitable growth region. Layers with dimensions 15×30 mm^2 were grown at various voltages between -0.900 and -1.050 V vs Ag/AgCl. The thickness of the i-ZnO layer was obtained by three methods for comparison, talysurf, SEM cross-section and the Faraday relation (2.3). The layers were characterised using XRD, SEM, optical spectroscopy, PEC, I-V and C-V measurements.

5.3 Results and Discussion - Intrinsic Zinc Oxide

5.3.1 Cyclic Voltammetry

Cyclic voltammetry was carried out using glass/FTO substrates to investigate a suitable growth voltage range. Figure 5.1 presents the voltammogram for the solution containing $Zn(NO_3)_2.6H_2O$ vs Ag/AgCl reference electrode with a sweep rate of 10 mV s^{-1}. The electrochemical growth mechanism of ZnO has previously been reported by various authors who identified the nitrate ion to be the oxygen source [Kemell *et al.* 2003, Yoshida *et al.* 2004].

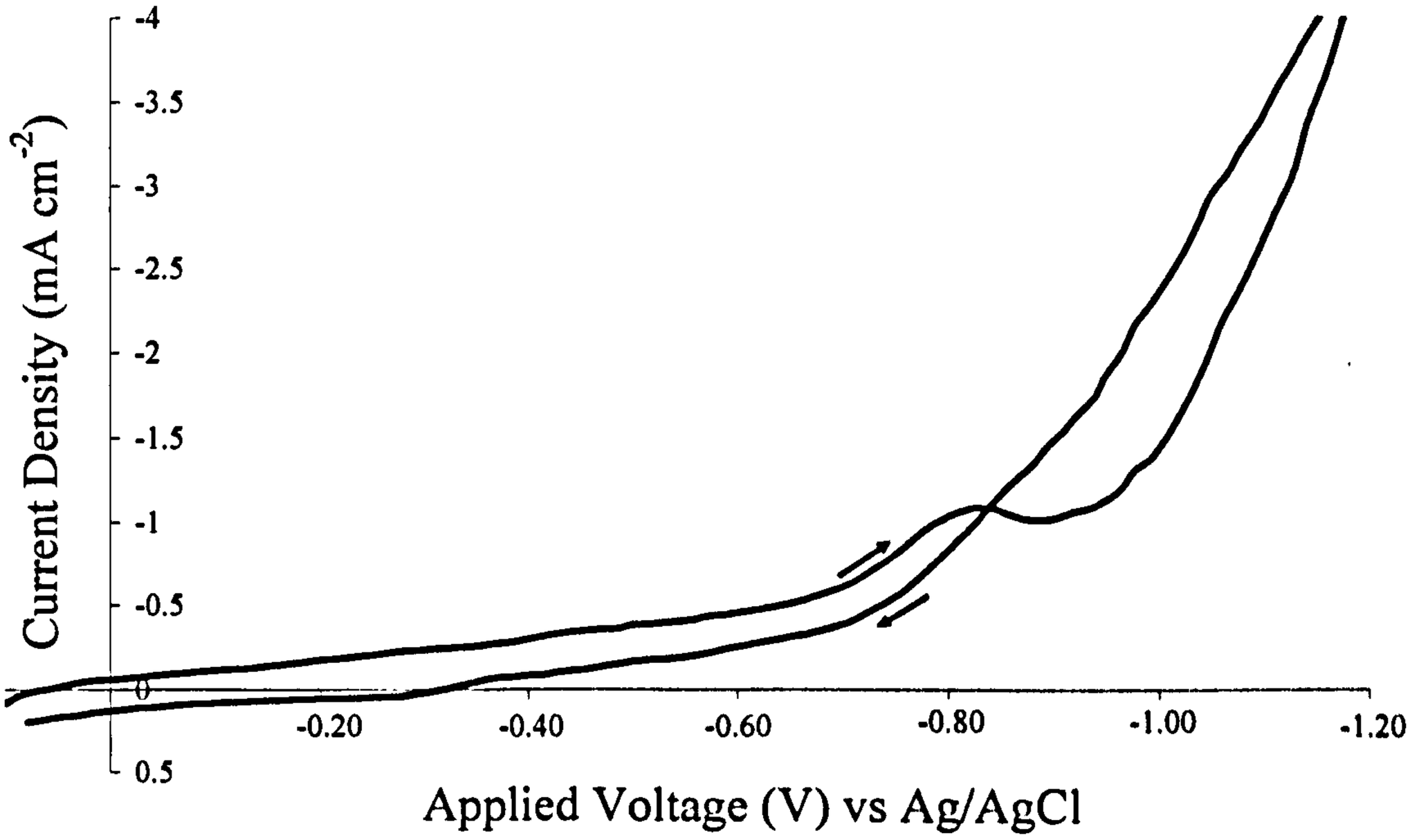

Figure 5.1. Cyclic voltammogram of 0.1M $Zn(NO_3)_2.6H_2O$ solution at 80°C, note the current density plateau between -0.80 and -0.99 V vs Ag/AgCl. The arrows indicate the direction of the voltage sweep.

According to reaction 3.6 (Chapter 3) the Zn^{2+} ions are released from the nitrate molecule. The initial current density onset is due to the reduction of the nitrate to nitrite ions in solution via reaction 3.7. When the applied voltage is suitable the Zn^{2+} reacts with hydroxide (OH^-) ions forming $Zn(OH)_2$ at the cathode via reaction 3.8. This molecule may subsequently decompose to form ZnO (reaction 3.4). The steep increase in current between -0.99 and -1.20 V vs Ag/AgCl is due to metallic Zn deposition and hydrogen evolution via reactions 5.1 and 5.2 respectively. In the reverse sweep direction the layer is stripped back into the solution at voltages less negative than -0.350 V vs Ag/AgCl.

$$Zn^{2+} + 2e^- \rightarrow Zn \qquad (5.1)$$

$$2H_2O + 2e^- \rightarrow H_2 + 2OH^- \qquad (5.2)$$

As-deposited layers grown using electrodeposition are comprised of a mixture of compounds of both $Zn(OH)_2$ and ZnO although after annealing the hydroxide decomposes to form ZnO.

A typical current-transient curve for ZnO deposited from the $Zn(NO_3)_2.6H_2O$ solution for 1 minute is presented in Figure 5.2. A high current density was apparent immediately after the voltage was applied due to nucleation at the substrate surface. This was followed by a steep decrease in current density until a plateau was reached at -1.0 mA cm^{-2} after 200 seconds. The plateau is reached when equilibrium between nucleation sites and diffusing ions is met.

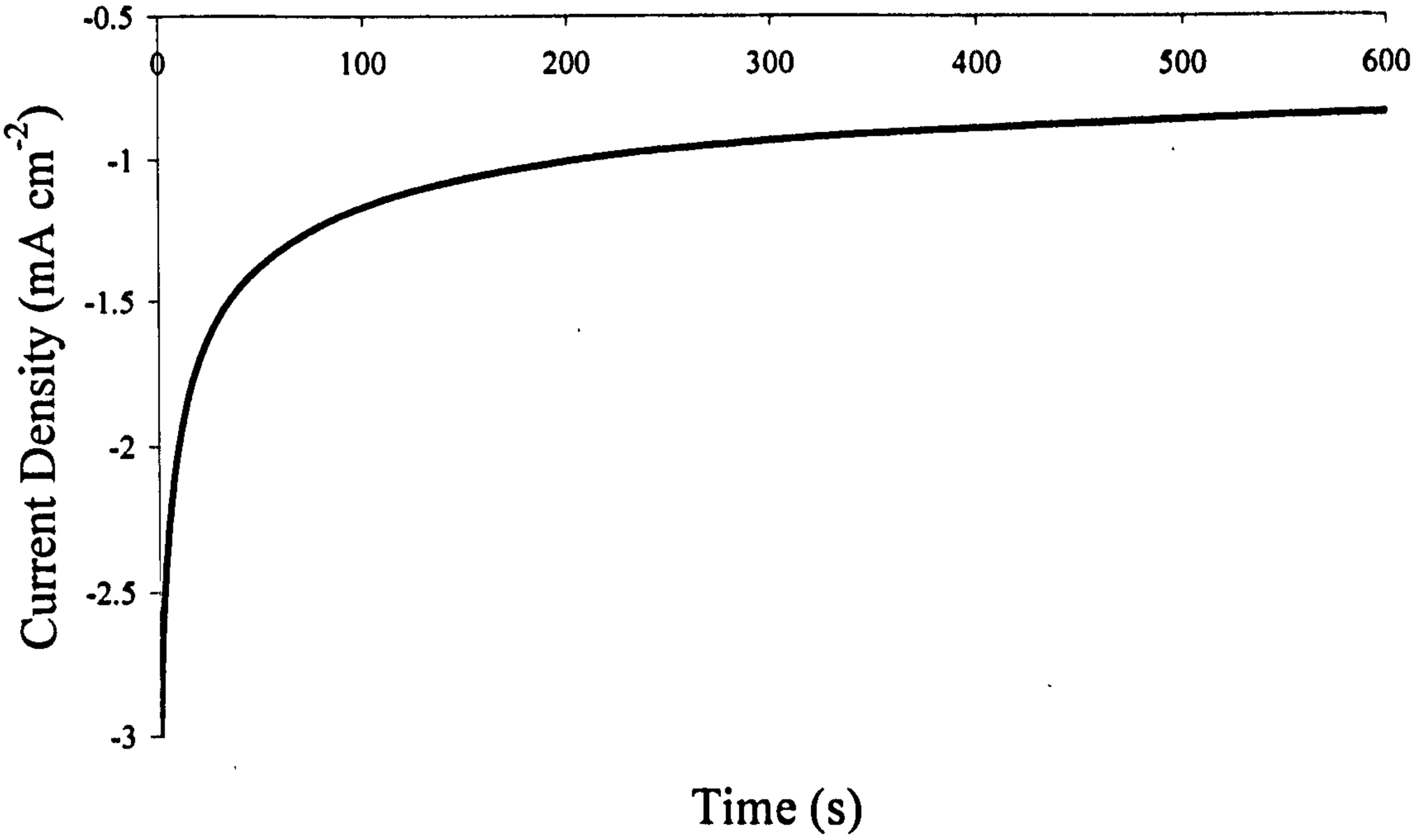

Figure 5.2. Current-transient of 0.1M $Zn(NO_3)_2.6H_2O$ solution at 80°C, the steep slope indicates the initial nucleation at the substrate surface followed by the steady deposition current density.

5.3.2 Thickness Measurements

The thicknesses of i-ZnO layers electrodeposited at -0.975 V vs Ag/AgCl for different periods of time were investigated using talysurf. The stylus was positioned to move across the surface over a step between the FTO substrate and the ZnO layer. These steps allow the thickness of the ZnO to be determined as evident in Figure 5.3. The figure presents the trace obtained for ZnO having growth times of (a) 2 and (b) 3 minutes, indicating thicknesses of 0.30 and 0.40 μm respectively.

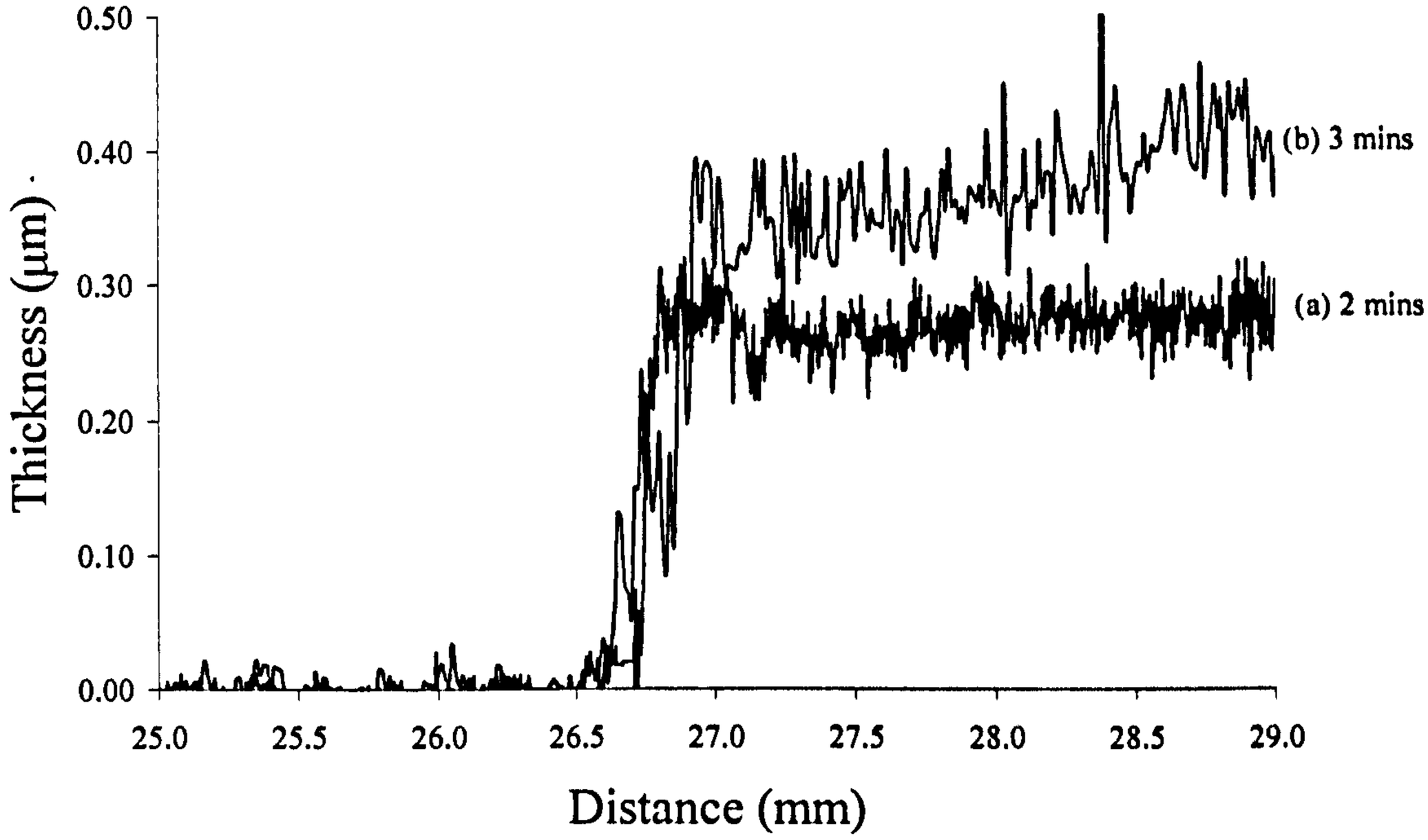

Figure 5.3. Thicknesses of i-ZnO measured using talysurf with growth time of (a) 2, and (b) 3 minutes.

Generally high efficiency CIGS devices consist of a 50-100 nm i-ZnO and 100-1500 nm ZnO:Al layers [Kemell *et al.* 2005]. The initial investigation indicated growth times of ~2 minutes produced layers around 0.30 μm in thickness. Talysurf was used to investigate the reproducibility of thickness with growth time ranging from 1 to 4 minutes as indicated in Table 5.1. This investigation suggests the deposition rate is faster at the initial stages of growth and decreases after 2 or 3 minutes which may be attributed to the change in sheet resistance of the cathode as a function of deposition time. It is clear from the table the thickness of layers deposited for 2 and 3 minutes do not agree with the initial investigation (Figure 5.3).

Table 5.1. Estimation of thickness as a function of growth time established using talysurf.

Sample Number	Growth Time (minutes)	Thickness (μm)
1	1	0.145
2	1	0.140
3	1	0.135
4	2	0.250
5	2	0.250
6	2	0.200
7	3	0.250
8	3	0.250
9	3	0.250
10	4	0.300
11	4	0.300
12	4	0.300

The image of the glass/FTO/ZnO cross-section taken using the SEM instrument is presented in Figure 5.4. The thickness of the ZnO layer is 0.39 μm after 3 minutes growth time as highlighted by the arrow which is greater than the estimation obtained using talysurf. Faraday's relation (2.3) was used to estimate the thickness using the electrodeposition data assuming the density of ZnO at 5.60 g cm^{-3} [Lide 2005]. Table 5.2 summarises and compares the thicknesses obtained using talysurf, and Faraday's relation as a function of growth time.

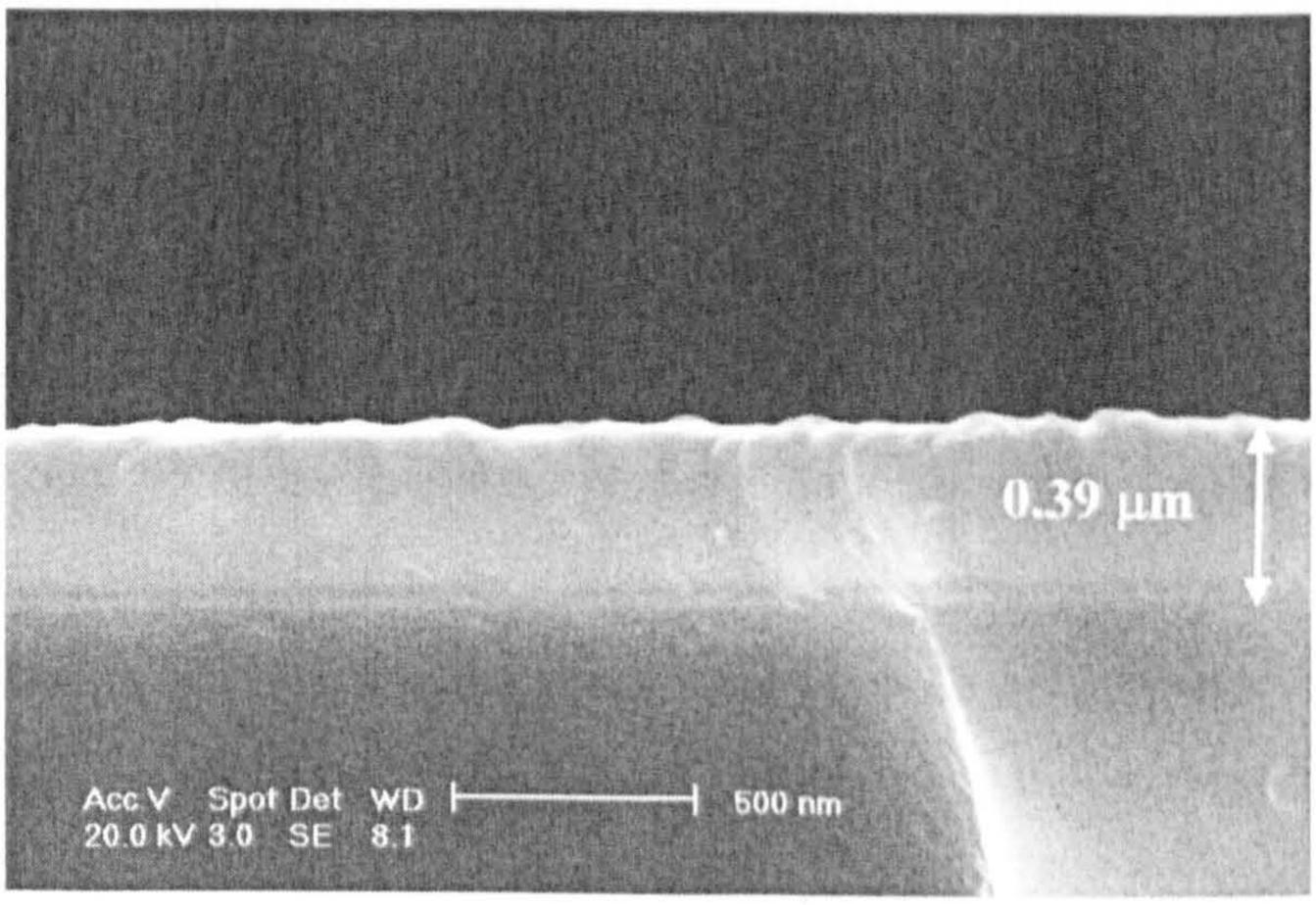

Figure 5.4. SEM cross-section of i-ZnO indicating a thickness of 0.39 μm after a growth time of 3 minutes.

Table 5.2. Summary of thickness of ZnO determined using talysurf and Faraday's relation.

Growth Time (minutes)	Thickness (μm) Talysurf	Thickness (μm) Faraday Relation
1	0.135 to 0.145	0.17
2	0.20 to 0.35	0.37
3	0.25 to 0.40	0.52
4	0.30	0.69

The thicknesses observed by talysurf, SEM and calculated by Faraday's relation are inconsistent. The reasons for this may be due to either error in the deposition time or solution conditions for example the pH, age of the bath which affects the growth rate. The difference in technique capability, talysurf measured the edge of the sample which was closest to the electrical contact during growth and is likely to have been exposed to a slightly higher voltage. It is known there is a voltage drop down the substrate away from the electrical contact affecting growth rate [Gibson *et al.* 2001]. Faraday's law over estimates the thickness of the layers as it assumes 100% deposition efficiency. The values in Table 5.2 indicate a Faradic efficiency of between 43 and 94%.

Optimisation of layer thickness is essential when considering device performance. The reason for this is two-fold; firstly the i-ZnO layer is highly resistive and therefore the device performance degrades due to increased series resistance if this layer is too thick. Secondly, to obtain a reproducible result especially when considering scale-up, the growth time must be carefully monitored and quantified to deposit the correct thickness each time.

It has been reported in the literature that the deposition rate of ZnO from a nitrate precursor is ~0.15 μm min^{-1}, which agrees with this study [Izaki *et al.* 1996]. Most sources in the literature have reported the i-ZnO layer to be between 70 to 100 nm in thickness in CIGS based devices. Therefore, when using electrodeposition to deposit ZnO the growth time would be less than 1 minute, which is beneficial with respect to commercialisation. In order to gain more controllability the temperature and/or molarity could be reduced to determine the effect on the deposition rate although these factors were not explored in this investigation.

5.3.3 X-Ray Diffraction

XRD studies were carried out on i-ZnO layers to determine phase and crystallographic analysis. Figure 5.5 (a-g) presents the XRD spectra for as-deposited i-ZnO electrodeposited at (a) -0.900, (b) -0.925, (c) -0.950, (d) -0.975, (e) -1.025 and (f) -1.050 V vs Ag/AgCl and (g) standard obtained for hexagonal, wurtzite ZnO from the online Daresbury Chemical Database Service [Sowa & Ahsbahs 2006]. All peaks were identified to be from polycrystalline ZnO having hexagonal phase.

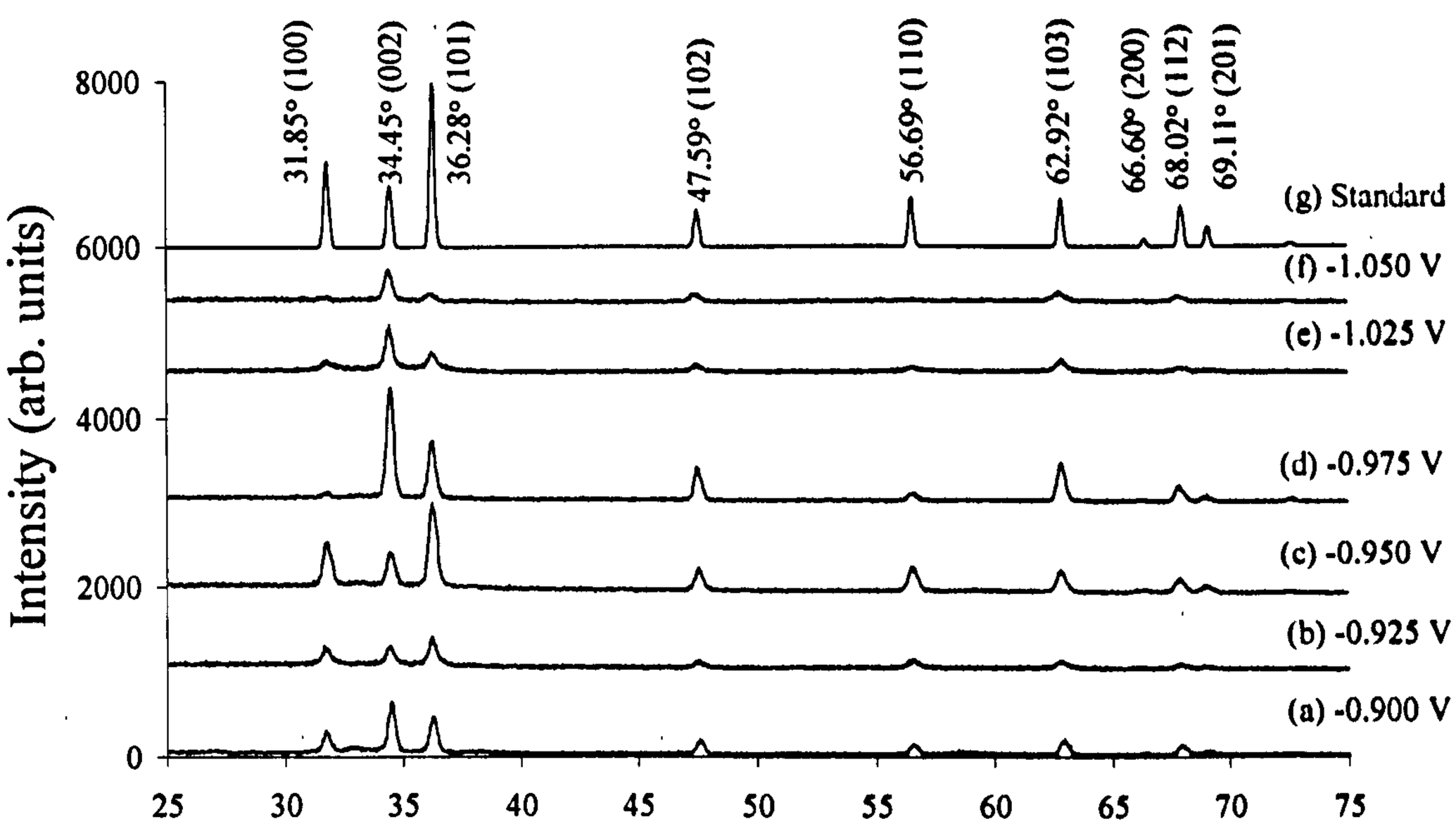

Figure 5.5. XRD diffractogram of as-deposited i-ZnO electrodeposited at (a) -0.900, (b) -0.925, (c) -0.950, (d) -0.975, (e) -1.025, (f)-1.050 V vs Ag/AgCl and (g) standard. All peaks were identified to be polycrystalline hexagonal ZnO, note the variation in orientation.

Table 5.3 lists the data obtained from the XRD study and is typical for all spectra; there was little or no deviation in d-spacing or 2θ values and therefore tables for all spectra have not been included.

Table 5.3. XRD data representative of all i-ZnO spectra obtained in this study, which were identified to be polycrystalline ZnO having hexagonal, wurtzite phase.

2θ (deg.)		d Spacing (Å)		Miller Indices
Standard	Observed	Standard	Observed	(hkl)
31.73	31.85	2.818	2.810	(100)
34.52	34.45	2.605	2.604	(002)
36.26	36.28	2.479	2.479	(101)
47.60	47.59	1.913	1.911	(102)
56.63	56.69	1.627	1.624	(110)
62.99	62.92	1.478	1.477	(103)
67.97	68.02	1.380	1.378	(112)
69.17	69.11	1.360	1.359	(201)

The spectra indicate a large change in preferential orientation with deposition voltage and the change in deposition rate with growth voltage cannot be ruled out. Layers deposited at -0.925 and -0.950 V vs Ag/AgCl match closest to the standard spectra shown in (g) having preferential orientation in the (101) plane. Yoshida and Izaki have both observed ZnO deposited from $Zn(NO_3)_2$ to be orientated in the (101) plane [Izaki & Omi 1996, Yoshida *et al.* 2003]. Whilst layers deposited at -0.900, -0.975, -1.025 and -1.050 V vs Ag/AgCl are preferentially oriented in the (002) plane. The change in preferential orientation of the grain structure is most likely to be due to a change in composition of the layer and change in growth voltage or oxygen concentration.

A new solution was prepared for each experiment and stirred for one hour before deposition. Although the layers for each experiment were deposited on the same day the deposition occurred at different times after the solution was produced. The solution was maintained at 85°C and thus the oxygen concentration was expected to deplete. Attempts to reuse the electrolyte ~2 days after preparation were unsuccessful as ZnO failed to deposit. Often no growth was observed and occasionally a dark grey metallic Zn layer grew instead due to the low pH=1-2. Yoshida suggested the oxygen availability depends on the age of the bath as nitrate (NO_3^-) reacts to form nitrite (NO_2^-) (reaction 3.7 Section 3.1.3.2) leaving the bath unusable after 2 to 3 days time [Yoshida *et al.* 1999].

The change in preferential orientation is most likely to be due to the change in oxygen concentration of the solution over time. Deposition at the same voltage for the

same amount of time was found to yield various orientations as discussed later in this section.

Using the hexagonal lattice parameter equation 2.8 discussed in Chapter 2, the lattice parameters *a* and *c* were calculated taking the XRD data from the (100) and (002) planes indicated in Table 5.3. The XRD data in the table is representative of all measurements, with no deviation in d-spacing, the values calculated are valid for all spectra, as changes in the fourth significant figure is within experimental error. The calculated values of a=3.244 Å and c=5.209 Å are close to the standard values of a=3.253 Å and c=5.120 Å for ZnO [Pearton *et al.* 2005].

The Scherrer relation (2.5) was used to calculate the crystallite size for the layers deposited at different growth voltages as indicated by Table 5.4. The data for the preferential peak of each trace was used as it provides the most accurate results. It is clear from the table there is little change in crystallite size with growth voltage, which was calculated to be in the range of 18 to 28 nm.

Table 5.4. Crystallite size (D) calculated using the Scherrer relation for i-ZnO layers deposited at various voltages using data from the preferential peak of the XRD spectra.

Deposition Voltage (V)	2θ (deg.)	(hkl)	FWHM (deg.)	D (nm)
-0.900	36.29	(101)	0.36	23
-0.925	36.24	(101)	0.44	18
-0.950	36.26	(101)	0.39	21
-0.975	36.25	(101)	0.42	20
-1.025	34.40	(002)	0.34	24
-1.050	34.42	(002)	0.42	20
Standard	36.30	(101)	0.30	28

Figure 5.6 illustrates the change in preferential orientation of the i-ZnO layer when deposited at the same deposition voltage of -0.975 V vs Ag/AgCl for the same length of time (2 minutes). This is attributed to the varying oxygen concentration with bath age. All peaks were identified to be hexagonal ZnO although the orientation changed. Traces (a) to (c) have preferential orientation in the (101) plane and trace (d) in the (002) plane.

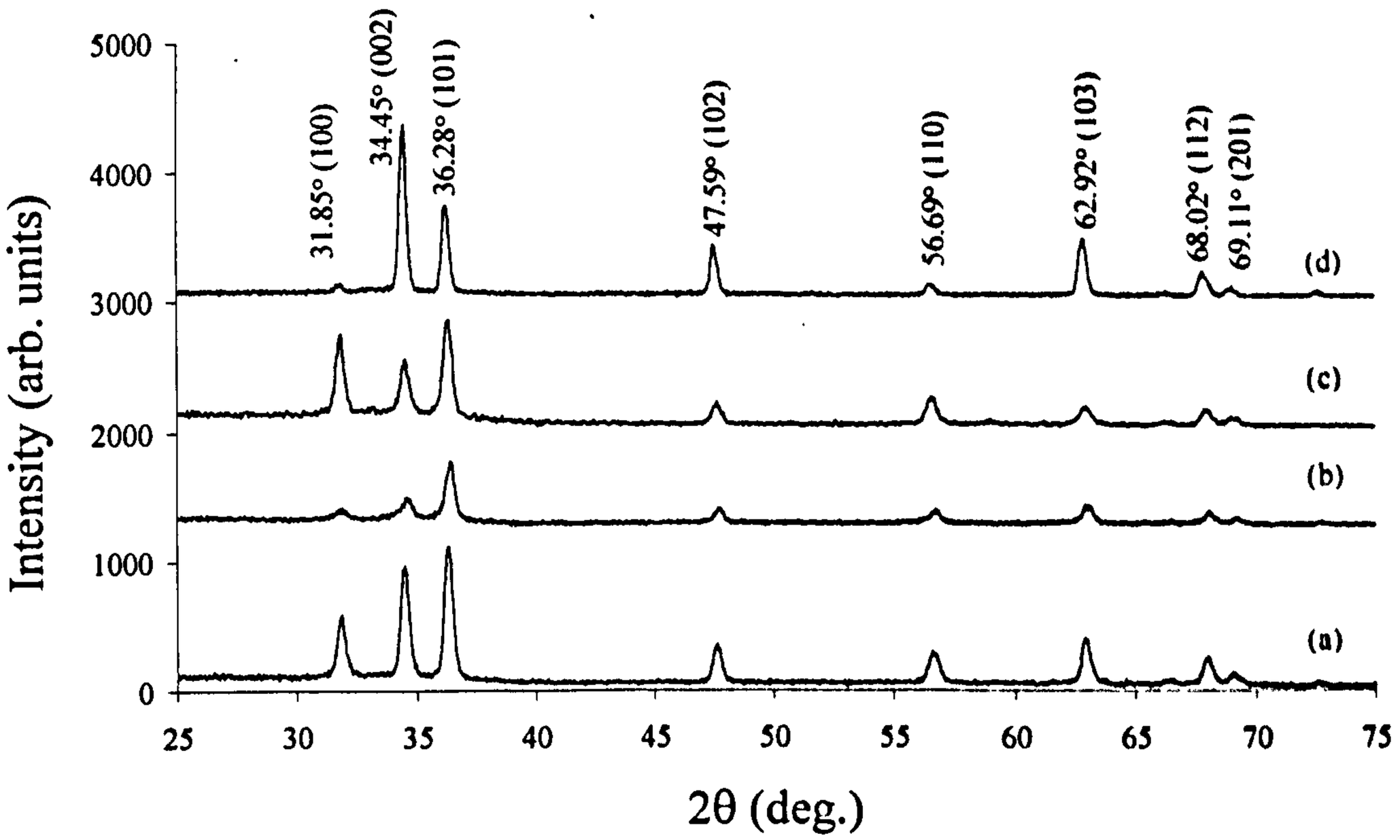

Figure 5.6. XRD spectra of as-deposited i-ZnO, all electrodeposited at -0.975 V vs Ag/AgCl from the same solution, with growth time of 2 minutes. All peaks were identified to be of polycrystalline hexagonal ZnO; note the variation in orientation.

The Preferential Orientation Index (POI) was calculated for the preferential peaks of Figure 5.6 (a-d) and equation 5.1. The POI is indicated in Table 5.5 with the POI for the standard spectra of Figure 5.5. When the POI is greater than one the material is preferentially oriented [Chaure *et al.* 2004]. POI less than one indicate the material is polycrystalline, which agree with this XRD study. All materials have a lower POI than the standard material indicating that the peaks are slightly less orientated in the (101) direction.

$$POI = \left(\frac{I_{(hkl)}}{\Sigma I} \right) \tag{5.1}$$

Table 5.5. POI for the spectra (a-d) of Figure 5.6 and the standard spectra for comparison.

Spectra	Preferential Peak	POI
a	(101)	0.282
b	(101)	0.174
c	(101)	0.159
d	(002)	0.120
Standard	(101)	0.326

The most likely explanation for the variation in preferential orientation is the changes in bath composition and pH during deposition. The only oxygen source during these experiments was from the nitrate precursor and therefore the concentration altered over time. It was observed the pH of the bath varied with time and became more acidic. This is most likely to be either due to holding the solution at 85°C or reactions occurring during deposition, the details of which remain unknown. According to the Pourbaix diagram metallic Zn deposits preferentially under acidic conditions [Goux *et al.* 2005].

The effect of annealing at 550°C for 20 minutes in air atmosphere was studied for layers deposited at -0.975 V vs Ag/AgCl. These annealing conditions were selected with the consideration of future requirements if ZnO layers were deposited on CIS. In this situation the temperature used to anneal ZnO would not exceed that of CIS, preserving this layer. Further annealing trials would have been required if CIS devices had been prepared with electrodeposited ZnO.

Typical XRD spectra for the as-deposited and annealed films are presented in Figure 5.7 (a & b) respectively. No noticeable change was observed in XRD spectra for the as-deposited and annealed layers. This indicates that structurally there are no noticeable changes between as-deposited and heat-treated material. Heat-treatment is required to improve electrical properties as discussed in Section 5.3.6.

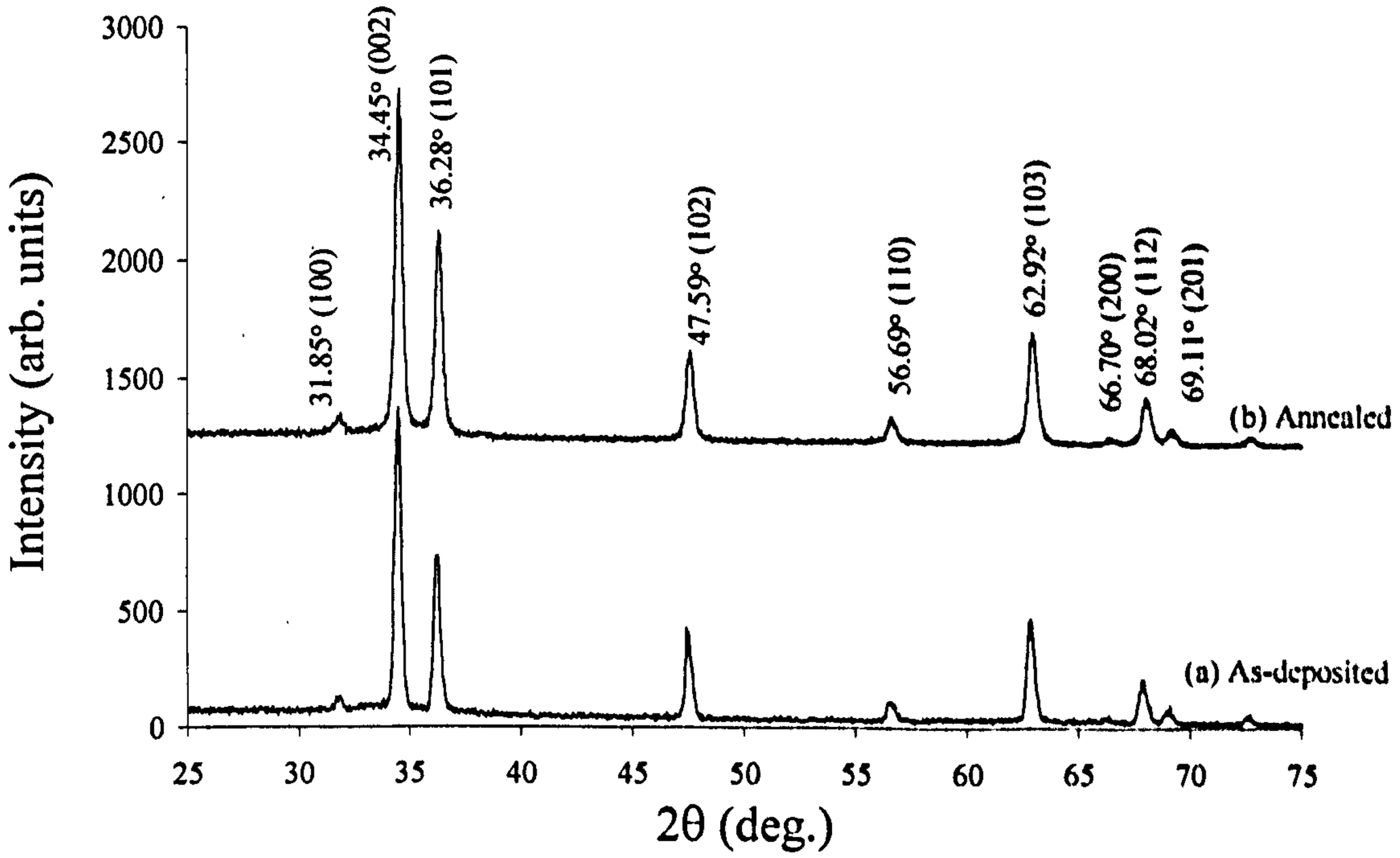

Figure 5.7. XRD spectra of i-ZnO deposited at -0.975 V VS Ag/AgCl (a) as-deposited and (b) annealed at 550°C for 20 minutes in air. Note there is little difference in the intensity and FWHM of peaks before and after heat-treatment.

The influence of additional oxygen bubbling through the $Zn(NO_3)_2$ solution during deposition was briefly investigated. Oxygen (O_2) was bubbled through the solution for 1 hour prior to deposition and reduced to a steady rate during deposition. The XRD spectra presented in Figure 5.8 (a-d) had the same preferential orientation, (100)/(101) consistently irrespective of the growth voltage. This contrasts the XRD spectra presented in Figure 5.5, which altered with deposition voltage. The oxygen content in the bath is more stable with additional bubbling and therefore the layers were grown in an oxygen rich environment, which may have favoured this orientation.

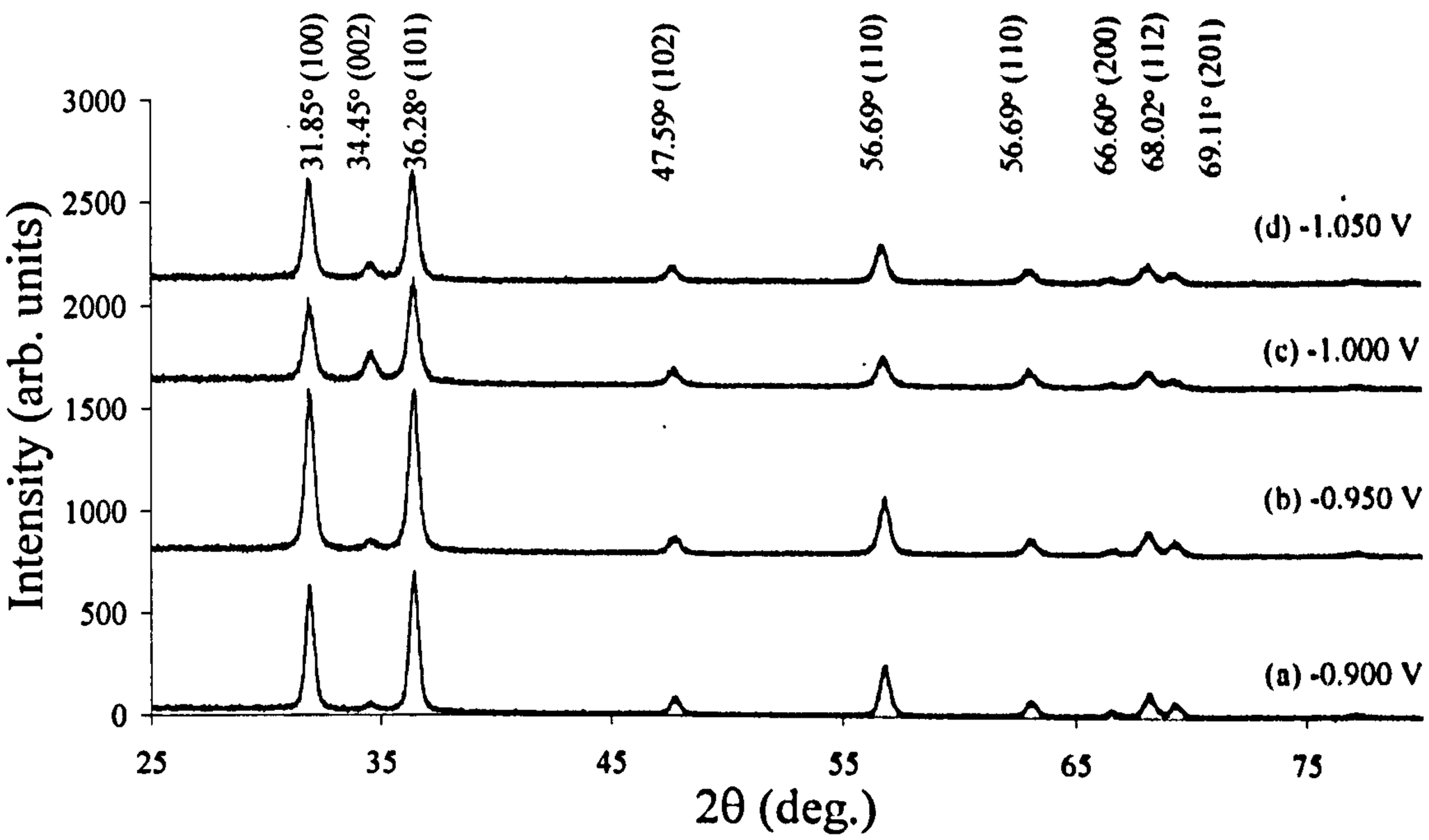

Figure 5.8. XRD spectra of annealed i-ZnO electrodeposited from $Zn(NO_3)_2$ at (a) -0.900, (b) -0.950, (c) -1.000 and (d) -1.050 V vs Ag/AgCl, with additional O_2 bubbled through the solution.

5.3.4 Scanning Electron Microscopy

SEM was used to study the morphology of selected i-ZnO layers. Figure 5.9 (a-d) illustrates the variety of different morphologies obtained from the same solution when deposited at the same deposition voltage of -0.975 V vs Ag/AgCl. The parameters which remained constant include the deposition time, temperature, substrate and stirring rate. The parameter that did uncontrollably changed during the experiment was the oxygen concentration in solution. Figure 5.9 (a & d) have remarkably resemblance,

although the crystallite size is different at 0.5 and 2.5 μm respectively with uniform circular shape.

Figure 5.9 (b) is a uniform layer with grain size ~0.25 μm exhibiting triangular shaped crystallites. Figure 5.9 (c) is different again forming a smooth uniform layer with flat platelet crystals around 1.0 μm in size. Figure 5.9 (e) illustrates the ZnO morphology of layer (d) after annealing at 550°C for 20 minutes is composed of both agglomerated rods and more pronounced hexagonal shaped crystals. In addition long, thin fibre-like crystals in between large grains were observed. There is little apparent variation in crystal size before and after annealing. A similar varied morphology for ZnO has been reported by Govender *et al.* who noted ZnO deposited from nitrate containing solutions produced less homogeneous layers [Govender *et al.* 2004]. The crystallite size did not change after annealing in the present study.

The effect of growth voltage on the morphology was investigated at voltages of -1.000 and -1.025 V vs Ag/AgCl (Figure 5.10 & 5.11). The layer deposited at -1.000 V vs Ag/AgCl has crystallite size of ~1.0 μm and consisted of hexagonal shaped crystals having varying orientation. The layer is not as uniform as those deposited at -0.975 V vs Ag/AgCl. Layers deposited at -1.025 V vs Ag/AgCl have a smaller crystal size of ~0.1 to 0.25 μm and nodular morphology.

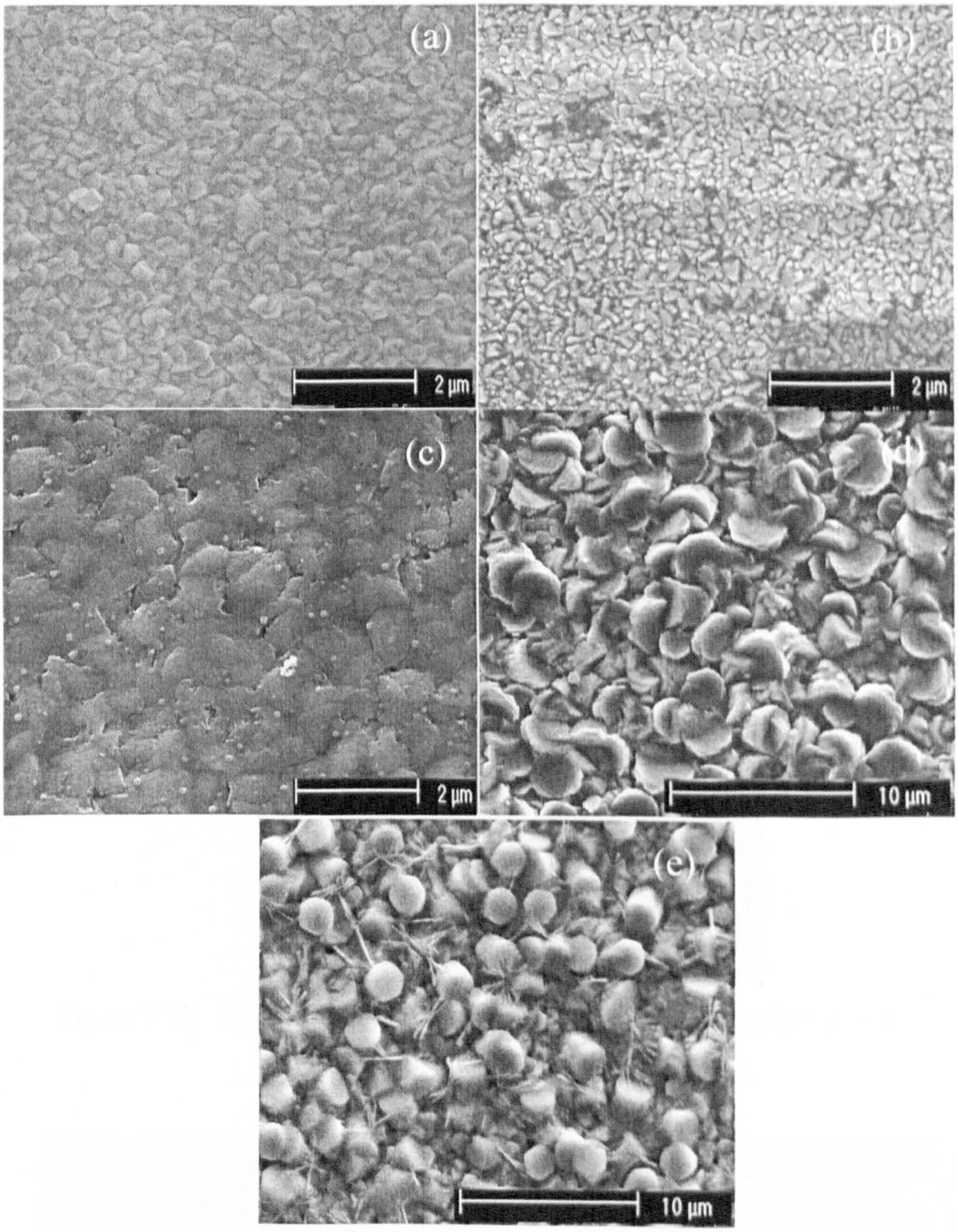

Figure 5.9. SEM images of as-deposited i-ZnO (a-d) deposited at -0.975 V vs Ag/AgCl to illustrate the variation in morphology, (e) is layer (d) after annealing at 550°C for 20 minutes.

The variation in morphology is likely to be due to the change in growth voltage yielding different composition and also the variation in oxygen concentration as a function of bath life-time. The oxygen concentration decreases to 0.75 mM at 80°C and depletes with bath age [Goux *et al.* 2005]. The nitrate molecule provides the oxygen source and therefore its availability is uncontrollable with bath age. Slight O_2 variations in the electrolyte have previously been shown to alter the nucleation and growth mechanism [Pauporte & Lincot 2000]. The nitrate molecules react to form nitrite releasing oxygen ions and therefore there is little control over the availability of oxygen. On application of the growth voltage nitrate ions release an oxygen ion, when the solution has been used for several hours the decreased to pH<3, leaving the bath unusable for ZnO deposition. This variation in available oxygen is likely to alter the morphology of the ZnO layers.

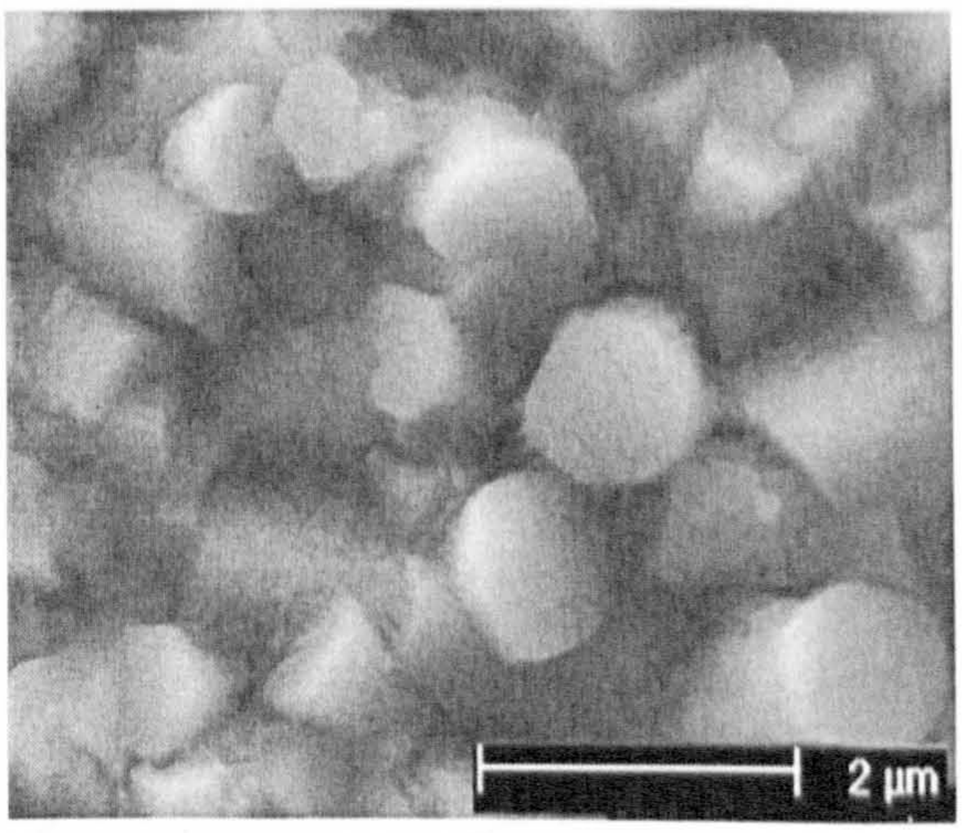

Figure 5.10. SEM image of as-deposited i-ZnO electrodeposited at -1.000 V vs Ag/AgCl from $Zn(NO_3)_2.6H_2O$ solution.

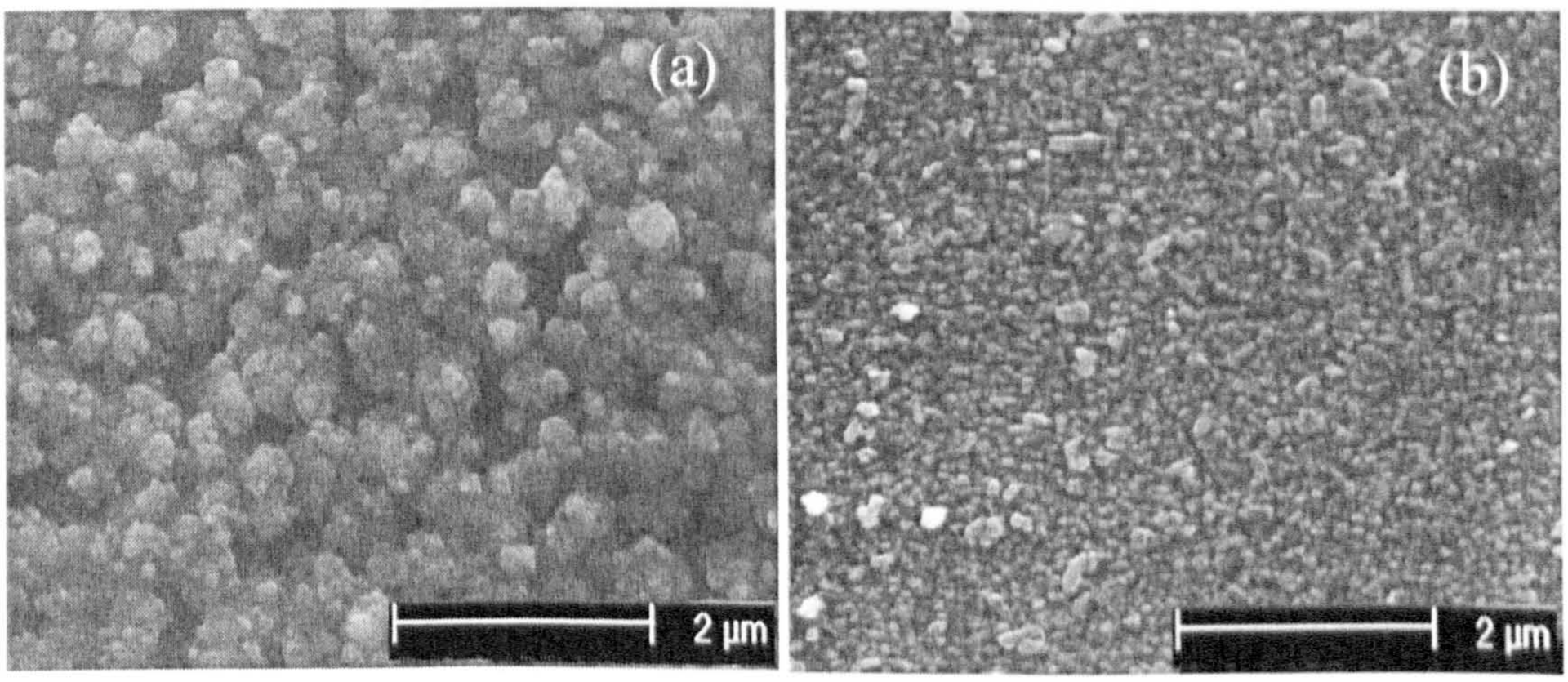

Figure 5.11. SEM images of i-ZnO electrodeposited at -1.025 V vs Ag/AgCl.

5.3.5 Optical Properties

The transmission spectra of as-deposited and annealed i-ZnO are presented in Figure 5.12. The absorption edge at ~400 nm is at higher wavelength than expected for ZnO, which has previously been identified at 380 nm [Gal *et al.* 2000]. The as-deposited material had a milky appearance which is likely to be due to the coexistence of ZnO with $Zn(OH)_2$ inclusions and surface roughness. The absorption slope of the as-deposited ZnO is gradual with highest transmission of 80% at 800 nm indicative of the samples cloudy appearance. After annealing the absorption edge shifted to ~380 nm, which agrees with previously reported values in the literature [Gal *et al.* 2000]. The absorption edge is much sharper and 85% of incident photons are transmitted at wavelengths above the absorption edge. The appearance of the layer changed post-annealed, increasing in transparency, this being attributed to the decomposition of $Zn(OH)_2$ forming ZnO as suggested by [Wang *et al.* 2005].

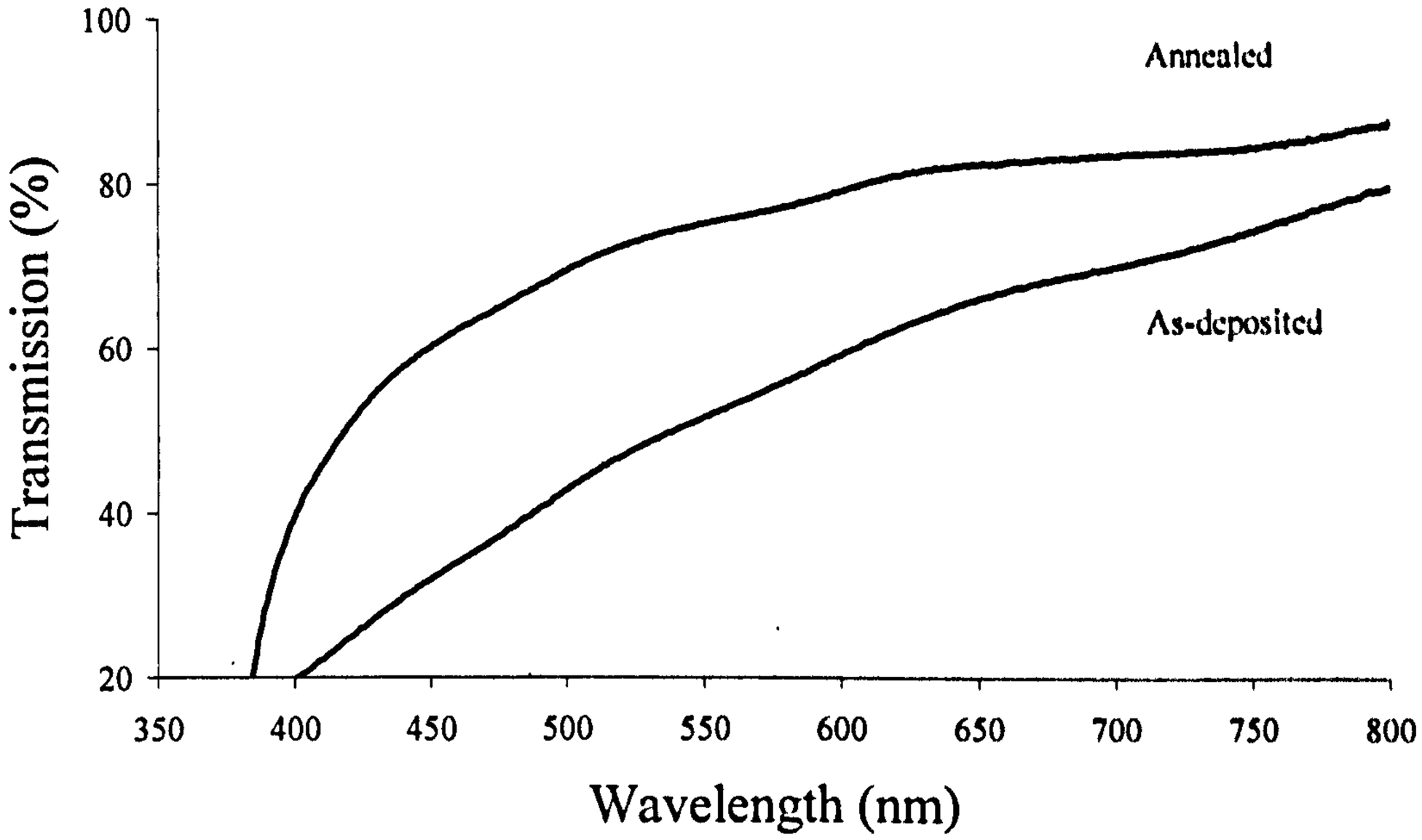

Figure 5.12. Transmission spectra of as-deposited i-ZnO having gradual absorption edge which steepened after annealed.

The optical absorption spectra of glass/FTO/i-ZnO deposited at -0.975 V vs Ag/AgCl was taken to determine the bandgap energy and absorption edge of the material. Figure 5.13 presents the absorption of ZnO as a function of wavelength indicting a sharper absorption edge of 380 nm for the as-deposited ZnO compared to 390 nm for the

annealed material; differing from the transmission curve. During annealing the $Zn(OH)_2$ decomposes to ZnO via reaction 3.4 of Chapter 3 thus the difference in composition of the material alters the absorption edge.

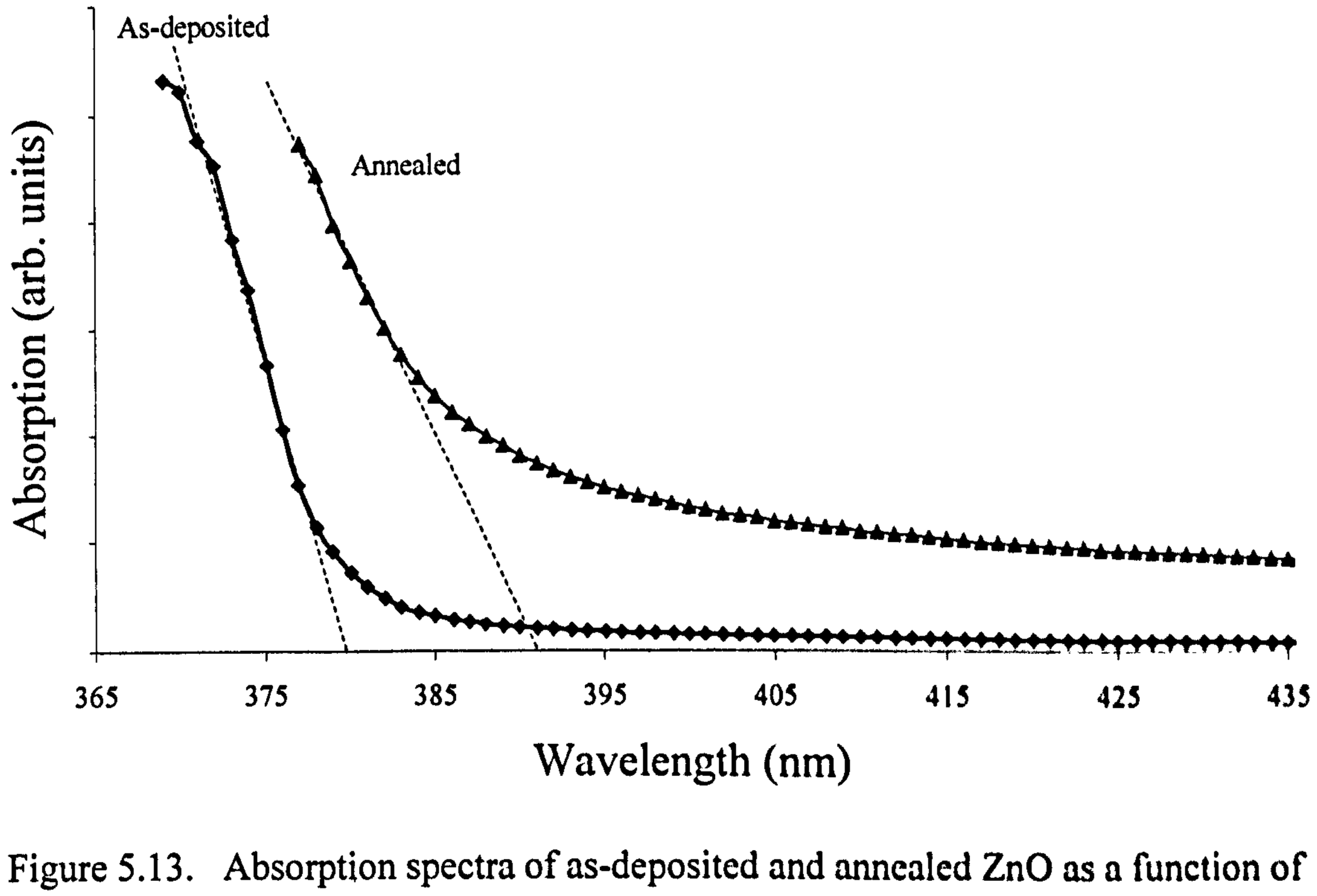

Figure 5.13. Absorption spectra of as-deposited and annealed ZnO as a function of wavelength.

The data obtained from the absorption vs wavelength curve and equation 1.1 indicated in Chapter 1 were used to calculate the absorption edge as a function of photon energy. Figure 5.14 presents the absorption edge as a function of photon energy for as-deposited and annealed ZnO, indicating a bandgap energy of E_{g1}=3.27 eV and E_{g2}=3.15 eV respectively. The decrease in bandgap energy after annealing indicates a change in composition, most likely to be due to the decomposition of $Zn(OH)_2$ forming ZnO.

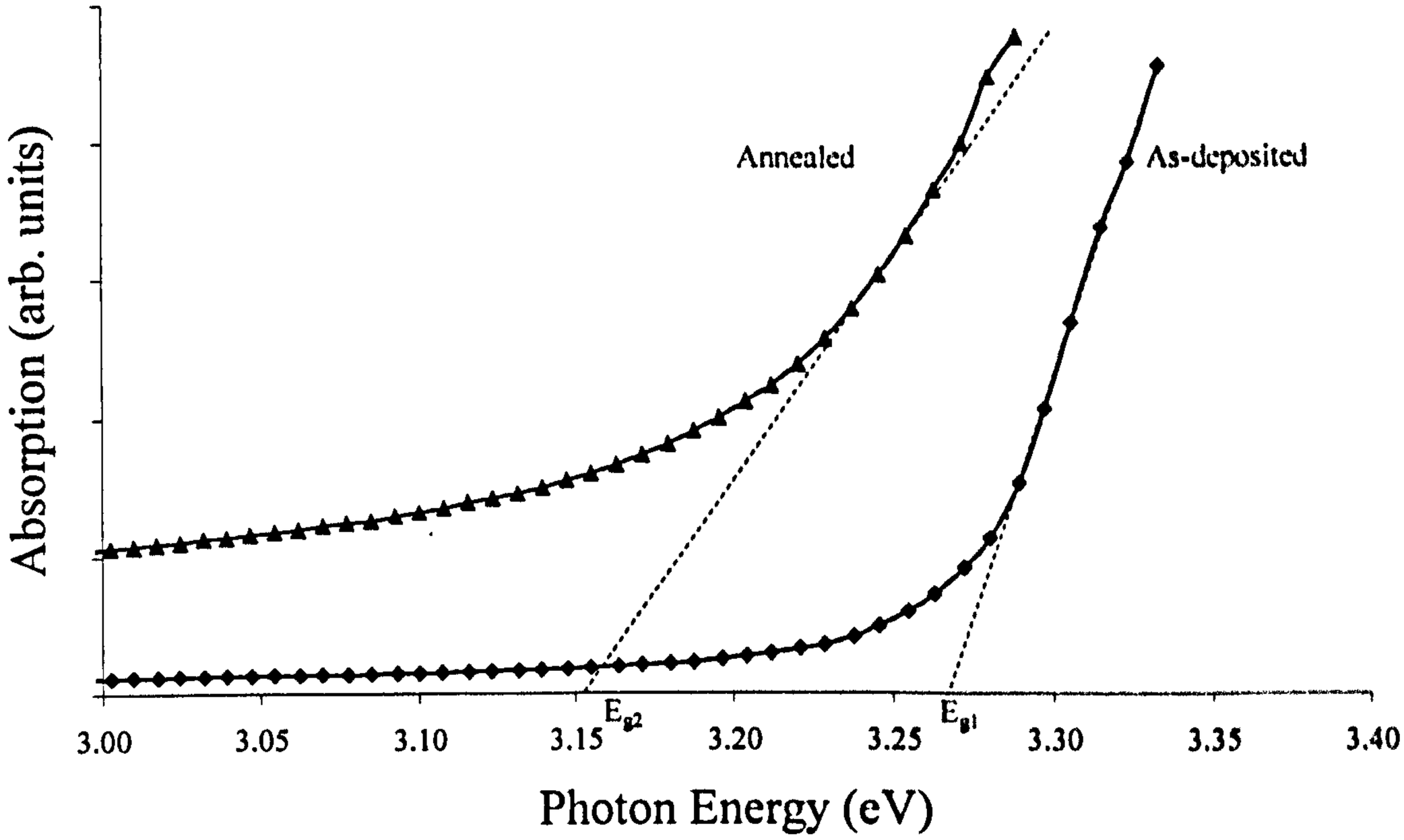

Figure 5.14. Absorption spectra of as-deposited and annealed ZnO having bandgap energy of E_{g1}=3.27 eV and E_{g2}=3.15 eV respectively.

The absorption coefficient was calculated using equation 2.11 described in Chapter 2 and plotted as a function of photon energy yielding a more accurate slope for the determination of the bandgap energy (Figure 5.15). The bandgap energy of the as-deposited material was determined at E_{g1}=3.29 eV compared E_{g2}=3.27 eV for the annealed material. As for Figure 5.14 the difference in bandgap energy was attributed to the change in composition when $Zn(OH)_2$ decomposes to form ZnO.

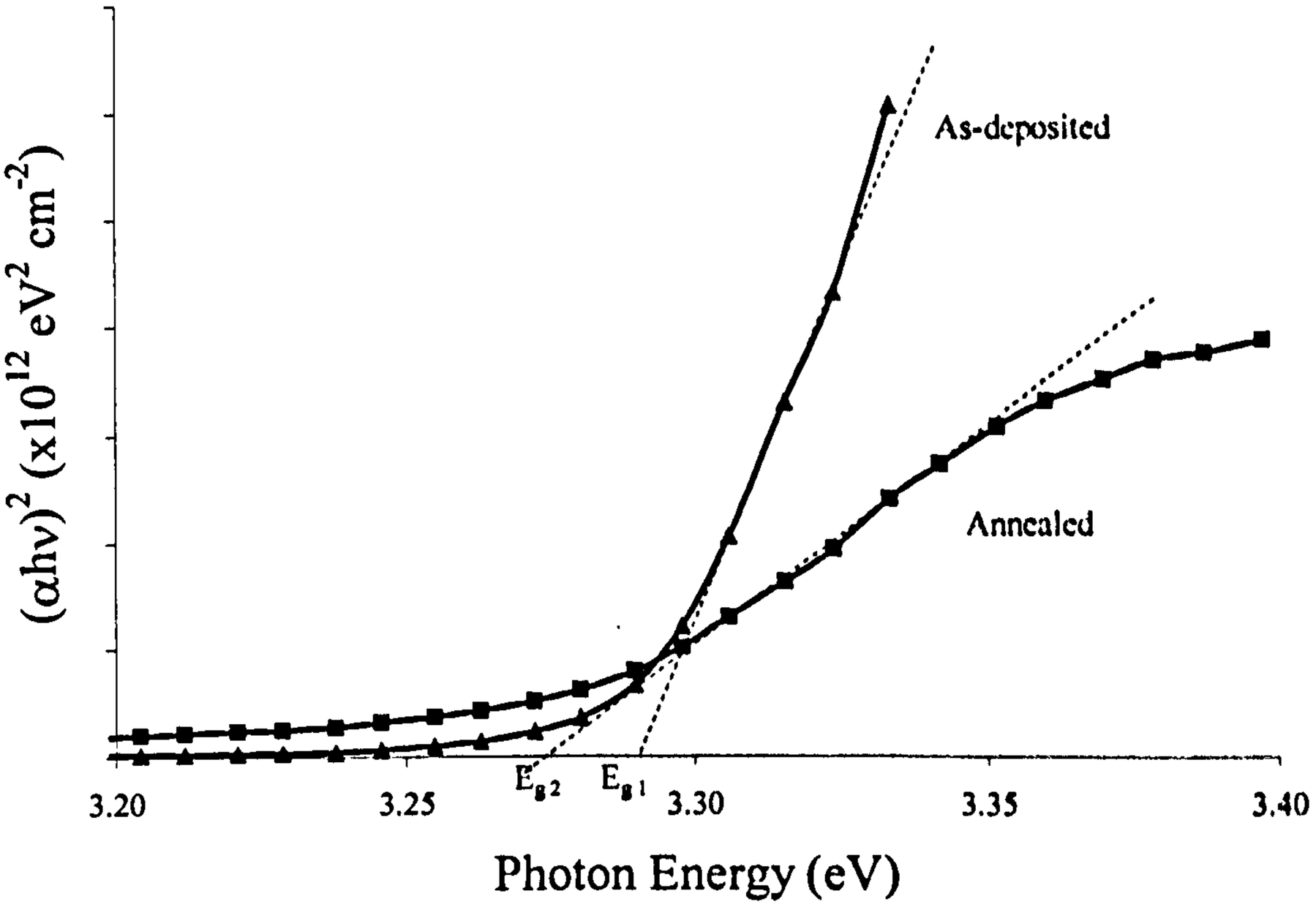

Figure 5.15. Optical absorption spectra of as-deposited and annealed i-ZnO electrodeposited at -0.975 V vs Ag/AgCl.

5.3.6 Electrical Properties

The I-V characteristics of glass/FTO/i-ZnO/Au structures were taken under dark conditions to determine the electrical properties of the ZnO thin films. Gold is a high work function metal (ϕ_b = 5.10 to 5.47 eV) and was used to form the back contact with the expectation of formation of a rectifying contact with ZnO [Lide 2005]. Log-linear and linear-linear curves are presented in Figures 5.16 and 5.17. The structures indicate rectification properties with a rectification factor of ~10^2 at 1.0 V, ideality factor of ~3.0 and barrier height >1.08 eV. The latter two parameters were taken from the automated solar simulator used for the measurements. Since the diodes are non-ideal, accurate barrier height cannot be estimated. The series resistance of the structure was estimated using the high forward biased region of the linear-linear I-V curve and found to be 2.2 kΩ. Equations 5.2 and 5.3 were used to calculate the electrical resistivity and conductivity of the ZnO layers. High forward bias values enable the bulk resistance of the material to be determined under flat band conditions. Making use of the known contact area of 0.031 cm^2 and the film thickness (300 nm), the bulk electrical resistivity and electrical conductivity were calculated at 6.9×10^6 Ω cm and 1.4×10^{-7} Ω cm^{-1} respectively.

$$R = \frac{\rho L}{A} \tag{5.2}$$

$$\rho = \frac{1}{\sigma} \tag{5.3}$$

where R = Resistance (Ω), ρ = Electrical Resistivity (Ω m), L = Thickness (m), Λ = Contact area (m^2) and σ = electrical conductivity (Ω m^{-1}).

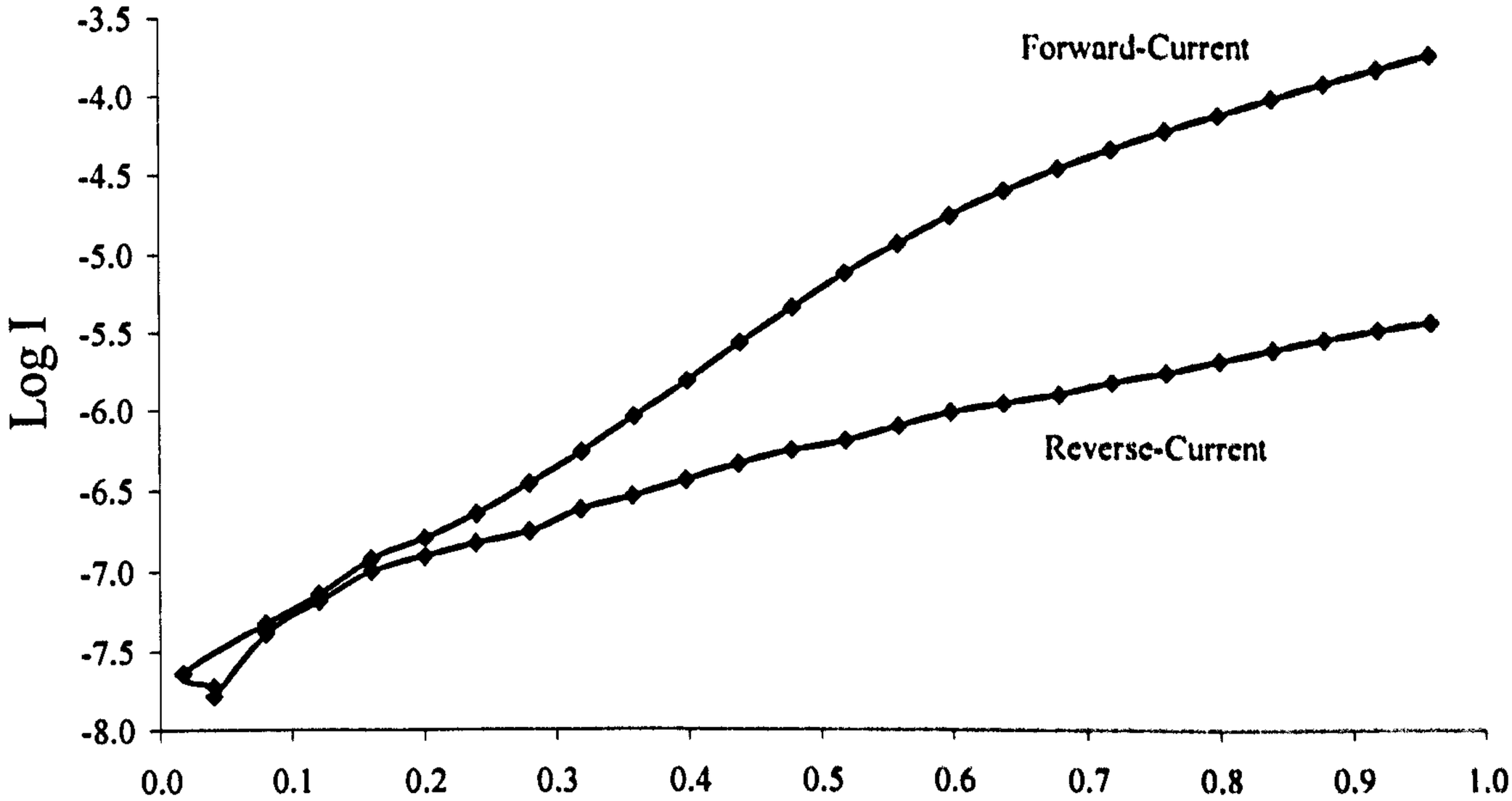

Figure 5.16. Log I vs voltage curves measured under dark condition of glass/FTO/i-ZnO/Au Schottky contacts.

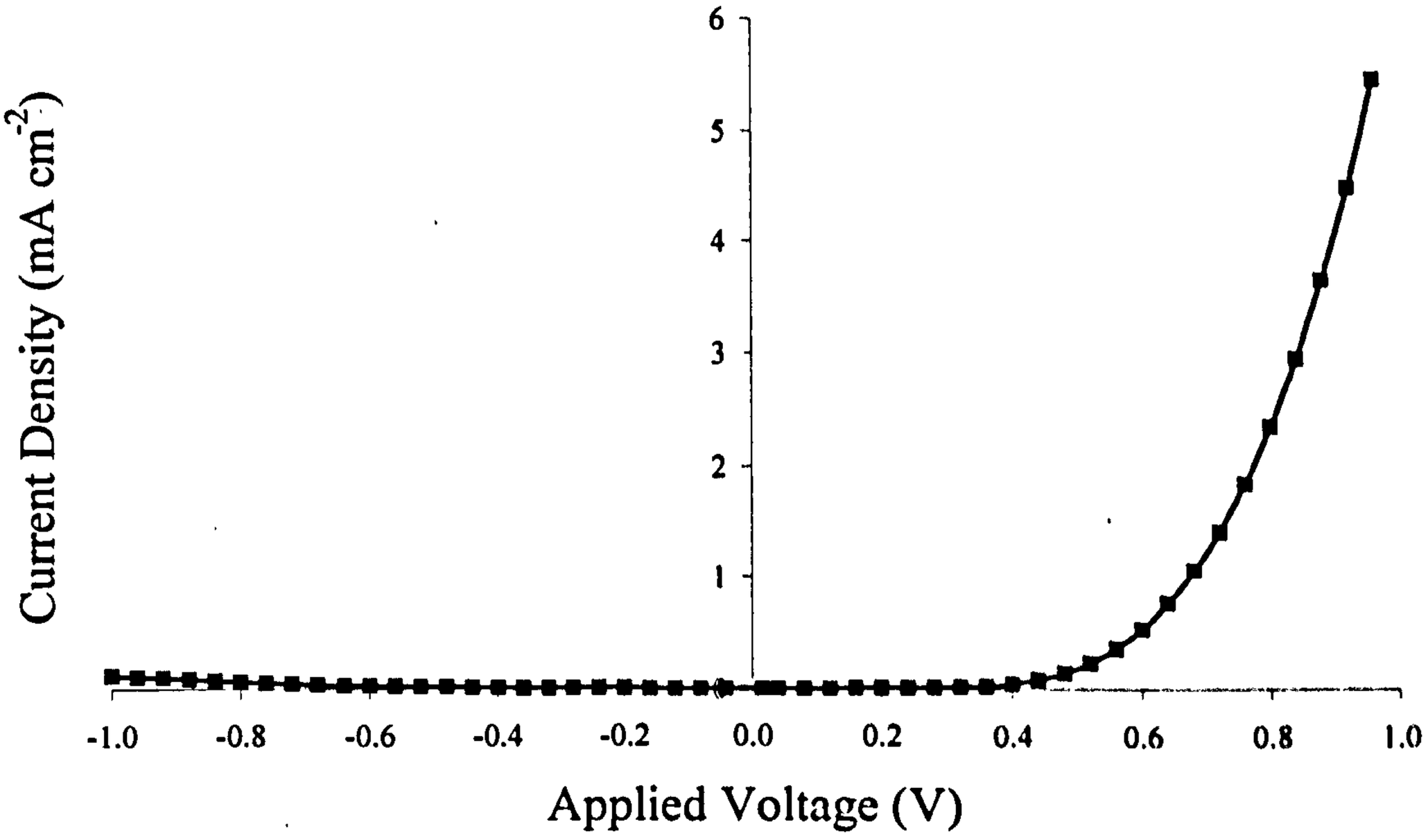

Figure 5.17. Linear I-V curve measured under dark conditions for glass/FTO/i-ZnO/Au structures.

Capacitance-voltage measurements of glass/FTO/ZnO/Au devices having contact area of 0.031 cm^2 were taken as a function of bias voltage with a detection signal frequency of 1 MHz as indicated by Figure 5.18. The free carrier concentration of 2.8×10^{12} cm^{-3} was estimated from the gradient of Schottky-Mott curve (Figure 5.18). It should be noted that the C-V measurements are prone to effects of defects and hence estimated free carrier concentrations can be far from accurate values. Assuming the above value for free carrier concentration and electrical conductivity from the I-V measurements the mobility was calculated at 1.25 cm^{-2} V s using equation 5.4.

$$\sigma = ne\mu \tag{5.4}$$

where σ = Electrical Conductivity (Ω m^{-1}), n = Free Carrier Concentration (m^{-3}), e = Electronic Charge (eV) and μ = Electron Mobility (m^{-2} V s).

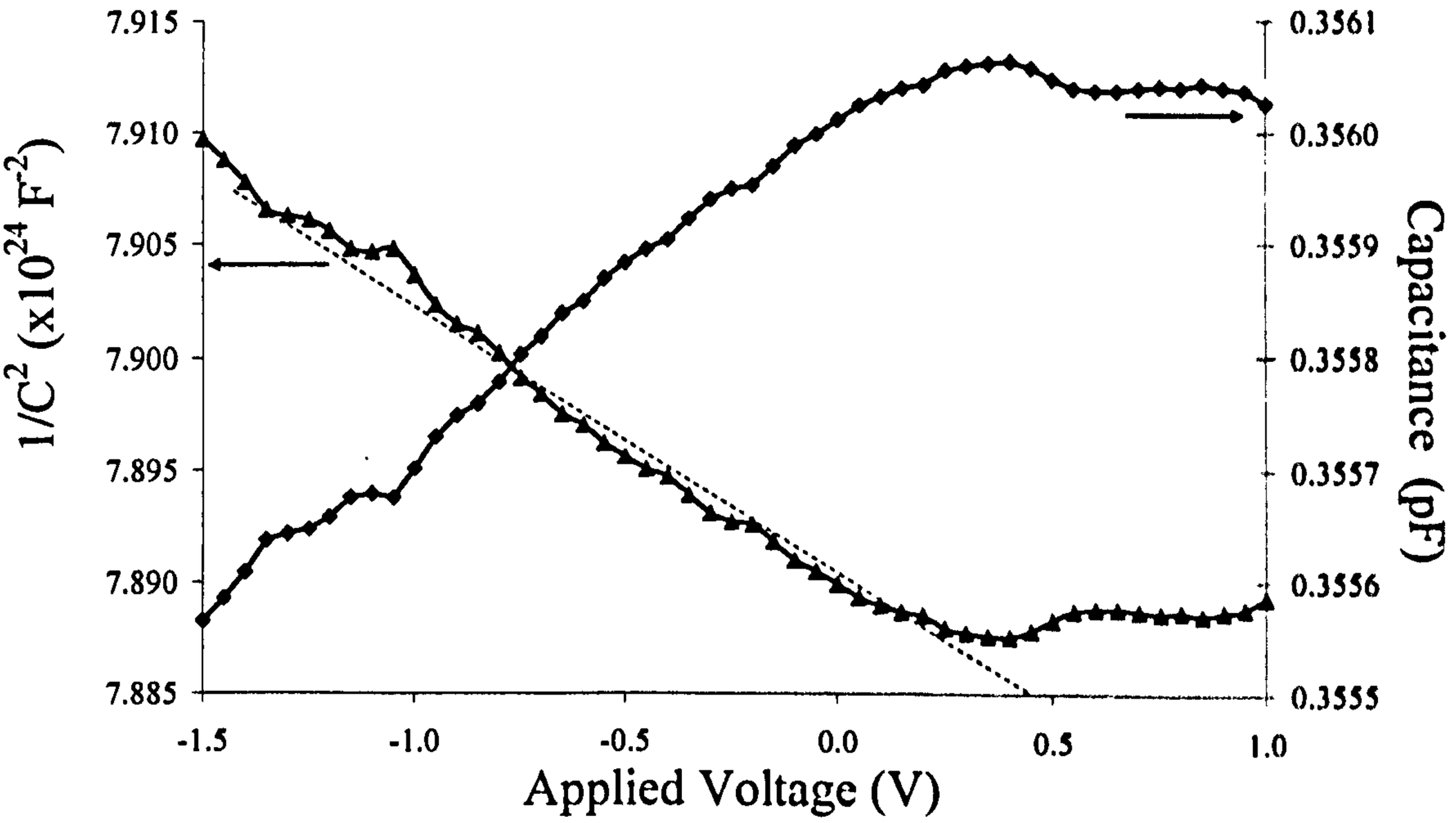

Figure 5.18. Capacitance as a function of applied DC voltage and Schottky-Mott plot for glass/FTO/i-ZnO/Au Schottky contacts.

5.4 Electrodeposition of Aluminium Doped Zinc Oxide

5.4.1 Experimental Procedure

The experimental procedure followed for the electrodeposition of ZnO:Al was similar to the i-ZnO except for the addition of $Al(NO_3)_3.9H_2O$ (having molar mass of 375.13 g mol^{-1}) to the solution in parts per billion (ppb) and parts per million (ppm) concentrations. Selected layers were annealed at 550°C for 20 minutes in air atmosphere and characterised using XRD, SEM and optical spectroscopy. In order to investigate the electrical properties of the material an array of 2 mm diameter contacts were evaporated using Al to form ohmic contacts forming glass/FTO/ZnO:Al/Al structure. In the following sections the results and discussion of ZnO:Al are presented.

5.4.2 Results

5.4.2.1 X-Ray Diffraction

The XRD spectra presented in Figure 5.21 presents annealed (a) undoped ZnO and (b) ZnO:Al electrodeposited from $Zn(NO_3)_2$ solution containing Al^{3+} ions having concentrations ranging from 10 to 1000 ppm as indicated in the figure. All layers were deposited at -0.975 V vs Ag/AgCl. XRD does not have the sensitivity to detect changes in crystal structure brought about by doping. The most likely detectable change is the lattice parameter. The presence of Al^{3+} in the solution may affect the crystallographic properties in other ways such as the growth mode and orientation of the crystallites. The pH of the solution reduced as a function of addition of $Al(NO_3)_3.9H_2O$, thus the growth conditions were not constant throughout the experiment and this change may have affected the orientation of the layers. As discussed in previous sections for i-ZnO the oxygen concentration varies as a function of bath lifetime, which alters the growth conditions and composition of the deposited material. The XRD has been included to illustrate this and demonstrate the lack of Al peak observation with the highest concentration of 1000 ppm.

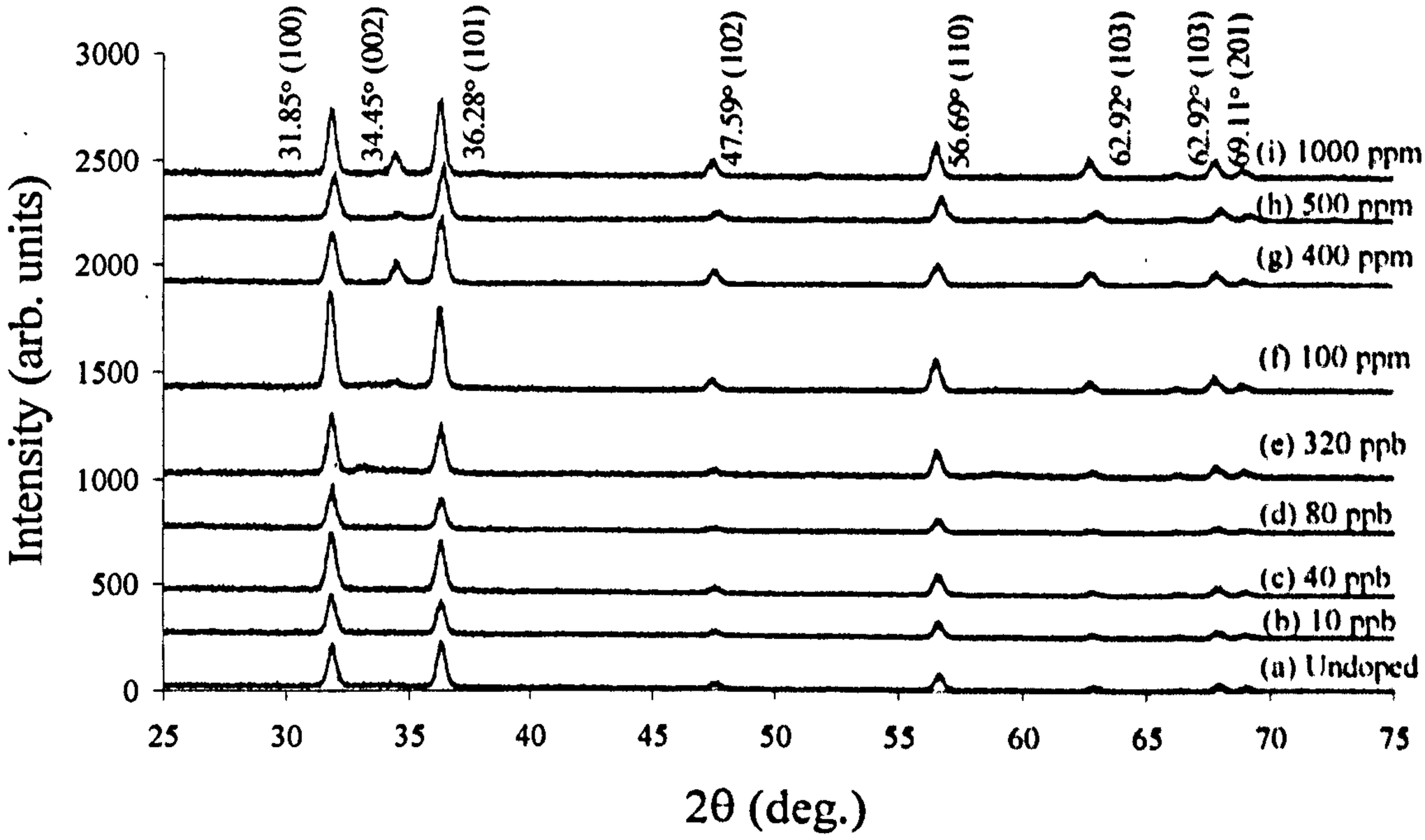

Figure 5.21. XRD spectra of annealed (a) undoped ZnO, (b) ZnO electrodeposited with 10, (c) 40, (d) 80 and (e) 320 ppb, and (f) 100, (g) 400, (h) 500 and (i) 1000 ppm Al^{3+} in the $Zn(NO_3)_2$ solution.

It is clear from the figure that the Al^{3+} did not alter the crystallographic properties of the layers. All spectra were identified to be polycrystalline ZnO having hexagonal, wurtzite phase. Table 5.5 presents the typical XRD data obtained for (a) undoped ZnO and ZnO:Al electrodeposited from solution containing Al^{3+} in the range 10 ppb to 100 ppm. Table 5.6 presents the typical XRD data obtained for layers deposited from $Zn(NO_3)_2$ containing Al^{3+} having concentration ranging from 400 to 1000 ppm.

Table 5.5. Typical XRD data obtained for (a) undoped, and layers deposited with (b) 10, (c) 40, (d) 80, (e) 320 ppb and (f) 100 ppm Al^{3+} added to the $Zn(NO_3)_2$ solution.

2θ (deg.)		d-Spacing (Å)		Miller Indices
Standard	Observed	Standard	Observed	(hkl)
31.73	31.85	2.818	2.810	(100)
36.26	36.28	2.479	2.479	(101)
47.60	47.59	1.913	1.911	(102)
56.63	56.69	1.627	1.624	(110)
62.99	62.92	1.478	1.477	(103)
67.97	68.02	1.380	1.378	(112)
69.17	69.11	1.360	1.359	(201)

Table 5.6. XRD data from Figure 5.21 for layers deposited with (g) 400, (h) 500 and (i) 1000 ppm Al^{3+} in the $Zn(NO_3)_2$ solution. All layers were identified to be of hexagonal, wurtzite ZnO.

2θ (deg.)		d-Spacing (Å)		Miller Indices
Standard	Observed	Standard	Observed	(hkl)
31.73	31.85	2.818	2.810	(100)
34.52	34.45	2.605	2.604	(002)
36.26	36.28	2.479	2.479	(101)
47.60	47.59	1.913	1.911	(102)
56.63	56.69	1.627	1.624	(110)
62.99	62.92	1.478	1.477	(103)
67.97	68.02	1.380	1.378	(112)
69.17	69.11	1.360	1.359	(201)

The Scherrer relation (2.5) was used to calculate the grain size of each layer using the XRD data. The mean grain size was calculated at 18.5 nm with negligible change from layer to layer as indicated by Table 5.7. The lattice parameters were calculated using the XRD data for the (100) and (101) peaks and equation (2.8) in Chapter 2, at a=3.254 Å and c=5.210 Å, which compares well with the standard data of a=3.253 Å c=5.120 Å [Sowa & Ahsbahs 2006].

Table 5.7. Crystallite size calculated using the Scherrer relation for the (100) peak of ZnO layers electrodeposited from $Zn(NO_3)_2$ solution containing varying amounts of Al^{3+}.

Sample	FWHM (deg.)	D (nm)
undoped	0.45	18
10 ppb	0.44	19
40 ppb	0.48	17
80 ppb	0.39	21
320 ppb	0.40	20
100 ppm	0.46	18
400 ppm	0.47	17
500 ppm	0.45	18
1000 ppm	0.44	19

5.4.2.2 Scanning Electron Microscopy

Figure 5.22 (a-f) further illustrates the variation in morphology of annealed ZnO grown using electrodeposition, as already indicated in Section 5.3.4. The layers were deposited at -0.975 V vs Ag/AgCl and had varying amounts of $Al(NO_3)_3.9H_2O$ in the solution. The layers (a & b) deposition from the solutions containing 80 ppb and 100 ppm Al^{3+} have hexagonal shaped crystals, ~0.5 μm in size and similar orientation. The SEM images of layers (c & d) deposited from solutions containing 400 and 500 ppm Al^{3+} clearly show thin needle shaped crystals ~ 0.5 μm in size and varying orientation. This type of morphology has been observed previously by [Wang *et al.* 2006].

Figure 5.22 (e & f) were both deposited from the same solution, containing 1000 ppm Al^{3+} and have crystallite size of 0.5 μm. The images indicate differing morphology despite the same Al^{3+} in the solution; the crystallites in (e) appear triangular in shape. The same morphology has been observed for undoped ZnO presented in Figure 5.9 (b) of Section 5.3.4. This suggests the variation in morphology is more likely to be due to a variation in oxygen content or solution pH than Al^{3+} in the solution.

It is clear from the images in Figure 5.22 there is a difference in morphology. The effect of Al^{3+} on the morphology of ZnO remains unclear. The presence of Al^{3+} in the electrolyte may cause the growth mode and orientation to change. The pH of the electrolyte decreased on addition of $Al(NO_3)_3.9H_2O$ and below pH=3 the electrolyte was unusable as ZnO failed to deposit. This is in accordance with the Pourbaix diagram which states that the solubility of ZnO increases above pH=5.5 at 90°C and is fully soluble in acidic solutions

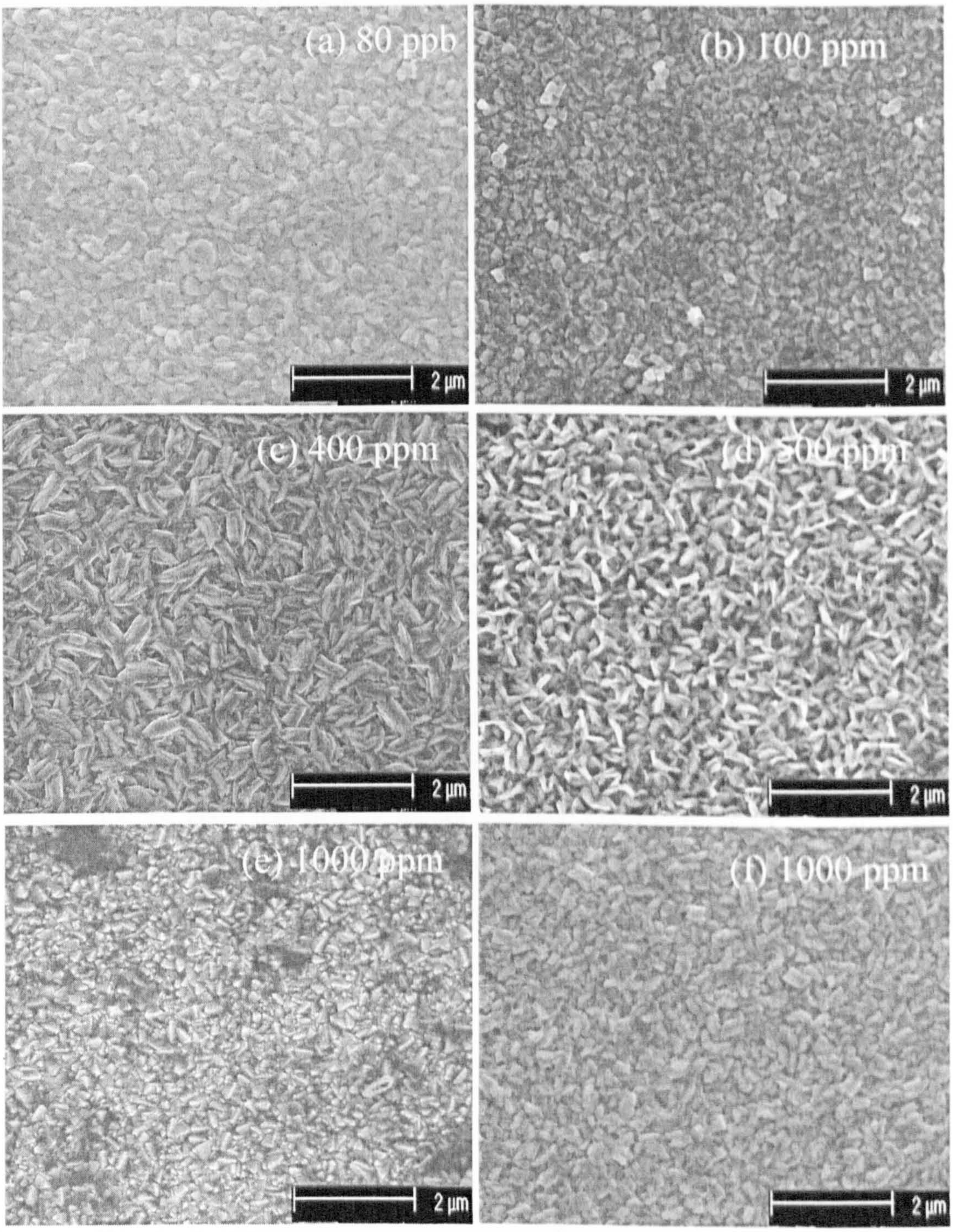

Figure 5.22. SEM images of ZnO electrodeposited from $Zn(NO_3)_2$ solution containing varying concentrations of Al^{3+} as indicated. Note the variation in morphology of the layer deposited from the solution containing the same amount of dopant.

5.4.2.3 Optical Properties

Optical absorption was carried out to investigate the change in absorption edge as a function of Al^{3+} in the electrolyte. The optical absorption spectra of annealed undoped ZnO and ZnO:Al deposited from solution containing 80 ppb, 500 ppm and 1000 ppm Al^{3+} are presented in Figure 5.23. The undoped spectra has a sharper absorption edge compared to the layers deposited from the electrolytes containing $Al(NO_3)_3$. The absorption spectra of layers deposited from the solution containing 80 ppb, 500 ppm and 1000 ppm Al^{3+} have a less steep absorption edge compared to the undoped layer.

The layers deposited from the solution containing the $Al(NO_3)_3$ were more opaque than the undoped ZnO which can be attributed to the formation of $Zn(OH)_2$ and possibly $Al(OH)_3$. Although the hydroxide was expected to decompose during annealing to form oxides it is possible the conversion was not complete or the ZnO remained inherently cloudy. The pH of the solution became more acidic as a function of $Al(NO_3)_3$ addition and this change in electrolyte conditions is likely to alter the properties of the layers. The layers were more conductive as discussed in Section 5.4.2.4 and appeared darker which altered the optical properties.

The undoped layer has slightly higher bandgap energy of 3.29 eV. All absorption spectra for layers deposited from the solution containing $Al(NO_3)_3$ have a similar shape and bandgap energy of 3.26 eV. It is apparent the doping concentration in the solution did not markedly alter the bandgap energy of the ZnO.

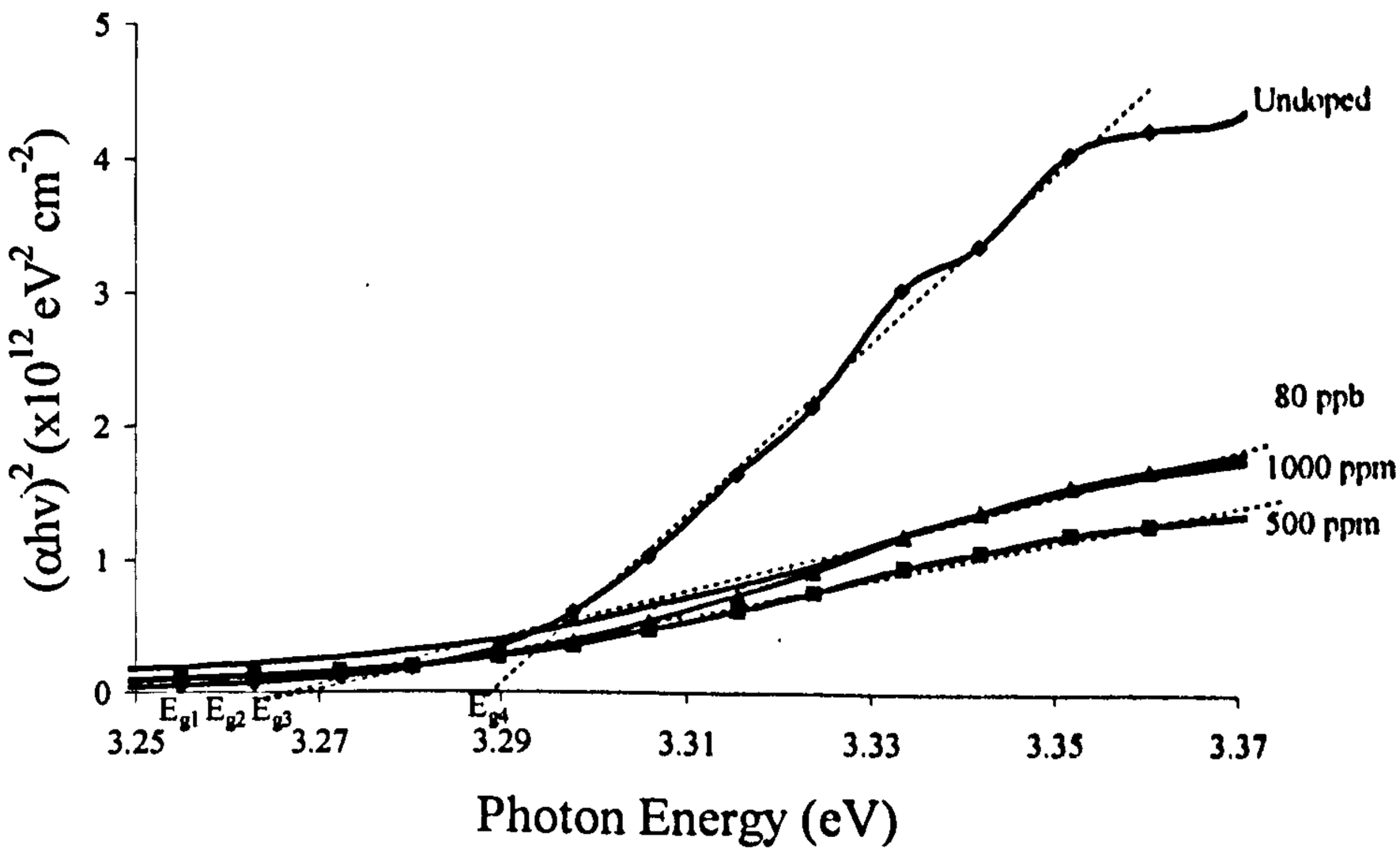

Figure 5.23. Optical absorption spectra for undoped ZnO and layers deposited from $Zn(NO_3)_2$ solution containing 80 ppb, 500 ppm and 1000 ppm Al^{3+}.

5.4.2.4 Electrical Properties

The I-V measurements of glass/FTO/ZnO:Al/Al were taken to study the affect of Al^{3+} addition to the electrolyte on the electrical properties of ZnO:Al. Al is a low work function metal (ϕ_b=4.06 eV) and is often used to form an low resistance front metal contact for solar cells with device structure glass/Mo/CIGS/CdS/i-ZnO/ZnO:Al/Al [Sze & Ng 2007]. It was expected the Al and n-type ZnO:Al would form an ohmic contact.

Figure 5.24 presents the linear-linear I-V curves of glass/FTO/ZnO:Al/Al taken under dark conditions, indicating ohmic behaviour. It was found the series resistance and electrical resistivity of the material decreased with increasing doping concentration between undoped and 80 ppb doping. Above 80 ppb the electrical properties saturated as illustrated in Table 5.8. This indicates increasing the doping concentration in the solution no longer affected the electrical properties and had the negative effect of reducing the solution pH.

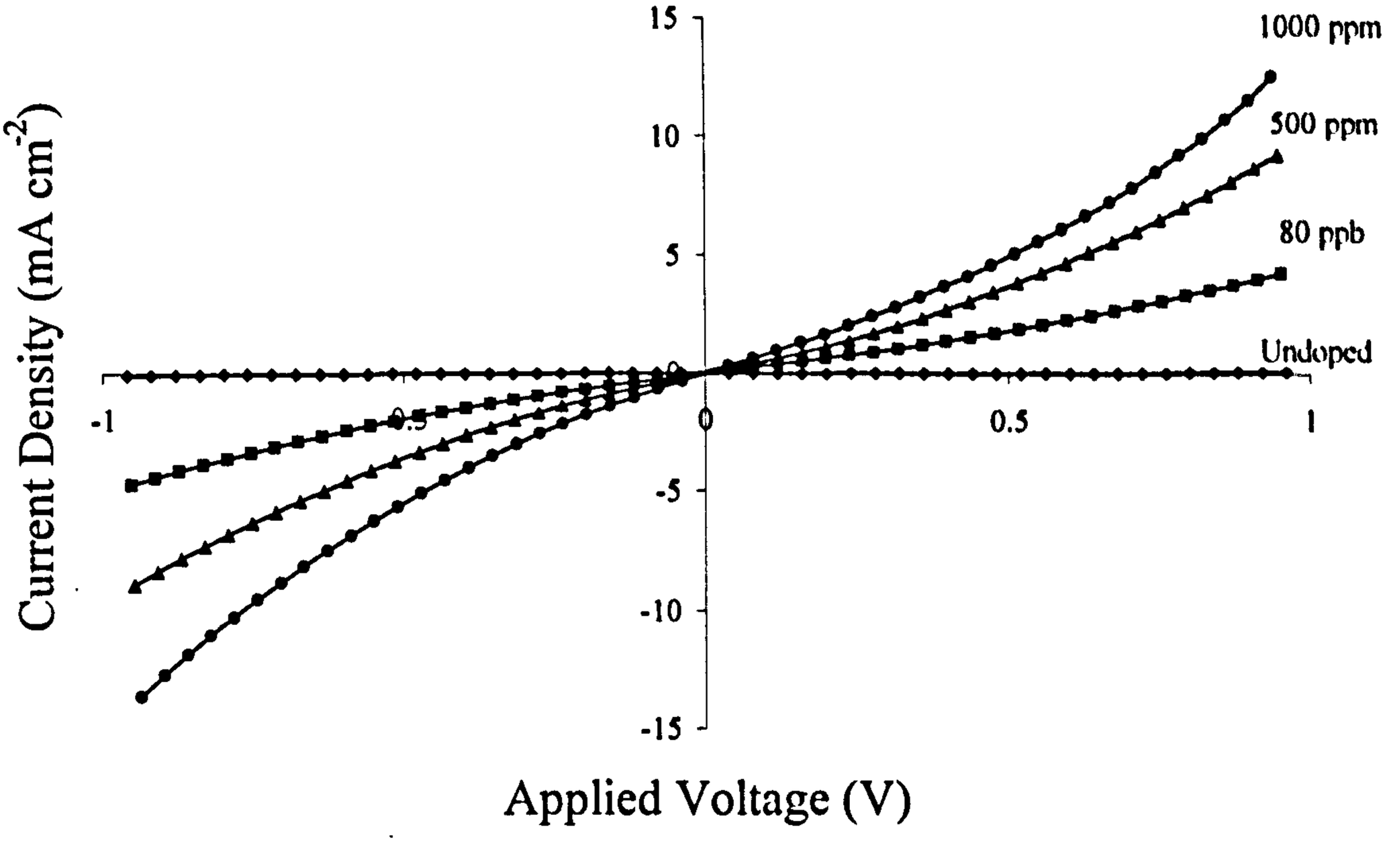

Figure 5.24. I-V curves of (a) undoped ZnO, and ZnO:Al deposited from an electrolyte containing (b) 80 ppb, (c) 500 and (d) 1000 ppm Al^{3+}.

It is worth noting that the series resistance and resistivity of the ZnO:Al is higher than previously reported values. The lowest reported electrical resistivity of ZnO of 10^{-4} Ω cm was deposited using r.f. sputtering [Chang & Hon 2001, Ozgur *et al.* 2005]. Sputtering enables a higher degree of controllability over the composition of deposited

layers compared to electrodeposition. Low resistivity ZnO is achieved by presence of oxygen vacancies and zinc interstitial atoms. In the case of electrodeposition of ZnO the layers exhibit higher resistivity most likely due to high oxygen content. The resistivity reported in Table 5.8 indicates the electrodeposited ZnO layers are oxygen rich.

Table 5.8. Electrical properties of undoped ZnO and ZnO:Al having varying amounts of Al^{3+} in the electrolyte.

Al^{3+} concentration in electrolyte	R_s (Ω)	ρ (Ω cm)	σ $(\Omega\ cm)^{-1}$
undoped	13000	4.0×10^{7}	2.5×10^{-8}
80 ppb	277	8.7×10^{5}	1.1×10^{-6}
500 ppm	151	4.7×10^{5}	2.1×10^{-6}
1000 ppm	101	3.2×10^{5}	3.1×10^{-6}

5.4.3 Discussion

The purpose of the experiments to dope ZnO with Al was to increase the electrical conductivity of the material as i-ZnO is highly resistive and does not form a good ohmic contact during device fabrication. The characterisation was carried out to investigate the structural, morphological and electrical properties aimed to observe any changes in the material properties with addition of Al^{3+} in the electrolyte. It was not expected that elemental Al would be detected during the XRD investigation as the deposition voltage of Al^{3+} is -1.662 V vs NHE and therefore is unlikely to rapidly deposit at the cathode [Lide 2005]. It was envisaged that some Al^{3+} may be either absorbed, chemisorbed or adsorbed at the cathode. In the latter case annealing would be required to form bonds between Al atoms and the ZnO lattice. In addition Kemell *et al.* suggested the Al^{3+} ions react more easily than Zn^{2+} with hydroxide ions thus forming aluminium hydroxide [Kemell *et al.* 2003].

Some difficulties were encountered during the addition of $Al(NO_3)_3$ to the electrolyte. Firstly it was unclear how much Al^{3+} remained in the solution after the deposition of each layer and therefore the actual amount of dopant in solution cannot be discussed with a large degree of accuracy. It is most likely very little Al^{3+} was deposited and therefore a cumulative concentration is expected. This problem may be overcome by the preparation of a new $Zn(NO_3)_2$ solution before each addition of

$Al(NO_3)_3$ although this would consequently be a lengthy process and would create significant chemical wastage. After the addition of several millilitres of $Al(NO_3)_3$ to the electrolyte the pH drastically decreased. This uncontrollable change in deposition parameters results in reproducibility issues and according to the Pourbaix diagram the solubility of ZnO increases below pH=5, resulting in the deposition of metallic Zn [Goux *et al.* 2005]. This was frequently observed during the present investigation by the dark appearance of the layers when the pH of the solution was low (pH<3). Addition of an alkaline solution to the electrolyte such as sodium hydroxide (NaOH) or ammonia hydroxide (NH_4OH) to adjust the pH has the disadvantage of unwanted impurities or formation of ammine complexes $[Zn(NH_3)_4]^{2+}$.

Ideally the performance of CIS solar cells containing the electrodeposited ZnO:Al layer would have been tested. Growth parameters would also have been optimised, including growth time and Al^{3+} concentration in the electrolyte most suited to the device. However due to growth issues with ZnO:Al and CIS from aqueous solution in our laboratory this was not possible.

5.5 Comparison of Sputtered and Electrodeposited Intrinsic Zinc Oxide and Aluminium Doped Zinc Oxide

5.5.1 X-Ray Diffraction

Figure 5.25 compares XRD spectra of the electrodeposited i-ZnO and ZnO:Al with sputtered material supplied by Pilkington Group Ltd. Peaks from the FTO coated glass substrate are identified by an asterisk (*). The XRD indicates the sputtered material is polycrystalline and all peaks were identified as hexagonal ZnO. The preferred crystallite orientation of each spectra was in the (101) plane, which compares with the standard spectra (Figure 5.9). The grain sizes of electrodeposited and sputtered i-ZnO and ZnO:Al were calculated using the Scherrer relation (2.5) and are compared in Table 5.9. It was shown there was a close similarity between the grain sizes for all materials.

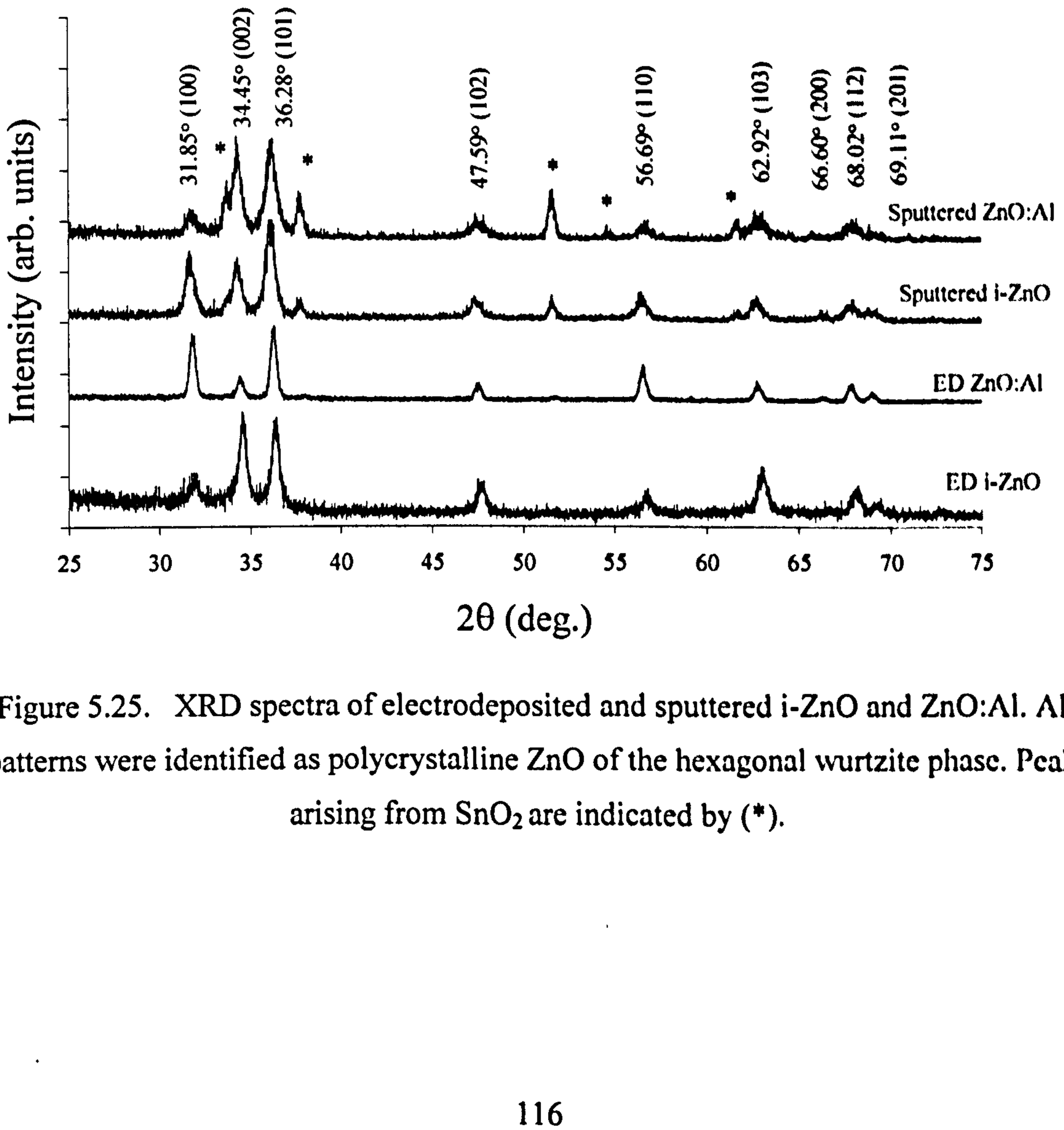

Figure 5.25. XRD spectra of electrodeposited and sputtered i-ZnO and ZnO:Al. All patterns were identified as polycrystalline ZnO of the hexagonal wurtzite phase. Peaks arising from SnO_2 are indicated by (*).

Table 5.9. POI and grain size of electrodeposited and sputtered i-ZnO and ZnO:Al.

	Electrodeposited i-ZnO	Electrodeposited ZnO:Al	Sputtered i-ZnO	Sputtered ZnO:Al
POI (101)	0.244	0.271	0.292	0.294
Grain Size (nm)	18	18	12	16

Although the intensity of the three main peaks (100), (002) and (101) for the electrodeposited material changed from i-ZnO to ZnO:Al this was not thought to be due to the addition of dopant atoms. Instead, slight variation of O_2 concentration in the electrolyte has been shown to alter the nucleation and growth mechanism [Pauporte & Lincot 2000]. However the addition of Al at 2 wt% could also change the nucleation and growth mechanism and hence cannot be completely ruled out. According to Ingham *et al.* the variation in morphology of ZnO grown using electrodeposition is still not fully understood [Ingham *et al.* 2008].

5.5.2 Scanning Electron Microscopy

SEM images of electrodeposited and sputtered i-ZnO, ZnO:Al layers deposited on FTO coated glass are presented in Figure 5.26. Both electrodeposited materials were deposited from 0.1 M $Zn(NO_3)_2.6H_2O$ electrolyte at -0.975 V vs Ag/AgCl, the latter containing ppm concentration of Al^{3+}. The electrodeposited (a) i-ZnO is compact and dense with apparent crystallite size of 0.16 μm. Pauporte *et al.* reported low oxygen concentration encourages larger crystal size due to fewer nucleation centers [Pauporte & Lincot 2000]. The oxygen source in this study was provided by the reduction of nitrate ions and no additional oxygen was bubbled through the solution.

As already discussed in Section 5.4.2.2 electrodeposition permits a lower controllability of film composition compared to sputtering. The films have varying orientation as confirmed by the POI estimation given in Section 5.5.1. The surface of electrodeposited (b) ZnO:Al is comprised of rectangular shaped crystals with dimensions 0.50 μm by 0.10 μm. The difference in morphology is likely to be due to either a change in oxygen concentration or difference in nucleation initiated by Al, both of which can lead to varying nucleation mechanism [Pauporte & Lincot 2000]. It has also been reported the growth mechanism of ZnO from nitrate solution is still not fully understood [Ingham *et al.* 2008, Yoshida *et al.* 2004].

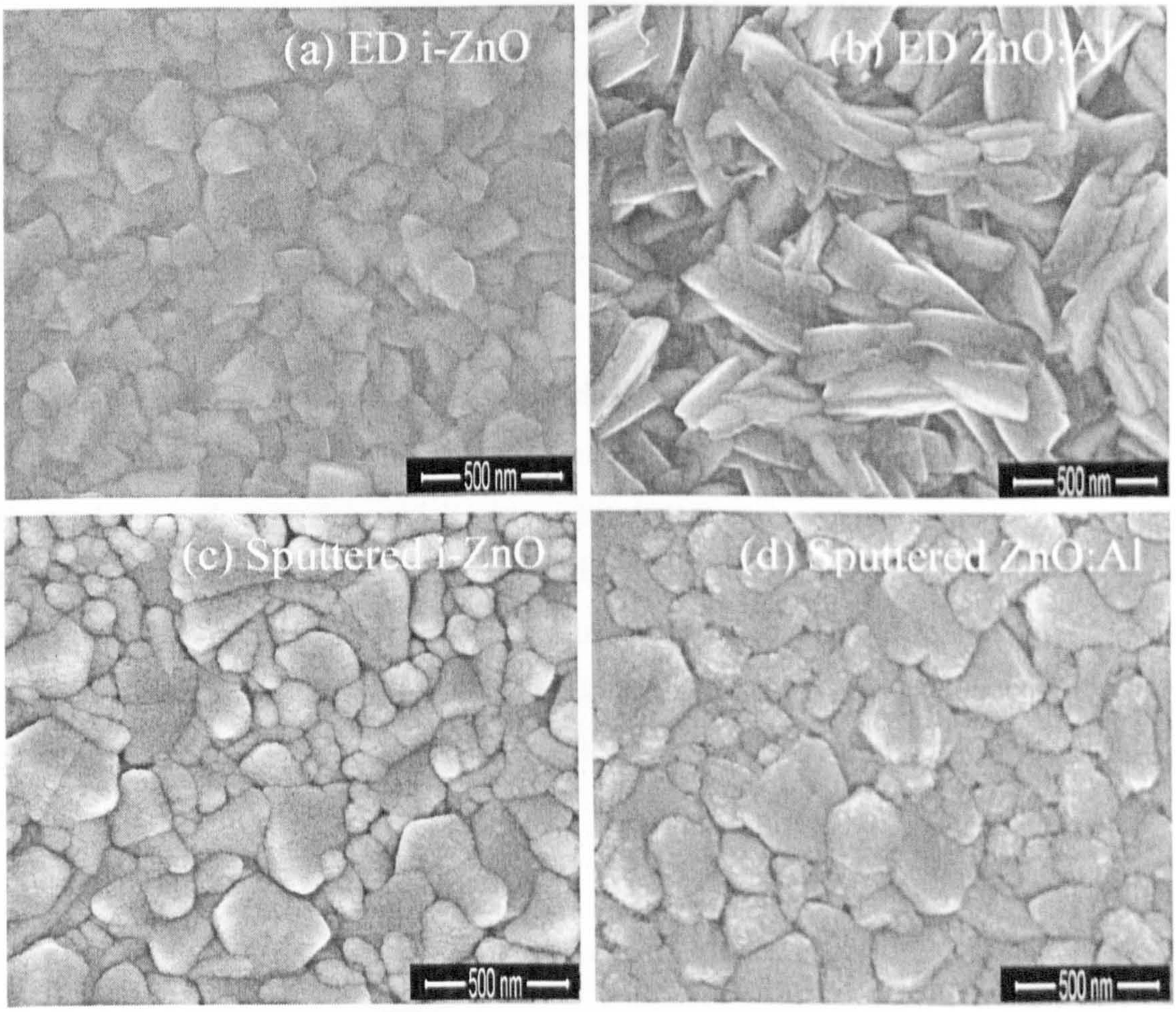

Figure 5.26. SEM micrographs of (a) electrodeposited (ED) i-ZnO having crystallite size of 0.16 μm, (b) electrodeposited ZnO:Al with crystallite dimensions of 0.50 by 0.10 μm. (c) Sputtered i-ZnO and (d) ZnO:Al both show agglomerated nanocrystallites of 0.10 to 0.40 μm in size.

The images of both (c) i-ZnO and (d) ZnO:Al deposited using sputtering are comprised of agglomerated nanocrystallites having formed larger granules of between 0.10 and 0.40 μm in size and the films appear highly compact. The difference in morphology is unavoidable when growing materials using different techniques due to the varying nucleation and growth mechanisms, substrate temperature and oxygen concentration.

It is interesting to compare the different grain sizes observed using XRD (11.7 to 27.6 nm) and SEM (0.10 to 0.50 μm) techniques. The one order of magnitude difference between these estimations is attributed to the difference in technique capability. XRD examines the reflection of the x-rays from atomic planes of

crystallites. The Scherrer relation uses the FWHM which provides information on the coherence length of reflected x-rays. SEM detects the surface morphology and indicates the nodule size which is of greater magnitude than the information provided by XRD, elucidating the factor of 10 discrepancy.

5.5.3 Optical Properties

Transmission spectra of electrodeposited and sputtered i-ZnO and ZnO:Al are presented in Figure 5.27. The sputtered material is highly transparent compared to the electrodeposited material which was white/opaque in appearance. Sputtered and electrodeposited ZnO materials transmitted 95% and 85% of incident photons respectively. The difference in transmission is attributed to thickness, surface roughness and scattering centres. The milky appearance of electrodeposited ZnO layers could arise due to inclusions of $Zn(OH)_2$ during electrodeposition from aqueous solution.

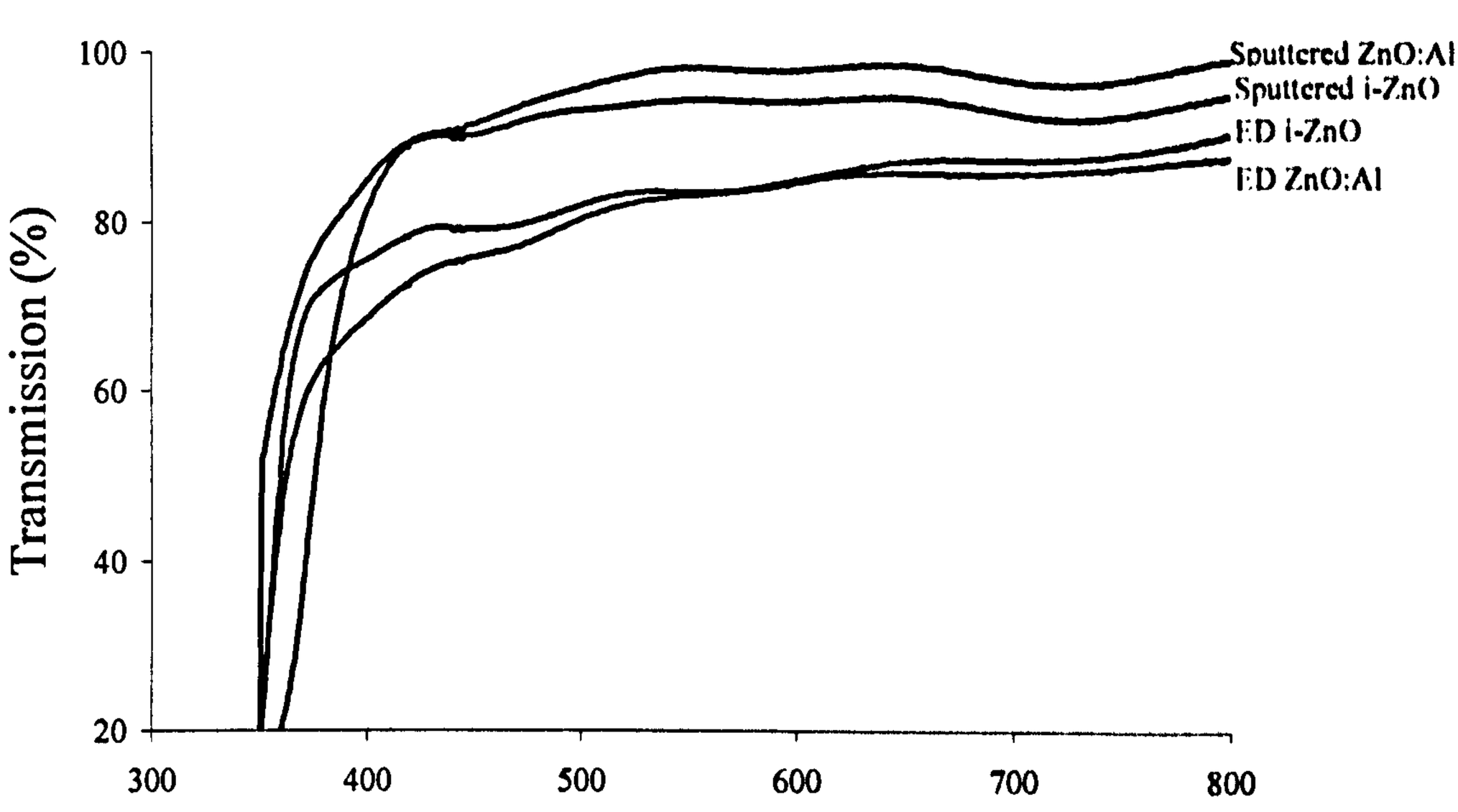

Figure 5.27. Transmission spectra of electrodeposited (ED) and sputtered ZnO layers having 85% and 95% transmission respectively.

Figure 5.28 presents the optical absorption spectra of electrodeposited and sputtered i-ZnO and ZnO:Al on FTO-coated glass substrates. The bandgap energy was estimated

by extrapolation of the plot of $(\alpha h\nu)^2$ vs E at 3.29 eV and 3.27 eV for electrodeposited i-ZnO and ZnO:Al compared to 3.39 eV and 3.45 eV for sputtered i-ZnO and ZnO:Al materials. These values agree with previously reported values for undoped ZnO (3.20–3.40 eV) [Pearton *et al.* 2005] within experimental error. The shift in bandgap may be attributed to a variation in stoichiometry. The Burnstein-Moss effect also offers an explanation for the shift in bandgap energy of sputtered ZnO:Al. The Burnstein-Moss effect occurs in degenerate semiconductors when the Fermi level position moves above the conduction band minimum. The fundamental edge of absorption transitions shifts from E_c-E_v =E_g to become E_F-E_v >E_g [Schubert 2007].

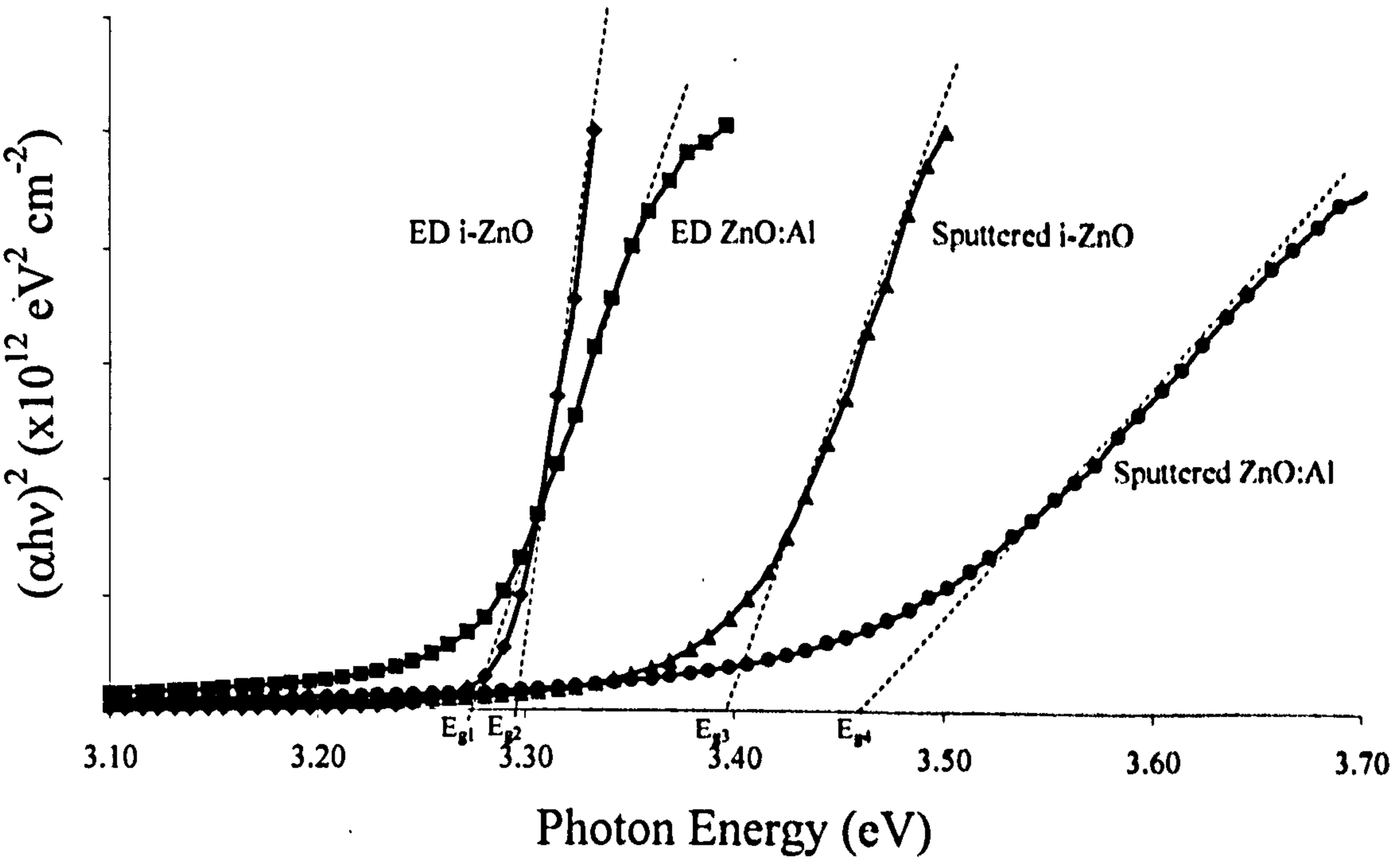

Figure 5.28. Optical absorption spectra indicated electrodeposited (ED) i-ZnO and ZnO:Al having bandgap energies of E_{g2}=3.29 eV and E_{g1}=3.27 eV; sputtered i-ZnO and ZnO:Al having E_{g3}=3.39 eV and E_{g4}=3.45 eV respectively.

5.5.4 Electrical Properties

Current-voltage measurements were carried out on devices having structures glass/FTO/i-ZnO/Au and contact areas of 0.031 cm^2. Figures 5.29 and 5.30 present the Log–linear and linear-linear I-V curves for sputtered i-ZnO. The I-V curve of electrodeposited i-ZnO may be found in Figure 5.19 of Section 5.3.6. As already discussed the electrodeposited ZnO:Al devices were ohmic in nature as indicated by

Figure 5.24 of Section 5.4.3.4. The series resistance of the structures was determined using the gradients of the ohmic curves or the gradients of high forward I-V curves in the case of rectifying devices.

Table 5.10 summarises the series resistance, bulk electrical resistivity and conductivity of both electrodeposited and sputtered ZnO layers for comparison. In this analysis the series resistance of the structure has been assumed to arise mainly from the bulk ZnO layer. The electrical resistivity of the electrodeposited and sputtered i-ZnO was 6.9×10^{6} and 6.2×10^{7} Ω cm respectively. This difference in bulk electrical resistivity is likely to be due to different grain sizes and the variation in stoichiometry due to the difference in growth technique. The high electrical resistivity of both materials indicates a high oxygen content which reduced the electrical conductivity. The electrical resistivity decreased after Al doping to 3.4×10^{5} and 2.3×10^{5} Ω cm for electrodeposited and sputtered ZnO:Al materials indicating Al has been assimilated into the crystal lattice as an n-type dopant. The electrical resistivity reduction is only 1-2 orders of magnitude which is much less than expected or previously reported for ZnO:Al; lowest reported to date is 10^{-4} Ω cm [Cheng & Hon 2001].

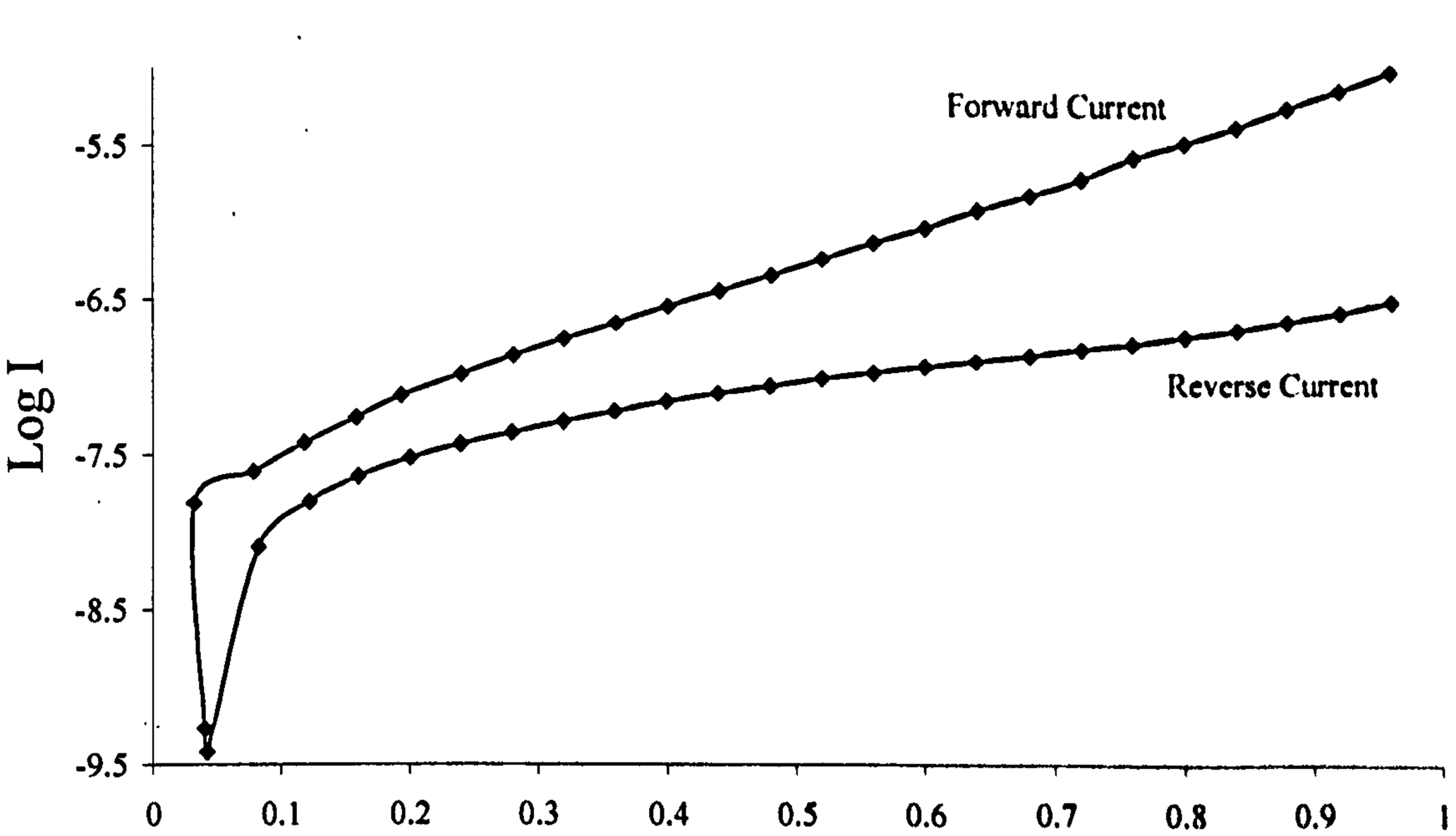

Figure 5.29. Log I vs V of glass/FTO/i-ZnO/Au structure forming a Schottky contact fabricated with sputtered material under dark conditions.

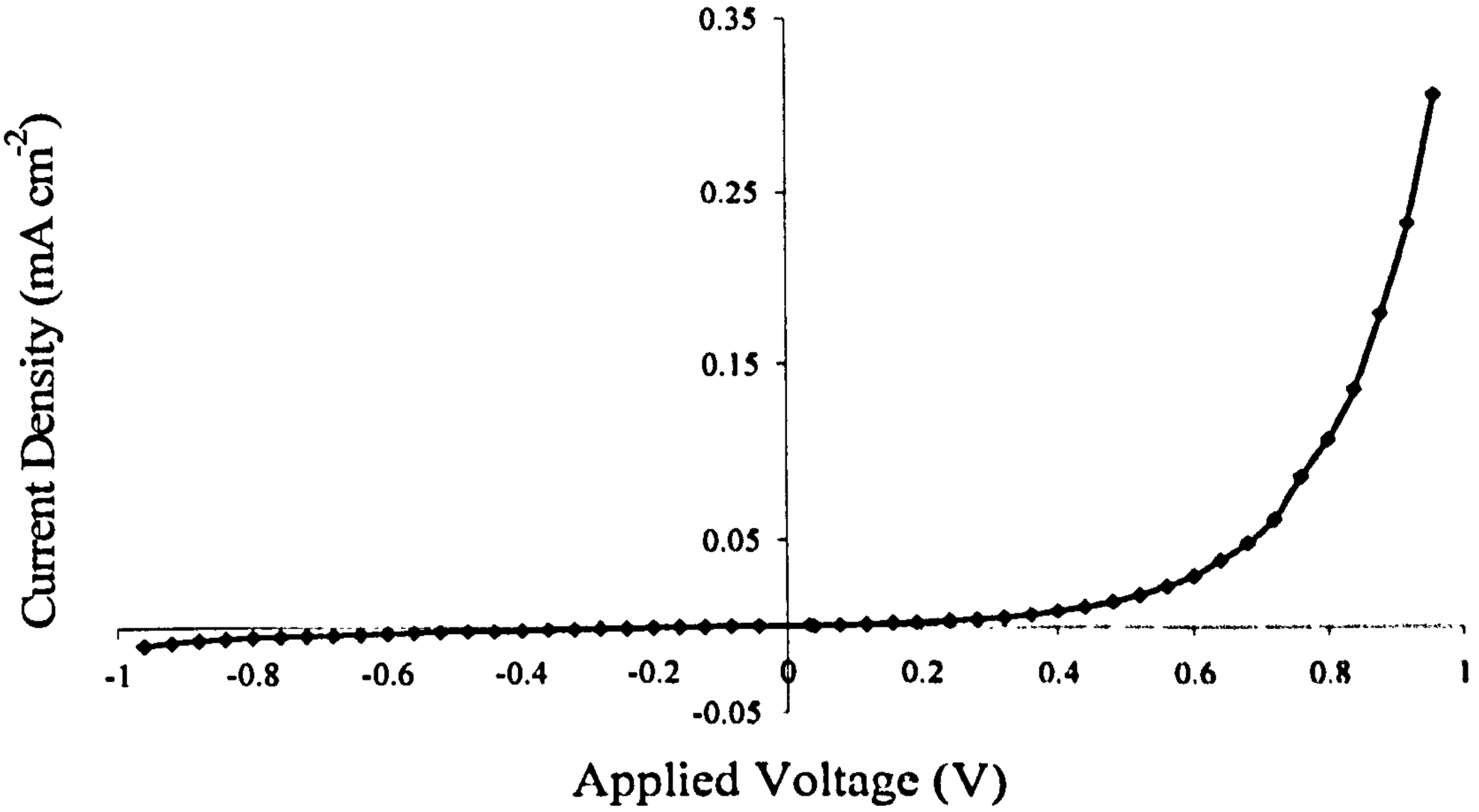

Figure 5.30. I-V curve observed under dark conditions for glass/FTO/i-ZnO/Au structure fabricated with sputtered i-ZnO.

Table 5.10. Summary of electrical properties of electrodeposited and sputtered i-ZnO and ZnO:Al for comparison, it is clear the series resistance decreased after doping.

Material	R_s (Ω)	ρ (Ω cm)	σ $(\Omega\ cm)^{-1}$
Electrodeposited i-ZnO	2.2×10^{3}	6.9×10^{6}	1.5×10^{-7}
Sputtered i-ZnO	2.0×10^{4}	6.2×10^{7}	1.6×10^{-8}
Electrodeposited ZnO:Al	1.1×10^{2}	3.4×10^{5}	2.9×10^{-6}
Sputtered ZnO:Al	7.3×10^{1}	2.3×10^{5}	4.4×10^{-6}

5.6 P-type Doping of Zinc Oxide

5.6.1 Experimental Procedure

The experimental procedure used for the attempted p-type doping of ZnO was identical to the description given in Section 5.2 for i-ZnO, except for the addition of p-type dopant atoms in ppb and ppm concentrations to the $Zn(NO_3)_2$ solution. The three reagents used for the doping experiments were arsenic oxide (As_2O_5), phosphoric acid (H_3PO_4) and silver nitrate ($AgNO_3$) having molar masses of 229.8, 98.0 and 169.8 g respectively. The layers were characterised using PEC to investigate the V_{oc} of the

layers under dark and illuminated conditions to establish the electrical conductivity type. A liquid/solid junction was formed using 0.1M $NaSO_3^{2-}$ and the photovoltage curves were taken using the GillAC computerised potentiostat. A brief summary of the findings is presented in Section 5.6.2.

5.6.2 Results and Discussion

Although XRD and optical absorption studies were carried out on all layers during this experiment no changes were observed compared to i-ZnO. Dopant atoms are present in ppb and ppm level and changes in the crystallographic structure are not detectable using XRD. In these investigations the bandgap energy was estimated by extrapolating the tangent to the curve to intersect the x-axis. This method of determination of bandgap energy is an estimate and does not give accurate enough values to identify changes with doping. The results of XRD and optical absorption have not been included as no significant differences were observed in comparison to undoped material. All XRD spectra were polycrystalline with varying orientation and no peaks arose from dopant atoms. Figure 5.33 presents the PEC curve for undoped ZnO indicating n-type electrical conductivity, which may be used for comparison with Figures 5.34 to 5.36.

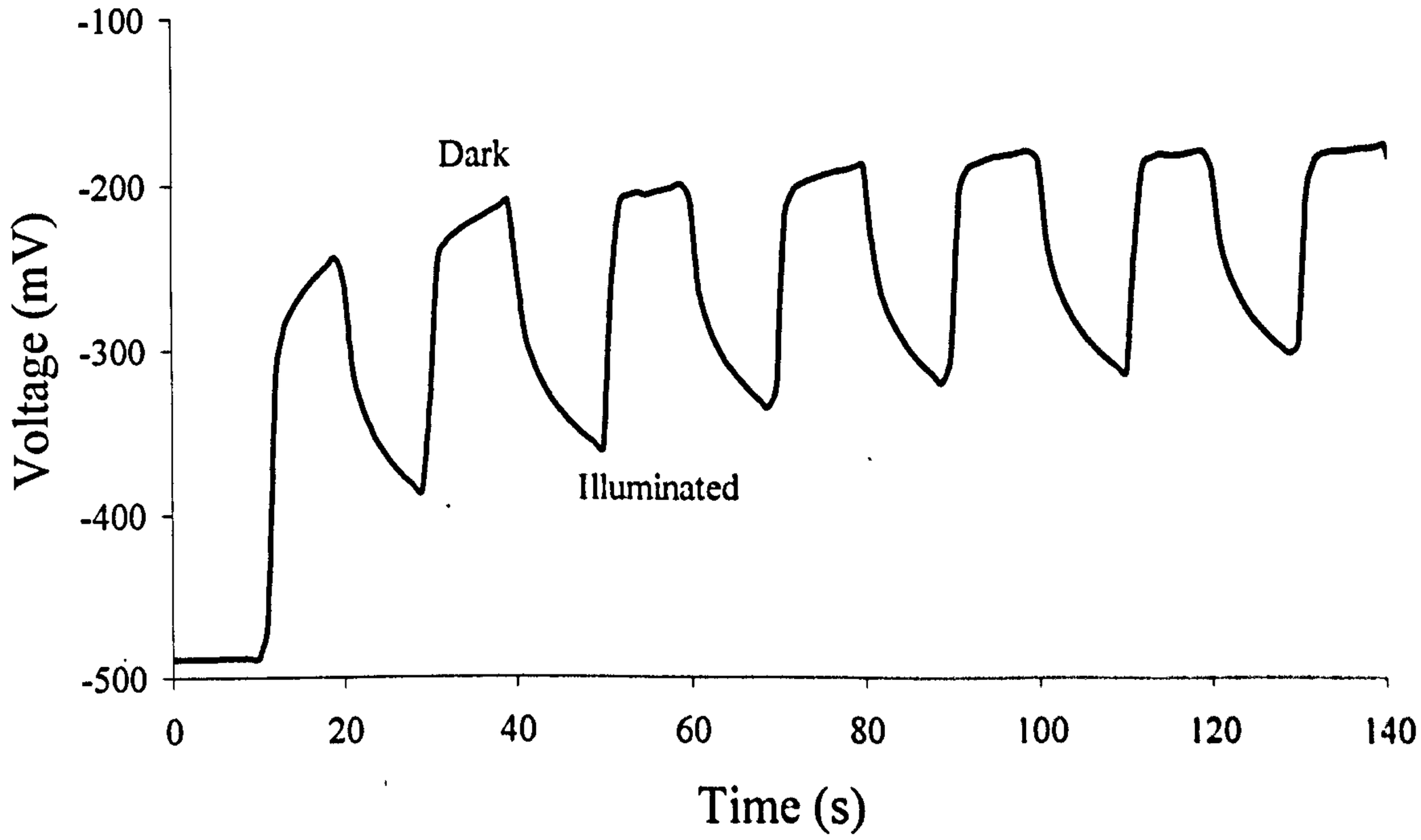

Figure 5.33. Photovoltage curve of undoped ZnO indicating n-type electrical conductivity.

5.6.2.1 Arsenic Doped Zinc Oxide

PEC was carried out to determine the effect on the electrical conductivity type of the layers deposited from an electrolyte containing ppm concentration of As^{5+}. Figure 5.34 presents the photovoltage curve of the ZnO layer deposited from the electrolyte containing 500 ppm As^{5+}. The electrical conductivity type of the layer was n-type as the illuminated voltage was more negative than the dark. This confirms that p-type doping of ZnO was not achieved using As^{5+}.

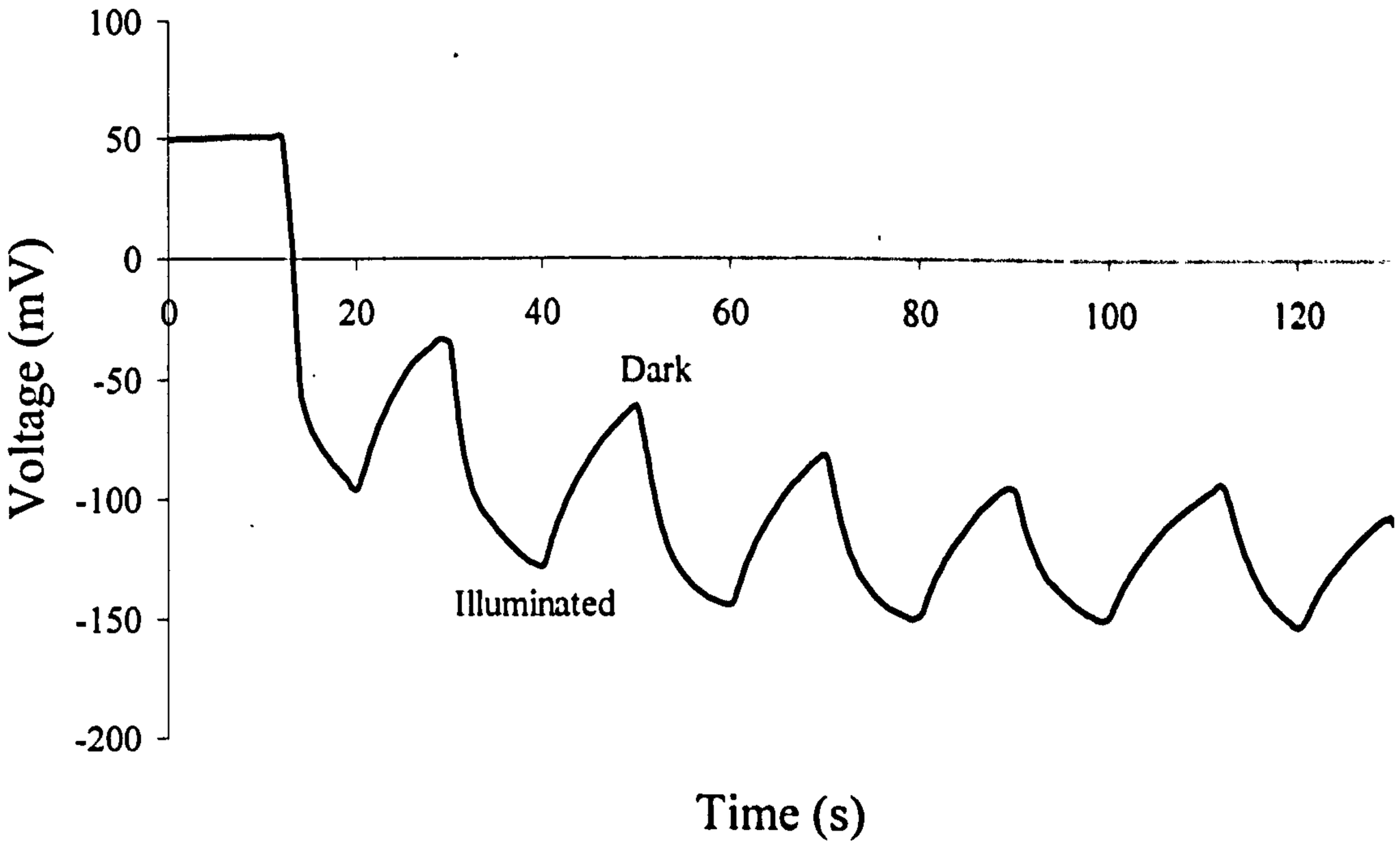

Figure 5.34. Photovoltage curve of ZnO deposited with the addition of As^{5+} to the electrolyte, indicating n-type electrical conductivity.

5.6.2.2 Phosphorus Doped Zinc Oxide

Figure 5.35 presents the photovoltage curve of the ZnO layer deposited from the electrolyte containing 500 ppm P^{5+}. The electrical conductivity of the layer was n-type as the illuminated voltage was greater than the dark. This confirms that p-type doping of ZnO was not achieved using P^{5+}.

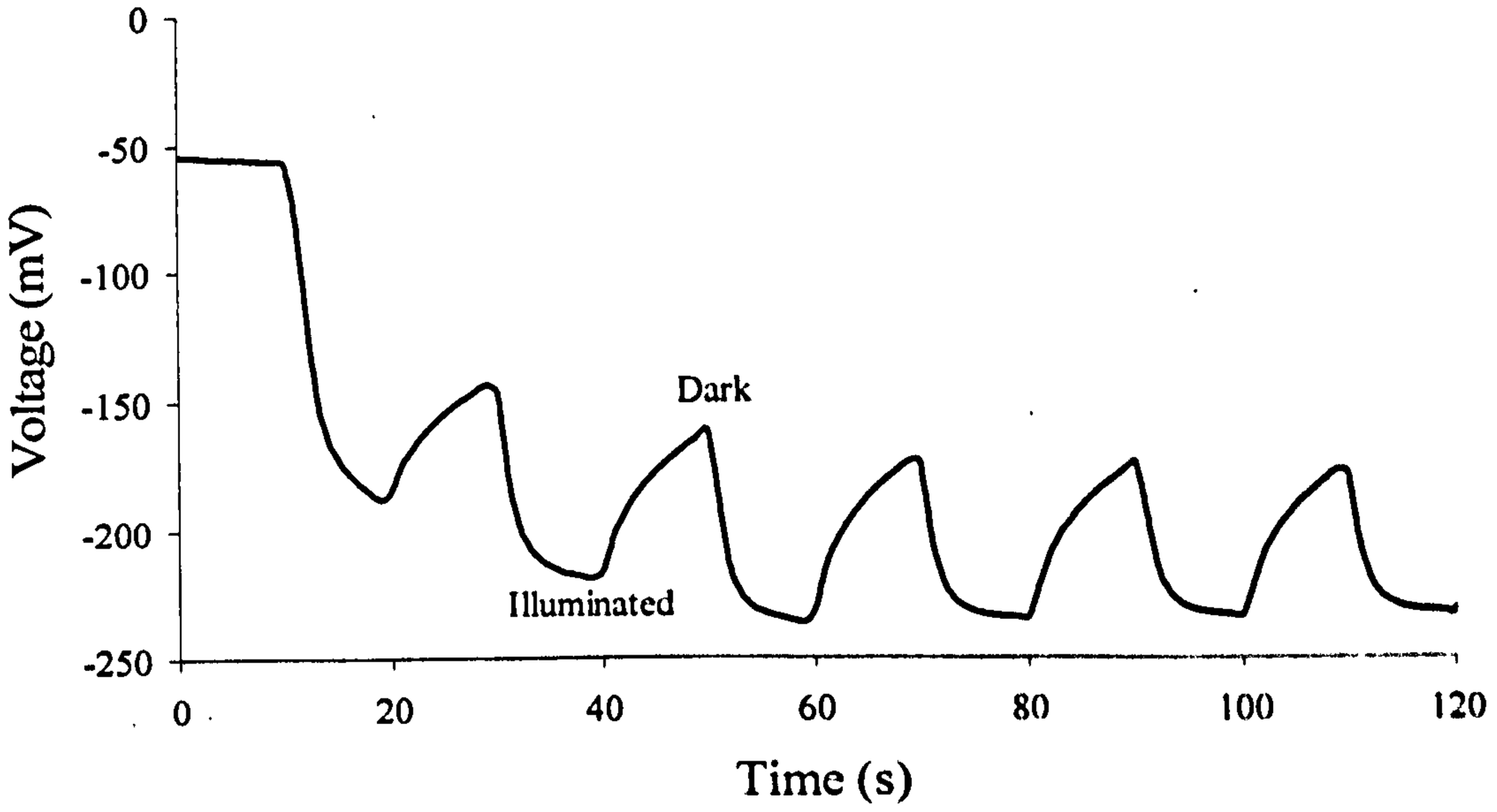

Figure 5.35. Photovoltage curve of ZnO deposited with the addition of P^{3+} to the electrolyte, indicating n-type electrical conductivity.

5.6.2.3 Silver Doped Zinc Oxide

Figure 5.36 presents the photovoltage curve of the ZnO layer deposited from the electrolyte containing 500 ppm Ag^{+}. The electrical conductivity of the layer was n-type as the illuminated voltage was more negative than in the dark. This confirms that p-type doping of ZnO was not achieved using Ag^{+}.

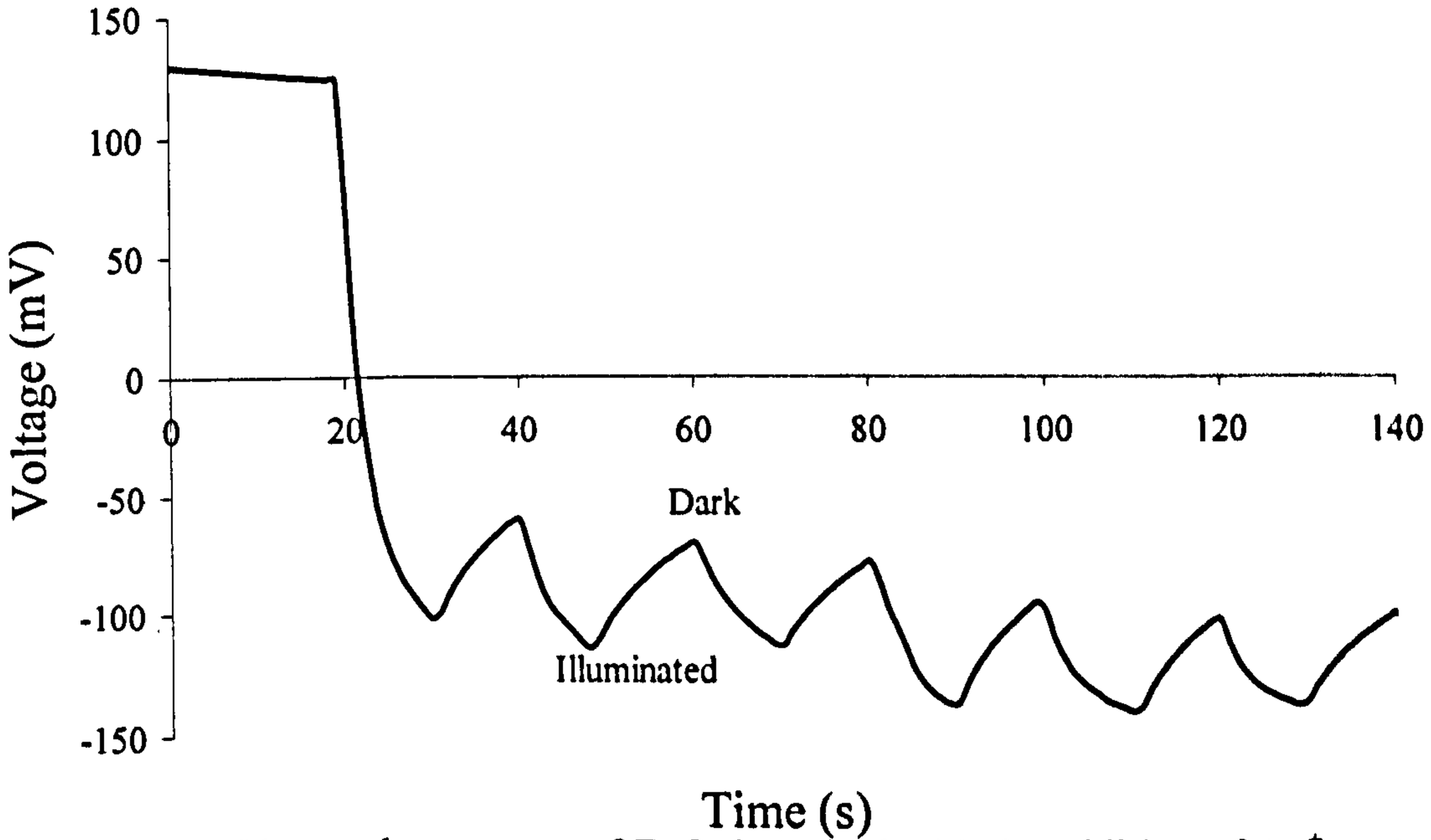

Figure 5.36. Photovoltage curve of ZnO deposited with the addition of Ag^{+} to the electrolyte, indicating n-type electrical conductivity.

5.7 Conclusions

In conclusion i-ZnO has been electrodeposited from zinc nitrate solution at a range of deposition voltages, vs Ag/AgCl. XRD identified the layers to be polycrystalline, hexagonal, wurtzite ZnO although the preferential orientation varied between layers. The material was consistently n-type in electrical conductivity and had a bandgap energy of ~3.27 to 3.29 eV. The electrical properties indicated the material to be highly resistive having electrical resistivity of 6.9×10^{6} Ω cm.

Certain difficulties were encountered during the development of ZnO that would limit the possibility of scale-up at this stage. The growth technique is undoubtedly suited to scale-up as already proven in the literature for $CuInSe_2$ [Ramdani *et al.* 2006]. However further work is needed to establish reproducibility of ZnO growth from a nitrate precursor. Difficulties were encountered during the development of i-ZnO particularly relating to electrolyte inconsistencies in pH preventing ZnO deposition. This may also be attributed to insufficient O_2 availability from the nitrate precursor when the solution was 2-3 days old.

To conclude the work on the development of ZnO:Al using electrodeposition, polycrystalline hexagonal ZnO thin films have been prepared from $Zn(NO_3)_2$ solution containing various concentrations of $Al(NO_3)_3$. The ZnO:Al doped material showed improved electrical properties although the electrical resistivity remained relatively high. It was not possible to deposit i-ZnO ZnO:Al onto glass/Mo/$CuInSe_2$/CdS structures during this research project due to reproducibility issues. To make this method suitable for commercialisation more work would need to be carried out to address consistency issues mainly regarding the electrolyte conditions, including pH and actual concentration of dopant in the solution as a function of growth time. The pH decreased as the Al dopant solution was added to the electrolyte, below pH=5 the solubility of ZnO is increased, thus inhibiting its deposition.

Comparison was made between properties of electrodeposited and sputtered i-ZnO and ZnO:Al thin films. XRD patterns showed all materials to be hexagonal wurtzite ZnO structure with similar orientation to the standard ZnO spectra. SEM showed a considerable change in morphology; the sputtered material surface having agglomerated nanocrystallites compared to the electrodeposited material, which had larger crystals. The bandgap energy of all materials was between 3.27 eV and 3.45 eV.

The mean bulk electrical resistivity of electrodeposited and sputtered i-ZnO was 6.9×10^{6} and 6.2×10^{7} Ω cm and decreased after Al addition to 3.4×10^{5} and 2.3×10^{5} Ω cm respectively. Although the resistivity decreased after doping for materials deposited using both techniques the lowest resistivity reported in the literature for sputtered material is considerably lower than these values.

Arsenic, phosphorus and silver were added to the ZnO electrolytes to attempt p-type doping of the material. Although XRD and optical spectroscopy were used to characterise the crystallographic and optical properties, it was not expected that these techniques would demonstrate any change compared to the i-ZnO. As expected no changes were observed and therefore the results were not included. All layers characterised using PEC exhibited n-type electrical conductivity. It is well documented that p-type electrical conductivity of ZnO is difficult to achieve.

Chapter 6 Electrodeposited Copper Indium Diselenide

6.1 Introduction

The majority of literature reports the electrodeposition of $CuInSe_2$ or CuInGaSe2 absorber materials for solar cells from aqueous media at room temperature. The advantages associated with the use of water include low temperature deposition, low-cost, non-toxicity of the medium and simplicity of operation. Disadvantages include hydrogen evolution, which may cause pin-holes, and the possibility of hydroxide formation at the cathode. Although low temperature deposition is an advantage in terms of cost, the crystallinity of the material is reduced, impacting the performance of the device. Post-deposition heat-treatment of electrodeposited layers is required before device fabrication to improve the crystallographic and electrical properties. The annealing step is usually carried out in a Se atmosphere to prevent loss of Se from the surface of the film. The toxicity of annealing in a Se atmosphere continues to be a drawback to the processing of $CuInSe_2$ and $CuInGaSe_2$ materials.

Use of non-aqueous media offers the possibility of allowing higher voltages to be applied without the hydrogen evolution at the cathode. Higher temperature deposition (>85°C) is also possible, which promotes improved crystallinity of the pre-annealed layer. There are few reports in the literature on the use of non-aqueous media for electrodeposition of $CuInGaSe_2$. Previously Bhattacharya *et al.* partially replaced the water with dimethyl sulfoxide (DMSO), which is a toxic organic solvent, to overcome this disadvantage [Bhattacharya *et al.* 1998]. Electrodeposition of Cu, In and Se from non-toxic ionic liquid ([BMP]Tf_2N) has previously been carried out by Zein El Abedin *et al.* at temperatures >100°C. Little improvement in the material properties was found despite the elevated deposition temperature [Zein El Abedin *et al.* 2007]. To the best of my knowledge there have been no publications reporting the electrodeposition of $CuInGaSe_2$ or $CuInSe_2$ from ethylene glycol ($HOCH_2CH_2OH$) and therefore this investigation was carried out to explore the possibility of improved structural, optical and electrical properties of the as-deposited material. The relatively high boiling point of 197.6°C of this medium and the relatively low toxicity are deemed significant advantages over previous publications.

Initial experiments were carried out to establish the feasibility of depositing $CuInSe_2$

from ethylene glycol. For the majority of the experiments a well established molarity often used for aqueous electrodeposition, was implemented. Cyclic voltammetry was used to establish a suitable voltage range and the structural and morphological properties of the layers were studied using XRD and SEM respectively. XRF and EDX analysis were used for compositional analysis of the layers. The thickness was measured using talysurf. In the following sections the results of growth of $CuInSe_2$ from ethylene glycol will be presented.

6.2 Experimental Procedure

$CuInSe_2$ precursor layers were electrodeposited from an ethylene glycol solution containing copper chloride ($CuCl_3$), indium chloride ($InCl_3$), selenium tetrachloride ($SeCl_4$) and lithium chloride (LiCl). The explored molarities are presented in Table 6.1.

Table 6.1. Precursor molarities used for electrodeposition of $CuInSe_2$ from ethylene glycol.

	$CuCl_3$ (mM)	$InCl_3$ (mM)	$SeCl_4$ (mM)	LiCl (M)
Concentration 1	6.00	8.00	8.00	0.50
Concentration 2	3.00	8.00	8.00	0.50
Concentration 3	2.56	2.40	4.47	0
Concentration 4	2.56	2.40	4.47	0.20

The solution was maintained at 150°C (± 2°C) throughout the deposition. Soda-lime glass coated with FTO having sheet resistance of 7 Ω/ □ (supplied by Pilkington Group Ltd.) was used as the cathode with area 2 cm^2. Prior to electrodeposition the substrates were cleaned ultrasonically in iso-propanol, rinsed in deionised water and dried with a nitrogen stream. A graphite plate was used for the anode with a selenium reference electrode (-0.40 V vs Ag/AgCl). Electrodeposition was carried out potentiostatically using a GillAC version 4 computerised potentiostat/galvanostat.

The cyclic voltammetry study was carried out with a scan speed of 10 mV s^{-1} to investigate and optimise the growth parameters. Layers were annealed using a Carbolite tube furnace with a central 10 cm region of guaranteed temperature. Se was introduced into the annealing atmosphere by addition of Se pellets to the sample holding box. The samples were loaded into the sample holding box and placed at one end of the tube furnace. The furnace was heated to 550°C at a rate of 1°C per minute; the tube was

evacuated and a stream of argon/5% hydrogen (Ar/5%H_2) gas was passed through the tube. When at temperature the sample box was positioned inside the 10 cm region for 20 minutes during which time the Se pellets evaporated. When the time elapsed the tube was moved to position the sample box outside the region held at 550°C and left to cool naturally.

The structural properties were investigated using XRD and SEM. Compositional analysis was carried out using EDX and XRF. The thickness was measured using a talysurf instrument.

6.3 Results and Discussion

6.3.1 Concentration 1

Figure 6.1 is a cyclic voltammogram of ethylene glycol at 150°C before the addition of the precursors. The curve is featureless which suggests the electrolyte should not present a problem during deposition in terms of any unwanted deposit. The increase in current density is most likely to be due to the breakdown of the electrolyte solution. Any water absorbed from the atmosphere will evaporate when the solution is heated to 150°C and therefore hydrogen evolution can be eliminated.

Figure 6.2 presents the cyclic voltammogram of ethylene glycol electrolyte containing 6 mM $CuCl_2$, 8 mM $InCl_3$, 8 mM $SeCl_4$ and 0.50 M LiCl. FTO coated glass substrates were connected to the cathode and the cyclic voltammogram was carried out with a scan rate of 10 mV s^{-1} at 150°C.

It should be noted that electrodeposition of ternary compounds such as $CuInSe_2$ is challenging due to the wide range of redox potentials of the elements. The potentials range from +0.750 V for Se, 0.340 V for Cu and -0.34 V for In vs NHE [Lincot *et al.* 2004].

The current density onset at 0.100 V to -0.400 V vs Se is due to the deposition of Se. The steep increase in current density at -0.400 V vs Se is likely to be the onset of Cu deposition which reacts with Se to form Cu-Se binary phases. As the deposition voltage becomes more negative it was expected that indium having a more negative redox potential will react with Cu-Se to form $CuInSe_2$ as explained by [Oliveira *et al.* 2002, Lincot *et al.* 2004]. Peak current density is reached at -0.800 V vs Se followed by a plateau up to -1.000 V vs Se. Another increase in current density at more negative

voltages than -1.000 V vs Se is likely to be due to a similar mechanism to that already indicated for Figure 6.1.

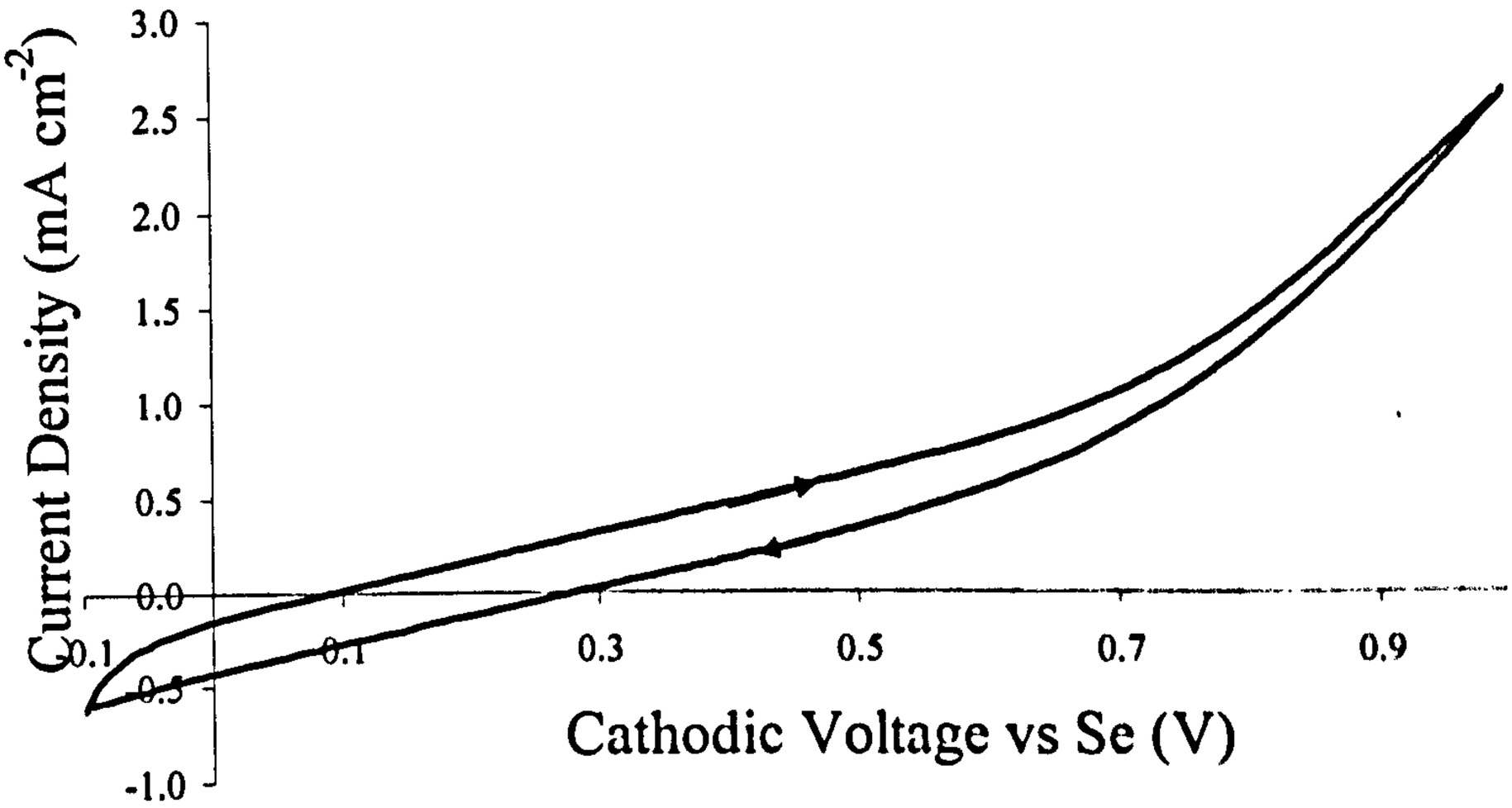

Figure 6.1. Cyclic voltammogram of ethylene glycol before the precursors were added having scan rate of 10 mV s^{-1}.

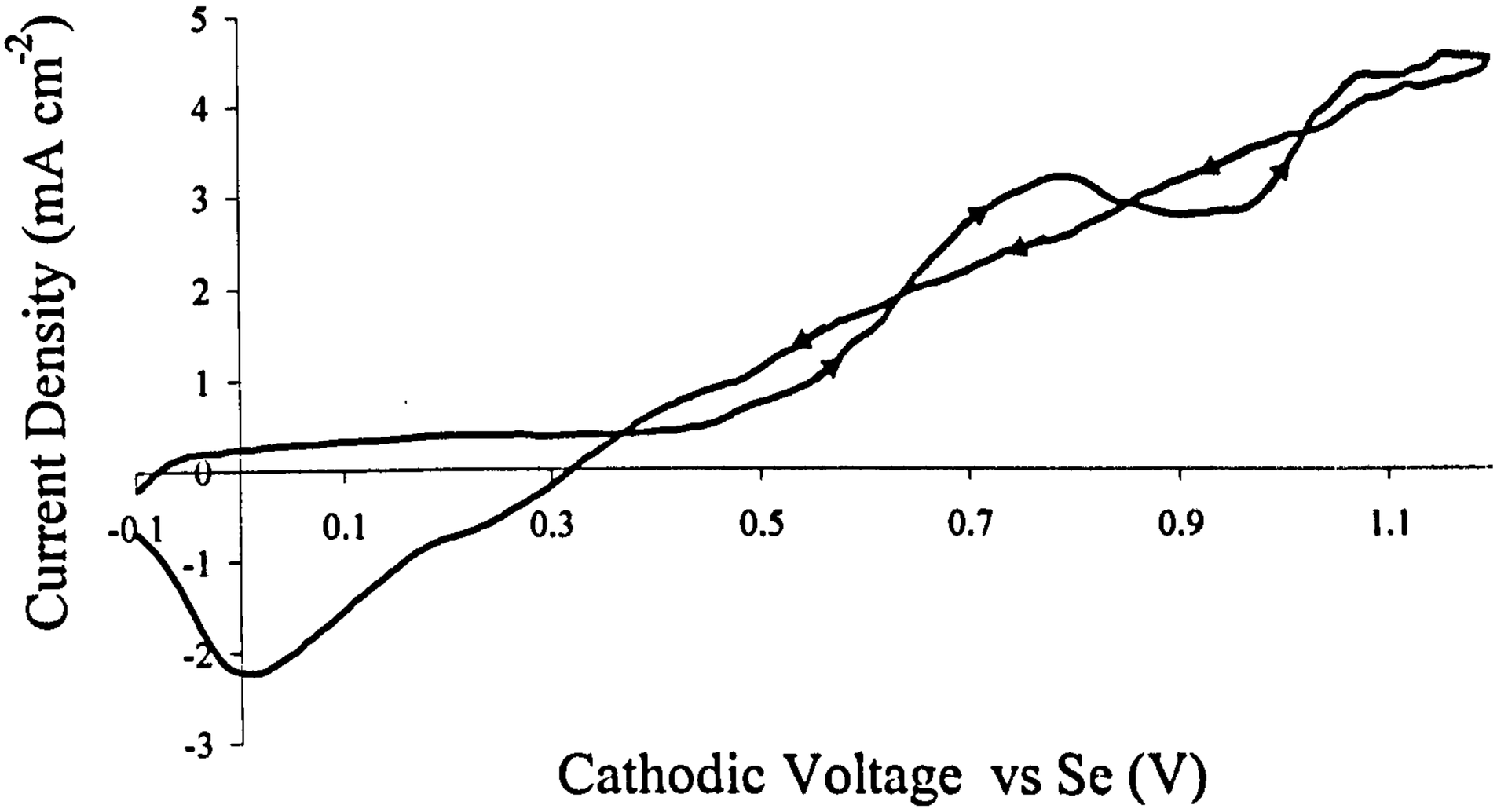

Figure 6.2. Cyclic voltammogram of ethylene glycol containing 6 mM $CuCl_2$, 8 mM $InCl_3$, 8 mM $SeCl_4$ and 0.5 M LiCl carried out with a scan rate of 10 mV s^{-1}.

To establish if the concentration of the precursors in the solution yield layers of suitable composition, XRF was carried out on a series of samples deposited over the voltage range from -0.650 to -1.100 V vs Se. Since the instrument is not calibrated, the atomic percentages are not exact. This investigation was carried out to establish the trend of composition with deposition voltage. The XRF study of the samples deposited from the solution containing 6 mM $CuCl_2$, 8 mM $InCl_3$, 8 mM $SeCl_4$ and 0.5 M LiCl is presented in Figure 6.3. The labels on the figure are used to describe the observations after deposition, such as appearance and nature of the layers.

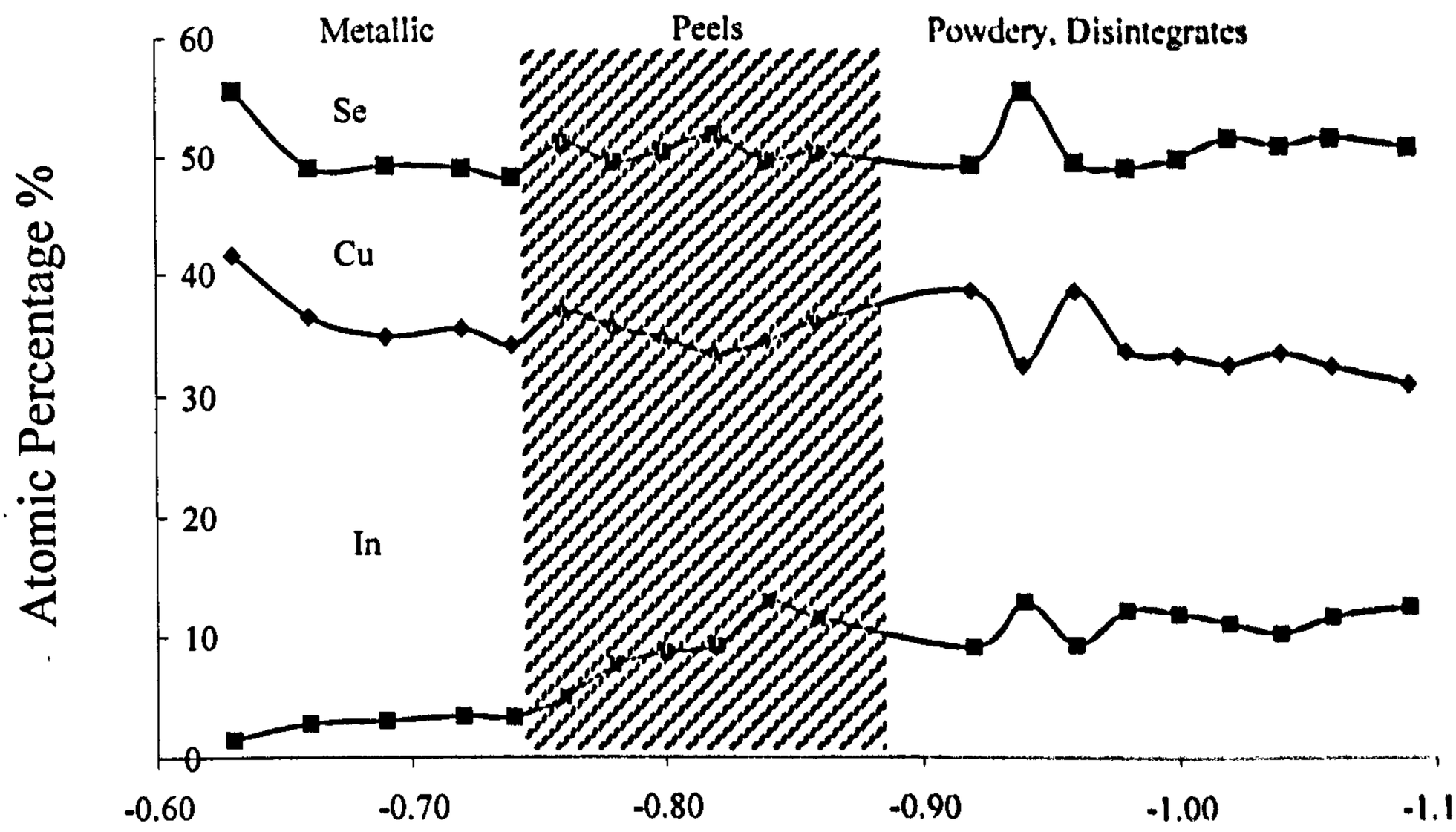

Figure 6.3. XRF study of a series of $CuInSe_2$ layers deposited from ethylene glycol containing 6 mM $CuCl_3$, 8 mM $InCl_3$, 8 mM $SeCl_4$ and 0.5 M LiCl. The labels describe the appearance and nature of the layers and the line is to indicate trend.

It was found that the Se content was almost constant for layers deposited at all growth voltages, where-as the Cu content decreased at more negative voltages away from the redox potential of Cu^{2+}. The indium content was almost constant although it increased at more negative deposition voltages due to the high overpotential. The atomic percentages of ~10 to 12% indium are less than required for a stoichiometric $CuInSe_2$ layer. Previous work has indicated the In content of $CuInSe_2$ to be 20 to 30% [Bhattacharya *et al.* 2005, Calixto *et al.* 2006].

The layers deposited at more positive deposition voltages were metallic in appearance due to Cu richness and were highly adhered to the substrate. Usually the

atomic percentage of Cu in the absorber layers is around 20 to 25% as determined using XRF [Kessler *et al.* 2005, Sene *et al.* 2008]. At more negative voltages than -0.800 V vs Se the layers were non-uniform, patchy and peeled on removal from the electrolyte. When the deposition voltages were more negative than -1.000 V vs Se the layers were powdery, non-adherent and often disintegrated after removal from the electrolyte. Previous studies reporting working solar cell devices contained lower Cu contents than found in this study.

6.3.2 Concentration 2

In order to reduce the amount of Cu in the layers a second experiment was performed, maintaining the In and Se molarities and halving that of Cu. An XRF study was carried out on a series of samples deposited over the voltage range -0.600 V to -1.050 V vs Se and is presented in Figure 6.4. The Se content of the layers increased from 60 to 70% as the Cu content decreased as a function of growth voltage. The Cu content decreased at more negative deposition voltages from ~40 to 20% from -0.600 to -1.050 V vs Se which is similar to the results obtained by Sene *et al.* [2008]. The In content of the layers increased from 1 to 10% with deposition voltages of -0.600 to -1.050 V vs Se. Although the Cu content decreased during this investigation the In content of the layers was insufficient for $CuInSe_2$ absorber materials.

As for concentration 1, similar observations were made during this study. Between -0.600 and -0.800 V vs Se the layers were metallic in appearance due to Cu richness and were highly adhered to the substrate. At more negative voltages than -0.800 V vs Se the layers were non-uniform dark and powdery and peeled on removal from the electrolyte. Sene *et al.* previously attributed this observation to Se-rich, Cu-poor layers; indeed XRF (Figure 6.4) indicated the Cu content decreased at more negative deposition voltages in the present study [Sene *et al.* 2008].

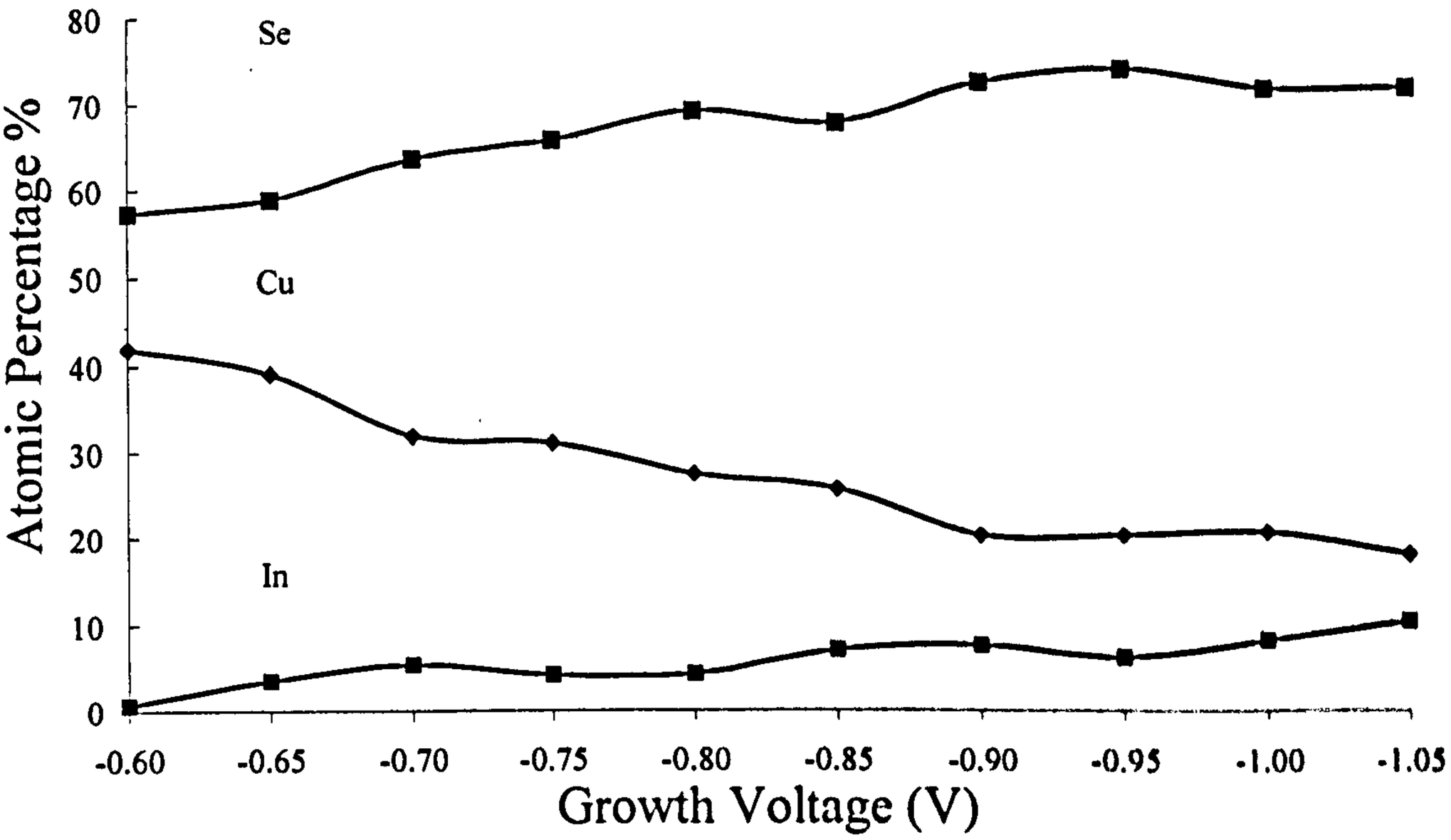

Figure 6.4. XRF study of a series of $CuInSe_2$ layer deposited from ethylene glycol containing 3 mM $CuCl_3$, 8 mM $InCl_3$, 8 mM $SeCl_4$ and 0.5 M LiCl.

6.3.3 Concentration 3 and 4

The fundamental difficulties associated with the deposition of uniform, consistent and well adhered layers from electrolytes using concentrations 1 and 2 lead to the use of an established precursor concentration often used for aqueous electrodeposition [Calixto *et al.* 2006]. An additional study was also carried out using this recipe to establish the effect of LiCl on the composition of the layers. Concentrations 3 contains LiCl and concentration 4 is without LiCl; the results are presented below.

6.3.3.1 Electrodeposition

Figure 6.5 presents the cyclic voltammogram of ethylene glycol electrolyte containing 2.56 mM $CuCl_2$, 4.80 mM $InCl_3$, 4.47 mM $SeCl_4$ and 0.20 M LiCl obtained using two different reference electrodes. FTO coated glass substrates were attached to the cathode with a scan rate of 10 mV s^{-1} at 25°C. The reason for this choice of temperature was three-fold; the Ag/AgCl reference electrode cannot be used above 80°C and at elevated temperature the rate of reaction is increased causing features on the cyclic voltammogram to deteriorate. When carried out at room temperature an

accurate comparison with the cyclic voltammogram obtained from an aqueous solution containing the same precursors could be made. The cyclic voltammograms were carried out with respect to (a) Ag/AgCl +0.220 V vs NHE and (b) Se reference (-0.400 V vs Ag/AgCl) electrodes as indicated in Figure 6.5. There is a voltage shift of approximately 0.400 V between the cyclic voltammogram curves obtained using the Ag/AgCl and Se reference electrodes. Figure 6.6 presents a cyclic voltammogram from an aqueous system for comparison.

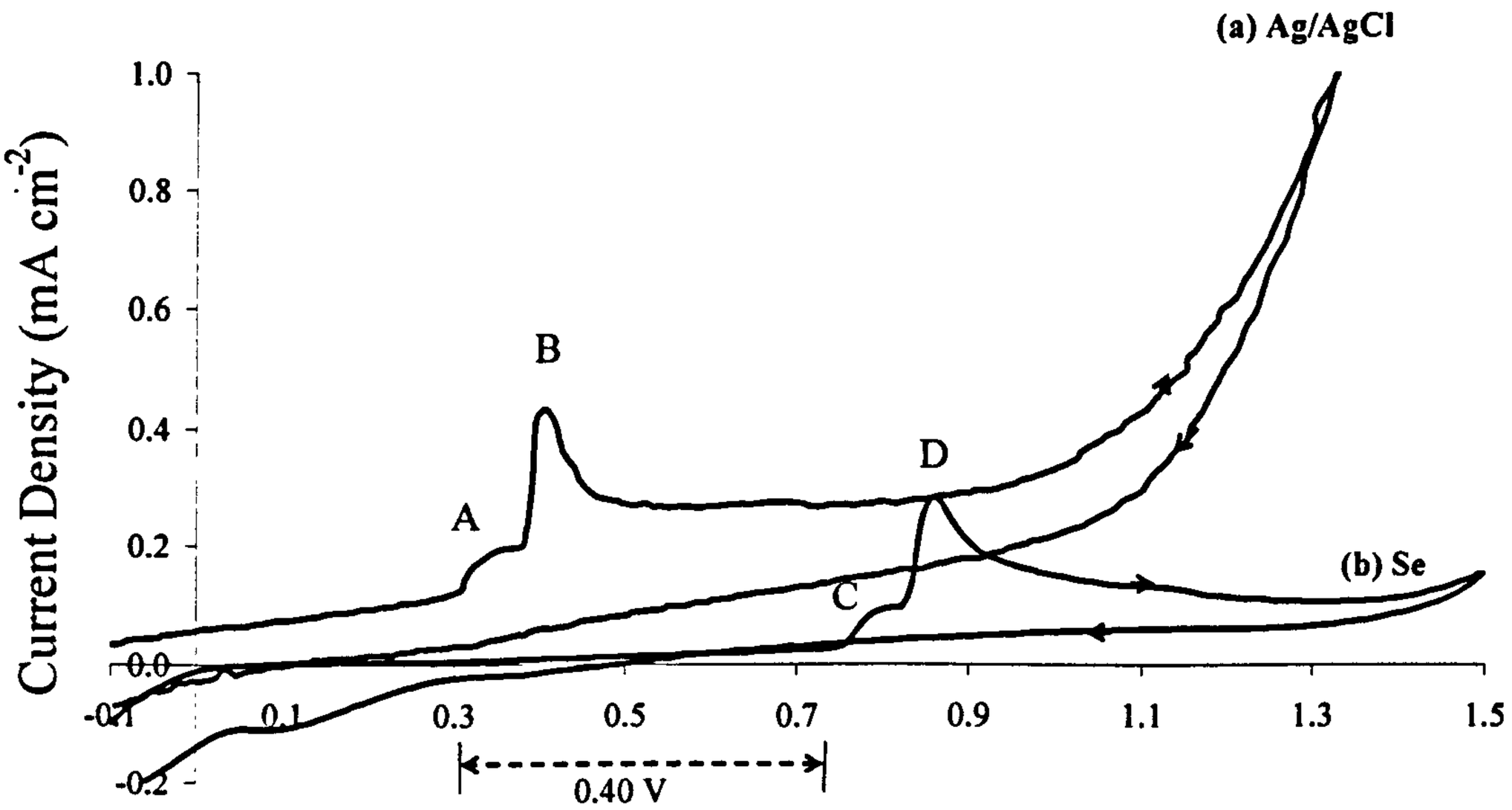

Figure 6.5. Cyclic voltammogram curves with scan rate 10 mV s^{-1} of (a) Ag/AgCl and (b) Se reference electrodes at 25°C. The cyclic voltammogram shows a shift in voltage of the main peaks by 0.40 V vs Se compared to those vs Ag/AgCl reference electrode (arrows show direction of sweep).

The current onset of the non-aqueous system (Figure 6.5) begins at 0.10 V reaching a peak current at 0.30 V vs Ag/AgCl cathodic voltage. Regions labelled A and C between 0.30 to 0.35 V vs Ag/AgCl and 0.75 to 0.80 V vs Se are likely to be due to the formation of Cu-Se binary phases due to the relatively positive voltage. The prominent increase in cathodic current density from 0.35 to 0.40 V vs Ag/AgCl (region B) and 0.80 to 0.85 V vs Se (region D) is again likely to be due to the formation Cu-Se binary phases. According to Kemell *et al.* and Kessler *et al.* the composition of the layers is controlled by the Se^{4+}/Cu^{2+} ratio arriving at the electrode surface. However it is not

possible to deduce from this study which particular Cu-Se binary phases were formed as described in more detail in the Section 6.3.3.2 [Kemell *et al.* 2005, Kessler *et al.* 2005].

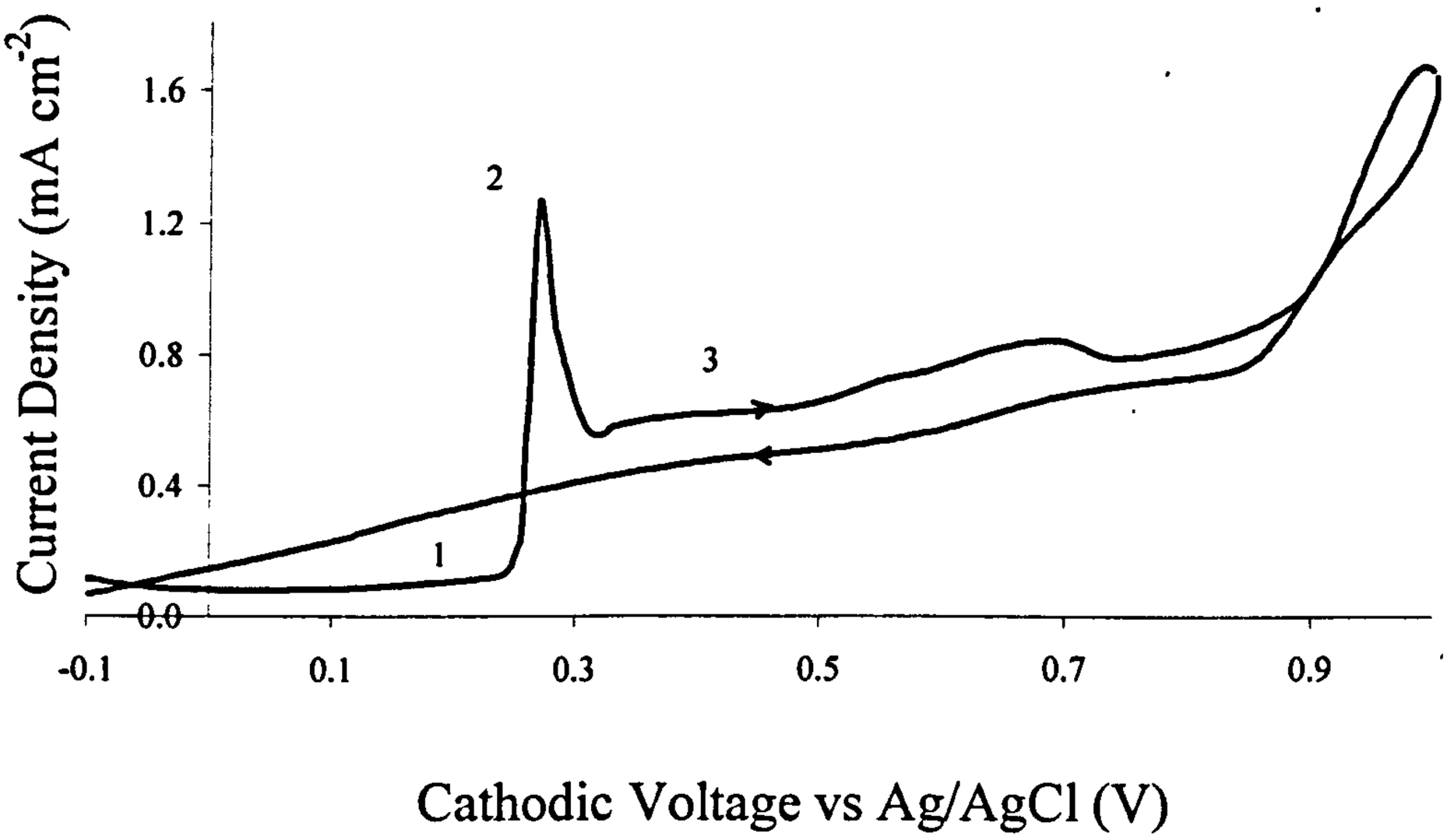

Figure 6.6. Cyclic voltammogram of aqueous solution containing same precursor concentrations as the ethylene glycol system for comparison.

The cyclic voltammogram from the aqueous system has a higher current density compared to the non-aqueous system. The literature clearly describes the reaction mechanism at regions labelled 1 to 3 in Figure 6.6 for growth from aqueous media. The region labelled 1 is due to the formation of Cu_3Se_2 and region 2 is the reduction of Cu_3Se_2 forming Cu_2Se; region 3 is due to the formation of $CuInSe_2$ with varying composition as established by [Mishra & Rajeshwar 1989, Calixto *et al.* 2005]. The cyclic voltammogram from the non-aqueous electrolyte is similar to the one obtained from the aqueous system containing the same precursor concentration, although region 1 of Figure 6.6 is less prominent than region A in Figure 6.5.

Figure 6.7 shows the effect of temperature on the cyclic voltammogram of ethylene glycol containing 2.56 mM $CuCl_2$, 4.80 mM $InCl_3$, 4.47 mM $SeCl_4$ and 0.20 M LiCl vs Se reference electrode. The cyclic voltammogram carried out at 25°C is the same as Figure 6.5 and has the lowest current density. The deposition current density increases with increasing bath temperature as indicated by the cyclic voltammogram carried out at 100°C and 150°C. The cyclic voltammogram at elevated temperature has fewer visible

features due to an increase in the rate of reaction mechanism. All layers characterised in the following sections were deposited at 150°C as this temperature gave the fastest deposition rate due to the highest current density. The aim of this work was to improve the grain size of the as-deposited material and explore the advantages of high temperature deposition.

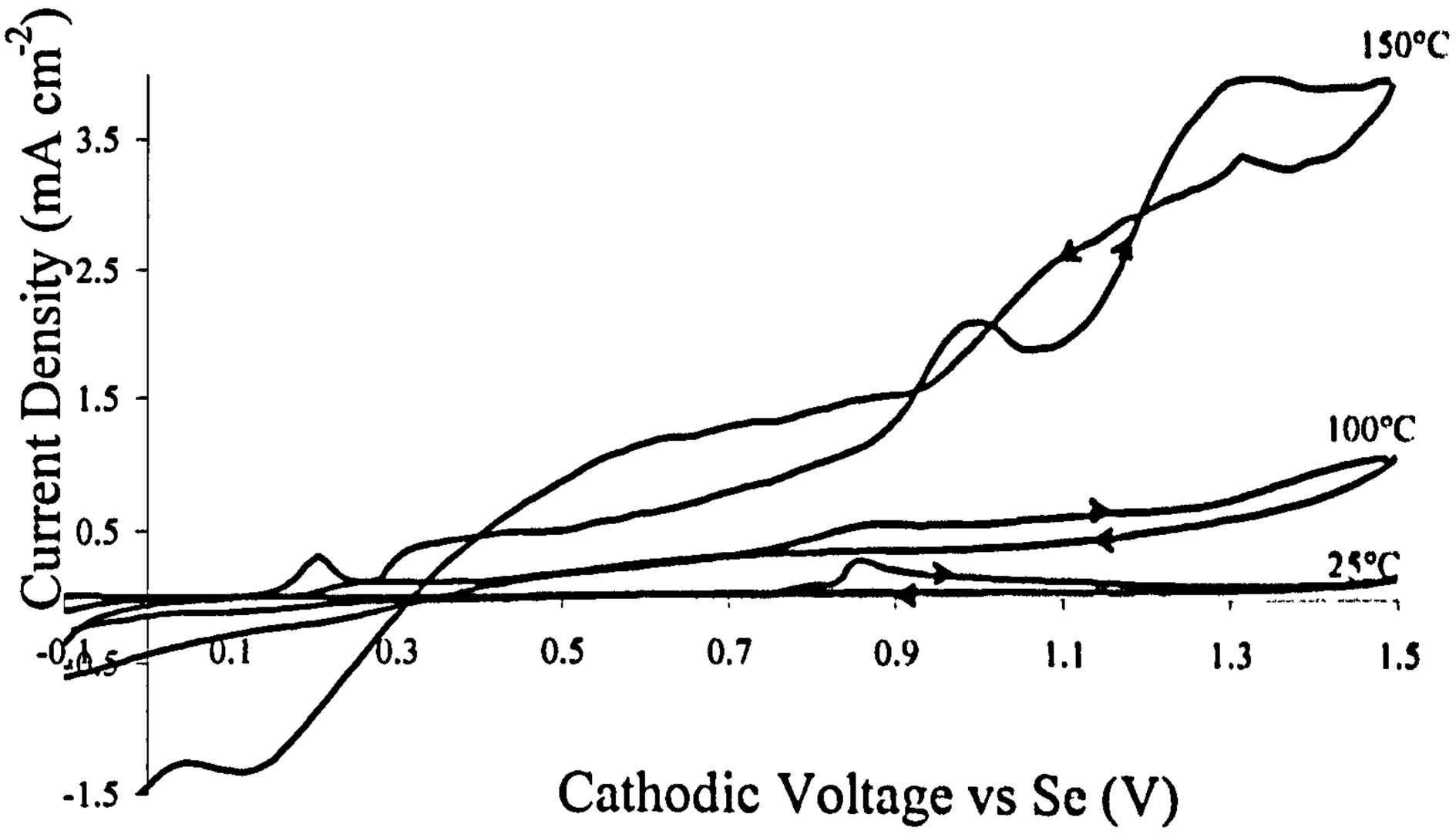

Figure 6.7. Effect of temperature on the cyclic voltammogram of ethylene glycol containing 2.56 mM $CuCl_2$, 4.80 mM $InCl_3$, 4.47 mM $SeCl_4$ and 0.20 M LiCl vs Se reference electrode at 25°C, 100°C and 150°C.

Figure 6.8 shows a typical thickness profile obtained for $CuInSe_2$ using a talysurf technique, scanning over a distance of 3.5 mm. The maximum film thickness is ~1.0 μm after a deposition time of 60 minutes. Using the Faraday relation (2.3) described in Chapter 2 the theoretical film thickness was calculated at ~1.1 μm, indicating over 90% Faradaic efficiency for non-aqueous electrodeposition of $CuInSe_2$. An SEM cross-section was taken for a $CuInSe_2$ layer deposited for 120 minutes and is presented in Figure 6.9. The thickness was determined at ~2.0 μm which suggests the deposition rate did not decrease significantly with time.

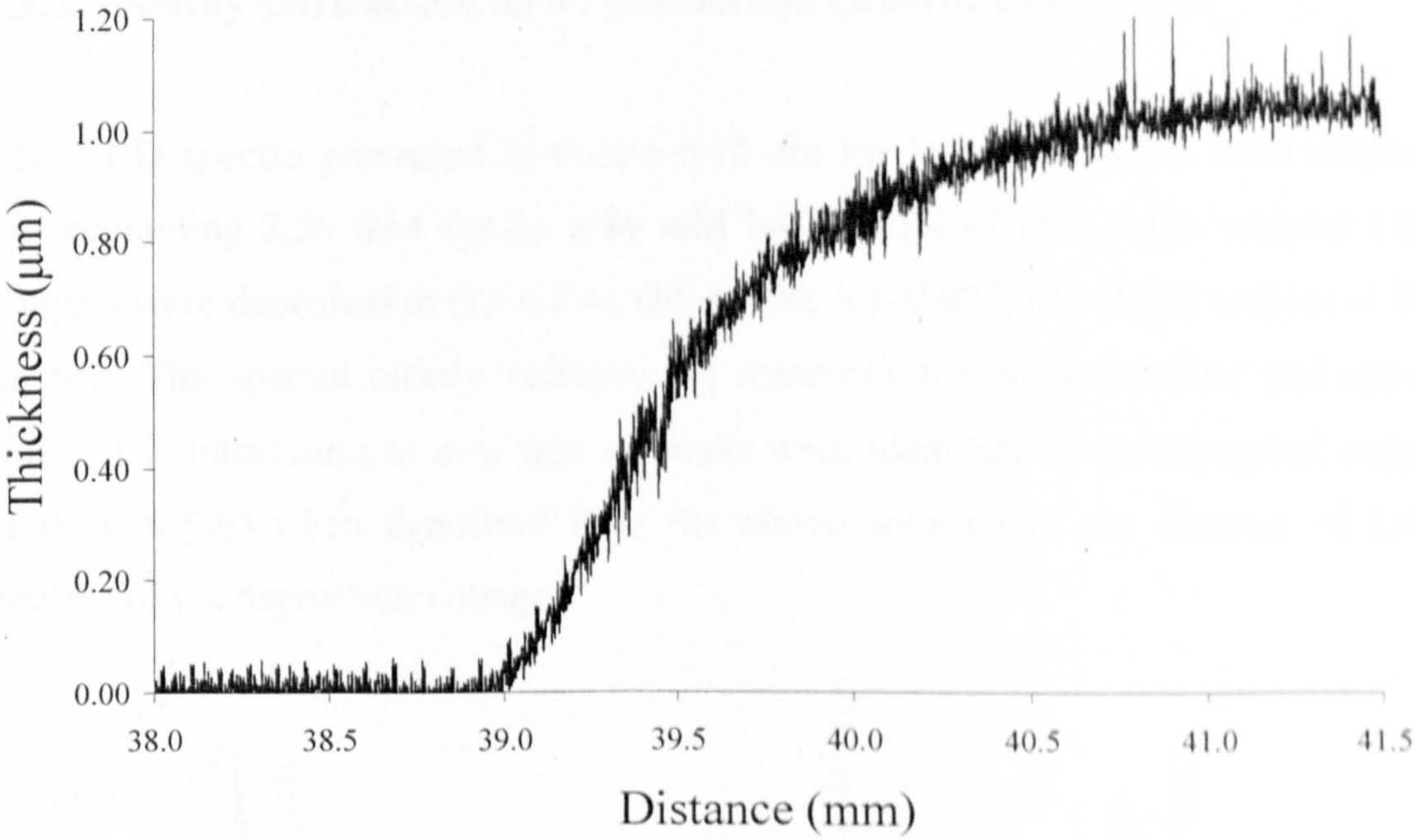

Figure 6.8. Thickness measurement of $CuInSe_2$ using talysurf showing the film to be ~1.0 μm after deposition for 60 minutes.

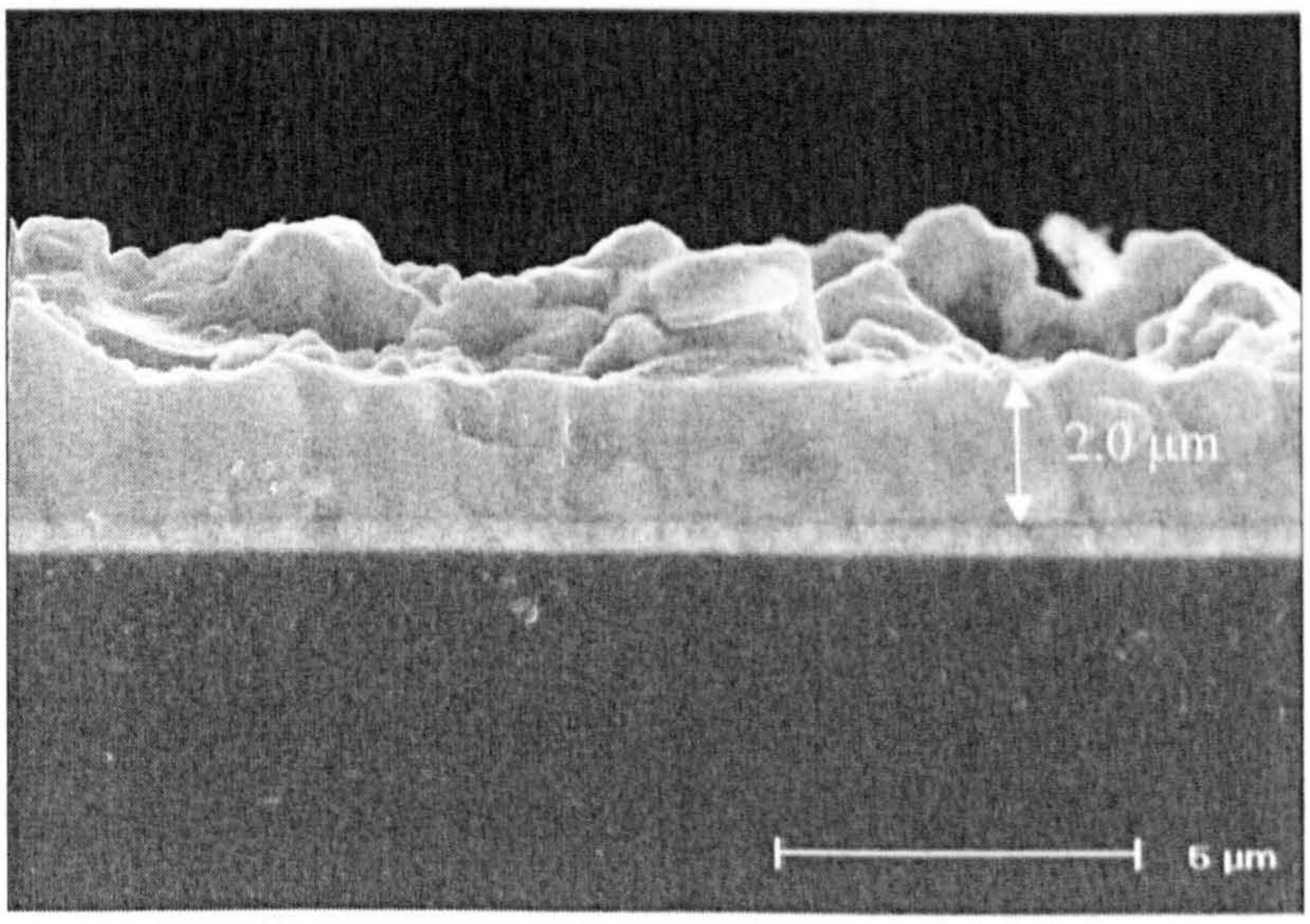

Figure 6.9. SEM cross-section of a $CuInSe_2$ layer deposited for 120 minutes, having a thickness of 2.0 μm.

6.3.3.2 X-Ray Diffraction as a Function of Growth Conditions

The XRD spectra presented in Figure 6.10 are for layers deposited from ethylene glycol containing 2.56 mM $CuCl_2$, 4.80 mM $InCl_3$ and 4.47 mM $SeCl_4$ without LiCl. The layers were deposited at (a) -0.850, (b) -0.900, (c) -0.925, (d) -0.950 and (e) -1.000 V vs Se. The spectra clearly indicates all materials are polycrystalline and appear similar. It is interesting to note that all peaks were identified to be tetragonal copper selenide (Cu_3Se_2) when deposited from the above solution in the absence of LiCl, regardless of the deposition voltage.

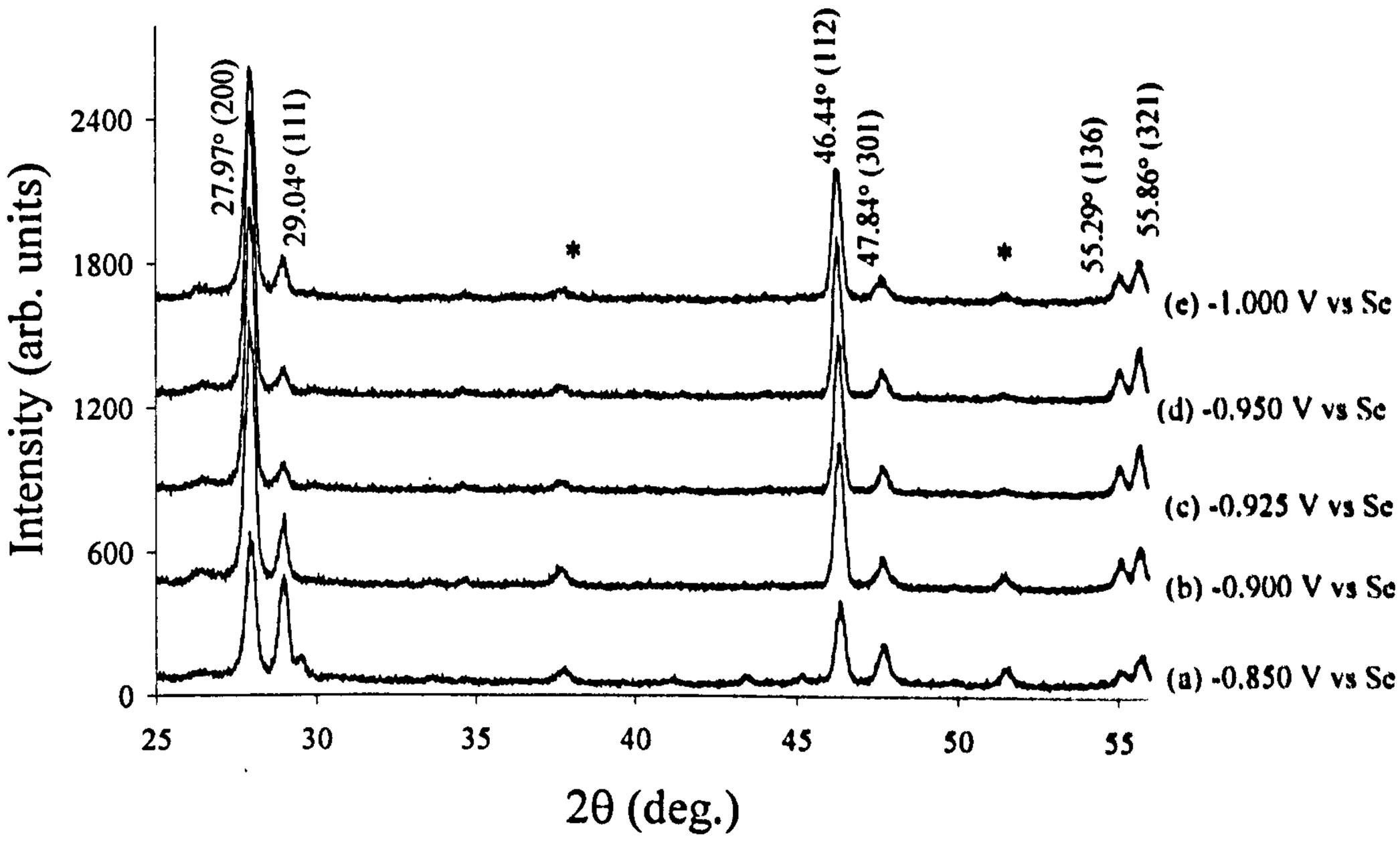

Figure 6.10. XRD spectra of layers electrodeposited at (a) -0.850, (b) -0.900, (c) 0.925, (d) -0.950 and (e) -1.000 V vs Se from 2.56 mM $CuCl_2$, 4.80 mM $InCl_3$ and 4.47 mM $SeCl_4$ without LiCl; all spectra were identified to be tetragonal Cu_3Se_2.

Table 6.2 presents the XRD data compared to the standard data for tetragonal Cu_3Se_2 obtained from the online Daresbury Chemical Database Service [Milman 2002]. Peaks arising from the FTO coated substrate are indicated by an asterisk (*). The average grain size was calculated using the Scherrer relation (2.5) at 22 nm. The lattice parameters were calculated for tetragonal Cu_3Se_2 using the tetragonal d-spacing equation 2.7 in Chapter 2, at a=6.425 Å and c=4.334 Å, which are close to the standard values of a=6.402 Å and c=4.279 Å [Milman 2002]. The difference in parameters may

be due to lattice strain or due to the experimental error in standard and observed d-spacing.

Table 6.2. XRD data representative of all XRD spectra presented in Figure 6.10. Layers were deposited from ethylene glycol containing 2.56 mM $CuCl_2$, 4.80 mM $InCl_3$ and 4.47 mM $SeCl_4$ without LiCl and were identified to be from tetragonal Cu_3Se_2.

2θ (deg.)		d-Spacing (Å)		Miller Indices	Compound
Standard	Observed	Standard	Observed	(hkl)	
27.84	27.97	3.212	3.190	(200)	Cu_3Se_2
28.67	29.04	3.115	3.075	(111)	Cu_3Se_2
37.91	37.91	2.374	2.373	(200)	SnO_2
46.94	46.44	1.936	1.956	(112)	Cu_3Se_2
47.58	47.84	1.911	1.902	(301)	Cu_3Se_2
51.96	51.59	1.760	1.772	(211)	SnO_2
55.09	55.29	1.662	1.662	(136)	Cu_3Se_2
55.96	55.86	1.642	1.648	(321)	Cu_3Se_2

XRD of the layers deposited from the electrolyte containing 0.2 M LiCl, indicated in Figure 6.11, show a different story to Figure 6.10. All layers indicated in Figures 6.10 and 6.11 are as-deposited. The layers were electrodeposited at (a) -0.850, (b) -0.900, (c) -0.925, (d) -0.950 and (e) -1.000 V vs Se.

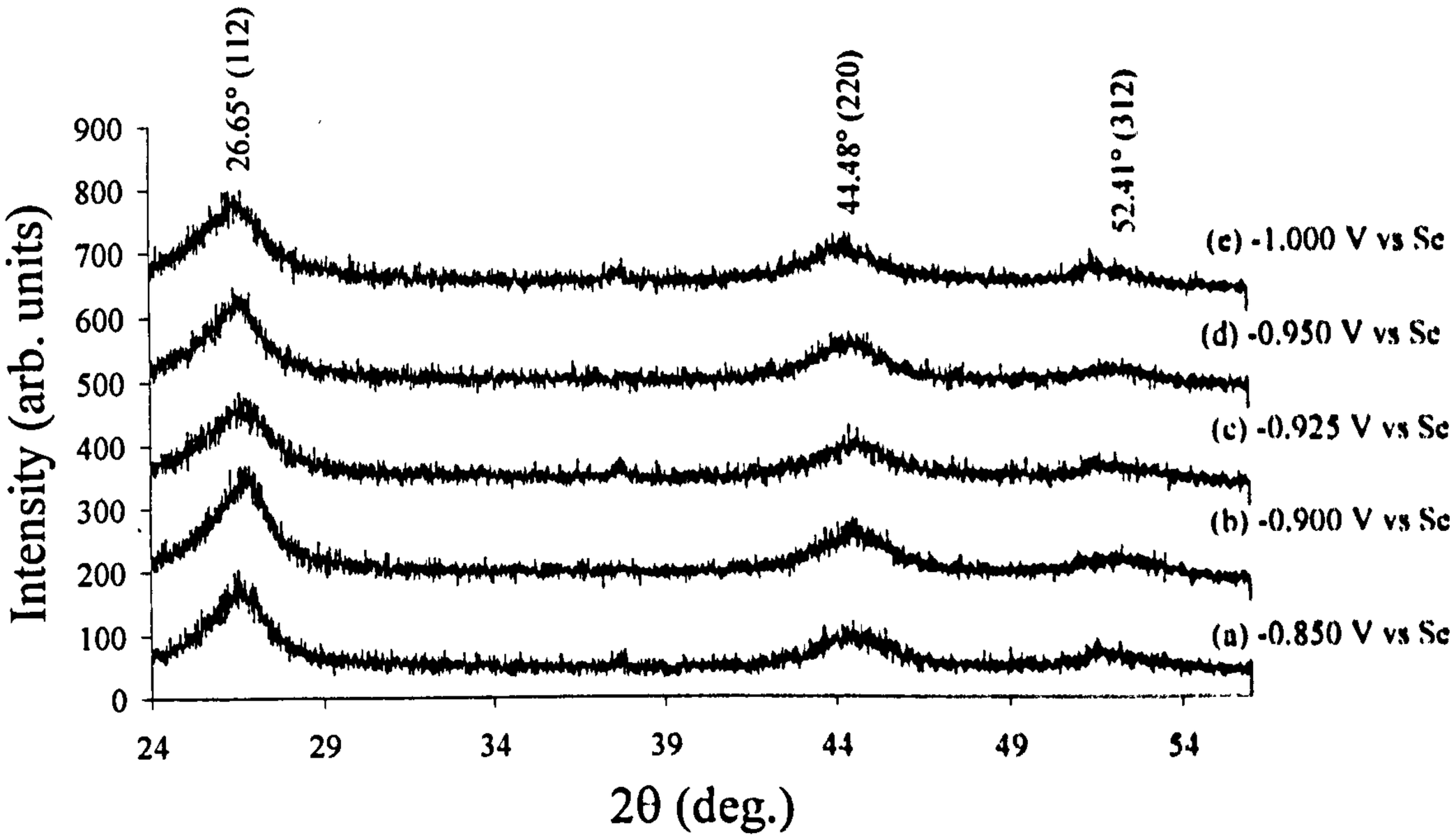

Figure 6.11. XRD spectra of material electrodeposited at (a) -0.850, (b) -0.900, (c) -0.925, (d) -0.950 and (e) -1000 V vs Se reference electrode, with the addition of 0.2 M LiCl to the solution. All peaks were identified to match closest to tetragonal $CuInSe_2$.

Table 6.3. XRD data representative of all XRD spectra presented in Figure 6.11, obtained from the XRD study of layers electrodeposited from ethylene glycol solution containing 2.56 mM $CuCl_2$, 4.80 mM $InCl_3$, 4.47 mM $SeCl_4$ and 0.2 M LiCl. All peaks were identified to match closest to tetragonal $CuInSe_2$.

2θ (deg.)		d-Spacing (Å)		Miller Indices
Standard	Observed	Standard	Observed	(hkl)
26.65	26.65	3.349	3.352	(112)
44.28	44.48	2.041	2.037	(220)
52.43	52.41	1.748	1.746	(312)

There is little apparent variation in the XRD spectra as a function of growth voltage. It is clear the addition of LiCl significantly altered the compound formed at the cathode. This confirms the function of LiCl as a supporting electrolyte to aid the availability of free In^{3+} and deposition of $CuInSe_2$. Without LiCl in the electrolyte indium did not deposit as indicated by Figure 6.10. When LiCl was present in the solution indium deposited and $CuInSe_2$ formed (Figure 6.11). It is known that LiCl is effective in aiding $CuInSe_2$ electrodeposition the exact mechanism remains unknown.

Table 6.3 indicates all peaks were identified to match closest to the tetragonal $CuInSe_2$ phase, compared to the standard data obtained from the Daresbury Chemical Database Service [Schorr & Geandier 2006]. The average grain size for $CuInSe_2$ was calculated at 5.0 nm using the Scherrer relation (2.5), which is one order of magnitude less than the value calculated for Cu_3Se_2. The nanocrystalline nature of the layers is unexpected considering the elevated solution temperature of 150°C. The broad width of the peaks suggests that the material is comprised of a mixture of compounds including $CuInSe_2$ and secondary Cu-Se binary phases [Mullan CA 1997, Lincot *et al.* 2004, Kessler *et al.* 2005,].

It should be noted that the XRD peaks match with numerous standard data files which overlap for $CuInSe_2$ and several Cu-Se binary phases. The broadness of the XRD peaks indicates low crystallinity and a mixture of compounds of $CuInSe_2$ and other Cu-Se binary phases. This is a drawback of the XRD technique for analysis of single compounds. Chassaing *et al.* also observed the XRD analysis was not straightforward reporting a variation in composition with deposition voltage [Chassaing *et al.* 2008]. Figure 6.12 and 6.13 illustrates the similarity in peak position of $CuInSe_2$ and Cu-Se binary phases from standard data files making identification of single phases difficult.

The lattice parameters for $CuInSe_2$ were calculated using the tetragonal d-spacing equation described in Chapter 2 (2.7). The values of a=5.795 Å and c=11.655 Å are close to the standard values of a=5.851 Å and c=11.726 Å obtained from the Daresbury Chemical Database Service [Schorr & Geandier 2006]. Table 6.4 presents the standard XRD data corresponding to Figure 6.12, which has been expanded between 2θ=24-29° to produce Figure 6.13.

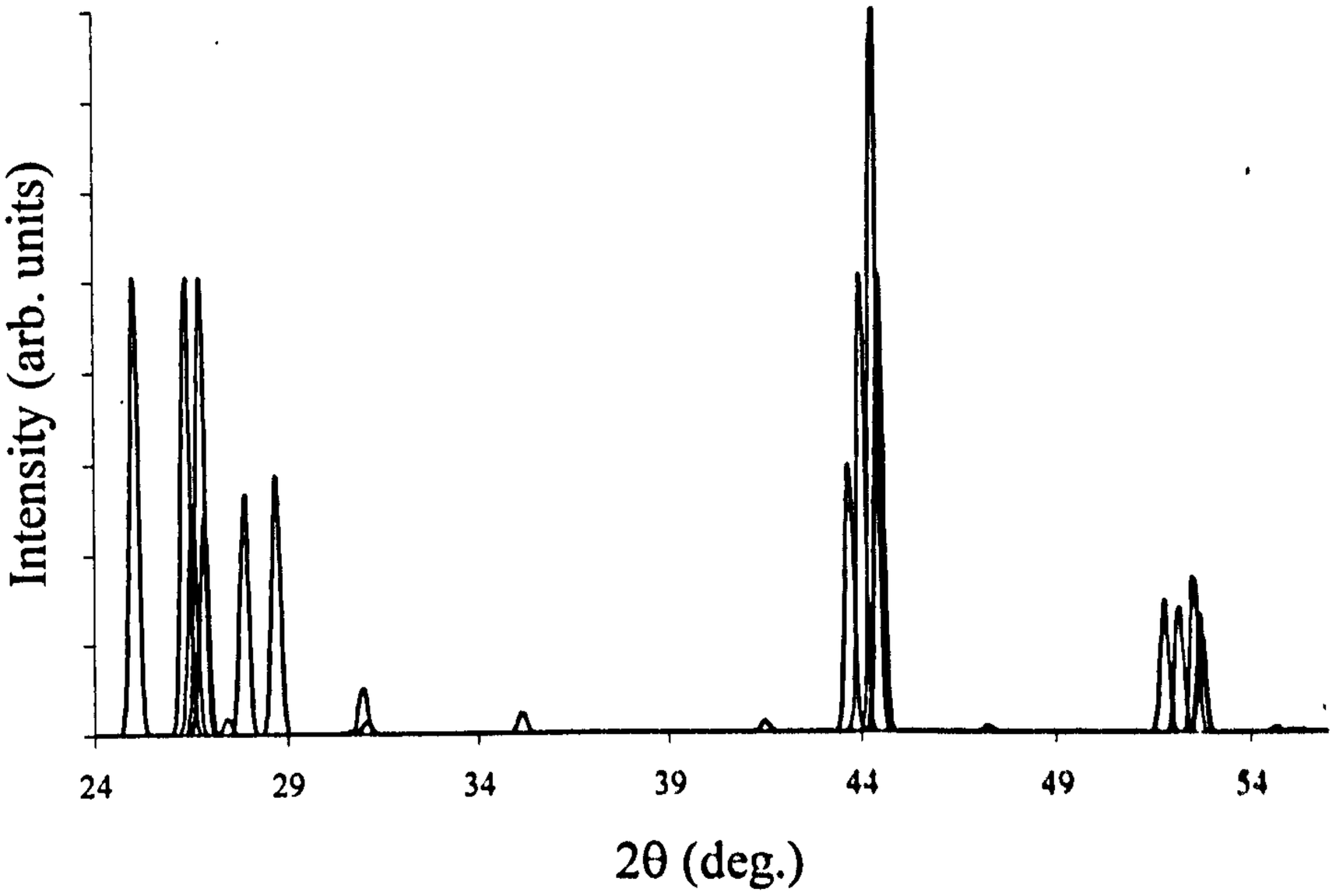

Figure 6.12. Standard XRD data for $CuInSe_2$ and Cu-Se binary phases.

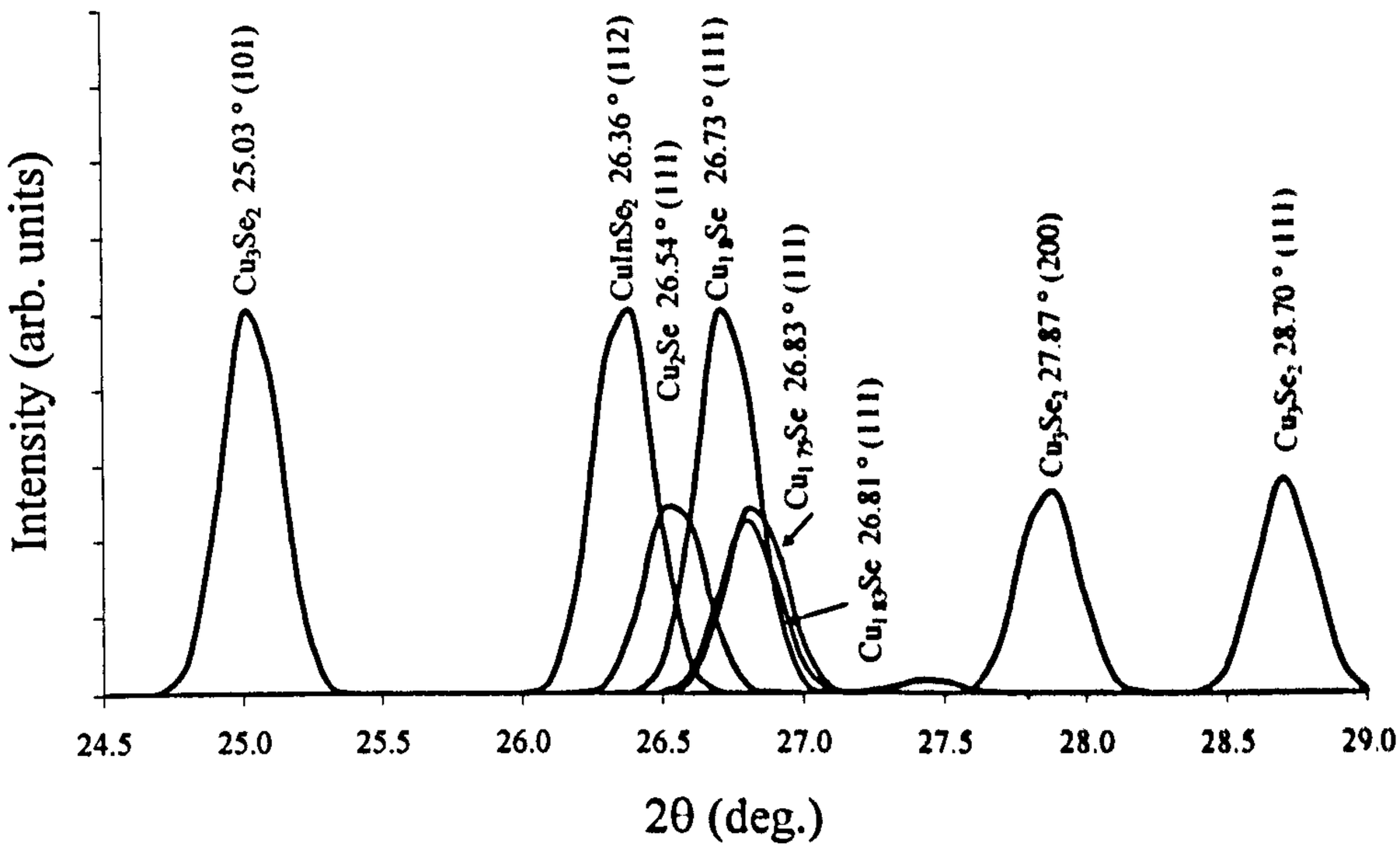

Figure 6.13. Expansion of standard XRD spectra presented in Figure 6.12 for $CuInSe_2$ and Cu-Se binary phases indicating the similarity in peak position of each compound.

Table 6.4. Standard XRD data of $CuInSe_2$ and Cu-Se binary compounds indicating the similarity in the peak position.

2θ (deg.)	d-spacing (Å)	(hkl)	Compound	Reference
26.36	3.380	(112)	$CuInSe_2$	Schorr & Geandier (2006)
26.83	3.322	(111)	$Cu_{1.75}Se$	Skomorokhov *et al.* (2006)
26.54	3.358	(111)	Cu_2Se	Machado *et al.* (2004)
26.73	3.334	(111)	$Cu_{1.8}Se$	Machado *et al.* (2004)
26.81	3.325	(111)	$Cu_{1.83}Se$	Bikkulova *et al.* (2003)
26.55	3.357	(101)	CuSe	Milman (2002)
25.03	3.557	(101)	Cu_3Se_2	Milman (2002)
27.87	3.201	(200)	Cu_3Se_2	Milman (2002)
28.70	3.114	(111)	Cu_3Se_2	Milman (2002)

6.3.3.3 X-ray Diffraction as a Function of Annealing Temperatures

The effect of annealing on the XRD spectra of $CuInSe_2$ has been investigated to assess the change in crystallographic properties. Figure 6.14 demonstrates the change in XRD spectra of a layer deposited at -0.900 V vs Se for (a) as-deposited and (b) annealed $CuInSe_2$ with annealing conditions of 450°C for 20 minutes in a Se atmosphere. Table 6.5 presents the XRD data representative of both spectra. The broader peaks of the as-deposited XRD indicate a mixture of compounds are likely to be present in the layer which cannot be distinguished as discussed in Section 6.3.3.2. The increase in intensity of the peaks indicates the material has become more ordered and preferentially orientated in the (112) plane. The reduction of the FWHM corresponds to an increase in grain size which increased by a factor of 4, as confirmed by the Scherrer relation as presented in Table 6.6.

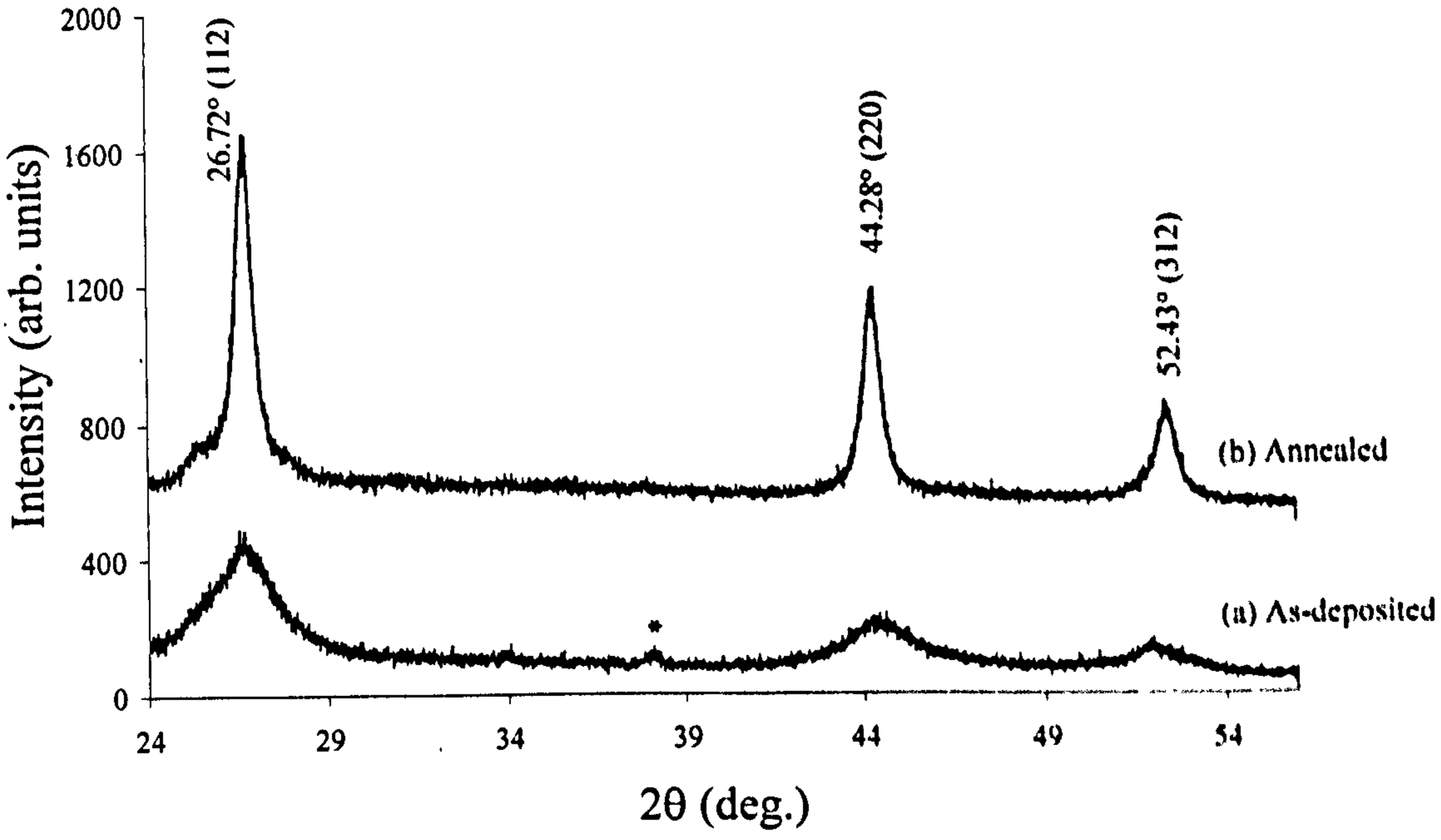

Figure 6.14. XRD spectra of (a) as-deposited and (b) annealed $CuInSe_2$ electrodeposited at -0.900V vs Se.

Table 6.5. XRD data of as-deposited and annealed $CuInSe_2$ electrodeposited at -0.900 V vs Se.

2θ (deg.)		d-Spacing (Å)		Miller Indices	Compound
Standard	Observed	Standard	Observed	(hkl)	
26.65	26.72	3.342	3.337	(112)	$CuInSe_2$
37.84	38.13	2.357	2.360	(200)	SnO_2
44.28	44.33	2.044	2.044	(220)	$CuInSe_2$
52.43	52.48	1.744	1.744	(116)	$CuInSe_2$

Table 6.6. Variation of grain size before and after annealing for $CuInSe_2$ determined using the Scherrer relation.

Material	FWHM (deg.)	Grain Size (nm)
As-deposited	2.14	4.0
Annealed	0.51	16

The effect of the annealing temperature on the $CuInSe_2$ XRD spectra was investigated. Figure 6.15 indicates the peak intensity increased sequentially for layers annealed at (a) 350, (b) 450, (c) 550 and (d) 650°C for 20 minutes in a Se atmosphere. It is clear from the XRD spectra the peak intensities increased as a function of annealing temperature, indicating improved crystallinity of the material. The annealing stage is an essential step to improve the material properties. When the grain size increases the number of grain boundaries decreases, reducing the defect density. As indicated in Figure 6.13 it is difficult to distinguish between $CuInSe_2$ and CuSe. It is likely the peaks in Figure 6.15 are reflections from both $CuInSe_2$ and Cu-Se binary phases; the peak arising from the SnO_2 substrate is labelled with an asterisk (*).

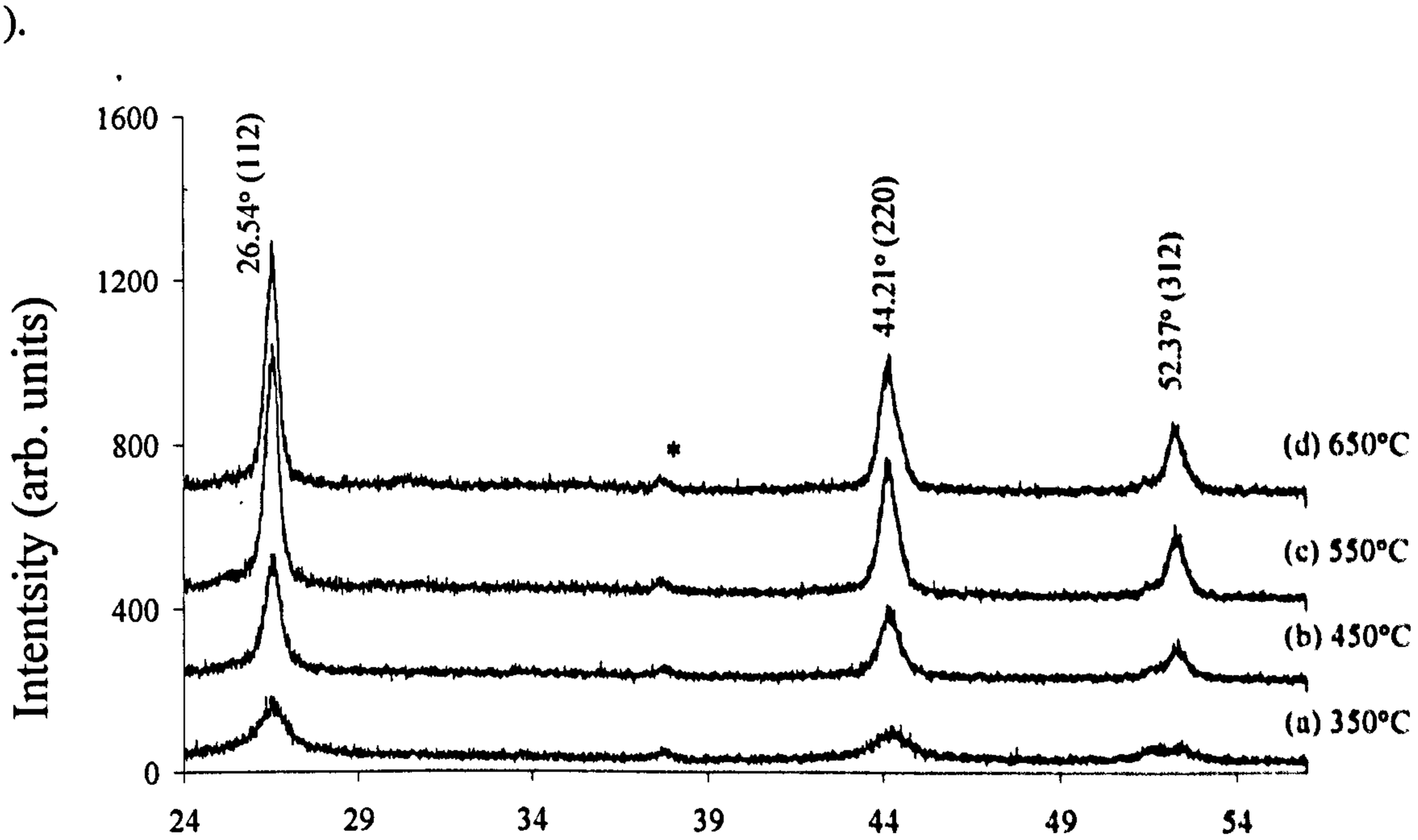

Figure 6.15. XRD diffractogram of $CuInSe_2$ or Cu-Se binary phases electrodeposited at -0.900 V vs Se and annealed for 20 minutes at (a) 350, (b) 450, (c) 550 and (d) 650°C, indicating improved crystallinity.

Table 6.7 presents the XRD data obtained from this study. The FWHM decreased with increasing annealing temperature with a concomitant increase in grain size as demonstrated by Table 6.8. Although the highest annealing temperature of 650°C produces the most crystalline material it was often observed the material did not withstand the highest temperatures and deteriorated, a loss of material was apparent by disintegration and peeling. It was concluded that 450°C improved the crystallinity and did not deteriorate the material as severely, therefore this temperature was chosen for subsequent annealing of the layers.

Table 6.7. XRD data representative of tetragonal $CuInSe_2$ electrodeposited at -0.900 V vs Se and annealed for 20 minutes at different temperatures as indicated by Figure 6.15, data representative of all spectra.

2θ (deg.)		d-Spacing (Å)		Miller Indices	Compound
Standard	Observed	Standard	Observed	(hkl)	
26.65	26.54	3.342	3.359	(112)	$CuInSe_2$ or Cu-Se
37.91	37.84	2.357	2.378	(200)	SnO_2
44.28	44.21	2.044	2.049	(220)	$CuInSe_2$ or Cu-Se
52.43	52.37	1.744	1.747	(312)	$CuInSe_2$ or Cu-Se

Table 6.8. Variation of FWHM and grain size of $CuInSe_2$ as a function of annealing temperature for a duration of 20 minutes.

Annealing Temperature (°C)	FWHM (deg.)	Grain Size (nm)
350	0.71	11
450	0.52	16
550	0.42	19
650	0.40	20

Complexities encountered during annealing made the processing of the CIS extremely difficult. The sequence of sample loading, heating and gas introduction caused a large temperature gradient on the furnace tube and cracking. Often adequate tube sealing was not established which prevented the vacuum production. Although the sample box was positioned outside the 10 cm temperature region heating of the sample during ramp up and ramp down was unavoidable, causing an over aggressive conditions and film sublimation. A more rapid ramp-up rate caused thermal shock to the tube due to the temperature gradient. A longer tube would have meant the sample could have

remained at room temperature until the furnace had reached 550°C although this was logistically impossible as the furnace needed to be under extraction and would not have fitted in the fume hood and again the tube would have suffered from thermal shock. These factors often resulted in partial or total sublimation of the layers and Se leakage from the furnace on cool down.

6.3.3.4 X-ray Fluorescence as a Function of Growth Conditions

An XRF study was carried out on a series of samples deposited from ethylene glycol containing 2.56 mM $CuCl_2$, 4.80 mM $InCl_3$ and 4.47 mM $ScCl_4$ both with and without 0.2 M LiCl. The variation in composition with and without LiCl is demonstrated in Figure 6.16. There is little variation in composition as a function of growth voltage as the trend is relatively uniform. It is clear from the figure there is a distinct change in the composition of the layers when LiCl was added to the electrolyte. The amount of indium and copper in the layers increases with the addition of LiCl. Indium increased from 2 to 7% with LiCl, although this remains inadequate as 20-30% In is required for working devices. The percentage of Se present in the layers decreased when LiCl was present in the electrolyte from 72 to 68%. The use of LiCl is well established in electrochemistry and is used as a supporting electrolyte, although the exact mechanism remains unclear [Calixto *et al.* 2006].

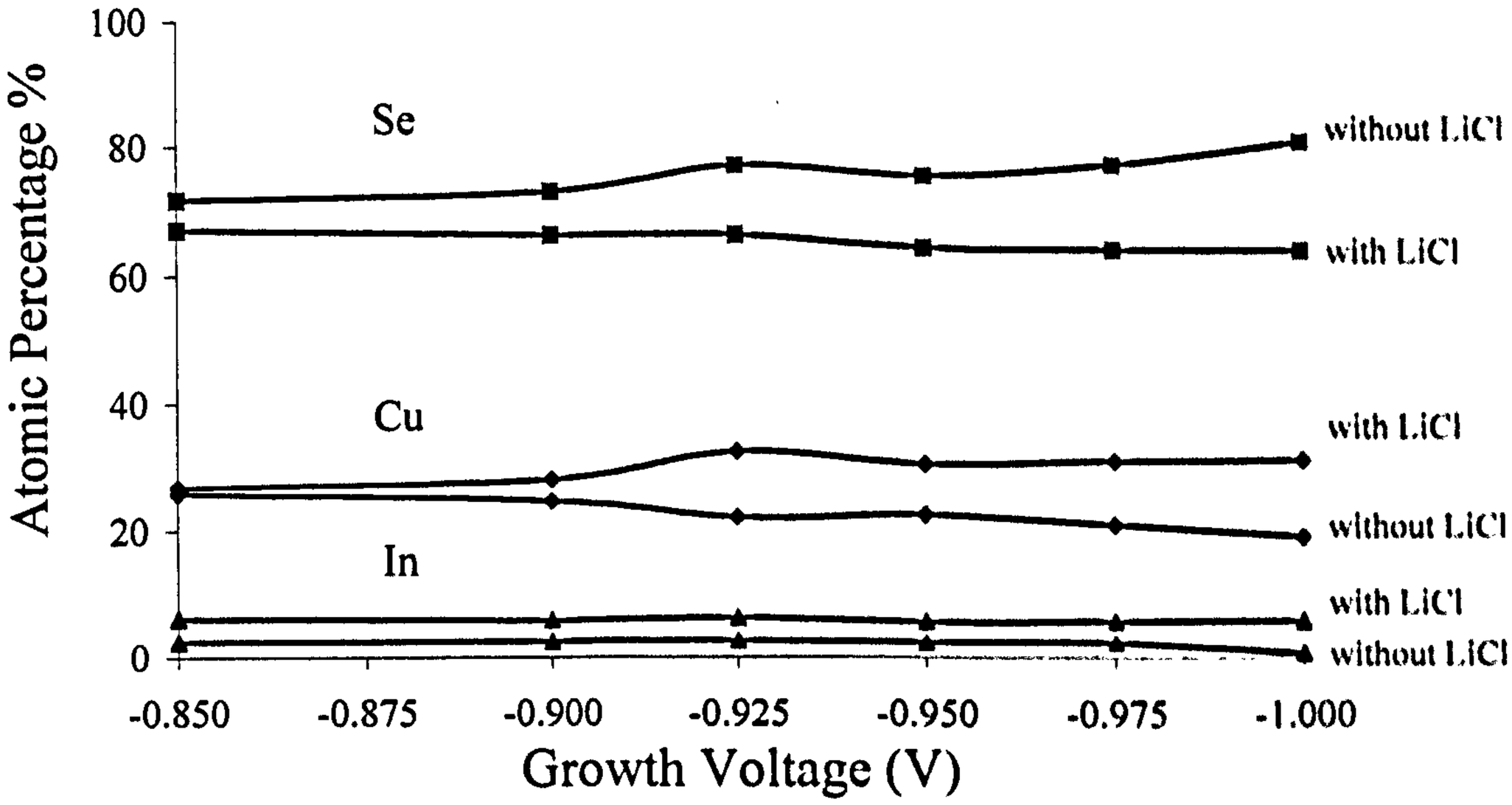

Figure 6.16. XRF of a series of layers deposited from ethylene glycol containing 2.56 mM $CuCl_2$, 4.80 mM $InCl_3$ and 4.47 mM $SeCl_4$ both with and without 0.2 M LiCl.

6.3.3.5 Energy Dispersive X-ray Analysis

EDX analysis was used to determine the bulk composition of the $CuInSe_2$ layers. The EDX analysis of the layer deposited at -0.800 V vs Se, presented in Figure 6.17 (a), identified the characteristic peaks of Cu and Se with a small In peak. The EDX of layers deposited at both -0.950 and -1.000 V vs Se were the same indicating Cu, In and Se to be present in the bulk as presented in Figure 6.17 (b). The Sn, O and Si peaks arise from the SnO_2-coated glass substrate.

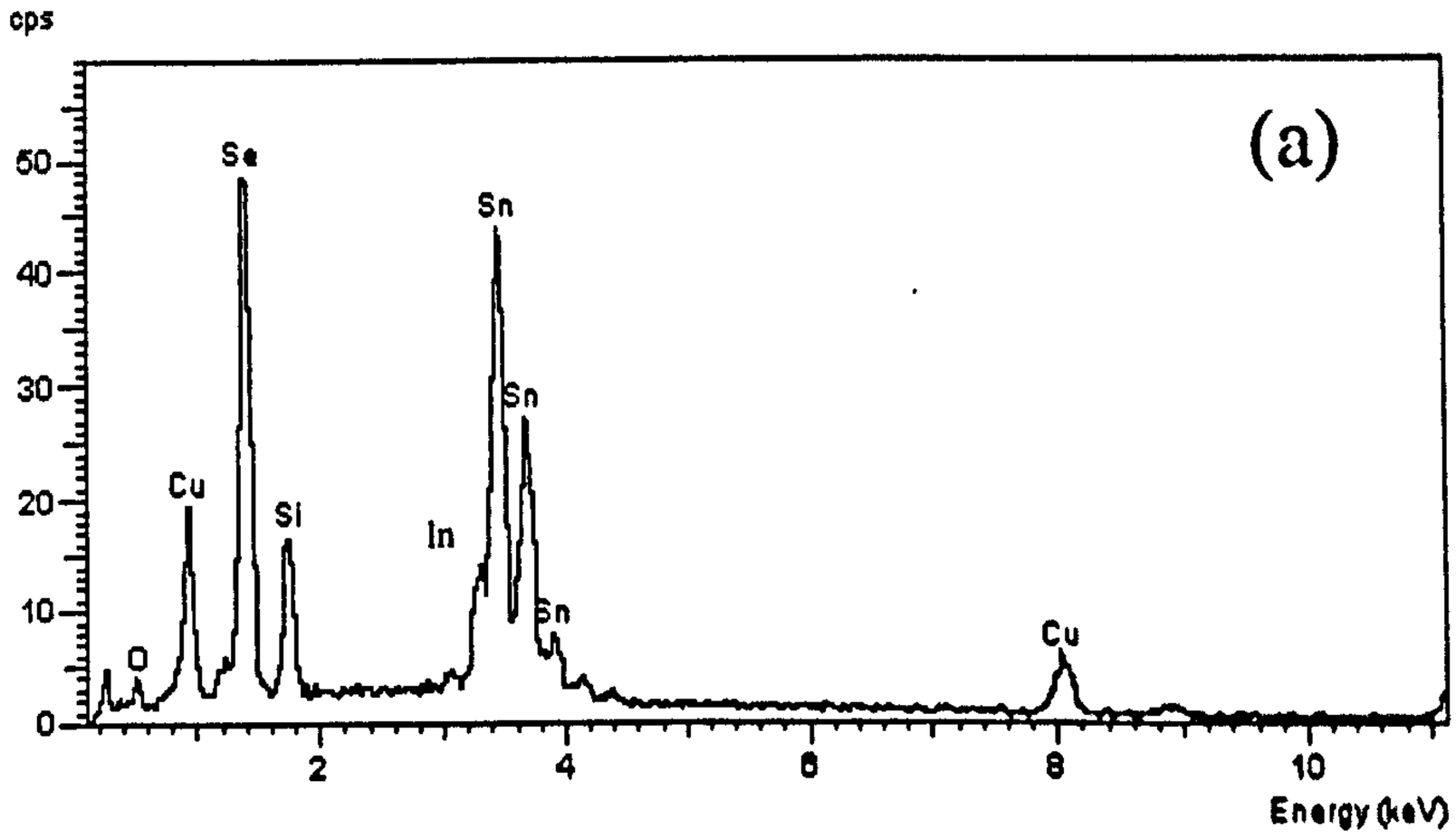

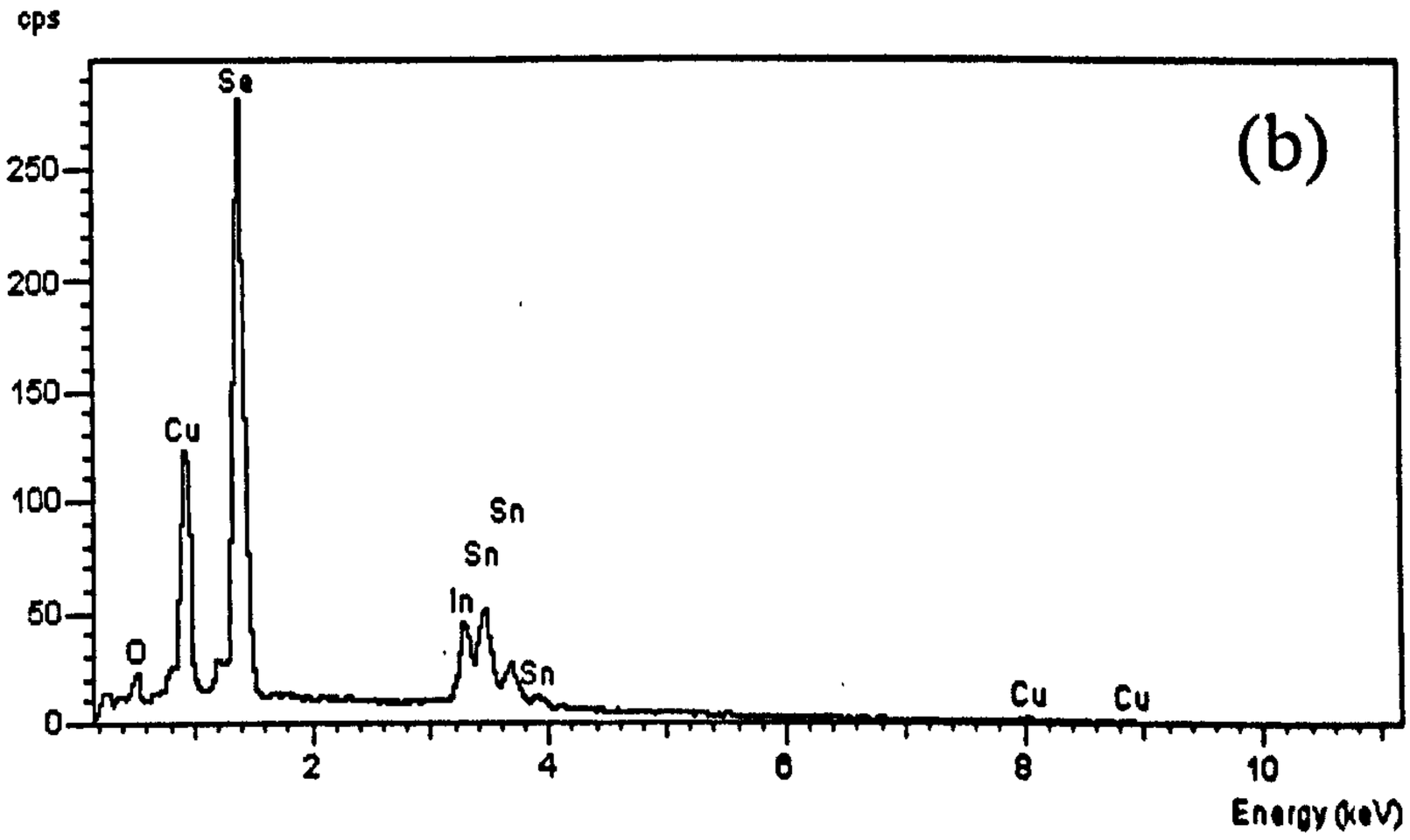

Figure 6.17. EDX analysis of layers deposited at 150°C at (a) -0.800 V vs Se indicating the presence of Cu In and Se in the bulk of the layer, (b) more In is incorporated into the layer with more negative deposition voltages of -0.950 and -1.000 V.

6.3.3.6 Scanning Electron Microscopy

SEM was carried out on selected layers in order to investigate the surface morphology. Figure 6.18 (a) presents the surface of the annealed layer deposited at -0.800 V vs Se is comprised of cauliflower shaped agglomerates around 1.0 μm in size with individual crystallites ~10 to 20 nm in size as indicated by the inset (Figure 6.18a). Similar morphology has previously been observed by [Oliveira *et al.* 2002, Calixto *et al.* 2006, Kois *et al.* 2006, Ihlal *et al.* 2007, Chassing *et al.* 2008]. According to EDX these structures contain Cu, In and Se elements insinuating $CuInSe_2$ formation although XRF suggests the presence of only 7% In at this growth voltage.

SEM of the layer deposited at -0.950 V vs Se is presented in Figure 6.18 (b) showing a different morphology compared to the film deposited at -0.800 V vs Se. The formation of larger crystallites is apparent with smoother appearance which may suggest a change in composition. The apparent crystallite size is around 0.5 to 1.0 μm. Figure 6.18 (c) presents the SEM image of the layer deposited at -1.000 V vs Se which has crystallite size of 0.2 to 0.5 μm with additional surface objects around 1.0 μm in size. Figure 6.18 (d) presented the enlarged SEM image of the layer shown in 6.18 (c).

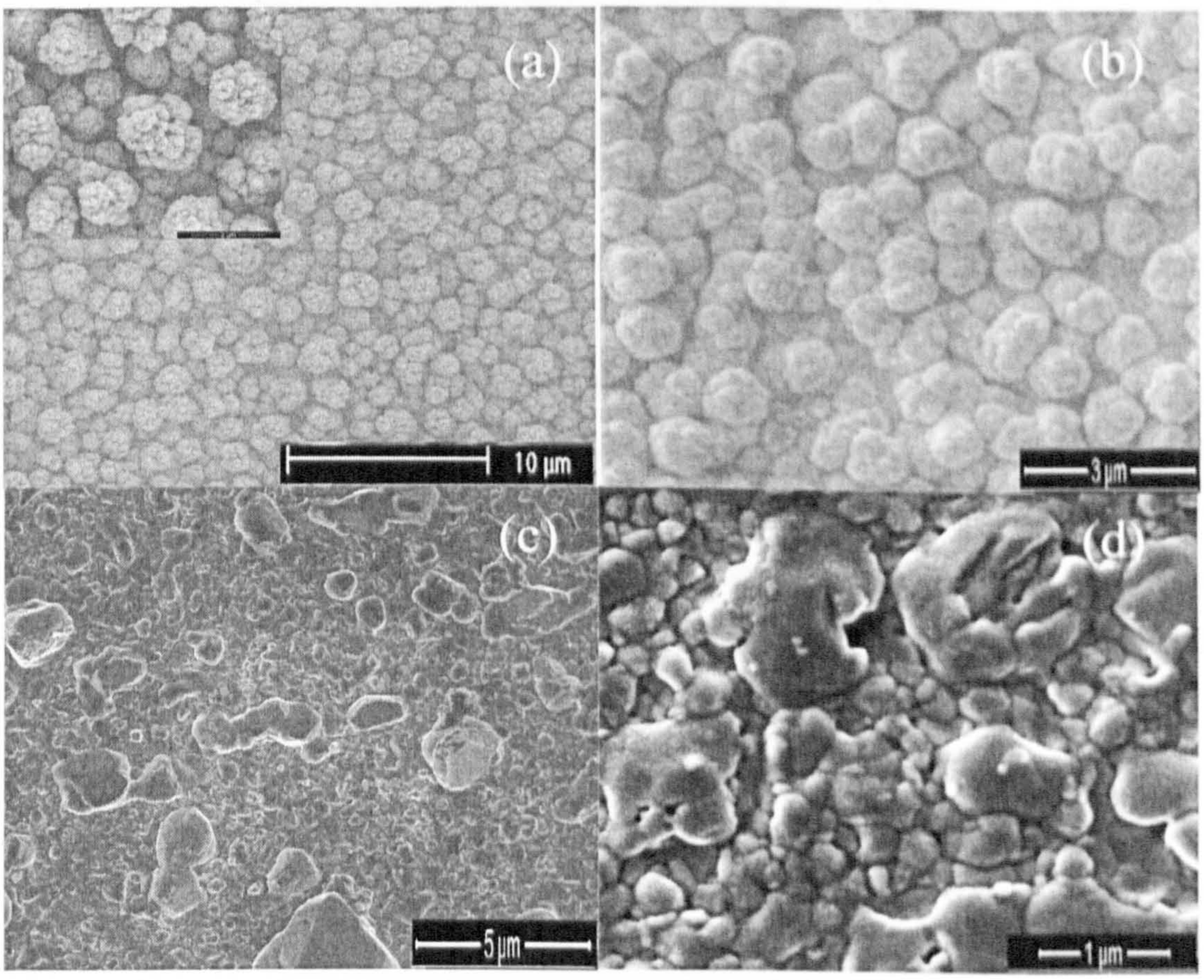

Figure 6.18. SEM micrographs of the layers electrodeposited from ethylene glycol at 150°C at voltages of (a) -0.800, (b) -0.950, (c) and (d) -1.000 V vs Se.

6.4 Discussion

This investigation was carried out to evaluate the possibility of producing $CuInSe_2$ precursor layers with improved crystallinity and properties compared to those grown at room temperature. Advantages include the possibility of reduced post-deposition processing such as lower temperature heat treatment and/or time. Various fundamental difficulties were encountered during the investigation leading to limited success of the

electrodeposition of $CuInSe_2$ from this medium. Although more than one precursor molarity was investigated this had little effect on the quality of the deposited material.

The initial reagent concentration 1 produced layers with excessive Cu as identified by XRF. The concentration of $CuCl_2$ reagent was halved and the XRF confirmed a concomitant reduction of Cu at% in the layers. Difficulties were encountered to obtain reproducible layers using concentrations 1 and 2. Layers deposited at relatively positive voltages between -0.600 and -0.800 V vs Se were metallic in appearance. XRF confirmed this material to be mainly comprised of Cu and Se, with 1<In<10 at%. At more negative deposition voltages between -0.800 V and -1.000 V vs Se the deposits were powdery/sludgy and rarely adhered to the substrate.

Concentration 3 and 4 were investigated, concentration 4 has previously been used for deposition of $CuInSe_2$ from aqueous medium producing device efficiencies of 6.2% [Calixto *et al.* 2006]. Layers were deposited from the solution both with (concentration 4) and without the presence of LiCl (concentration 3). Comparing the XRD and XRF investigations of the layers with and without LiCl indicated a significant change in the material properties. Both XRD and XRF indicated a much lower content of In in the layer deposited in the absence of LiCl. The XRD of layers deposited from solution containing LiCl indicated the formation of a different compound, matching closely to $CuInSe_2$ with secondary Cu-Se binary phases present. The In content in the layers remained insufficient for device fabrication after LiCl was added to the solution. EDX agreed with the XRF investigation identifying the presence of In in the layers deposited at -0.800, -0.950 and-1.000 V vs Se.

Difficulties were encountered when identifying the XRD peaks as numerous standard files have d-spacing which overlap making identification of single phases challenging. Broad peaks indicate a low degree if crystallinity and small grain size and it was envisaged that a mixture of compound of $CuInSe_2$ and secondary Cu-Se binary phases existed in the layers. After annealing the peak intensity increased and FWHM decreased indicating an increased degree of crystallinity and larger grain size.

Other difficulties were encountered during the annealing stage. A range of annealing temperatures was explored between 300 and 650°C. The annealing temperature was optimised at 450°C, above which the material often disintegrated and partially sublimed. Previous reports in the literature have suggested 450 to 550°C to be required for the recrystallisation of $CuInSe_2$ to occur [Lincot *et al.* 2004].

Further work would be needed to produce material of suitable quality for device fabrication from ethylene glycol. During this investigation no noticeable improvements were observed compared to layers deposited from aqueous solution in our laboratory. I would not recommend the use of this medium for further investigations and do not envisage that the non-aqueous growth route has a large amount of potential for the future development of CIS. Growth at 150°C did not improve the properties of the material. Due to the time-scale and deadlines stipulated by the funding body this work was suspended in favour of development of CdTe absorber materials. Being a binary semiconductor it is well known the electrodeposition of CdTe is simpler to form and a suitable material for device fabrication compared to ternary compounds such as $CuInSe_2$ [Lincot *et al.* 2004].

6.5 Conclusions

In conclusion ethylene glycol was used to electrodeposit $CuInSe_2$ with additional Cu-Se binary phases. The as-deposited material exhibited low-crystallinity as identified by XRD despite the elevated growth temperature of 150°C and thus required heat-treatment. The broad nature of the XRD peaks before and after annealing indicated the layers were comprised of multiple phases. It was confirmed that LiCl was required to aid the deposition of In as indicated by the XRF study, which identified the In content to increase at more negative deposition voltages. The quantity of In remained insufficient despite the presence of LiCl. The layers deposited at more positive deposition voltages were metallic and mainly Cu-Se binary phases. At more negative deposition voltages the formation of $CuInSe_2$ was confirmed although above -1.000 V vs Se the layers were often powdery and disintegrated on removal from the electrolyte. There were no noticeable improvements in the $CuInSe_2$ layers deposited from ethylene glycol compared to reports from aqueous media; which is less toxic and lower cost, therefore electrodeposition from aqueous solution is preferable.

Chapter 7 Electrodeposited Cadmium Telluride

7.1 Introduction

The majority of literature reports the electrodeposition of CdTe from aqueous media at elevated temperatures of between 60 to 85°C. Aqueous solution provides a low-cost medium for growth although the disadvantage is the low solubility of tellurium dioxide (TeO_2) which is known to control the rate of CdTe deposition. Use of CdTe absorber materials for solar cell devices is already proven technology with the production of 0.90 m^2 10.4% efficient solar panels by BP Solar Ltd. [Cunningham 2002].

The development of CdTe absorber materials in this project was carried out with the aim of producing a working solar cell device. Cyclic voltammetry was used to establish a suitable growth region and layers were characterised using XRD, SEM, optical spectroscopy and PEC. Devices were produced and tested using I-V measurements. The results of CdTe thin film characterisation and device measurements are presented in the following sections.

7.2 Experimental Procedure

Cadmium sulphide substrates deposited using CBD onto FTO were annealed in air for 20 minutes at 450°C. The surfaces were etched in glacial acetic acid for 3 minutes to remove surface oxides and rinsed in deionised water. Cyclic voltammetry and film growth were carried out using a GillAC computerised potentiostat/galvanostat instrument. Deposition was carried out potentiostatically in a three-electrode cell with a graphite plate counter electrode and saturated calomel reference electrode (SCE), with cadmium chloride ($CdCl_2$) solution instead of potassium chloride (KCl) solution.

The 150 ml of electrolyte contained 0.8 M cadmium sulphate ($3CdSO_4.8H_2O$), 600 ppm $CdCl_2$ and <50 ppm TeO_2. The pH of solution was adjusted to pH~2.00 using sulphuric acid (H_2SO_4). The electrolyte was purified at -0.600 V for 100 hours before film deposition. Although the salts used were 99.999% pure this purification stage was used to remove contaminants by applying a more positive deposition voltage than used to deposit CdTe. The temperature was maintained at 85°C throughout the experiments unless otherwise stated. A magnetic stirrer follower was used to enhance the deposition of Te, which is controlled by mass transport. All CdTe layers having area 2×3 cm^2 were deposited from the same Cd solution and Te was replenished as required. The Te was

added using a calibrated pipette from a solution containing 50 ppm TeO_2 when the current density dropped below 150 μA cm^{-2}.

Layers were annealed in a Carbolite furnace in air atmosphere at various temperatures as indicated in Section 7.3.2. The layers were annealed in air atmosphere for 20 minutes at 450°C before etching in a diluted potassium dichromate ($K_2Cr_2O_7$) solution, for 10 seconds to oxidise the surface, followed by reducing etch of 0.1M NaOH and 0.1M $Na_2S_2O_3.5H_2O$, for 2 minutes to remove excess oxide from the surface [Dharmadasa 1989, Sobiesierski 1988]. An array of electrical contacts was evaporated through a mask using Cu/Au with area 0.031 cm^2 (2 mm diameter contacts). The layers were studied using XRD, SEM, optical spectroscopy and I-V measurements were made of devices using a fully automated system.

7.3 Results and Discussion - Materials Properties

7.3.1 Electrodeposition

The cyclic voltammetry of the aqueous solution containing 0.8M of $3CdSO_4.8H_2O$ and 600 ppm $CdCl_2$ was carried out to determine the effect of the applied voltage on the deposition of Cd^{2+}. The cyclic voltammetry investigation was carried out using a CdS substrate at 85°C with scan rate 10 mV s^{-1}. The cyclic voltammetry presented in Figure 7.1 is featureless in the forward sweep direction. It was expected the current density would remain low and constant until the deposition voltage of Cd^{2+} was reached (-0.643 V vs SCE). The current density remained constant at <0.05 mA cm^{-2}, a small increase in current density was observed between 0.600 to 0.750 V vs SCE cathodic voltage, attributed to the deposition of elemental Cd. The steep increase in current density between 0.750 and 1.000 V vs SCE cathodic voltage was attributed to hydrogen evolution at the cathode and metallic Cd deposition. The large anodic peak between 0.400 and 0.650 V vs SCE is due to the stripping of elemental Cd deposited in the forward direction.

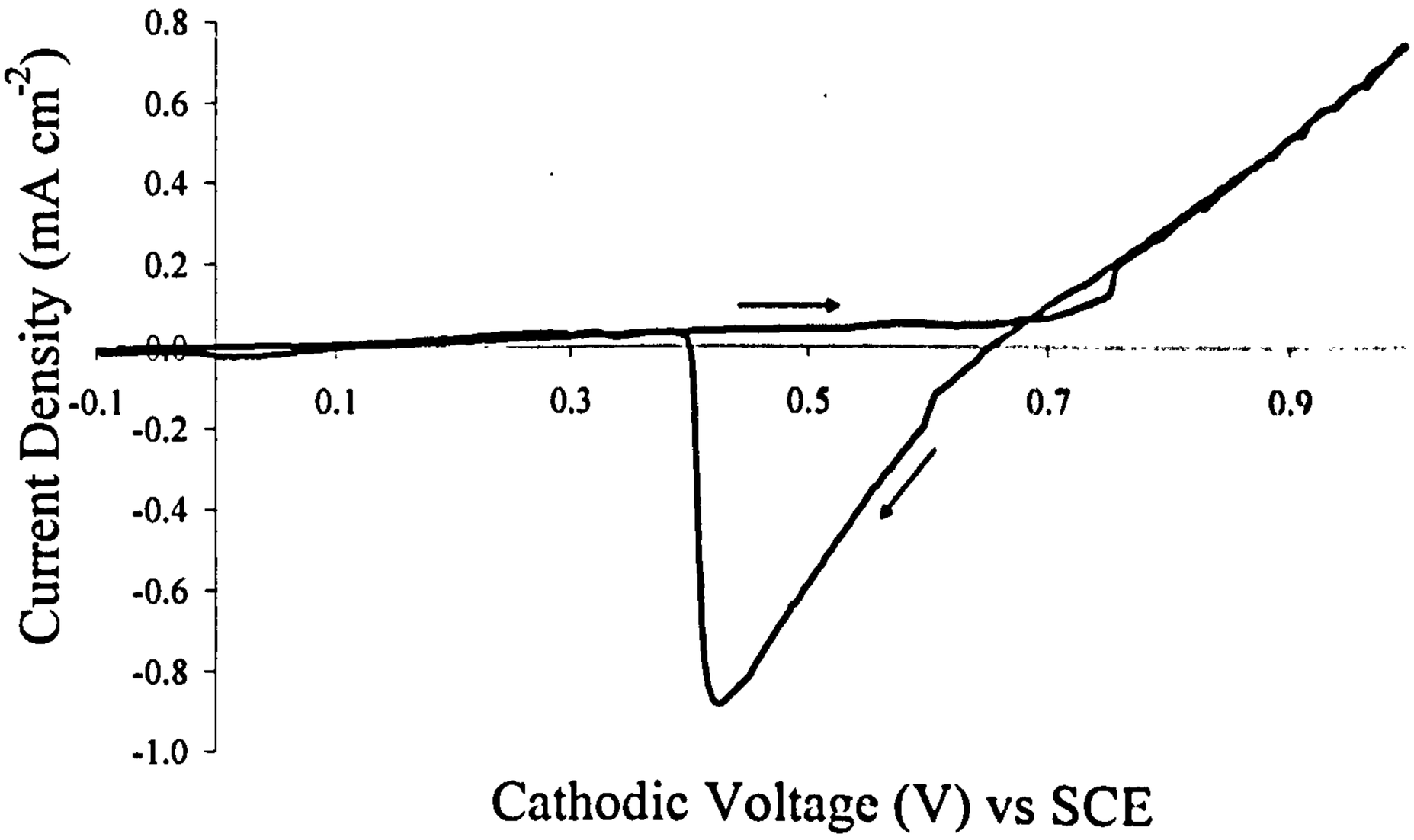

Figure 7.1. Cyclic voltammogram of aqueous solution containing 0.8M $3CdSO_4.8H_2O$ and 600 ppm $CdCl_2$. The arrows indicate the direction of the voltage sweep with scan rate 10 mV s^{-1}.

The cyclic voltammetry taken after the addition of TeO_2 to the aqueous solution containing 0.8M $3CdSO_4.8H_2O$ and 600 ppm $CdCl_2$ is presented in Figure 7.2. When added to the electrolyte it is known that TeO_2 reacts with water to produce $HTeO_2$ [Meulenkamp & Peter 1996]. On application of 0.296 V vs SCE, Te is released from $HTeO_2$ and deposits at the cathode via reaction 3.9, described in Chapter 3. It was envisaged the cyclic voltammetry of this solution would present more features compared to Figure 7.1, due to the reaction of Te with Cd forming CdTe.

The current density onset at -0.10 V reaching a peak at 0.080 V vs SCE cathodic voltage is due to the reaction of $HTeO_2$ forming Te. The current density increases between 0.150 V reaching another peak centred at 0.200 V vs SCE attributed to the underpotential deposition of Cd^{2+} which gains the free energy released from Te deposition forming CdTe + Te. The plateau reached between 0.250 and 0.500 V vs SCE is diffusion controlled deposition associated with the reaction of Te and hence formation of CdTe + Te. In this voltage region, applying a more negative growth voltage has no effect on the current density. Between 0.500 and 0.600 V vs SCE the doublet peak was expected to be due to the formation of CdTe as the voltage is closer to elemental Cd deposition. It was verified by XRD this material was Te-rich CdTe

denoted by the presence of a Te peak. The plateau reached between 0.600 and 0.690 V vs SCE was attributed to CdTe formation as established and described in the material characterisation and device fabrication sections.

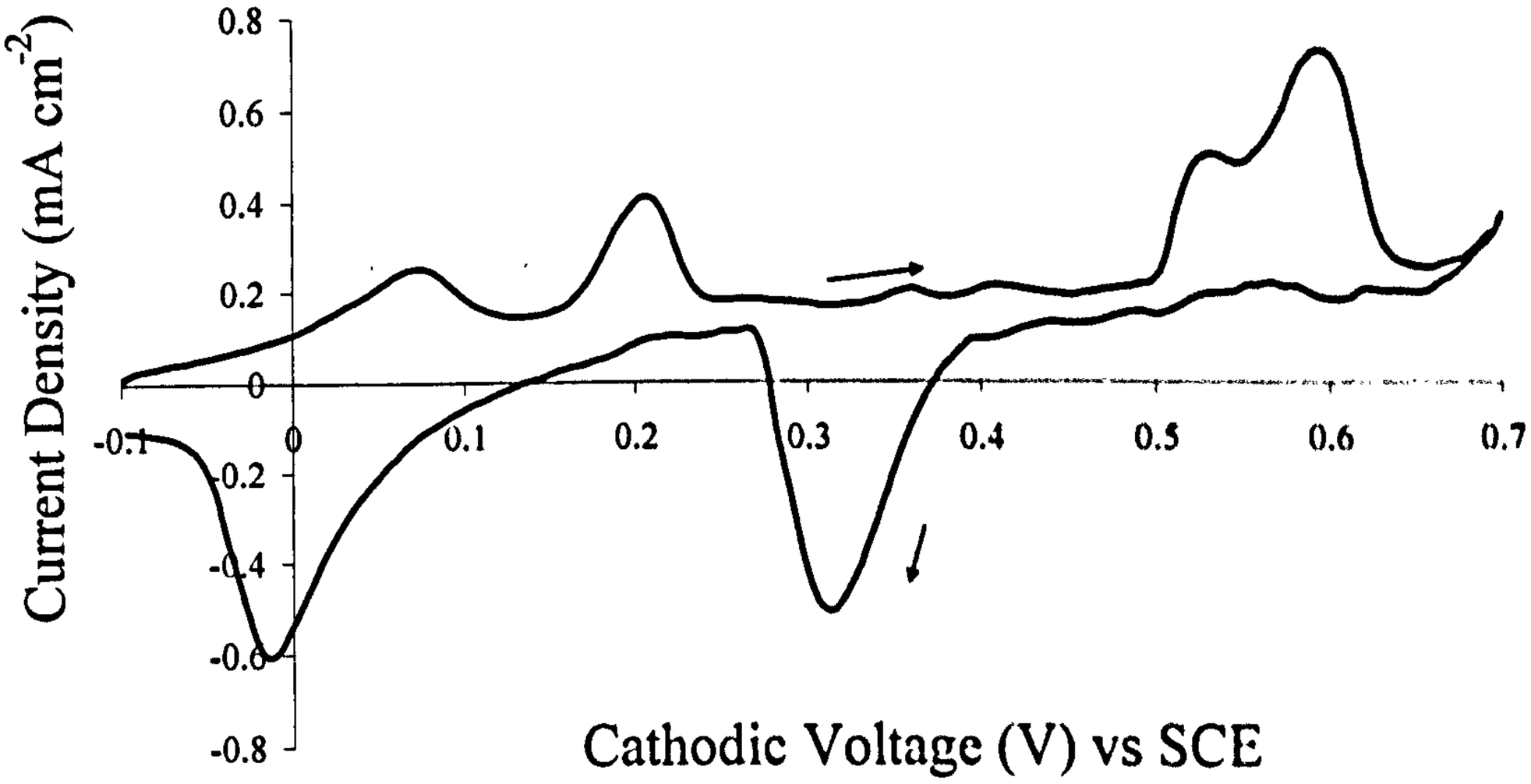

Figure 7.2. Cyclic voltammogram of aqueous solution containing 0.8M $3CdSO_4.8H_2O$, 600 ppm $CdCl_2$ and <50 ppm TeO_2. The arrows indicate the direction of the voltage sweep.

The solubility of TeO_2 is dependent on the solution pH and according to Duffy *et al.* has a solubility of 6.5×10^{-4} mol dm^{-3} at pH=1.4 and 85°C [Duffy *et al.* 2000]. According to Barker *et al.* the Te content in the electrolyte was 50 ppm during deposition of CdTe for the BP solar Apollo project. During the present investigation 50 ppm TeO_2 was added to 50 ml of the electrolyte and the pH adjusted to 2.33. Initially 5 ml of this solution was added to the electrolyte to form a background level of TeO_2. The current density was monitored during growth of each layer and 1 ml of the TeO_2 solution added if the current density decreased below 150 mA cm^{-2}. Barker *et al.* noted the current density at 150 mA cm^{-2} and the formation a 2 μm thick layer after 8 hours of growth [Barker *et al.* 1995].

The pH of the solution was monitored throughout this investigation and is plotted against growth voltage (Figure 7.3) identifying the pH of the solution for each sample. It should also be noted the layers were deposited sequentially with increasing voltage. The trend of the curve indicates the solution did not alter significantly over time.

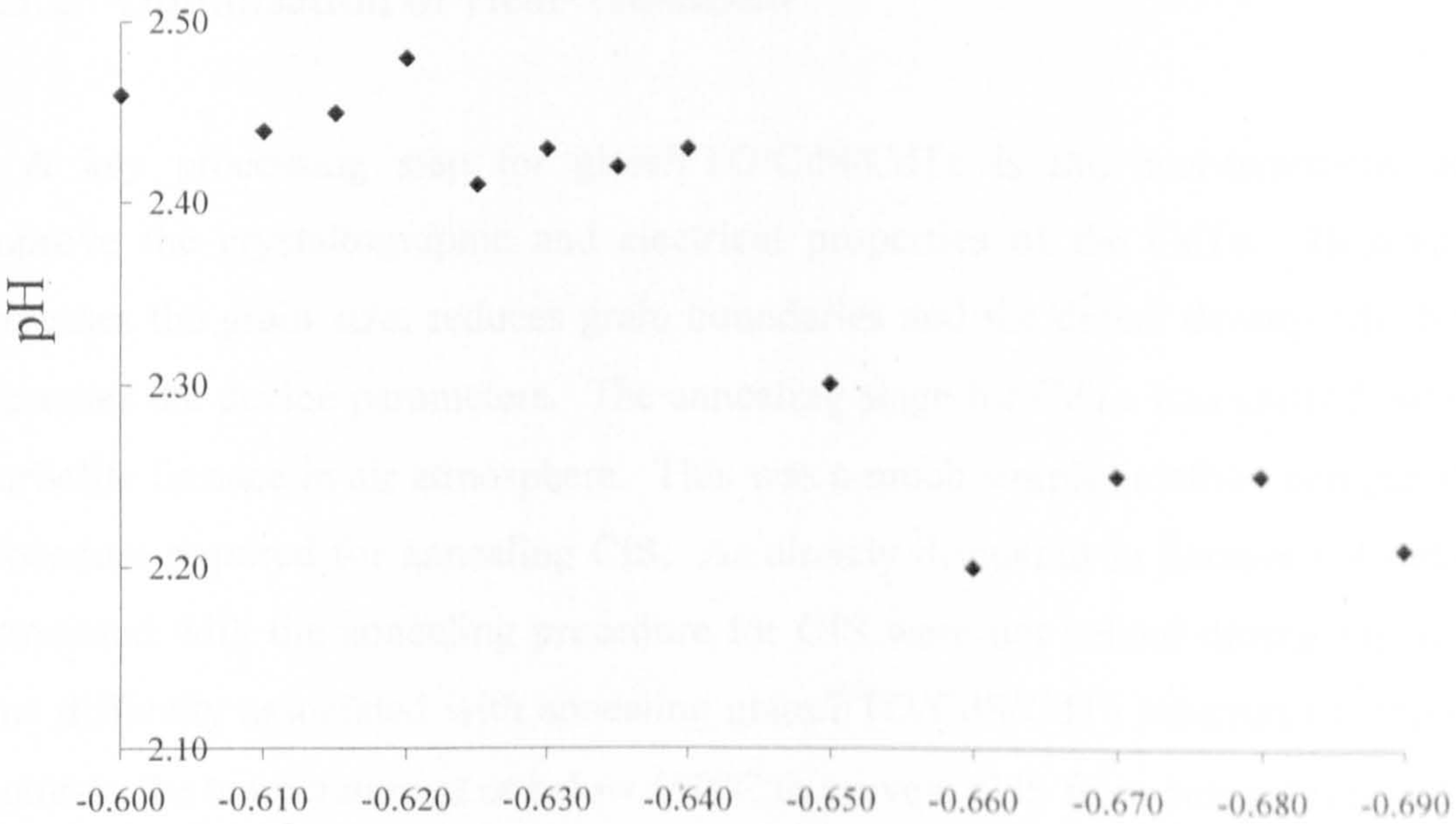

Figure 7.3. pH of the electrolyte at the beginning of growth of each CdTe layer, deposited sequentially from less to more negative voltage.

An SEM cross-section was taken for a CdTe layer deposited for 8 hours to estimate the thickness and is presented in Figure 7.4. The thickness was determined at 1.0 μm as indicated in the figure, which suggests the deposition rate was not as rapid as expected or as reported by Barker *et al*. [1995]. The Faraday relation was used to estimate the layer thickness using the electrodeposition data. The thickness was determined at 1.3 μm after growth for 8 hours and assuming the density of CdTe at 5.80 g cm^{-3} [Lide 2005]. This indicates a Faradaic efficiency of 0.76.

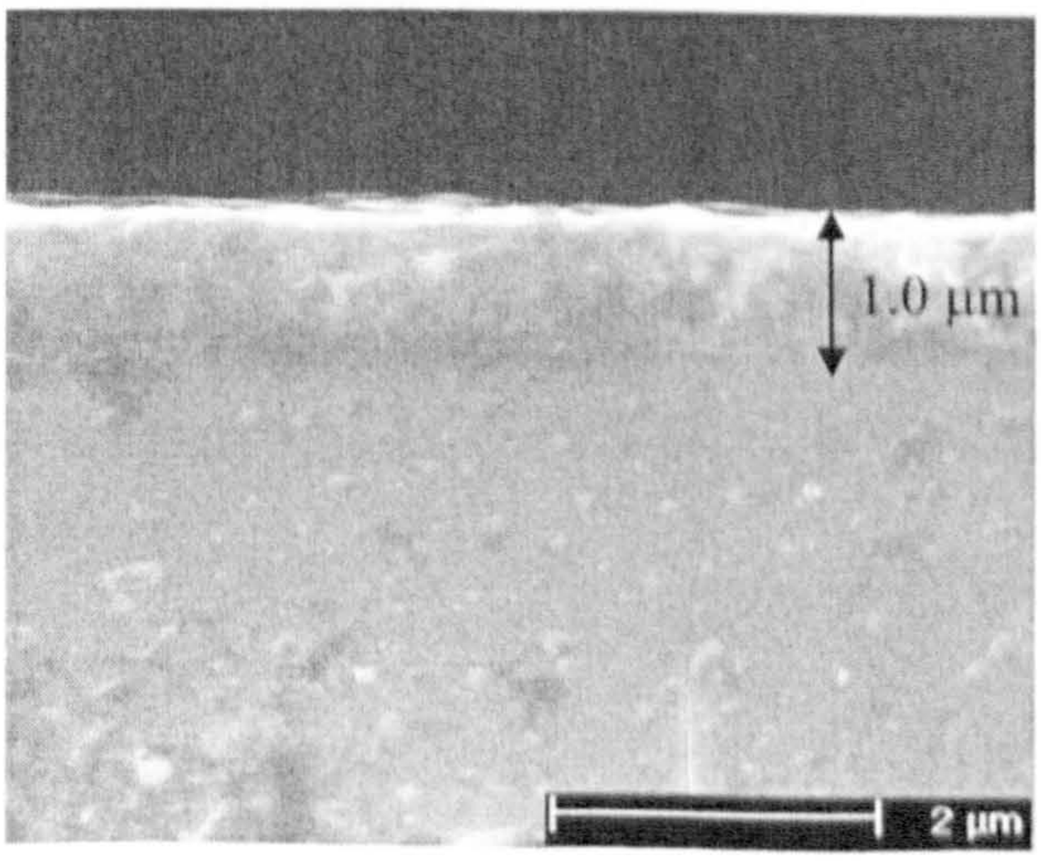

Figure 7.4. SEM cross-section of CdTe deposited for 8 hours indicating a thickness of 1.0 μm.

7.3.2 Optimisation of Heat-Treatment

A key processing step for glass/FTO/CdS/CdTe is the heat-treatment stage to improve the crystallographic and electrical properties of the CdTe. Heat-treatment increases the grain size, reduces grain boundaries and the defect density which in turn increases the device parameters. The annealing stage for CdTe was carried out using a Carbolite furnace in air atmosphere. This was a much simpler method compared to the procedure required for annealing CIS. As already discussed in Section 6.4 difficulties associated with the annealing procedure for CIS were not solved during this research. One difficulty associated with annealing glass/FTO/CdS/CdTe structures is the need to maintain the temperature at or below 450°C to prevent CdS from being destroyed.

Numerous heat-treatment experiments were carried out before an optimum process was established for annealing CdTe. Table 7.1 to 7.10 summarises the range of experiments that were conducted, exploring different temperatures and time periods for heat-treatment. The initial annealing trials were carried out on CdTe plates 10×10 cm^2 supplied by Ionotec Ltd. These samples were chosen for these experiments as they could be cut into several pieces for direct comparison of the annealing conditions. The general method used for all annealing trials was to first heat the furnace to the required temperature before placing the layers inside. When the time period had elapsed the layers were removed from the furnace and left to cool down naturally.

Table 7.1 presents the initial annealing experiment carried out on CdTe layers supplied by Ionotec Ltd. A strip 2×1 cm^2 was cut from a 10×10 cm^2 plate (deposited at -0.650 vs SCE), cut into six and heat-treated at one of the temperatures indicated in the Table 7.1 for 15 minutes in an air atmosphere. During this initial experiment the CdTe completely sublimed either as the temperature was too high or time period too lengthy. Another factor to consider is the quality of the material. If the material has a strongly bonded CdTe crystal structure and is highly adhered to the substrate it should withstand these temperatures and time as reported several times in the literature [Barker *et al.* 1995, Lapiller *et al.* 2000].

Table 7.1. Temperatures used for heat-treatment of CdTe layers taken from a strip cut from a 10×10 cm^2 plate and cut into six pieces. The layers were annealed for 15 minutes, (experiment 1 Ionotec samples).

Temperature (°C)	Comment
350	Layers Destroyed
370	Layers Destroyed
390	Layers Destroyed
410	Layers Destroyed
430	Layers Destroyed
450	Layers Destroyed

The lowest temperature in the first annealing experiment was 350°C which destroyed the layer. The temperature range was reduced for the second experiment between 300 and 410°C as indicated in Table 7.2 and the time remained constant at 15 minutes. As for experiment 1, a strip 2×1 cm^2 was cut from a different 10×10 cm^2 CdTe plate supplied by Ionotec Ltd., deposited at -0.650 V vs SCE. All layers survived the heat-treatment and were etched before evaporation of metal contacts. The I-V characteristics of all layers were measured and are presented in Table 7.2 together with the annealing temperatures of each layer.

Table 7.2. Temperatures used for heat-treatment of CdTe layers taken from a strip cut from a 10×10 cm^2 plate and cut into six pieces. The annealing time was 15 minutes, (experiment 2, Ionotec samples).

Temperature (°C)	V_{oc} (mV)	J_{sc} (mA cm^{-2})	FF
300	200	0.32	0.28
320	300	0.32	0.29
340	200	0.32	0.28
360	300	0.32	0.29
380	150	0.32	0.26
410	ohmic	-	-

All devices except the one annealed at 410°C had similar V_{oc} between 150 to 300 mV and the same current density of 0.32 mA cm^{-2}. The ohmic behaviour of the device heat-treated at 410°C was attributed to excessive temperature or annealing time, or non-uniformity over the plate. Some annealing temperatures in experiment 1 and 2 overlap and indicate contradictory results. This irregularity may be attributed to varying

material quality; the layers annealed in the second experiment were likely to have stronger adhesion to the substrate.

Several annealing experiments were subsequently conducted varying either the annealing temperature or time period as indicated by Table 7.3 to 7.7. For annealing experiments three to seven layers with areas of 3×4 cm^2, were cut into several pieces to ensure comparative results. The layers were deposited with growth voltage between -0.610 to -0.635 V vs SCE. Each set of heat-treatment results was considered before the next annealing experiment was planned to optimise the outcome.

The layers used for all subsequent annealing trials were deposited in the laboratory at Sheffield Hallam University (SHU), at different voltages. Experiment 3 used material deposited at -0.620 V vs SCE, Table 7.3 indicates the materials did not withstand temperatures above 370°C and were either destroyed or the devices were ohmic. A similar situation was observed for layers deposited at -0.635 V vs SCE and annealed with conditions described for experiment 4 in Table 7.4. At higher temperatures of 360°C and above the devices were ohmic or the layers were destroyed.

Table 7.3. Temperatures used for heat-treatment of CdTe layers for 15 minutes, (experiment 3 SHU samples).

Temp (°C)	V_{oc} (mV)	J_{sc} (mA cm^{-2})	FF
350	400	7.0	0.30
370	ohmic	-	-
390	destroyed	-	-

Table 7.4. Temperatures used for heat-treatment of CdTe layers for 15 minutes, (experiment 4, SHU samples).

Temp (°C)	V_{oc} (mV)	J_{sc} (mA cm^{-2})	FF
320	100	3.2	0.25
340	180	3.2	0.26
360	ohmic	-	-
380	destroyed	-	-

Layers destroyed during annealing had either partially or completely sublimed from the substrate, indicating either poor adhesion or weak crystallinity. The ohmic behaviour of devices indicates the metal contact covered a pin-hole and shorted or the material wasn't semiconducting either due to the growth conditions or partial sublimation during heat-treatment.

The time period used during annealing was varied and results are presented in Tables 7.5 and 7.6. Table 7.5 indicates the variation in device parameters with increasing annealing time at a temperature of 390°C. The layers for experiment 5 were deposited at -0.650 V vs SCE. All layers were destroyed during the heat-treatment and therefore metal contacts could not be made. Sublimation of the material may be due to over exposure or high temperature.

For experiment 6 the layers were annealed at 340°C and time range was reduced. The layers were deposited at -0.635 V vs SCE for experiment 6. After annealing for 35 minutes the layer had sublimed indicating the heat-treatment was too long. Layers annealed for 15 and 25 minutes survived the annealing and metal contacts were made. The device parameters are indicated in the Table 7.6 from which it is clear the shorter annealing period yielded improved results. The annealing time period for experiment five and six overlap and the latter produced working devices. This discrepancy is likely to be due to improved material properties which withstood the heat-treatment. Factors influencing the material properties of the layers were expected to be the growth voltage, which influences the composition of the material and the Te concentration in the solution.

Table 7.5. Annealing times used for heat-treatment of CdTe layers at 390°C, (experiment 5, SHU samples).

Time (mins)	Comment
15	Layers pin-holed for all annealing times
20	
30	
45	
50	
60	

Table 7.6. Annealing temperatures used for heat-treatment of CdTe layers at 340°C, (experiment 6, SHU samples).

Time (mins)	V_{oc} (mV)	J_{sc} (mA cm^{-2})	FF
15	400	2.9	0.30
25	100	2.4	0.26
35	Destroyed	-	-

Experiment 6 indicated annealing for a shorter period of time improved the device performance. According to [McGregor 1999] the optimum annealing time for CdTe

was 12 minutes. Taking this into consideration together with the poor adhesion and apparent crystallographic weakness (sublimation occurred for most annealing experiments) the minimum annealing time period was reduced. Table 7.7 indicates the annealing times for experiment 7 carried out at 390°C. A marked improvement in the device parameters was observed with annealing times of 5, 6, and 7 minutes. The current density was highest for the shorter times of 5 and 6 minutes although the open circuit voltages were similar.

Table 7.7. Times used for heat-treatment at 390°C of CdTe layers deposited at -0.620 V vs SCE, (experiment 7, SHU samples).

Time (mins)	V_{oc} (mV)	J_{sc} (mA cm^{-2})	FF
5	350	8.0	0.36
6	400	8.0	0.38
7	400	4.8	0.35

To test the reproducibility of the annealing time periods indicated in Table 7.7 several experiments were carried out. The device parameters of these experiments are presented in Tables 7.8 to 7.10. The annealing temperature was maintained at 390°C for experiments 8 to 10. It is clear from Tables 7.8 to 7.10 that annealing for shorter periods of time prevents the sublimation of the CdTe from the substrate. The layers annealed during experiment 8 were deposited at -0.620 V vs SCE and produced the highest current density of J_{sc}=10 mA cm^{-2} after annealing for 6 minutes.

The layers annealed during experiment 9 were deposited at -0.640 V vs SCE and indicated the highest device parameters after an annealing time period of 6 minutes, in agreement with experiment 8. The high J_{sc} indicates a reduction in the defect density of the material compared to the other layers. A reduction in the J_{sc} was observed for layers annealed for 10 minutes, which is attributed to the degradation of the material.

Layers deposited at -0.650 V vs SCE were annealed during experiment 10 at 390°C for differing time periods as indicated in Table 7.10. The device parameters varied depending on the annealing time, the biggest improvement was after annealing for 6 minutes. From the annealing experiments 1 to 10 it was confirmed that annealing at 390°C for 6 minutes produced devices with the highest V_{oc} and J_{sc}. These conditions were used for all subsequent annealing experiments.

When the temperature was too high or the annealing time period too long sublimation of the layers was observed. It should be noted that the optimised annealing

conditions are dependent on the stability of the material and adhesion to the substrate. CdTe electrodeposited in a different way or using another growth technique may perform differently during annealing and may withstand higher temperatures or longer time periods.

Table 7.8. Times used for heat-treatment at 390°C of CdTe layers deposited at –0.630 V vs Se, (experiment 8 SHU samples).

Time (mins)	V_{oc} (mV)	J_{sc} (mA cm^{-2})	FF
5	420	5.0	0.43
6	400	10.0	0.46
7	400	8.0	0.39

Table 7.9. Times used for heat-treatment at 390°C of CdTe layers deposited at –0.640 V vs Se, (experiment 9, SHU samples).

Time (mins)	V_{oc} (mV)	J_{sc} (mA cm^{-2})	FF
5	500	6.6	0.41
6	550	19.1	0.46
10	400	3.2	0.32

Table 7.10. Times used for heat-treatment at 390°C of CdTe layers deposited at –0.650 V vs Se, (experiment 10, SHU samples).

Time (mins)	V_{oc} (mV)	J_{sc} (mA cm^{-2})	FF
5	200	10.0	0.31
6	350	10.0	0.47
7	400	4.8	0.34
9	300	3.2	0.35

7.3.3 X-Ray Diffraction

XRD was carried out on as-deposited CdTe layers electrodeposited at various growth voltages from -0.600 to -0.690 V vs SCE as indicated in Figure 7.5, to investigate the crystallographic properties. It was found that all growth voltages produced CdTe layers with preferential orientation in the (111) plane agreeing with the literature [Duffy *et al.* 2000]. The intensity of the preferential peak varied and was at a maximum for the layer deposited at -0.620 V vs SCE, indicating the largest crystal size. The crystallography of the as-deposited layers is most likely to be influenced by the composition of the

material as a consequence of the growth voltage. Another factor influencing the composition of the layer is the amount of dissolved TeO_2 in the electrolyte. The high molarity of the Cd in the electrolyte ensures its constant composition.

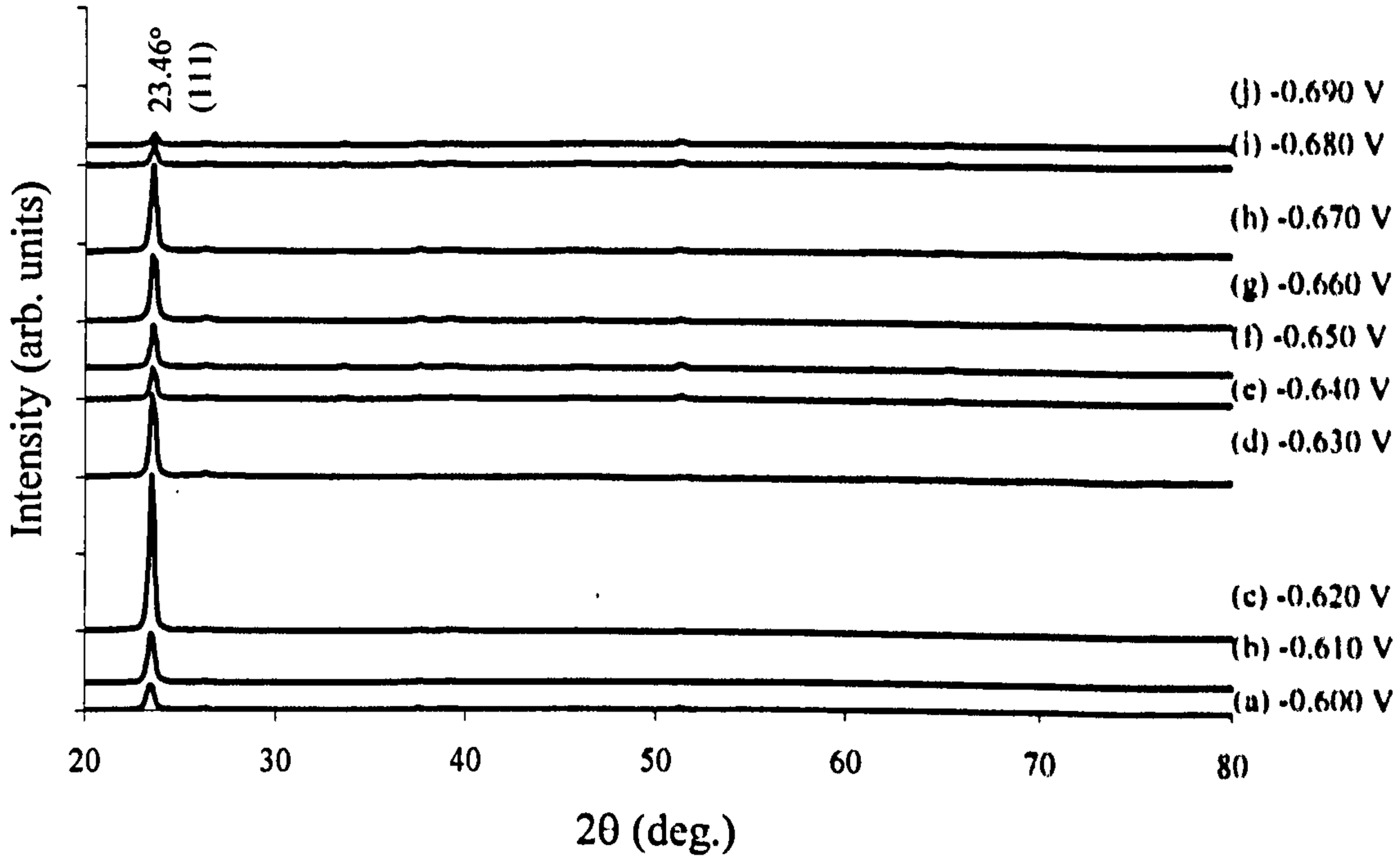

Figure 7.5. XRD spectra of CdTe as-deposited at (a) -0.600, (b) -0.610, (c) -0.620, (d) -0.630, (e) -0.640, (f) -0.650, (g) -0.660, (h) -0.670, (i) -0.680 and (j) -0.690 V vs SCE.

Table 7.11 presents the FWHM and grain size of CdTe layers as function of growth voltage indicating a small variation. The layer deposited at -0.620 V vs SCE exhibited the largest grain size and smallest FWHM. The layers investigated using XRD were all deposited for a constant time period to keep the thickness of the layers constant. The variation in the (111) peak intensity indicates the difference in the crystallographic properties of the CdTe layers.

Table 7.11. Grain size and FWHM as a function of growth voltage of CdTe.

Growth Voltage (V)	FWHM (deg.)	Grain Size (nm)
-0.600	0.46	18
-0.610	0.42	19
-0.620	0.30	27
-0.630	0.34	24
-0.640	0.38	21
-0.650	0.34	24
-0.660	0.40	20
-0.670	0.38	21
-0.680	0.40	20
-0.690	0.38	21

Figure 7.6 presents the variation in intensity of the (111) peak as a function of growth voltage for as-deposited and annealed layers. The least intense peaks were from the layers deposited at -0.600, -0.610, -0.615, -0.680 and -0.690 V vs SCE indicating reduced crystallinity.

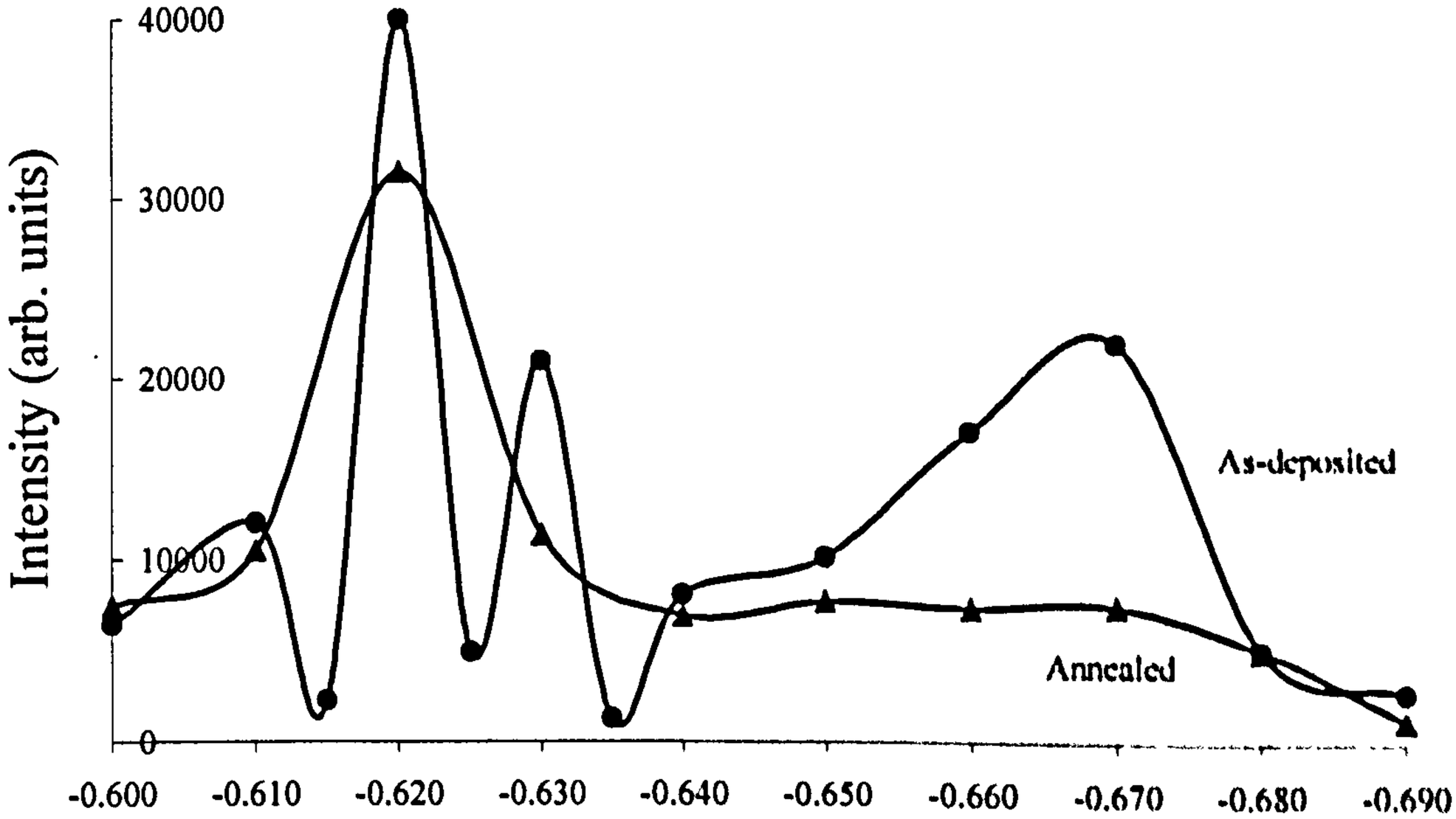

Figure 7.6. Variation of (111) peak intensity of as-deposited and annealed CdTe layers as a function of growth voltage.

Figures 7.7 and 7.8 present the FWHM and grain size as a function of growth voltage. The annealing conditions were 390°C for 6 minutes in air atmosphere. The variation in intensity, FWHM and grain size is most likely to be due to the change in composition of the CdTe layers, which is influenced by the growth voltage and the Te content of the solution.

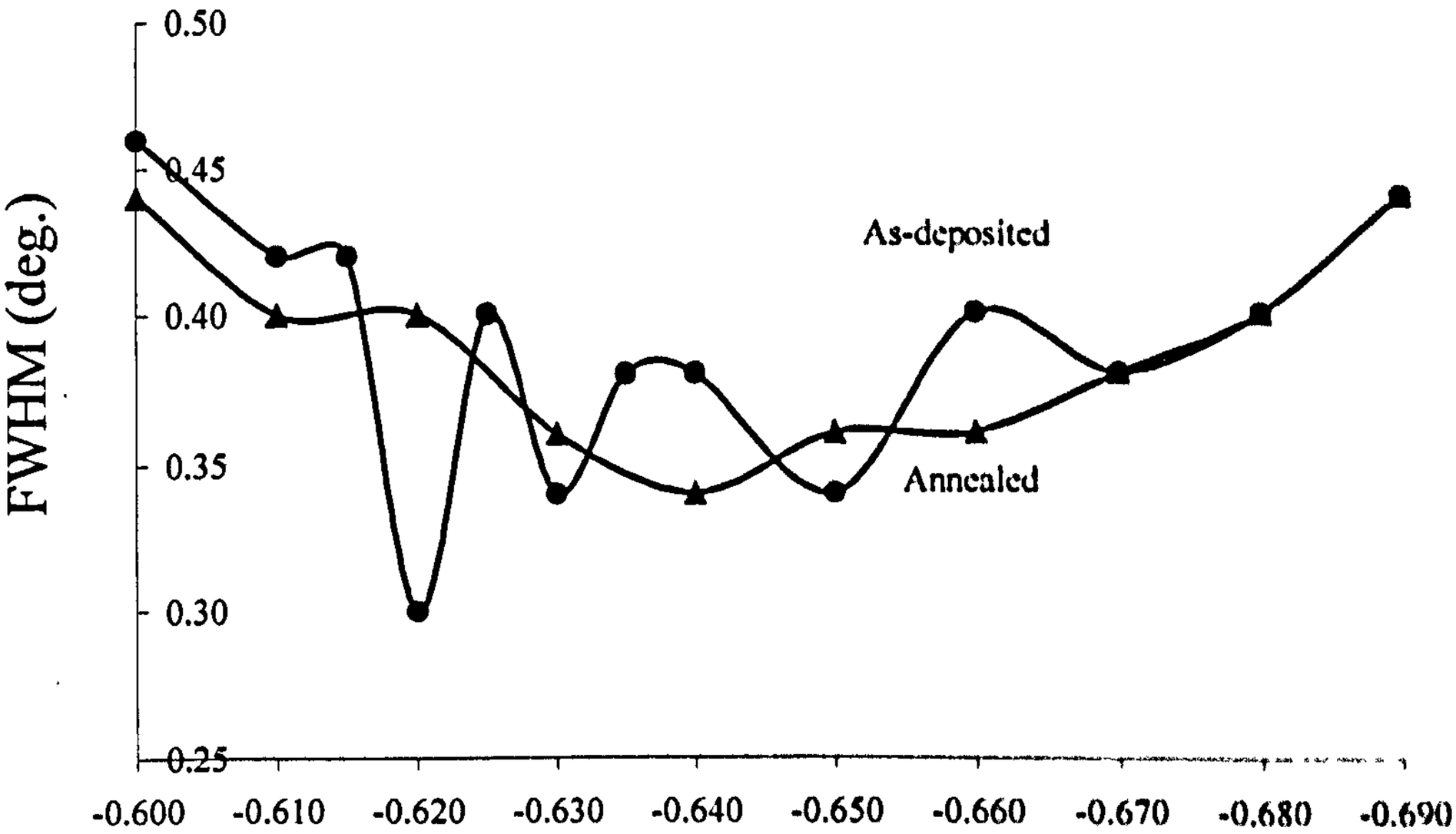

Figure 7.7. Variation of FWHM of as-deposited and annealed CdTe layers as a function of growth voltage.

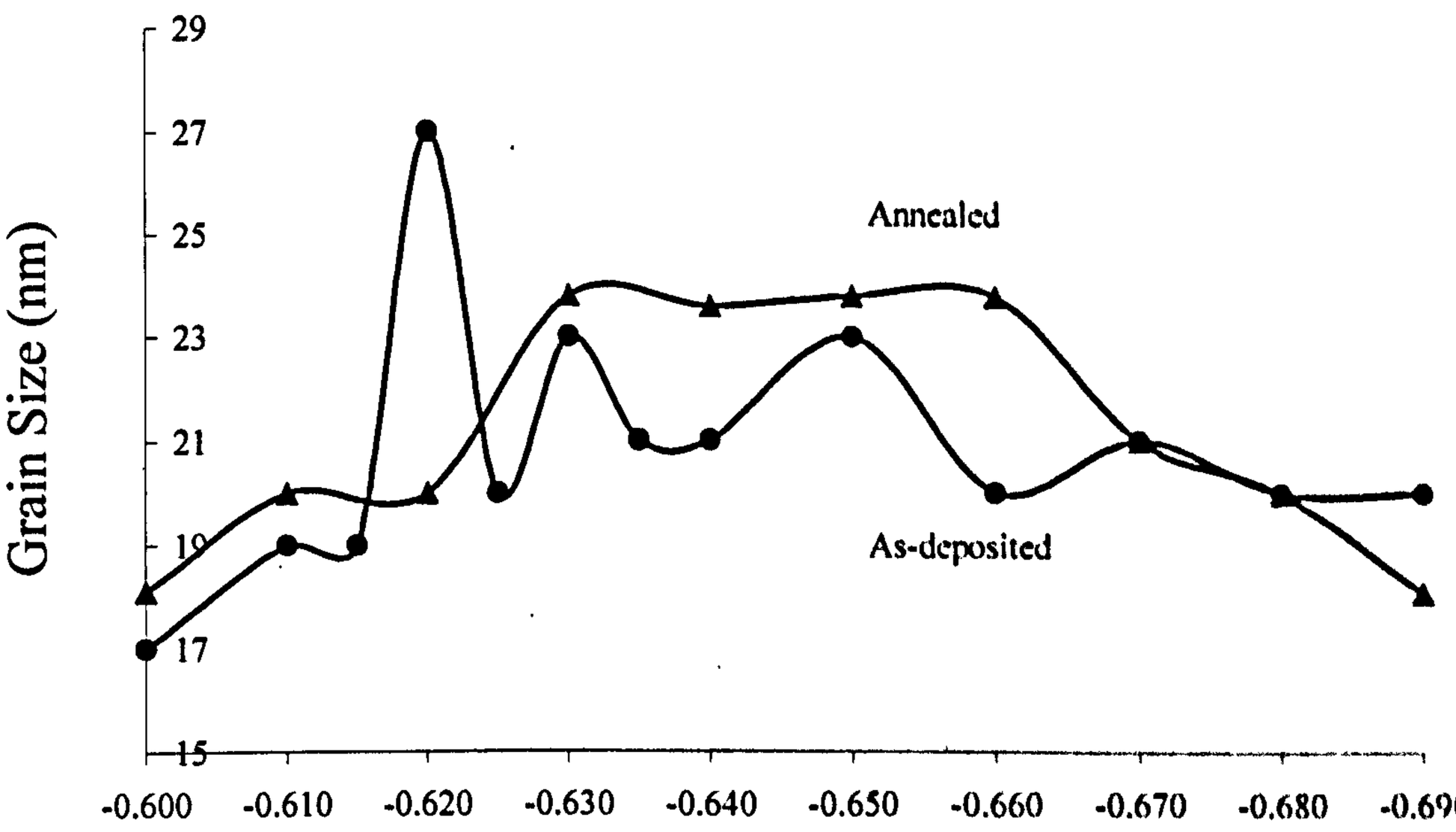

Figure 7.8. Variation of FWHM of as-deposited and annealed CdTe layers as a function of growth voltage.

Figure 7.9 presents the XRD spectra of as-deposited and annealed CdTe layers. Annealing was carried out at 390°C for 6 minutes. There was no variation in the FWHM and grain size of the layers which remained at 0.38° and 21 nm, although the intensity decreased slightly. The decrease in the peak intensity suggests some of the material sublimed during annealing.

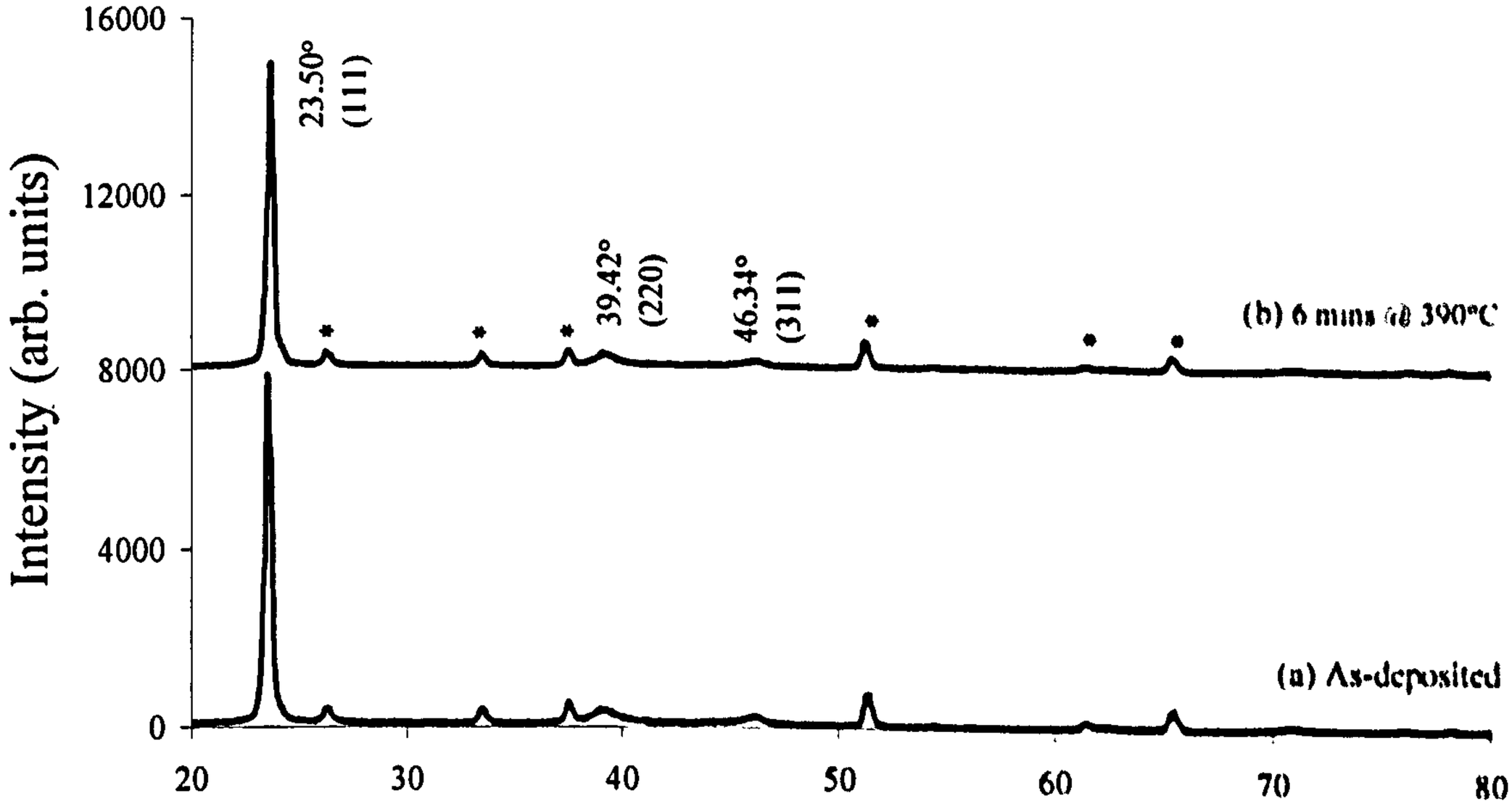

Figure 7.9. XRD spectra of CdTe (a) as-deposited and (b) annealed at 390°C for 6 minutes.

Table 7.12 presents the XRD data for as-deposited and annealed CdTe layers compared to standard data obtained from the online Daresbury Chemical Database Service [Rabadanov *et al.* 2001]. The layers were identified as cubic and the lattice parameters were calculated using the d-spacing equation (2.6) described in Chapter 2 and the XRD data, at a=6.560 Å compared to the standard value of a=6.483 Å.

Table 7.12. XRD data representing all XRD spectra for CdTe layers deposited at various voltages.

2θ (deg.)		d-Spacing (Å)		Miller Indices	Compound
Standard	Observed	Standard	Observed	(hkl)	
23.77	23.46	3.743	3.794	(111)	CdTe
26.74	26.42	3.335	3.374	(110)	SnO_2
34.00	33.18	2.649	2.660	(101)	SnO_2
37.91	37.66	2.368	2.389	(200)	SnO_2
39.31	39.18	2.292	2.300	(220)	CdTe
46.46	46.22	1.955	1.964	(311)	CdTe
51.73	51.40	1.768	1.778	(211)	SnO_2
54.80	54.68	1.675	1.679	(220)	SnO_2
61.92	61.52	1.502	1.499	(310)	SnO_2
65.93	65.48	1.415	1.425	(301)	SnO_2
71.26	70.80	1.323	1.331	(422)	CdTe

7.3.4 Optical Properties

Transmission spectra of CdTe layers deposited at different growth voltages was carried out to determine the variation in absorption edge and transmission. Figure 7.10 presents the transmission spectra for glass/FTO/CdS/CdTe for CdTe deposited at -0.600, -0.620, -0.640, -0.660 and -0.680 V vs SCE. The absorption edge of the layer deposited at -0.600 V vs SCE is at 730 nm and shifts to 750 nm for the other layers. The absorption edge gradually reached maximum transmission above 825 nm. The maximum transmission is greatest for the CdTe deposited at -0.600 V at 85% and decreases to ~80% for layers deposited at -0.660 and -0.680 V and 65% for layers deposited at -0.640 and -0.620 V vs SCE. The reason for the change in transmission is unclear as the alteration is not sequential with deposition voltage. It is possible the variation in percentage transmission is due to a change in composition of the layer or different thicknesses due to material loss during annealing.

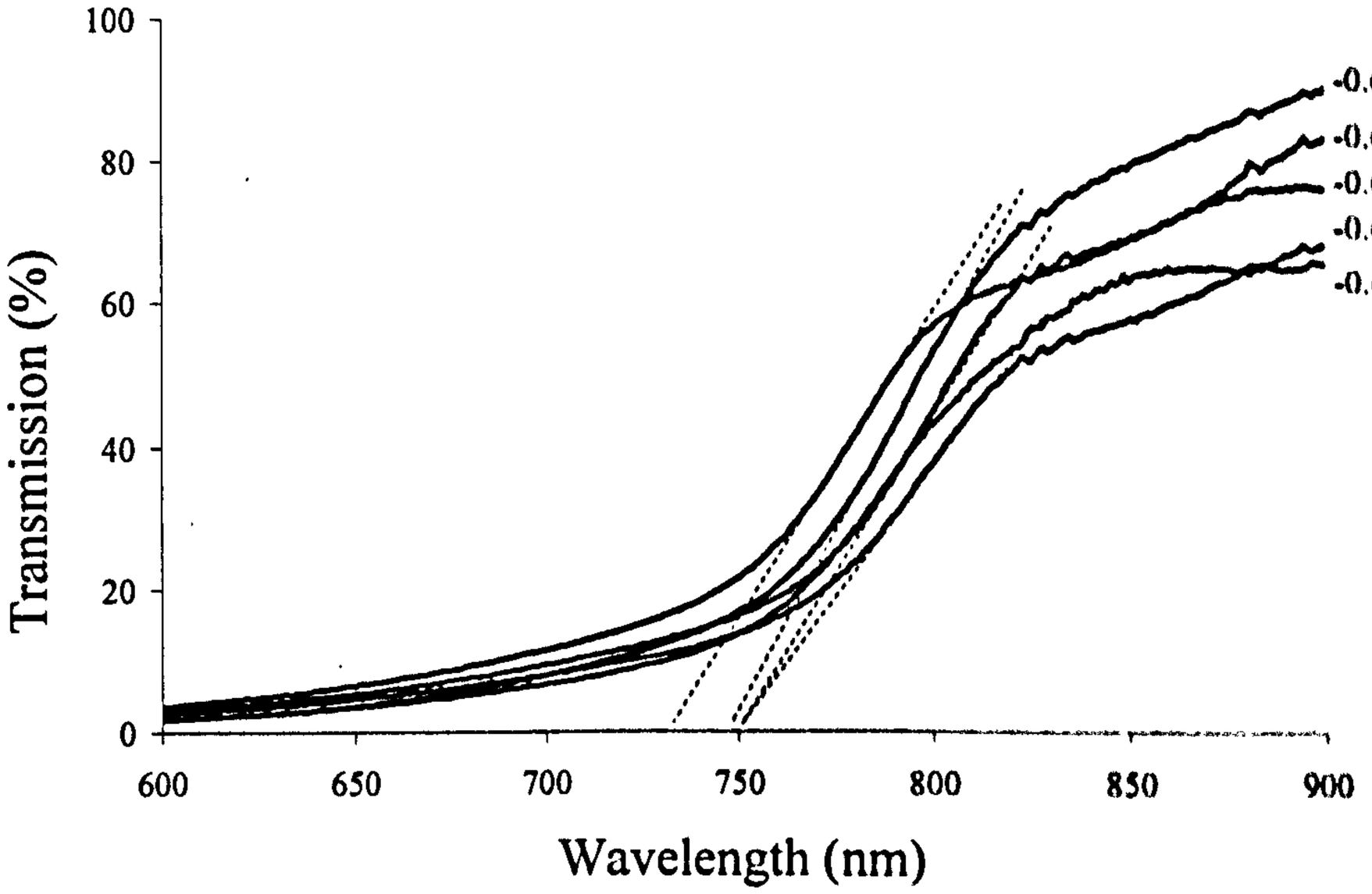

Figure 7.10. Transmission spectra of annealed CdTe deposited at various growth voltages.

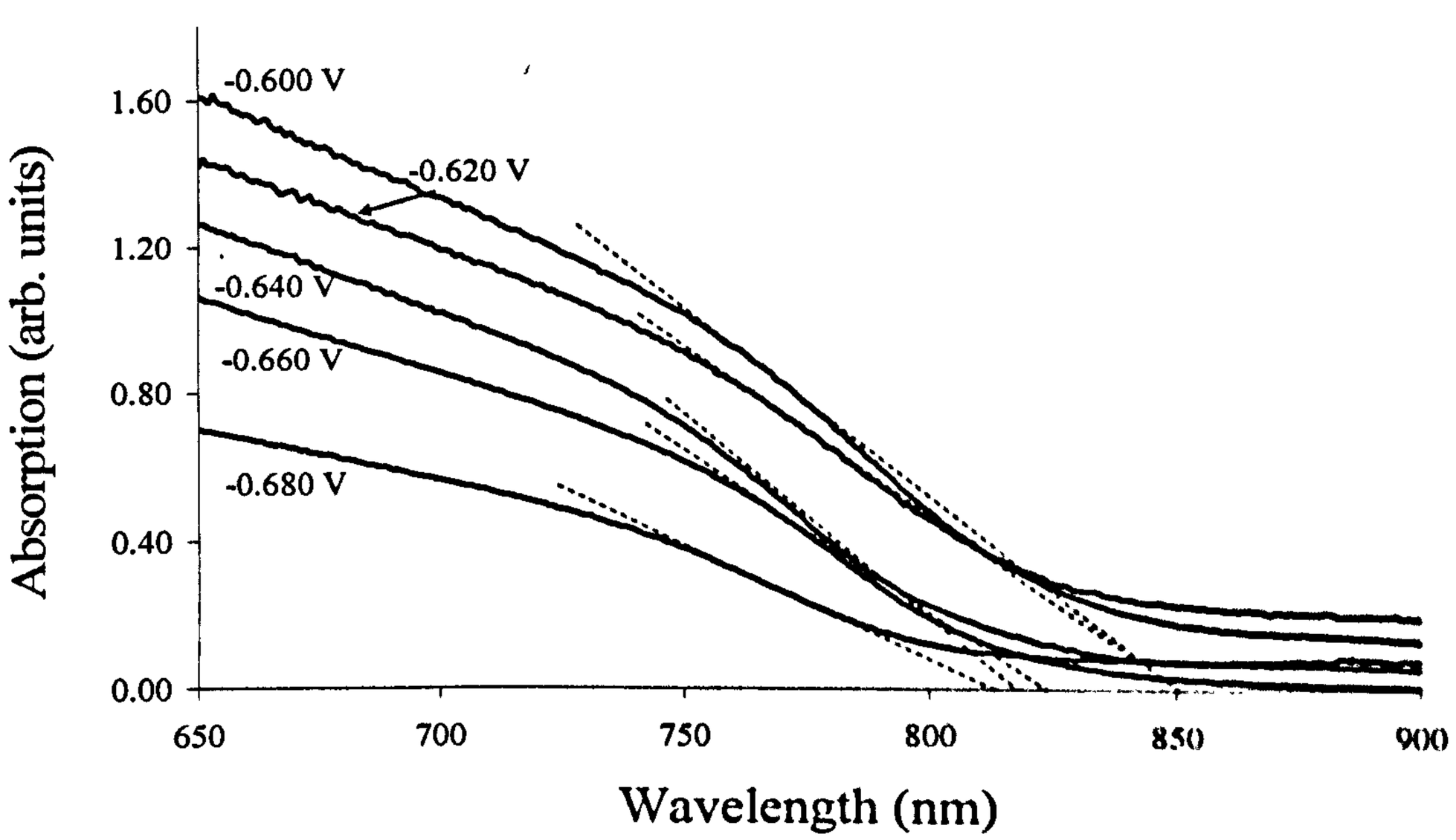

Figure 7.11. Absorption spectra as a function of wavelength of CdTe deposited at different growth voltages.

The optical absorption experiments were carried out on annealed CdTe layers to determine the absorption edge and bandgap energy. The plot of absorption as a function of wavelength is presented in Figure 7.11 for CdTe layers grown at different voltages. It is clear the absorption edge shifts to lower wavelength for layers deposited at more

negative deposition voltages. The change in absorption edge from 850 nm for layers deposited at -0.600 and -0.620 V to 800 nm for layers grown at -0.640, -0.660 and -0.680 V vs SCE is most likely to be due to the changing composition as a function of growth voltage.

The data obtained from the absorption vs wavelength curve and equation (1.1) described in Chapter 1 were used to calculate the absorption edge of glass/FTO/CdS/CdTe as a function of photon energy. Figure 7.12 indicates the variation in absorption spectra as a function of photon energy for CdTe layers deposited at different growth voltages as indicated in the figure. The bandgap energy was estimated at 1.45 eV for layers deposited at -0.600 and -0.620 V and 1.50 eV for layers grown at -0.640 to -0.680 V vs SCE. The change in bandgap energy is an indication of change in composition as a function of growth voltage.

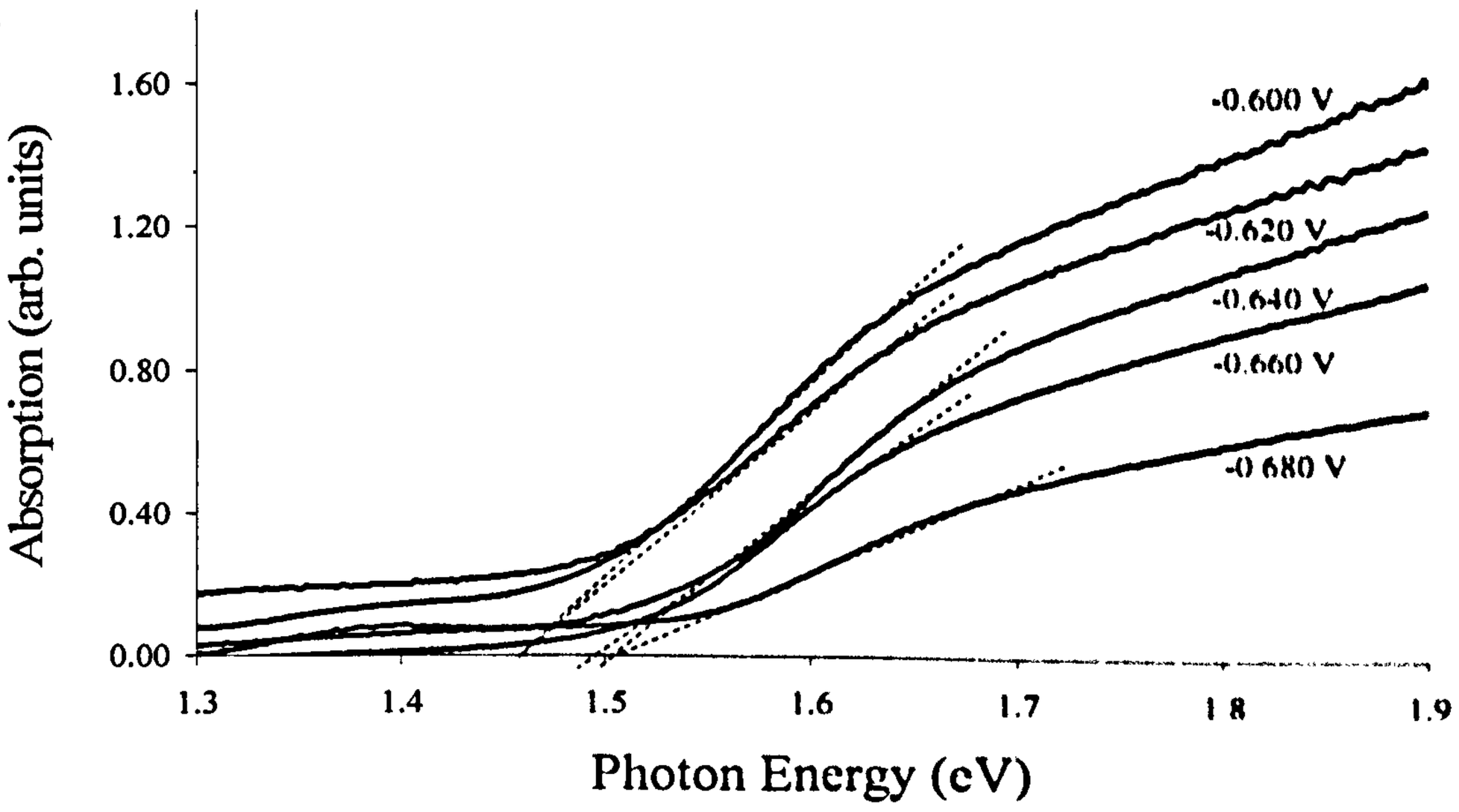

Figure 7.12. Absorption spectra as a function of photon energy of CdTe deposited at different growth voltages.

The absorption coefficient was calculated using equation (2.11) described in Chapter 2 and plotted as a function of photon energy yielding a more accurate slope for the determination of the bandgap energy (Figure 7.13). The bandgap energy of the CdTe deposited at -0.600 V was determined at 1.52 eV compared to 1.54 eV for layers deposited at -0.620 to -0.680 V vs SCE which agrees with values reported in the literature [Meulekamp & Peter 1996]. The difference in bandgap energy may be attributed to a change in composition due to the change in deposition voltage. More

positive growth voltages are closer to the redox potential of Te and it is therefore expected that these layers are Te-rich.

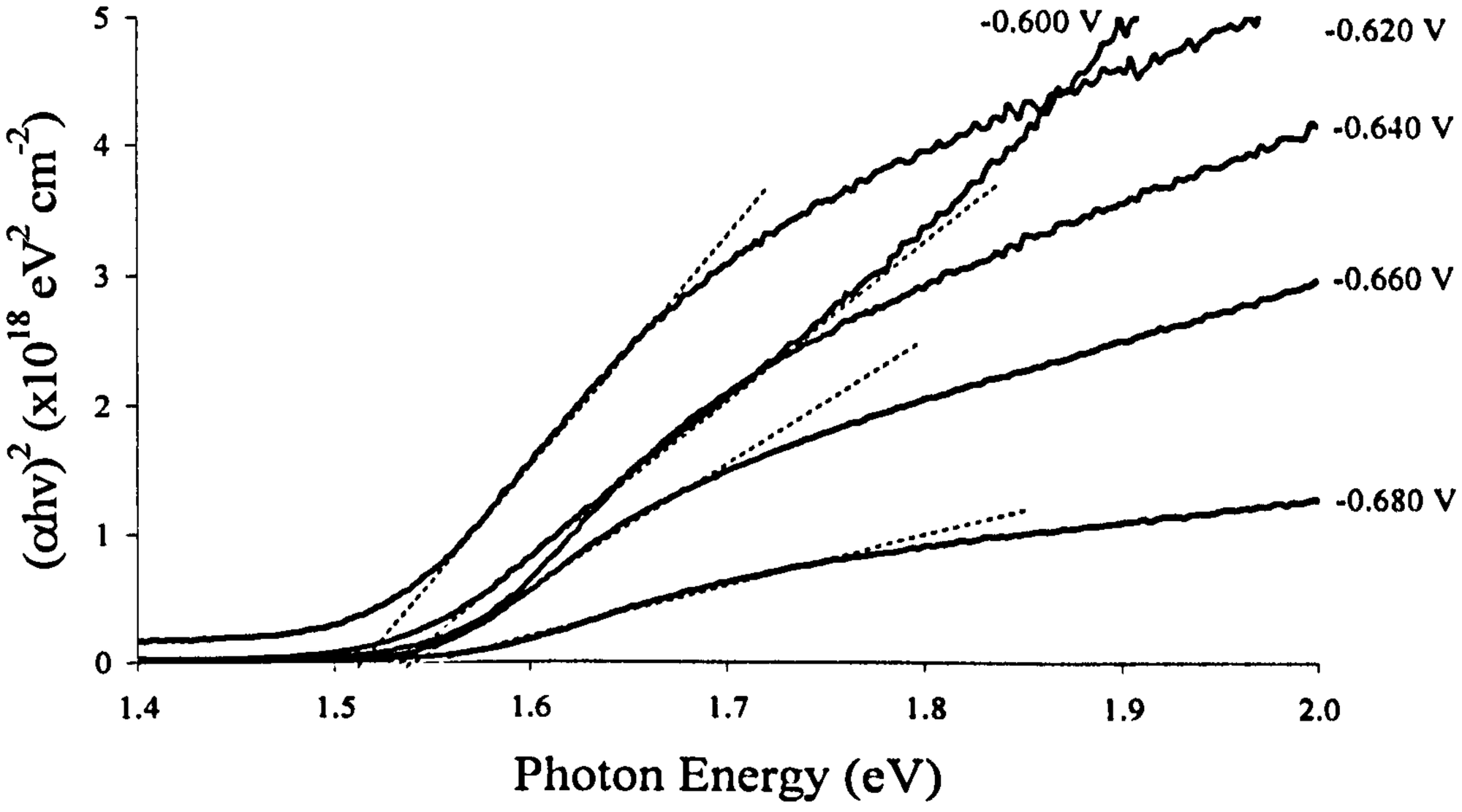

Figure 7.13. Optical absorption spectra of CdTe deposited at various growth voltages.

7.3.5 Scanning Electron Microscopy

SEM was used to study the morphology of the CdTe layers. Figure 7.14 (a & b) illustrates the morphology of the as-deposited and annealed CdTe deposited at -0.630 V vs SCE. The as-deposited material appears uniform with nodular clusters around 0.1 μm in size. After annealing the CdTe in air atmosphere for 6 minutes at 390°C a change in morphology was apparent. The crystallites appeared to have agglomerated forming larger clusters around 0.4 μm in size although some smaller grains (0.1 μm) remain visible. This suggests that although the annealing conditions were optimised for this material the heat-treatment was not sufficient to produce uniformly distributed grain growth. In order to produce a more uniform layer the heat-treatment temperature or time should be increased. As already confirmed in the heat-treatment investigation such conditions are not suitable for this material and degradation was observed.

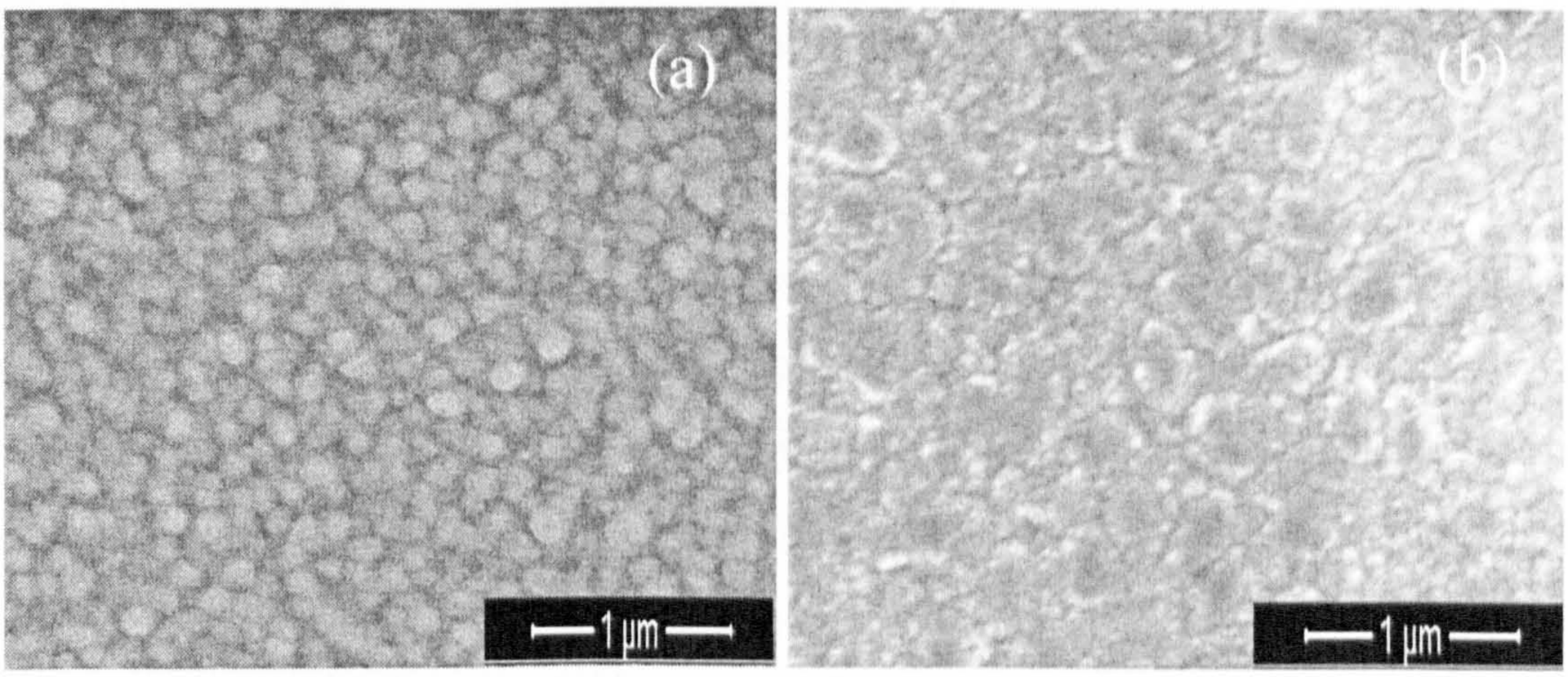

Figure 7.14. SEM images of (a) as-deposited and (b) annealed CdTe deposited at -0.630 V vs SCE.

Figure 7.15 (a to g) illustrates the morphology of CdTe deposited at (a) -0.620, (b) -0.640, (c) -0.650, (d) -0.660, (e) -0.670, (f) -0.680, and (g) -0.690 V vs SCE and annealed for 6 minutes at 390°C in air atmosphere. All layers appear to have uniform morphology and crystallite size with nodular shaped crystals. The layer deposited at -0.620 V vs SCE has the smallest crystallite size of 0.05 µm. The crystallite size increased to 0.5 µm for the layer deposited at -0.640 V vs SCE. The crystallite size was around 0.25 µm for layers deposited at -0.650 to -0.680 V vs SCE, with all layers having similar appearance. The layer deposited at -0.690 V vs SCE had the least uniform morphology with crystallite size between 0.2 to 0.4 µm. This layer was deposited at the most negative voltage, which may be a reason for the difference in uniformity, as the layer may deposit more rapidly in a less ordered fashion.

Overall the layers appear smooth and have similar orientation, agreeing with the XRD study, which indicated preferential orientation in the (111) plane. Although the layer is polycrystalline the high degree of preferential orientation aids the device performance as crystallites are predominantly oriented in the same direction which may alleviate resistance to current flow. Increasing the grain size reduces grain boundaries reducing the defect density of the layer. This reduces recombination centres at grain boundaries and in the bulk of the material.

The occasional void in the layers (c to g) is most likely to be due to loss of material during the annealing stage. Sublimation of Te, during annealing leaves behind pin-holes in the layer which act as shunt paths. Conversely annealing may alleviate pin-

holes if crystallites agglomerate forming larger grains. Sublimation also gives rise to a change in stoichiometry of the layer, if the layer is Te-rich, loss of this element would improve the material. Oxidation may also take place forming native oxides, which are detrimental for CdTe devices and are removed during etching before device fabrication.

There is a large difference in the crystallite size of the layers according to XRD (~20 nm) and SEM (0.2 to 0.5 μm). The Scherrer relation uses the FWHM that provides information on the coherence length of reflected x-rays. SEM detects the surface morphology and indicates the nodule size which is of greater magnitude than the information provided by XRD.

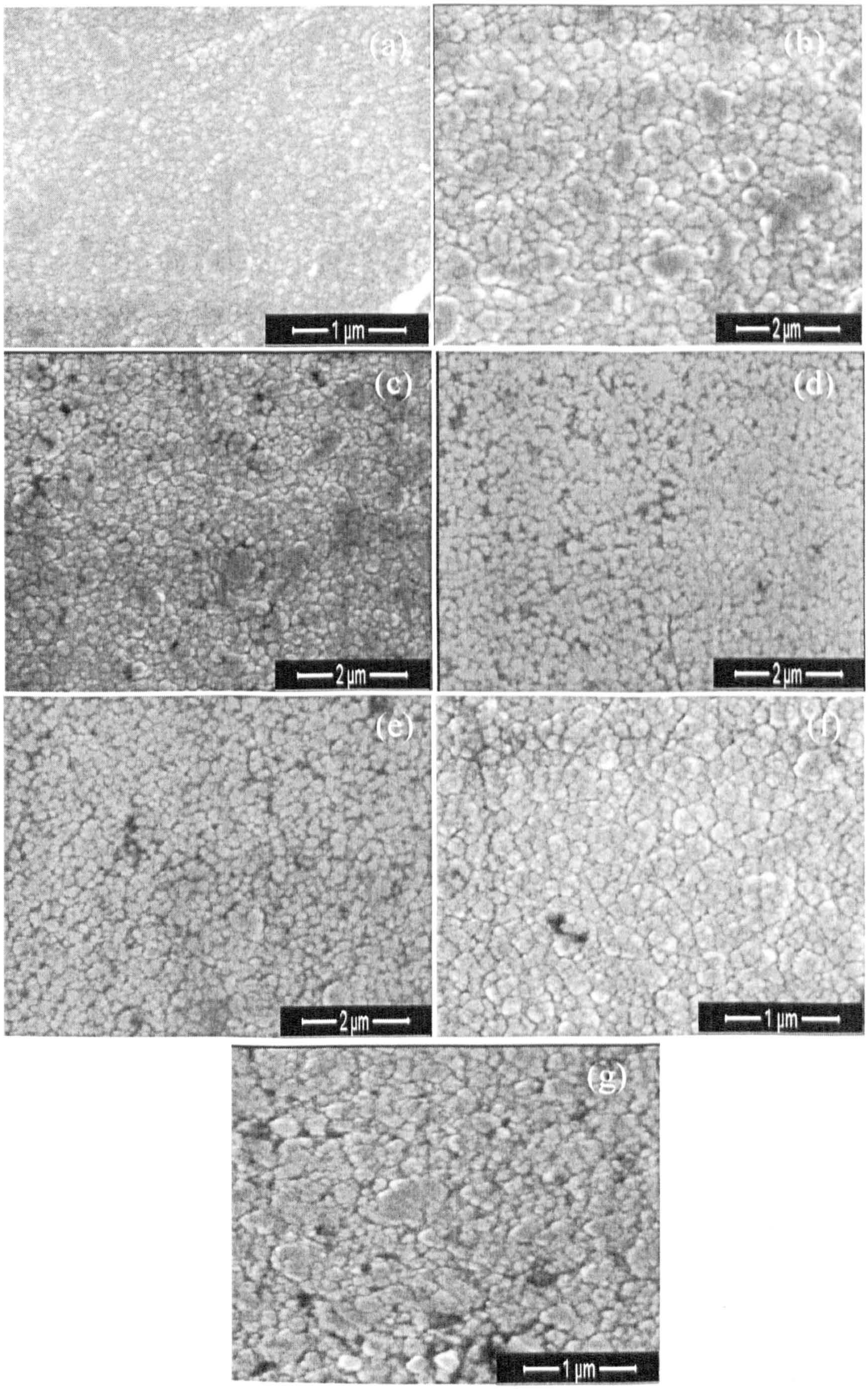

Figure 7.15. SEM images of annealed CdTe deposited at (a) -0.620, (b) -0.640, (c) -0.650, (d) -0.660, (e) -0.670, (f) -0.680 and (g) -0.690 V vs SCE.

7.3.6 Photoelectrochemical Cell Studies

A liquid/solid junction was formed between sodium sulphite (Na_2SO_3 and CdTe/FTO/glass to carry out PEC studies and determine the electrical conductivity type of the material. This technique measures the open circuit voltage produced by the liquid-solid junction. The photovoltage response to repeated periods of illumination is presented in Figure 7.16. Both as-deposited and annealed layers exhibited p-type electrical conductivity as the dark voltage was more negative than the illuminated. The as-deposited material indicated a larger PEC signal compared to the annealed, which showed an immediate photoresponse.

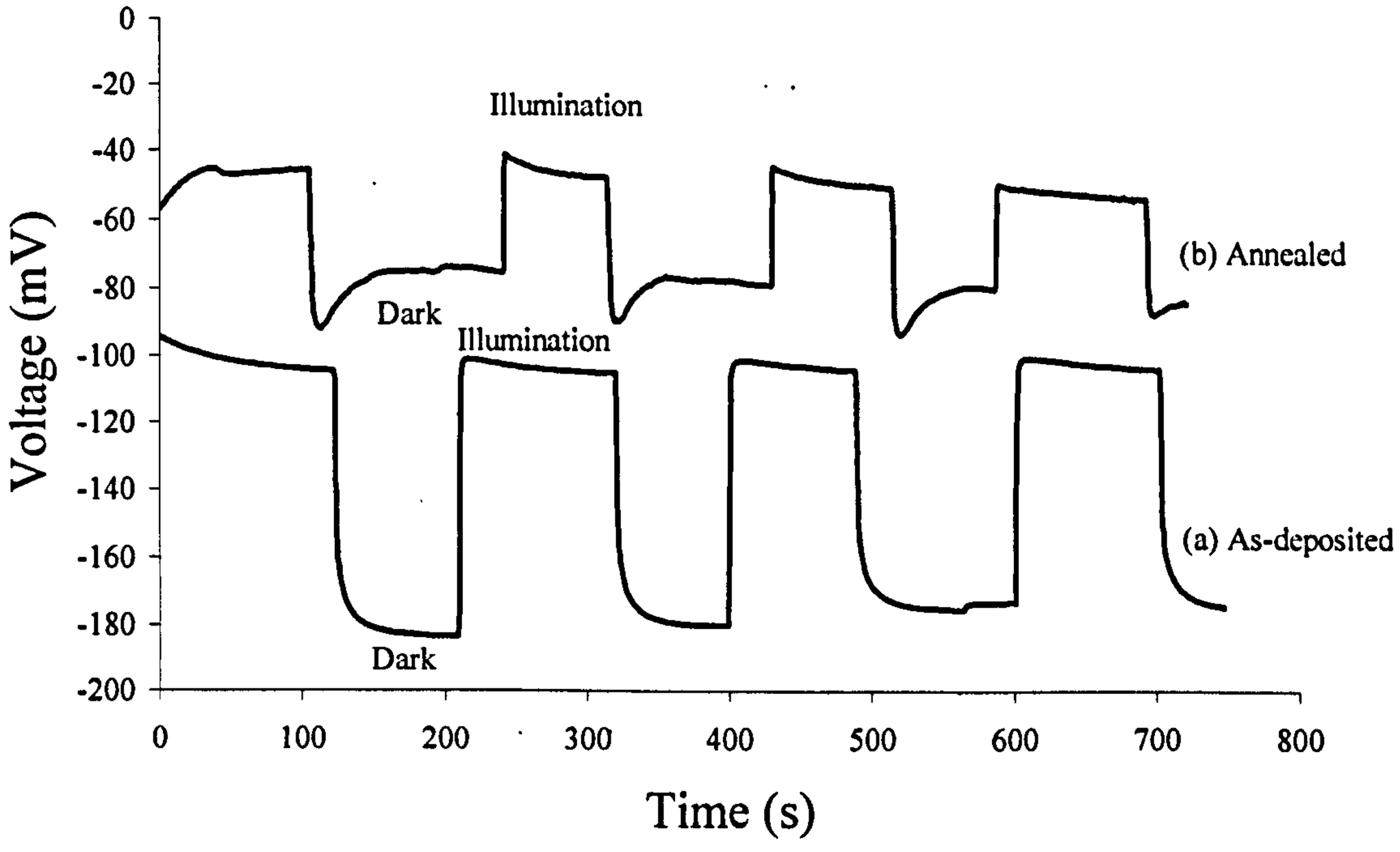

Figure 7.16. Typical PEC signal for glass/FTO/CdTe for (a) as-deposited and (b) annealed material, indicating p-type electrical conductivity.

Figure 7.17 presents the electrical conductivity type of various as-deposited and annealed CdTe layers as a function of growth voltage. The annealed layers followed a similar trend to the as-deposited although the PEC signal decreased after heat-treatment. This may be attributed to the change in doping concentration of the material during heat-treatment which alters the barrier formation at the liquid/solid junction. Both n and p-type electrical conductivity was expected to be observed as it has previously been reported Te-rich layers deposited at more positive voltages are p-type and Cd-rich layers

deposited at more negative voltages are n-type. It is possible this may have been observed if the voltage range had been expanded.

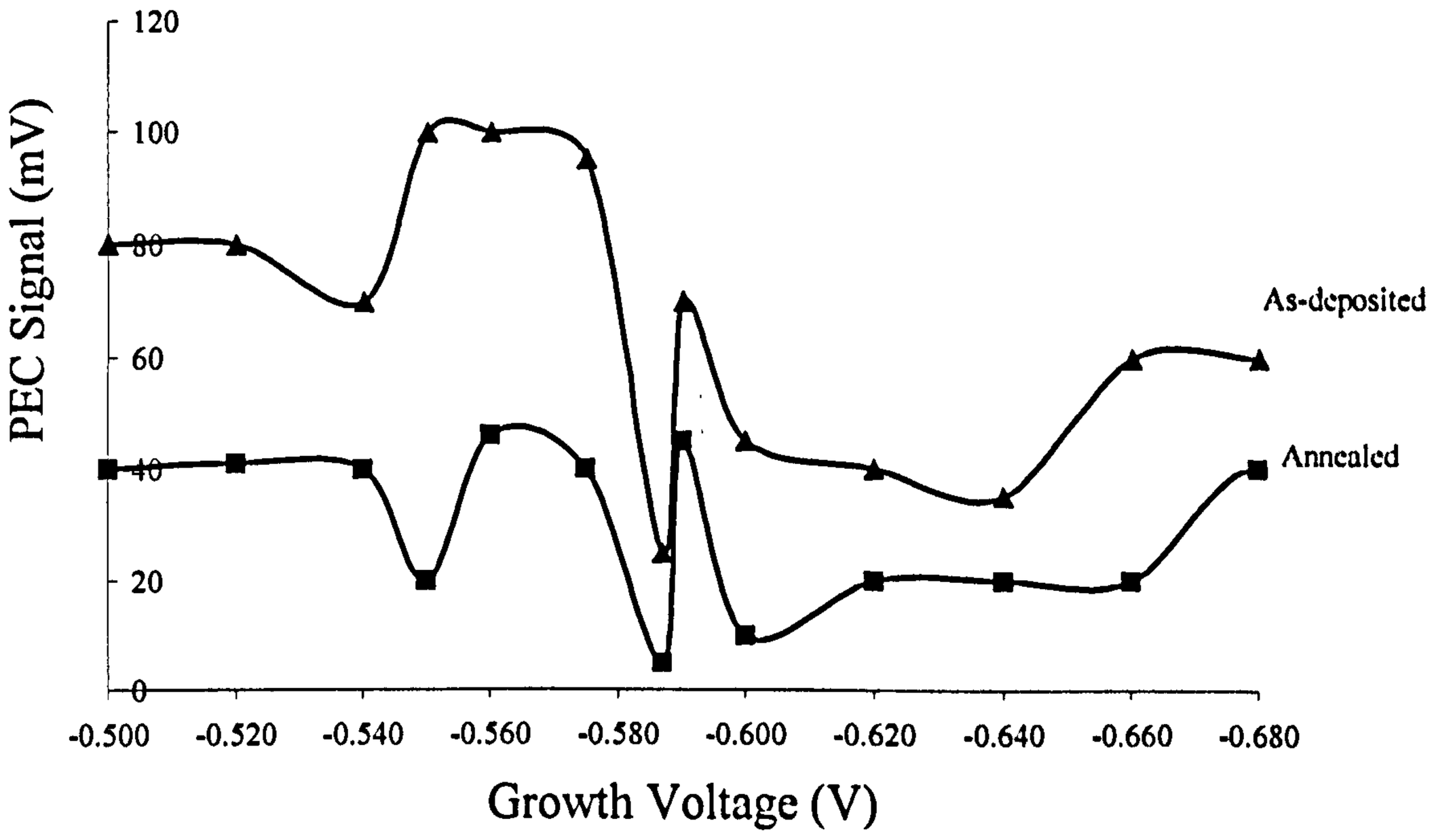

Figure 7.17. PEC signal as a function of growth voltage of as-deposited and annealed glass/FTO/CdTe structures. All material was found to exhibit p-type electrical conductivity.

7.4 Device Fabrication

Prior to metallisation the CdTe layers deposited on glass/FTO/CdS were annealed at 390°C for 6 minutes before being chemically etched. Metal contacts, 2 mm in diameter were evaporated onto the superstrate glass/FTO/CdS/CdTe structures using Cu-Au. Au is a high work function metal forming an ohmic contact to p-type semiconductors or a rectifying contact to n-type material. The presence of Cu in the metal contact ensures the position of the Fermi level close to the valence band due to the p-type doping of the surface layer. Current-voltage measurements were made for glass/FTO/CdS/CdTe/Cu-Au devices to assess the variation of performance as a function of CdTe growth voltage.

A typical log-linear curve taken of glass/FTO/CdS/CdTe/Cu-Au structures under dark conditions is presented in Figure 7.18 for CdTe deposited at -0.620 V vs SCE. These structures indicate rectifying properties with a rectification factor of $\sim 10^3$ at 1.0 V. The ideality factor was n=2.7 and barrier height >1.14 eV taken from the automated

solar simulator. Since the diodes are non-ideal, accurate barrier heights cannot be estimated.

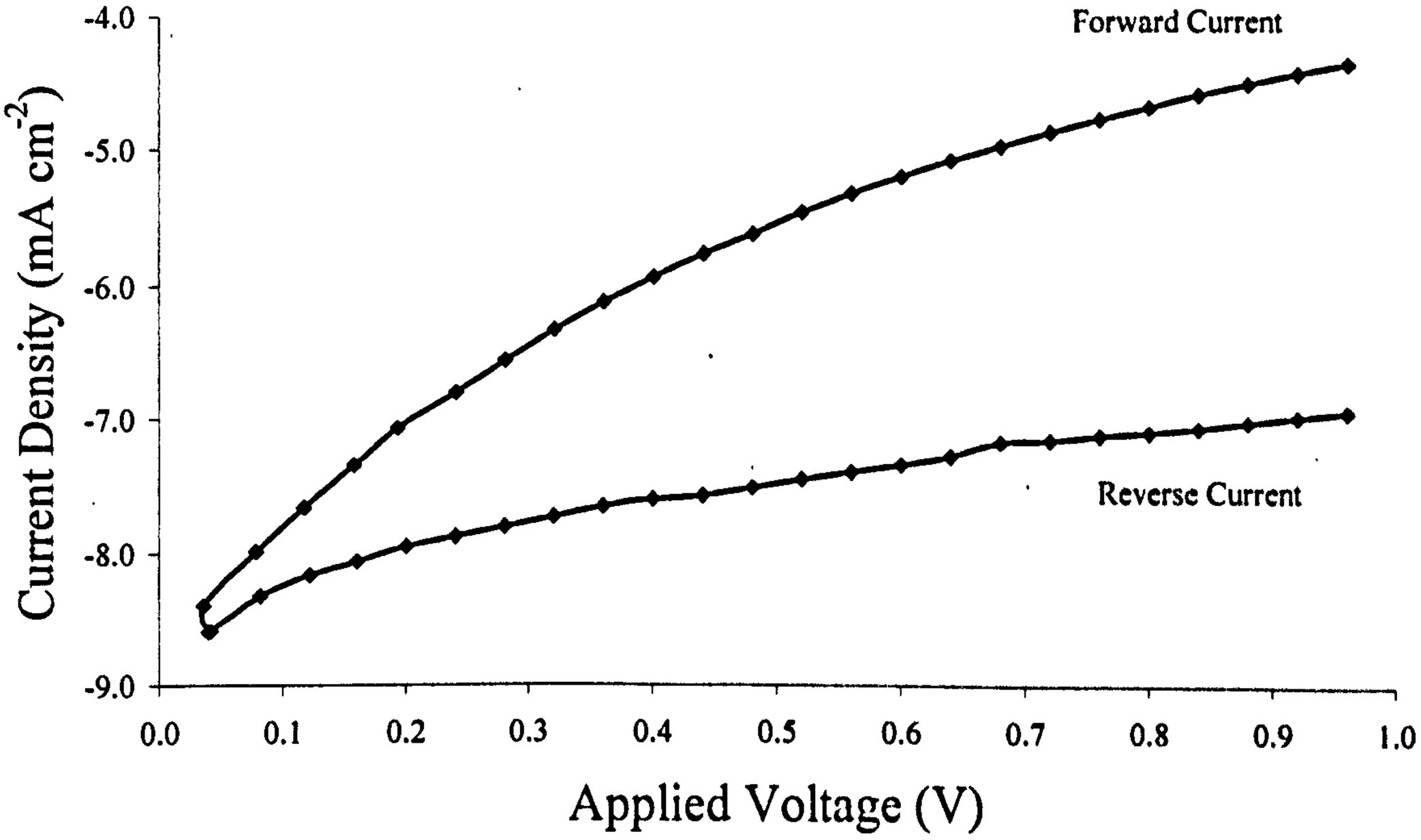

Figure 7.18. Log-linear I-V characteristics of glass/FTO/CdS/CdTe/Cu-Au under illumination; the CdTe was deposited at -0.620 V vs SCE.

The linear I-V curve under dark conditions is presented in Figure 7.19 for the CdTe deposited at -0.620 V vs SCE. The high forward bias region of the linear I-V curve was used to estimate the R_s of the structure. Making use of the known contact area of 0.031 cm^2 and estimated film thickness of 1 μm, the bulk electrical resistivity and electrical conductivity of CdTe were determined using equations 5.2 and 5.3 in Chapter 5. Since the CdTe has the largest thickness (~1000 nm) compared to the negligible thickness of CdS (~80 nm), the total resistance observed was assumed to be created by the CdTe, despite this being the combined effect in reality.

Table 7.13 presents the R_s, ρ and σ as a function of CdTe growth voltage. It is clear the series resistance fluctuates as a function of growth voltage, which is likely to be due to a change in composition of the layers. No pattern emerged to indicate the layers became more conducting when deposited at a more negative deposition voltage closer to the redox potential of Cd^{2+}.

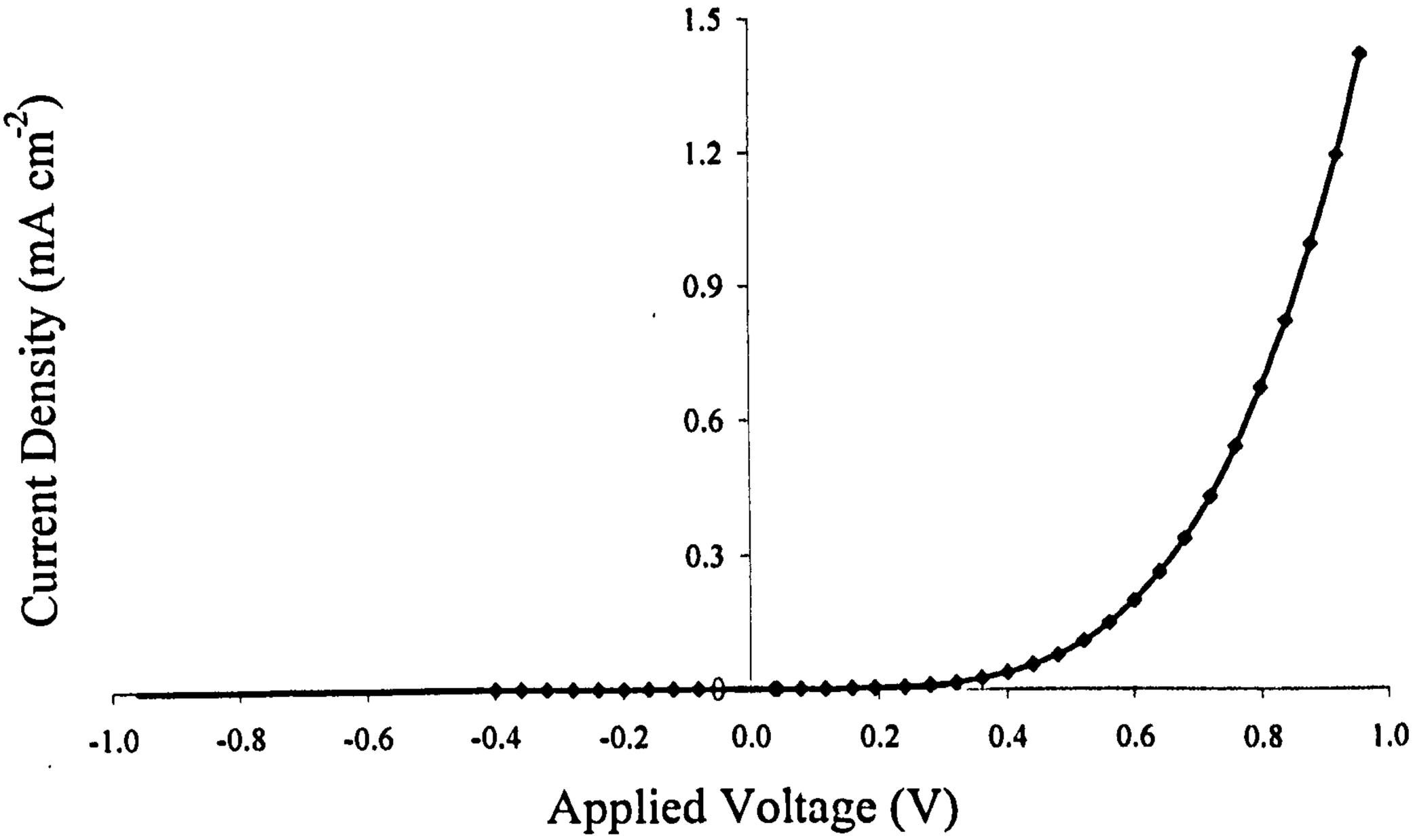

Figure 7.19. Linear I-V characteristics of glass/FTO/CdS/CdTe/Cu-Au under dark conditions; the CdTe was deposited at -0.620 V vs SCE.

Table 7.13. Series resistance, bulk electrical resistivity and electrical conductivity of glass/FTO/CdS/CdTe/Cu-Au, the CdTe layers were deposited at various voltages.

Growth Voltage (V)	R_s (Ω)	ρ (Ω cm)	σ $(\Omega\ cm)^{-1}$
-0.610	125	39×10^3	2.6×10^{-5}
-0.615	364	114×10^3	8.7×10^{-6}
-0.620	1333	419×10^3	2.4×10^{-6}
-0.625	120	38×10^3	2.7×10^{-5}
-0.630	606	190×10^3	5.3×10^{-6}
-0.635	200	63×10^3	1.6×10^{-5}
-0.640	200	63×10^3	1.6×10^{-5}
-0.650	1000	314×10^3	3.2×10^{-6}
-0.660	800	251×10^3	4.0×10^{-6}
-0.670	2222	698×10^3	1.4×10^{-6}
-0.680	667	209×10^3	4.8×10^{-6}
-0.690	1000	314×10^3	3.2×10^{-6}

A typical linear-linear I-V curve for glass/FTO/CdS/CdTe/Cu-Au under illumination is presented in Figure 7.20; the CdTe was electrodeposited at -0.620 V vs SCE. The I-V curve was used to determine the solar cell parameters of V_{oc}=500 mV, J_{sc}=15 mA cm^{-2} and FF=0.40. The shunt resistance was determined as R_{sh}=0.1 Ω. Since the light source was not calibrated accurately, device efficiency cannot be calculated.

Figure 7.21 illustrates the device performance for layers deposited at -0.680 V vs SCE. More negative growth voltages than -0.670 V vs SCE produced poor PV devices with high electrical conduction, most likely to be due to Cd-richness. Figure 7.22 is a enlarged version of Figure 7.21 to illustrate the shape of the curve more clearly, indicating a V_{oc} of 100 mV. The shunt resistance was determined at R_{sh}=0.01 Ω from the reverse bias region.

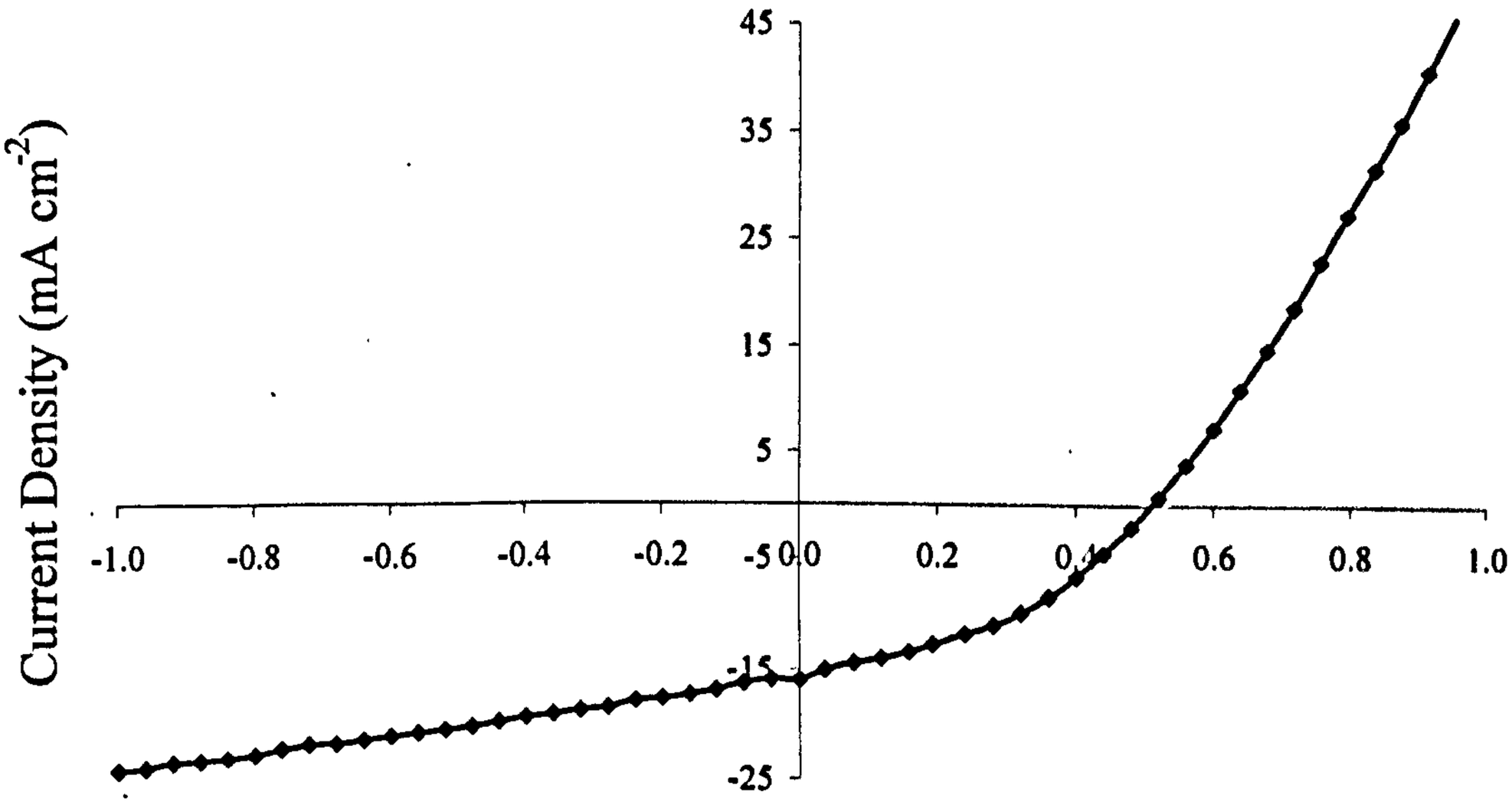

Figure 7.20. Linear I-V characteristics of glass/FTO/CdS/CdTe/Cu-Au under illumination; the CdTe was deposited at -0.620 V vs SCE.

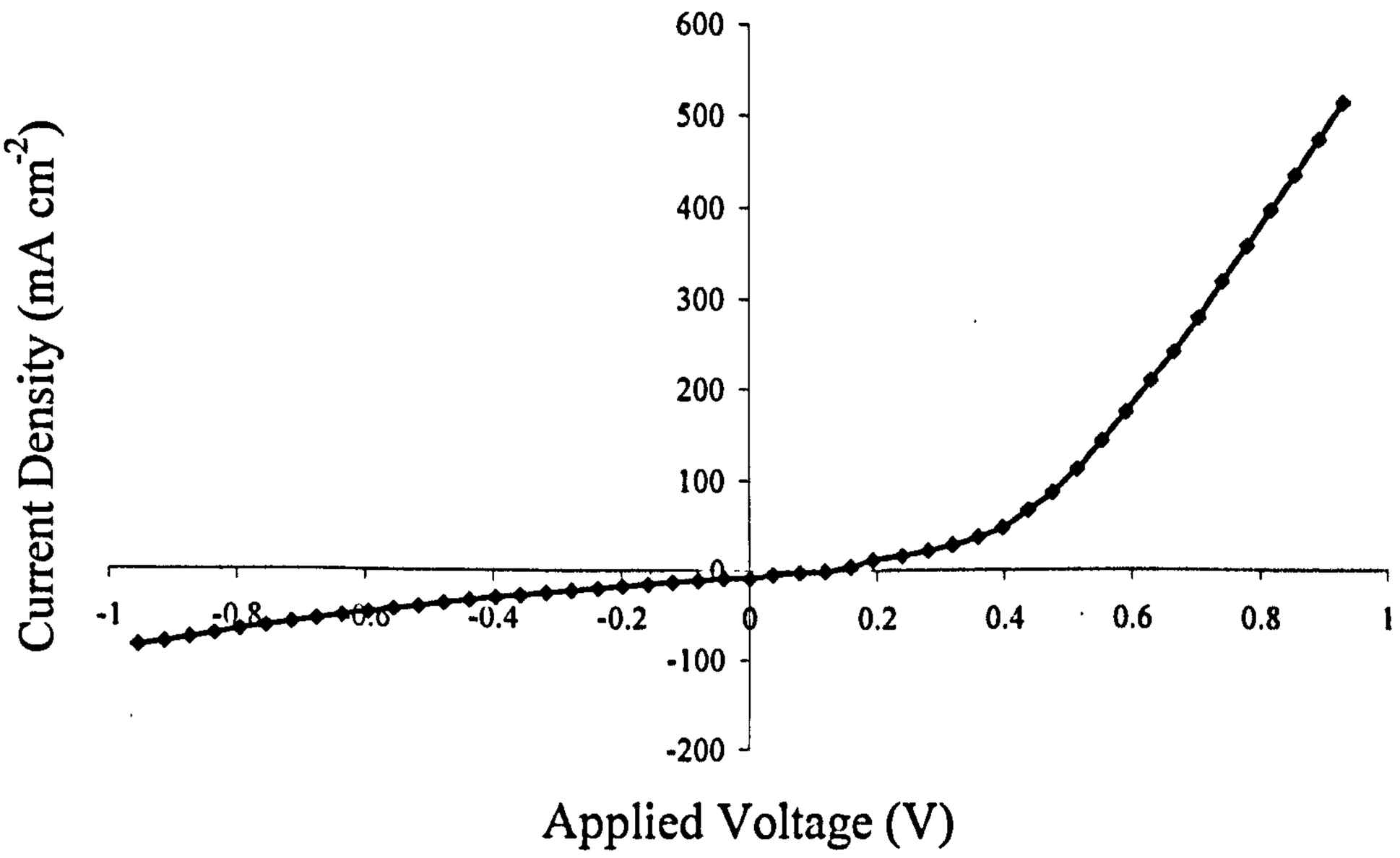

Figure 7.21. Linear I-V characteristics of glass/FTO/CdS/CdTe/Cu-Au under illumination; the CdTe was deposited at -0.680 V vs SCE

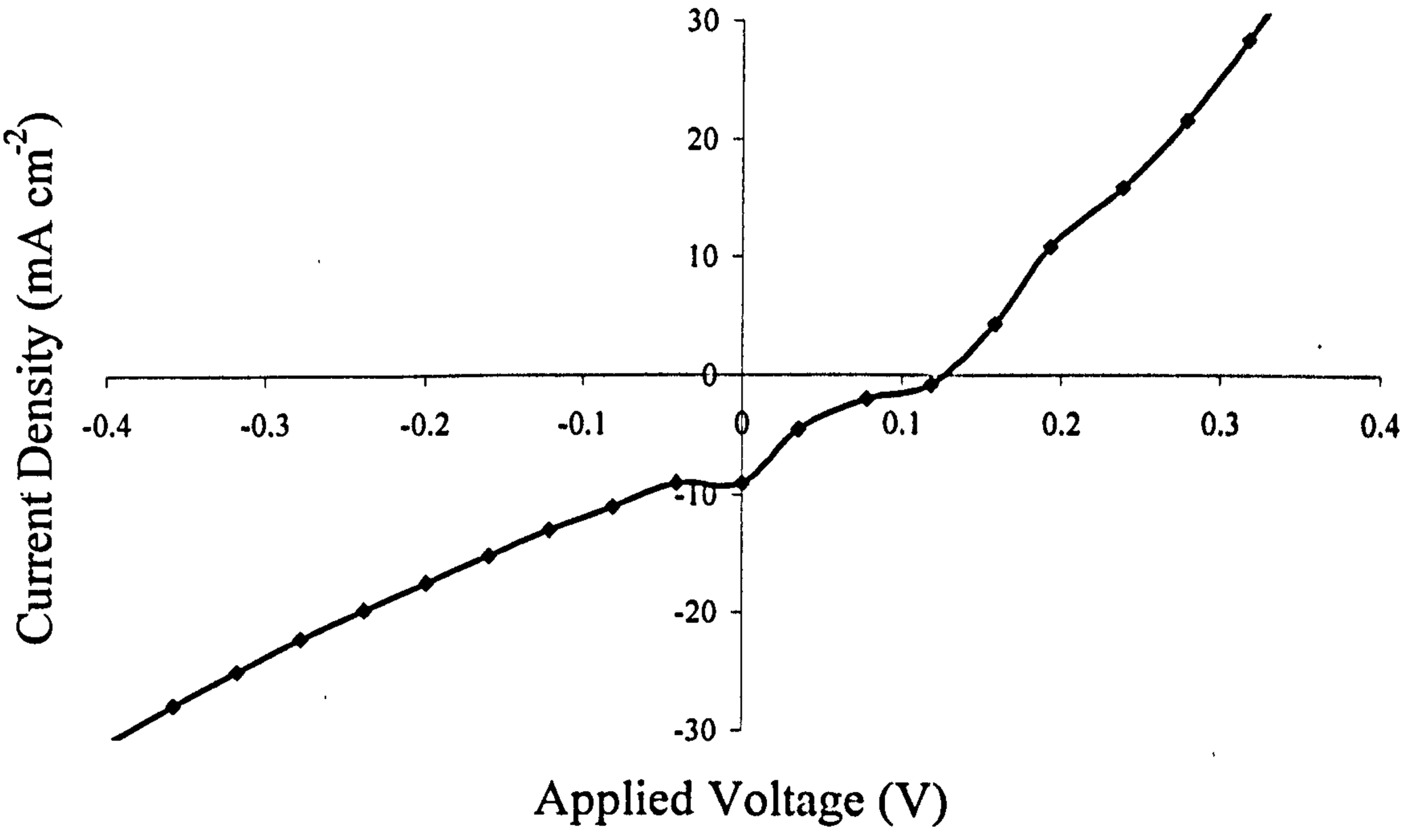

Figure 7.22. Enlarged linear I-V characteristics of the curve presented in Figure 7.21.

Table 7.14 presents average device parameters for glass/FTO/CdS/CdTe/Cu-Au as a function of CdTe growth voltage. The efficiency is only approximate as the light source was not calibrated. This set of device parameters were obtained for the optimised annealing conditions discussed in Section 7.3.2. The V_{oc}, J_{sc} and FF were plotted as a function of growth voltage and are presented in Figures 7.23 to 7.25 respectively. It is clear the V_{oc} fluctuates and reduces for more negative growth voltages between -0.660 to -0.690 V vs SCE. The decrease in V_{oc} may be attributed to the change in composition with growth voltage. It is expected the layers are more Cd-rich at more negative growth voltages which are closer to the redox potential of Cd^{2+}. The layers deposited at -0.615, -0.625 and -0.635 V vs SCE were deposited after all other layers to optimise the growth voltage in the region with highest device parameters. The fluctuation in V_{oc} is expected to be due to the change in composition of the layers as a function of growth voltage and the Te concentration in solution.

Table 7.14. Device parameters of glass/FTO/CdS/CdTe/Cu-Au as a function of the deposition voltage of CdTe, note the efficiency is approximate as the light source was not calibrated.

V_g (V)	V_{oc} (mV)	V_{max} (mV)	J_{sc} (mA cm^{-2})	J_{max} (mA cm^{-2})	FF	Efficiency (%)
-0.610	350	195	3.4	2.0	0.33	0.4
-0.615	300	195	6.8	4.5	0.43	0.9
-0.620	525	295	15.0	10.0	0.40	3.0
-0.625	300	175	3.1	2.0	0.38	0.4
-0.630	500	290	10.0	8.0	0.46	2.0
-0.635	420	200	4.5	3.5	0.48	0.9
-0.640	540	295	6.1	5.0	0.45	1.5
-0.650	450	250	3.2	2.5	0.43	0.6
-0.660	380	230	8.0	5.0	0.38	1.0
-0.670	410	200	9.1	6.5	0.35	1.0
-0.680	120	75	10.0	5.0	0.31	0.4
-0.690	300	150	10.0	7.5	0.39	1.0

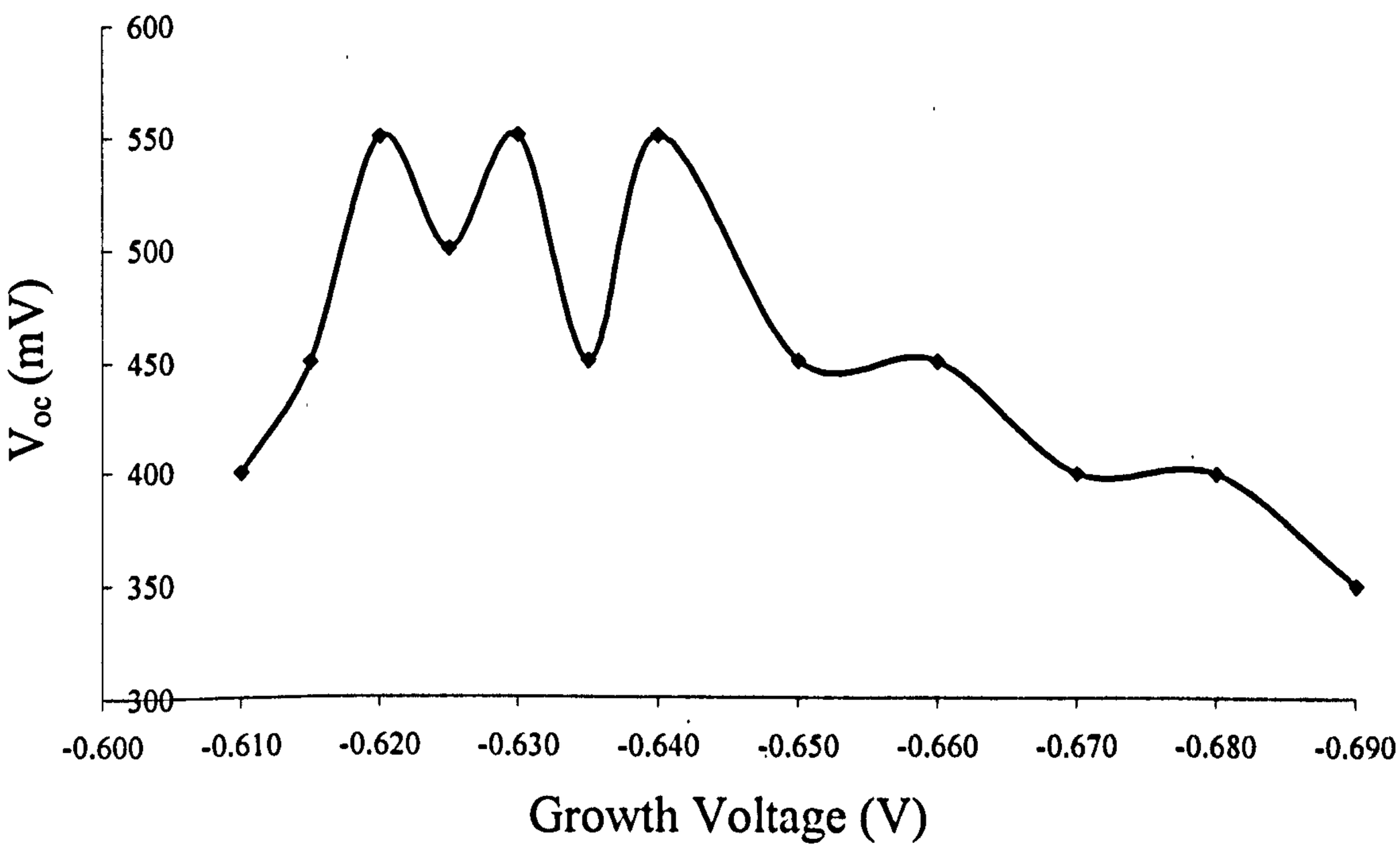

Figure 7.23. Open circuit voltage of glass/FTO/CdS/CdTe/Cu-Au devices as a function of CdTe growth voltage.

The J_{sc} fluctuated and was maximum for layers deposited at -0.620 and -0.630 V vs SCE. The J_{sc} is dependent on the grain structure and improves for material with lower defect density; a parameter that is dependent on the annealing stage. Annealing the layers increases the grain size and decreases grain boundaries, which improves the J_{sc} as

there are fewer charge carrier traps. The FF was calculated using equation (1.2) presented in Chapter 1 and was found to fluctuate as a function of growth voltage. The fluctuation in device parameters suggests a change in bath composition over time. The high molarity of Cd prevents significant change in the availability of this element as a function of time. On the contrary, Te has a low solubility in aqueous solution and fluctuated during the growth. Te is known to control the rate of growth thus a reduction in growth current indicated the decrease of available Te [Meulenkamp & Peter 1996]. The current density was monitored during the growth of each layer although some fluctuations were unavoidable. The composition was also expected to vary as a function of growth voltage.

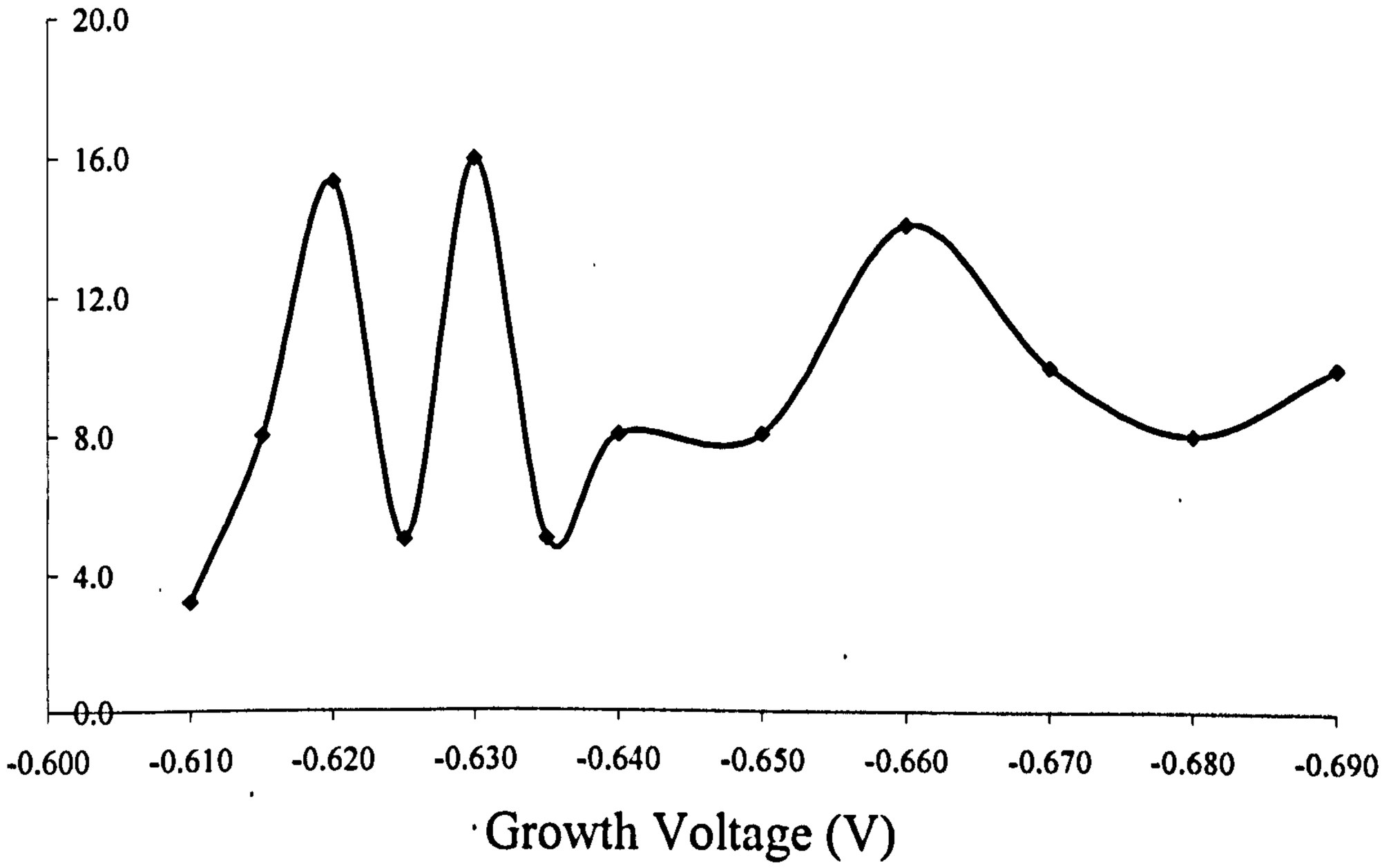

Figure 7.24. Short circuit current of glass/FTO/CdS/CdTe/Cu-Au devices as a function of CdTe growth voltage.

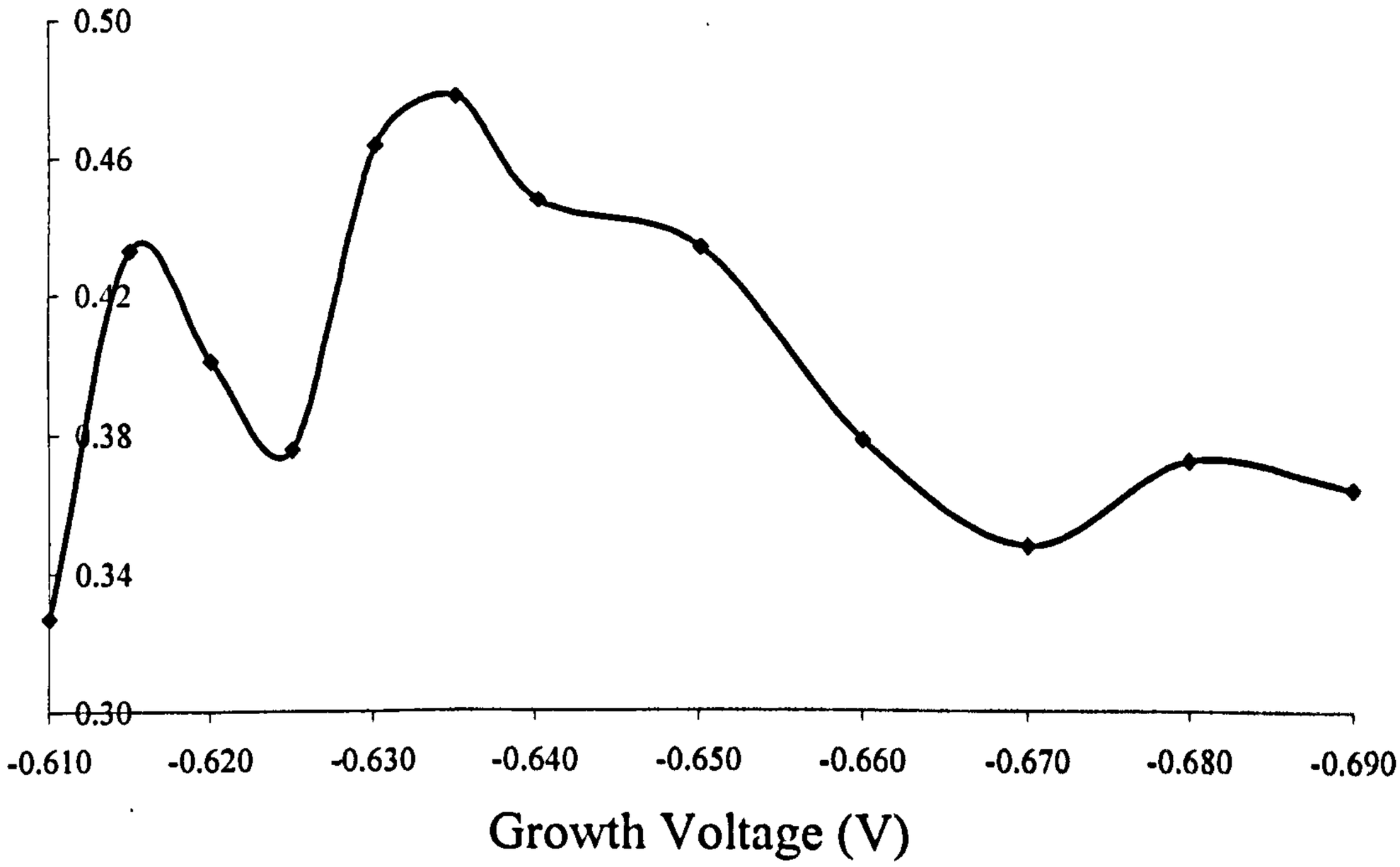

Figure 7.25. Fill factor of glass/FTO/CdS/CdTe/Cu-Au devices as a function of the CdTe growth voltage.

All metallised layers were tested for reproducibility by measuring the I-V parameters of each device as illustrated by Figure 7.26. Several working devices from the array were observed although the parameters varied between devices. This suggests non-uniformity of composition of the CdTe layer and in the case of ohmic behaviour the metal contact may be covering a pin-hole. The range of device parameters observed for a layer deposited at -0.640 V vs SCE is presented in Table 7.15. The metallised layers were ~2 cm^2, containing an array of 2 mm diameter metal contacts (A=0.031 cm^2). Further optimisation must be considered to attempt improved uniformity over the layer. This may include surface treatment of the CdS prior to CdTe deposition or modified electrical contact during growth for improved voltage distribution.

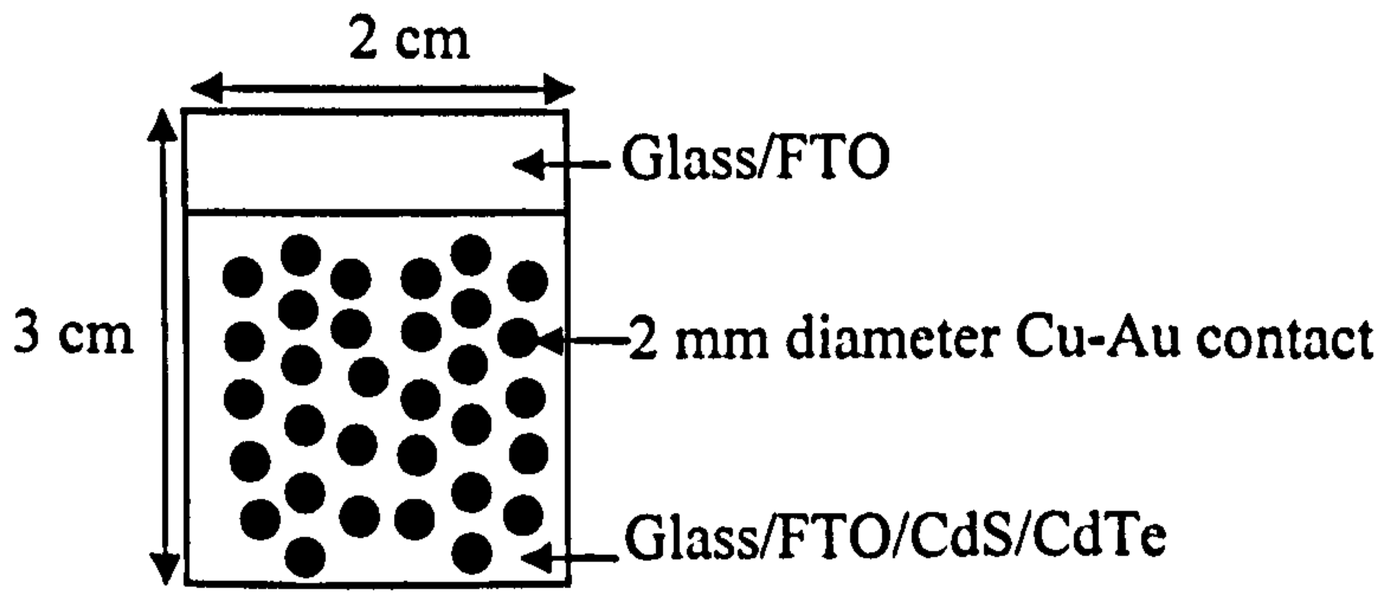

Figure 7.26. Diagram of glass/FTO/CdS/CdTe/Cu-Au illustrating the spread of devices on a single layer.

Table 7.15. Device parameters of glass/FTO/CdS/CdTe/Cu-Au for CdTe deposited at -0.640 V vs SCE illustrating uniformity for various tested devices.

V_{oc} (mV)	J_{sc} (mA cm^{-2})	FF
500	6.6	0.37
520	6.6	0.32
480	6.6	0.35
540	9.6	0.36
500	6.6	0.37
500	15.9	0.34
300	15.9	0.32
540	6.1	0.45
300	12.0	0.38
500	19.1	0.34

7.5 Discussion

CdTe layers have been deposited at a range of deposition voltages from -0.600 to -0.690 V vs SCE. The main difficulty encountered during this investigation was the controllability of the TeO_2 in the solution. The low solubility of this compound means the amount dissolved in the solution at any time remains unknown and inconsistent. Although the current density was monitored throughout the growth of each layer and Te added to the solution when this parameter reduced, this method is inadequate for reproducibility purposes. The availability of Te is the main factor for depositing reproducible layers, an issue which is essential when considering scale-up. The question of improving controllability was not addressed during this investigation. A possibility for future work would be to use a pumping system that enables a controlled amount of Te to be fed into the solution, maintaining a consistent background concentration.

XRD indicated the layers to be similar having preferential orientation in the (111) plane at all deposition voltages although the intensity of the peak varied as a function of growth voltage. The variation in peak intensity was attributed to the change in degree of crystallinity of the layers. The composition and crystallinity were expected to vary with growth voltage and Te concentration in the solution. Annealing the layers did not indicate significant improvement in the XRD spectra with little increase in the height of the (111) peak. Recrystallisation of the CdTe layers was not observed

which has previously been attributed to Te-richness in the literature. This lack of significant change in the structure during heat-treatment and strong nature of the (111) peak suggests the non-uniform crystallographic properties with deposition voltage. Annealing for long periods of time (15 to 60 minutes) and high temperatures (400 to 450°C) destroyed the layers due to oxidation and sublimation. The sublimation may be due to poor adhesion to the substrate and the lack of stoichiometry within the material layer.

The bandgap energy was estimated to be between 1.52 and 1.54 eV which is in agreement with the values reported in the literature for CdTe [Meulekamp & Peter 1996]. The PEC investigation indicated all layers to have p-type electrical conductivity when deposited at growth voltages of -0.500 to -0.690 V vs SCE. It was expected that both electrical conductivity types would be observed as both n and p-type CdTe has been reported in the literature. P-type behaviour is usually associated with Te-rich material and Cd-rich layers yields n-type material [Kampmann *et al.* 1995, Cowache *et al.* 1989, Basol 1988]. Te-richness is achieved by deposition at a relatively positive growth voltage compared to Cd-richness. If the deposition voltage range had been extended, both n and p-type material may be have been established. Further work would need to be carried out to establish CdTe with n-type electrical conductivity and verify the composition of the layers at each growth voltage. It is possible that a p-type dopant such as Cu exists in the solution from the electrical terminals and therefore the material exhibited only p-type electrical conductivity, irrespective of the deposition voltage. One way to address the issue of unwanted Cu would be to replace the electrical terminals with an alternative metal such as Al.

The heat-treatment was optimised at 390°C for 6 minutes producing devices with highest parameters. When heat-treated for longer or at a higher temperature the device performance deteriorated, where the layer totally or partially sublimed. Higher temperatures and longer annealing times may be used for CdTe with a higher degree of stability and adhesion to the substrate. Longer annealing times and higher temperatures are known to increase the grain size further, decreasing the defect density and improving the device performance. These issues were not addressed in this investigation.

SEM indicated the morphology was similar for all deposition voltages investigated between -0.620 to -0.690 V vs SCE. Crystal growth was observed for annealed layers compared to the as-deposited material, which is an important factor for device

performance as grain boundaries and the defect density decreases. The crystal size of annealed layers was between 0.2 to 0.5 μm.

Working solar cell devices were consistently produced during this investigation irrespective of the growth voltage of the CdTe, although some voltages produced improved device parameters. The growth voltage region between -0.630 and -0.650 V vs SCE was found to produce devices with the highest parameters. Growth voltages more negative then -0.670 V vs SCE inhibited the device quality. Ways to further improve the device performance would be to prepare CdTe layers which could withstand higher annealing temperatures and times expecting increased grain size and reduced defect density, improving the J_{sc}. The etching stage was not varied and this could be addressed in future work to optimise the etching time including consideration of different etchants which may improve the device performance. Other parameters that could be optimised for improved device performance are the pH of the solution during growth, solution temperature and substrate surface cleaning.

7.6 Conclusions

In conclusion CdTe has been electrodeposited from aqueous medium at a range of deposition voltages to assess the most suitable growth region. It was determined the highest quality devices were deposited in the range of -0.630 to -0.650 V vs SCE. The heat-treatment stage was optimised at 390°C for 6 minutes for this material. All materials exhibited p-type electrical conductivity. Little improvement in XRD spectra was observed for annealed layers compared to the as-deposited material which exhibited (111) preferential orientation. The bandgap energy was between 1.52 and 1.54 eV for all CdTe layers. SEM indicated crystal growth after annealing with maximum crystallite size of 0.5 μm. All devices fabricated using CdTe grown at -0.610 to -0.690 V vs SCE indicated photovoltaic activity although layers deposited between -0.630 and -0.650 V vs SCE indicated the highest performance, with device parameters of V_{oc}=420-540 mV, J_{sc}=3.2-19.1 mA cm^{-2} and FF=0.48 with approximate efficiency of 5%. Further work must be carried out to improve the controllability of TeO_2 in the solution and ensure reproducibility.

Chapter 8 Recommendations for Future Work

The recommendations for future work in continuation of this research will be discussed separately for $CuInSe_2$ and CdTe based solar cells. Some predictions for the future expectations of this research field will also be briefly described.

8.1 CIS Based Solar Cells

The electrodeposition of $CuInSe_2$ from ethylene glycol was found to produce material with no noticeable improvement compared to that from aqueous solution, despite the elevated growth temperature of 150°C. One of the main difficulties associated with CIS deposition was the annealing stage which proved difficult. Annealing CIS layers without cracking or partial or complete sublimation was challenging. Other complexities preventing the development of CIS were the device processing and fabrication stages. Furthermore the material was of inferior quality indicating substantial work would need to be carried out in the future if this material was to contribute to the PV field. The recommendation on this front is to focus efforts on the growth of CdTe using electrodeposition rather than $CuInSe_2$. The electrodeposition of binary semiconductors such as CdTe is relatively simple compared to growth of ternary or quaternary compounds.

ZnO was electrodeposited from aqueous solution with the aim of development for use in the $CuInSe_2$ device structure. Although ZnO was deposited there were certain difficulties encountered which limited the overall success of this material for fulfilment of the initial objectives. Reproducibility issues of ZnO film growth related to the electrolyte life-time and controllability of oxygen content. The reduction in pH of the solution after heating to 80°C and growth of a few layers left the bath unusable as ZnO is soluble below ~ pH=3. The gradual reduction of oxygen content in the solution and reduction in pH resulted in the deposition of dark metallic Zn layers. The as-deposited and annealed layers did not have a high degree of transparency due to $Zn(OH)_2$ clusters. This cloudiness is not favourable for use in the $CuInSe_2$ device structure as the inherent benefit of using ZnO would be lost.

It is therefore suggested that the use of $Zn(NO_3)_2$ as a reagent for ZnO deposition has limitations especially if considering scale-up. Other alternatives may be considered such as $ZnCl_2$ although in this case oxygen must be bubbled through the solution. The

ZnO layers deposited in this work were not suitable for use in the $CuInSe_2$ solar cell device structure. At this stage it is suggested that growth of ZnO using electrodeposition onto substrate configuration devices is not feasible. Development of ZnO using electrodeposition for devices having the superstrate configuration is an area that may be considered in the future.

In addition to the bath life time issues encountered for ZnO, a rapid decrease in pH was observed on addition of the Al dopant for ZnO:Al electrodeposition. A limited degree of improvement in electrical conductivity was observed for the ZnO:Al compared to i-ZnO. It was concluded that this was related to the high negative redox potential of Al compared to ZnO and Al doping if any was due to the absorption, adoption or chemisorption of Al at the cathode rather than the electrodeposition. Thus little control is available on the doping of ZnO with Al and therefore this growth route is not advised for this material in the future.

8.2 CdTe Based Solar Cells

At the end of this research program the growth procedure for CdTe based solar cells had been established and devices were performing with reasonable cell parameters. Working devices were fabricated over a range of growth voltages with superior performance being observed for materials deposited between -0.630 to -0.650 V vs SCE. Furthermore high uniformity over a 2 cm^2 area completed with an array of 2 mm diameter contacts was observed for devices deposited in this growth voltage range.

Areas that may be addressed in the future are precise optimisation of the growth voltage, in the range already mentioned, for consistent deposition. Gradual scale-up of devices from 4 mm diameter contacts to larger 0.5 cm^2 solar cells may then be considered. This procedure is dependent on the elimination of pin-holes which would cause device shorting and failure. However one major factor influencing pin-holes is the quality of the substrate (glass/FTO/CdS) which according to Pilkington for FTO and observed results is of sufficient quality. The fabrication of devices on other substrates such as glass/FTO/n-ZnO may be considered to observe the effect on device parameters.

Difficulties that may be addressed in the future would be to establish tighter control over the tellurium content in the deposition solution by adopting a more accurate way of adding tellurium to the bath. This may be achieved by means of a calibrated pumping

system or a dosing pump. Another alternative would be to use a different reagent for the source of Te. The only possibility being telluric acid ($H_2TeO_4.2H_2O$) which is soluble in aqueous solution allowing a larger degree of controllability for tellurium.

Further considerations for the development of the device for improved efficiency are to carryout controlled doping experiments. Very few experiments of this nature have been conducted for CdTe to date, although the benefits of iodine doping have already been realised for CdTe devices [Chaure *et al.* 2003]. Other group VII halogens that may be considered for replacement of Te atoms are fluorine (F), chlorine (Cl) or bromine (Br). Similarly group III elements such as boron (B), aluminium (Al), gallium (Ga) or indium (In) may be used to replace Cd atoms with the aim of increasing the electrical conductivity of the material. The doping concentraiton would need to be carefully controlled to optimise the charge carrier concentration to establish ideal doping levels of between 10^{14} to 10^{17} cm^{-3}.

Formation of CdTe graded bandgap structures having p-i-n electrical conductivity may be investigated by exploring the suitable growth voltage for production of such material. PEC may be used to monitor the electrical conductivity type of deposited layers. Predictions for the future of CdTe based devices is the improved efficiency and lower cost due to innovative breakthroughs as a result of the better understanding of solar cell device physics, coupled with the advantage of lower cost growth using electrodeposition. In addition the radical thinking which has come into the public domain in recent years [Dharmadasa *et al.* 2002, 2003, 2005, Chaure *et al.* 2003] will tackle the fundamental issues that have caused stagnation of the CdTe solar cell at 16.5% efficiency [Wu *et al.* 2001].

Table of Abbreviations

Abbreviation	Definition
λ	Wavelength
α	Absorption Coefficient
ρ	Electrical Resistivity
σ	Electrical Conductivity
ε_r	Relative Permittivity
ε_0	Permittivity of Free Space
ε_s	Relative Permittivity × Permittivity of Free Space
μ	Mobility
k	Boltzmann Constant
A	Area
A^*	Richardson Constant
Abs	Absorbance
Ag/AgCl	Silver/Silver Chloride
Al-N/Al	Aluminium-Nitride, Aluminium
AM 1.5	Air Mass 1.5
BP	British Petroleum
c	Speed of Light
C	Capacitance
CBD	Chemical Bath Deposition
Cd_i	Cadmium Interstitial
CdS	Cadmium Sulphide
CdTe	Cadmium Telluride
$CuInSe_2$ or CIS	Copper Indium Diselenide
$CuInGaSe_2$ or CIGS	Copper Indium Gallium Diselenide
$CuInGa(SeS)_2$ or CIGSS	Copper Indium Gallium Sulphur Selenide
C-V	Capacitance-Voltage
d	d-Spacing
D	Grain Size
DC	Direct Current
DMSO	Dimethyl Sulfoxide
e	Electronic Charge
E_C	Conduction Band
EDX	Energy Dispersive X-Ray Analysis
E_F	Fermi Level
E_g	Bandgap Energy
E_p	Photon Energy

Table of Abbreviations

E_v	Valence Band
FF	Fill Factor
FTO	Fluorine Doped Tin Oxide
FWHM	Full Width Half Maximum
(hkl)	Miller Indices
h	Planck's Constant
HV	High Vacuum
I	Light Intensity
I_0	Intensity of the Incident Radiation
I_F	Forward Bias
I_m	Maximum Current
IR	Infra-Red
I_r	Reverse Bias
I_{sc}	Short Circuit Current
I-V	Current-Voltage
i-ZnO	Intrinsic Zinc Oxide
JCPDS	Joint Committee on Power Diffraction Standards
J_{sc}	Short Circuit Current Density
LBIC	Laser Beam Induced Current
M	Molar Mass
MIS	Metal-Insulator-Semiconductor
MOCVD	Metal Organic Chemical Vapour Deposition
MS	Metal-Semiconductor
n	Ideality Factor
N_d or N_a	Doping Concentration
NHE	Normal Hydrogen Electrode
NREL	National Renewable Energy Laboratory
ODC	Orderered Defect Compound
PEC	Photoelectrochemical Cell
P_{in}	Input Power
POI	Point Orientation Index
PV	Photovoltaic
PVD	Physical Vapour Deposition
r.f.	Radio Frequency
R	Resistance

R_s	Series Resistance
R_{sh}	Shunt Resistance
RTA	Rapid Thermal Annealing
SCE	Saturated Calomel Electrode
SEM	Scanning Electron Microscopy
T	Temperature (K)
TCO	Transparent Conductive Oxide
Te_i	Tellurium Interstitial
UHV	Ultra High Vacuum
UV	Ultra violet
V_{Cd}	Cadmium Vacancy
V_{dark}	Voltage in the Dark
V_F	Forward Bias
V_{light}	Voltage Under Illumination
V_m	Maximum Voltage
V_o	Oxygen Vacancy
V_{oc}	Open Circuit Voltage
V_R	Reverse Bias
V_{Te}	Tellurium Vacancy
W	Depletion Width
XRD	X-Ray Diffraction
Zn_i	Zinc Interstitial
ZnO	Zinc Oxide
$Zn(OH)_2$	Zinc Hydroxide

Appendix

Publications

Directly related to this research

- **JS Wellings,** AP Samantilleke, SN Heavens, P Warren, IM Dharmadasa 'Electrodeposition of $CuInSe_2$ from Ethylene Glycol at High Temperature', submitted to Solar Energy Material and Solar Cells (09/08).

- **JS Wellings**, AP Samantilleke, P Warren, SN Heavens, IM Dharmadasa, 'Comparison of Electrodeposited and Sputtered Intrinsic and Aluminium Doped Zinc Oxide Thin Films', Semiconductor Science and Technology 23 (2008) 125003.

- **JS Wellings**, NB Chaure, SN Heavens, IM Dharmadasa, 'Growth and Characterisation of Electrodeposited Zinc Oxide Thin Films', Thin Solid Films 516 (2008) 3893.

- **JS Wellings**, NB Chaure, SN Heavens, P Warren, IM Dharmadasa, 'Characterisation of Electrodeposited and Sputtered Zinc Oxide', Proceedings 22nd European Photovoltaic Solar Energy Conference, Milan, Italy (2007).

Unrelated to this research

- ABMO Islam, NB Chaure, **JS Wellings**, G Tolan, IM Dharmadasa, 'Development of Electrodeposited ZnTe Layers as Window Materials in ZnTe/CdTe/CdHgTe Multi-Layer Solar Cells' Materials Characterisation 60 (2) (2009) 160.

- IM Dharmadasa, NB Chaure, O Islam, **J Wellings,** T Maddock, 'Electrodeposition of Copper Indium Gallium Sulphur Selenide Thin Films using a Two-Electrode System for Applications in Solar Cells', Proceedings 21st European Photovoltaic Solar Energy Conference Dresden Germany (2006)

- NC Hyatt, MC Stennett, SG Fiddy, **JS Wellings**, SS Dutton, ER Maddrell, AJ Connelly, WE Lee, 'Synthesis and Characterisation of Transition Metal Substituted Barium Hollandite Ceramics' Material Research Society 932 (2006) 583.

Atkins P, Paula JD, Elements of Physical Chemistry 4th Edition, Oxford University Press (2005).

Barker J, Calif SJ, Marshall RJ, Sadeghi M, US Patent 5,478,445 December (1995).

Basol BM, Journal of Applied Physics 55 (2) (1984) 601.

Basol BM, Solar Cells 23 (1988) 69.

Bhattacharya RN, Rajeshwar K, Solar Cells 16 (1986) 237.

Bhattacharya RN, Batchelor W, Wiesner H, Hasoon F, Granata JE, Ramanathan K, Alleman J, Keane J, Mason A, Matson RJ, Noufi RN, Journal of the Electrochemical Society 145 (10) (1998) 3435.

Bhattacharya RN, Contreras MA, Keane J, Tennant AL, Tuttle JR, Ramanathan K, Noufi R, Preparation of copper indium gallium diselenide films for solar cells, U.S. Patent 5 804 054 (1998).

Bhattacharya RN, Batchelor W, Hiltner JF, Sites JR, Applied Physics Letters 75 (1999) 1431.

Bhattacharya RN, Hiltner JF, Batchelor W, Contreras MA, Noufi RN, Sites JR, Thin Solid Films 361 (2000) 396.

Bhattacharya RN, Ramanathan K, Gedvilas L, Keyes B, Journal of Physics and Chemistry of Solids 66 (2005) 1892.

Bikkulova NN, Danilkin SA, Fuess H, Yadrovskii EL, Beskrovnyi AI, Skomorokhov AN, Yagafarova ZA, Asylguzhina GN, Crystallography Reports 48 (2003) 273.

Birkmire RW, Solar Energy Material & Solar Cells 65 (2001) 17.

Boyle G, Renewable energy, Oxford University Press, Open University, (2004).

Bragg WL, Proceedings of the Cambridge Philosophical Society, 17 (1913) 43.

Bunshah RF, Handbook of Deposition Technologies for Films and Coatings: Science Technology and Applications, Park Ridge New Jersey Publications, (1994).

Calixto ME, Dobson KD, McCandless BE, Birkmire RW, Materials Research Society Symposium Proceedings 865 (2005) 431.

Calixto ME, Dobson KD, McCandless BE, Birkmire RW, Journal of the Electrochemical Society 153 (6) (2006) G521.

Canava B, Lincot D, Journal of Applied Electrochemistry 30 (2000) 711.

Canava B, Vigneron J, Etcheberry A, Guimard D, Guillemoles JF, Lincot D, Ould Saad Hamatly S, Djebbour Z, Mencaraglia D, Thin Solid Films 403 (2002) 425.

Chang JF, Hon MH, Thin Solid Films 386 (2001) 79.

Chaure NB, Samantilleke AP, Dharmadasa IM, Solar Energy Materials & Solar Cells 77 (2003) 303.

Chaure NB, Bordas S, Samantilleke AP, Chaure SN, Haigh J, Dharmadasa IM, Thin Solid Films 437 (2003) 10.

Chaure NB, Chaure S, Pandey RK, Solar Energy Materials & Solar Cells 81 (2004) 39.

Chaure NB, Samantilleke AP, Burton RP, Young J, Dharmadasa IM, Thin Solid Films 472 (2005) 212.

Chassaing E, Ramdani O, Grand PP, Guillemoles JF, Lincot D, Physica Status Solidi (c) 5 (11) (2008) 3445.

Chu TL, Chu SS, Ferekides C, Wu CQ, Britt J, Wang C, IEEE CH2953 (1991) 952.

Contreras MA, Egaas B, Ramanathan K, Hiltner J, Swaetzlander A, Hasoon F, Noufi R, Progress in Photovoltaics Research and Applications 7 (1999) 311.

Contreras MA, Romero MJ, To B, Hasoon F, Noufi R, Ward S, Ramanathan K, Thin Solid Films 403 (2002) 204.

Contreras MA, Ramanathan K, Abushama J, Hasoon F, Young Dl, Egaas B, Noufi R, Progress in Photovoltaics Research and Applications 13 (2005) 209.

Cooray NF, Kushiya K, Fujimaki A, Sugiyama I, Miura T, Okumura D, Sato M, Ooshita M, Yamase O, Solar Energy Materials & Solar Cells 49 (1997) 291.

Cowache P, Lincot D, Vedel J, Journal of the Electrochemical Society 136 (6) (1989) 1646.

Cullity BD, Stock SR, Elements of X-Ray Diffraction 3rd Edition, New Jersey Prentice Hall (2001).

Cunningham DW, Rubcich M, Skinner D, Progress in Photovoltaics: Research and Applications 10 (2002) 159.

Dang WL, Fu YQ, Luo JK, Flewitt AJ, Milne WI, Superlattices and Microstructures 42 (2007) 89.

Das SK, Morris GC, Solar Energy Materials & Solar Cells 28 (1993) 305.

Dennison S, Journal of Material Chemistry 4 (1) (1994) 41.

Dharmadasa IM, Thornton JM, Williams RH, Applied Physics Letters 54 (2) (1989) 137.

Dharmadasa IM, Progress in Crystal Growth and Characterisation 36 (4) (1998) 249.

Dharmadasa IM, Samantilleke AP, Chaure NB, Young J, Semiconductor Science and Technology 17 (2002) 1238.

Dharmadasa IM, Chaure NB, Young J, Samantilleke AP, Delsol T, Semiconductor Science & Technology 18 (2003) 813.

Dharmadasa IM, Solar Energy Materials & Solar Cells 85 (2005) 293.

Dharmadasa IM, Roberts JS, Hill G, Solar Energy Materials & Solar Cells 88 (2005) 413.

Dharmadasa IM, Bunning JD, Samantilleke AP, Shen T, Solar Energy Materials & Solar Cells 86 (2005) 373.

Dharmadasa IM, Haigh J, Journal of the Electrochemical Society 153 (1) (2006) 1.

Dharmadasa IM, Tolan GJ, Roberts JS, Hill G, Ito S, Liska P, Grätzel M, 21st European Solar Energy Conference, 5-8th September 2006, Dresden Germany.

Dharmadasa IM, GJ Tolan, Cazaux M, Semiconductor Science & Technology 23 (2008) 035023.

Dharmadasa IM, Chaure NB, Samantilleke AP, Hassan A, Solar Energy Materials & Solar Cells 92 (2008) 923.

Duffy NW, Peter LM, Wang RL, Lane DW, Rogers KD, Electrochimica Acta 45 (2000) 3355.

Duffy NW, Lane D, Ozsan ME, Peter LM, Rogers KD, Wang RL, Thin Solid Films 361-362 (2000) 314.

Duffy NW, Peter LM, Wang RL, Journal of Electroanalytical Chemistry 532 (2002) 207.

Ellmer K, Journal of Physics D: Applied Physics 33 (2000) R17.

Engelken RD, Van Doren TP, Journal of the Electrochemical Society, Electrochemical Science and Technology 132 (12) (1985) 2910.

Esaki L, Physical Reviews 109 (1958) 603.

Etcheberry A, Iranzo-Marin F, Novakovic E, Triboulet R, Debiemme-Chouvy C, Journal of Crystal Growth 184/185 (1998) 213.

Ezema FI, Osuji RU, Chalcogenide Letters 4 (6) (2007) 69.

Ferekides C, Britt J, Solar Energy Materials & Solar Cells 35 (1994) 255.

Fernandez AM, Bhattacharya RN, Thin Solid Films 474 (2005) 10.

First Solar Inc (2009), Lowering the cost of solar electricity, www.firstsolar.com/technology, accessed (04/2009)

Gal D, Hodes G, Lincot D, Schock HW, Thin Solid Films 361-362 (2000) 79.

Gibson PN, Maker MA, Dunlop ED, Ozsan ME, Lincot D, Froment M, Agostinelli G, Thin Solid Films 387 (2001) 92.

Goetzberger A, Hebling C, Schock HW, Materials Science and Engineering R 40 (2003) 1.

Goodhew P, Humphreys J, Beanland R, Electron Microscopy and Analysis 3rd Edition London: Taylor & Francis, (2001).

Goux A, Pauporte T, Chivot J, Lincot D, Electrochimica Acta 50 (2005) 2239.

Govender K, Boyle DS, Kenway PB, O'Brien P, Journal of Materials Chemistry 14 (2004) 2575.

Gracia L, Beltran A, Andres J, Journal of Physical Chemistry B 111 (2007) 6479 http://cds.dl.ac.uk/ accessed 07/08.

Grätzel M, Nature 414 (2001) 338.

Green MA, Progress in Photovoltaics: Research & Application 9 (2001) 123.

Green MA, Physica E 14 (2002) 11.

Green MA, Solar Energy 76 (2004) 3.

Green MA, Progress in Photovoltaics: Research & Applications 15 (2007) 425.

Guimard D, Grand PP, Bordereau N, Cowache P, Guillemoles JF, Lincot D, Taunier S, Ben-Farah M, Mogensen P, Kerrec O, 29th IEEE Photovoltaic Specialists Conference, (2002) New Orleans 692.

Gupta A, Matulionis J, Drayton J, Compaan AD, Materials Research Society Symposium Proceedings 668 (2001) H6.4.1.

Hammond C, The Basics of Crystallography and Diffraction, Oxford University Press (1997).

Hammond R, The World in 2030, editions yago, (2007) section 2.

Hariskos D, Powalla M, Chevaldonnet N, Lincot D, Schindler A, Dimmler B, Thin Solid Films 387 (2001) 179.

Hodes G, Cahen D, Solar Cells 16 (1986) 245.

Howson RP, Pure & Applied Chemistry 66 (6) (1994) 1311.

Ingham B, Illy B, Ryan P, Current Applied Physics 8 (2008) 455.

Ihlal A, Bouabid K, Soubane D, Nya M, Ait-Taleb-Ali O, Amira Y, Outzourhit A, Nouet G, Thin Solid Films 515 (2007) 5852.

Ishizuka S, Sakurai K, Yamada A, Matsubara K, Fons P, Iwata K, Nakamura S, Kimura Y, Baba T, Nakanishi H, Kojima T, Niki S, Solar Energy Materials & Solar Cells 87 (2005) 541.

Izaki M, Omi T, Journal of the Electrochemical Society 143 (3) (1996) L53.

Izaki M, Omi T, Applied Physics Letters 68 (17) (1996) 2439.

Izaki M, Omi T, Journal of the Electrochemical Society 144 (6) (1997) 1949.

Jaswon MA, Rose MA, Crystal Symmetry, Theory of Colour Crystallography, Ellis Horwood (1983).

Jayakrishnan R, Hodes G, Thin Solid Films 440 (2003) 19.

Jenkins R, X-ray Fluorescence Spectrometry, New York Wiley, (2001).

Johnson DR, Thin Solid Films 361-362 (2000) 321.

Jost S, Schurr R, Hergert F, Hock R, Schulze J, Kirbs A, Voβ T, Purwins M, Palm J, Mys I, Solar Energy Materials & Solar Cells 92 (4) (2008) 410.

Kampmann A, Cowache P, Vedel J, Lincot D, Journal of Electroanalytical Chemistry 387 (1995) 53.

Kampmann A, Lincot D, Journal of Electroanalytical Chemistry 418 (1996) 73.

Karg FH, Solar Energy Materials & Solar Cells 66 (2001) 645.

Kemell M, Dartigues F, Ritala M, Leskela M, Thin Solid Films 434 (2003) 20.

Kemell M, Ritala M, Leskelä M, Critical Reviews in Solid State and Material Science 30 (2005) 1.

Kessler J, Sicx-Kurdi J, naghavi N, Guillemoles JF, Lincot D, Kerrec O, Lamirand M, Legras L, Mogensen P, 20th European Photovoltaic Solar Energy Conference 6-10th June (2005), Barcelona Spain.

Kois J, Bereznev S, Mellikov E, Öpik A, Thin Solid Films 511 (2006) 420.

Konovalov I, Thin Solid Films 451-452 (2004) 413.

Kreith D, Goswami DY, Handbook of Energy Efficiency and Renewable Energy, Boca Raton; London: Taylor & Francis, (2007).

Kroger FA, Journal of the Electrochemical Society 125 (12) (1978) 2028.

Kushiya K, Tachiyuki M, Nagoya Y, Fujimaki A, Sang B, Okumura D, Satoh M, Yamase O, Solar Energy Materials & Solar Cells 67 (2001) 11.

Kushiya K, Solar Energy 77 (2004) 717.

Lane DW, Conibeer GJ, Wood DA, Rogers KD, Capper P, Romani S, Hearne S, Journal of Crystal Growth 197 (1999) 743.

Lapiller C, Cowache P, Guillemoles JF, Gibson N, Ozsan E, Lincot D, Thin Solid Films 361 (2000) 118.

Lee JC, Kang KH, Kim SK, Yoon KH, Park IJ, Song J, Solar Energy Materials & Solar Cells 64 (2000) 185.

Liao D, Rockett A, Applied Physics Letters 82 (17) (2003) 2829.

Lide DR, CRC Handbook of Chemistry and Physics, CRC Press, (2005).

Lincot D, Gomez Meier H, Kessler J, Vedel J, Dimmler B, Schock HW, Solar Energy Material 20 (1990) 67.

Lincot D, Guillemoles JF, Taunier S, Guimard D, Sicx-Kurdi J, Chaumont A, Roussel O, Ramdani O, Hubert C, Fauvarque JP, Bodereau N, Parissi L, Panheleux P, Fanouillere P, Naghavi N, Grand PP, Benfarah M, Mogensen P, Kerrec O, Solar Energy 77 (2004) 725.

Lincot D, Thin Solid Films 487 (2005) 40.

Machado KD, de Lima JC, Grandi TA, Campos CEM, Maurmann CE, Gasperin AAM, Souza SM, Pimenta AF, Acta Crystallographica B 60 (2004) 282.

Machado G, Guerra DN, Leinen D, Ramos-Barrado JR, Marotti RE, Dalchiele EA, Thin Solid Films 490 (2005) 124.

Markvart T, Solar Electricity 2nd Edition, Wiley, (2000).

Markvart T, Castaner L, Practical Handbook of Photovoltaics: Fundamentals and Applications, New York Elsevier Advanced Technology, (2003).

Martinez MA, Herrero J, Gutierrez MT, Solar Energy Materials & Solar Cells 45 (1997) 75.

Mason NB, Oktik S, Patterson MH, Ransome SJ, Roberts S, Sadeghi M, Sherborne JM, Sivapathasundaram D, Walls IA, Solar Energy Materials & Solar Cells 35 (1994) 263.

McCandless BE, Hededus SS, Birkmire RW, Cunningham D, This Solid Films 431-432 (2003) 249.

McCandless BE, Moulton LV, Birkmire RW, Progress in Photovoltaics 5 (1997) 249.

McGregor SM, PhD thesis, Solar Cells based on electrodeposited CdS and CdTe films Sheffield Hallam University, (1999).

Meulenkamp EA, Peter LM, Journal of the Chemical Society, Faraday Transactions 92 (20) (1996) 4077.

Milman V, Acta Crystallographica B 58 (2002) 437 http://cds.dl.ac.uk/ accessed 10/08.

Mironov VE, Pashkov GL, Stupko TV, Russian Chemical Reviews 61 (9) (1992) 944, http://cds.dl.ac.uk/ accessed 10/08.

Mishra KK, Rajeshwar K, Journal of Electroanalytical Chemistry 271 (1989) 279.

Mitchell KW, Fahrenbruch AL, Bube RW, Journal of Applied Physics 48 (10) (1977) 4365.

Moutinho HR, Dhere RG, Jiang CS, Gessert T, Duda A, Young M, Metzger WK, Al-Jassim MM, Journal of Vacuum Science Technology B 25(2) (2007) 361.

Nagoya Y, Sang B, Fujiwara Y, Kushiya K, Yamase O, Solar Energy Materials & Solar Cells 75 (2003) 163.

Nair JP, Chaure NB, Jayakrishnan R, Pandey RK, Journal of Materials in Electronics 12 (2001) 377.

Nakada T, Hirabayashi Y, Tokado T, Ohmori D, Mise T, Solar Energy 77 (2004) 739.

Niemegeers A, Burgelman M, Herberholz R, Rau U, Hariskos D, Schock HW, Progress in Photovoltaics: Research and Applications 6 (1998) 407.

Oliveira MFC, Azevedo M, Cunha A, Thin Solid Films 405 (2002) 129.

Ortega-Borges R, Lincot D, Journal of the Electrochemical Society 140 (12) (1993) 3464.

Ozgur U, Alivov YI, Teke LA, Reshchikov MA, Dogan S, Avrutin SJ, Morkoc H, Journal of Applied Physics 98 (4) (2005) 1301.

Pandey RK, Sahu SN, Chandra S, Handbook of Semiconductor Electrodeposition, New York Dekker, (1996).

Panicker MPR, Knaster M, Kroger FA, Journal of the Electrochemical Society 125 (4) (1978) 566.

Palm J, Probst V, Karg FH, Solar Energy 77 (2004) 757.

Pauporte T, Lincot D, Electrochimica Acta 45 (2000) 3345.

Pauporte T, Lincot D, Journal of the Electrochemical Society 148 (4) (2001) C310.

Pearton SJ, Norton DP, Ip K, Heo YW, Steiner T, Progress in Materials Science 50 (2005) 293.

Peulon S, Lincot D, Advanced Materials 8 (2) (1996) 166.

Peulon S, Lincot D, Journal of the Electrochemical Society 145 (3) (1998) 864.

Peter LM, Wang RL, Electrochemistry Communications 1 (1999) 554.

Powalla M, Dimmler B, Solar Energy Materials & Solar Cells 75 (2003) 27.

Rabadanov MK, Verin IA, Ivanov YM, Simonov VI, Kristallografiya 46 (2001) 703, http://cds.dl.ac.uk/ accessed 10/08.

Ramanathan K, Hasoon FS, Smith S, Young DL, Contreras MA, Johnson PK, Padov AO, Sites J, Journal of Physics and Chemistry 64 (2003) 1495.

Ramdani O, Guillemoles JF, Lincot D, Grans PP, Chassaing E, Kerrec O, 21st European Photovoltaic Solar Energy Conference, 4-8th September (2006), Dresden Germany.

Repin I, Contreras M, Egaas B, Dehart C, Scharf J, Perkins CL, To B, Noufi R, Progress in Photovoltaics: Research and Applications 16 (2008) 235.

Repins I, Contreras M, Romero M, Yan Y, Metzger W, Li J, Johnston S, Egaas B, Dehart C, Scharf J, McCandless BE, Noufi R, 33rd IEEE Photovoltaic Specialists Conference May 11–16th (2008), San Diego California.

Rockett A, The Materials Science of Semiconductors, New York: Springer, (2008).

Rodic D, Spasojevic V, Bajorek A, Oennerud P, Journal of Magnetism and Magnetic Materials 152 (1996) 159, http://cds.dl.ac.uk/ accessed 08/08.

Rogers KD, Painter JD, Healy MJ, Lane DW, Ozsan ME, Thin Solid Films 339 (1999) 299.

Romeo A, Terheggen M, Abou-Ras D, Batzner DL, Haug FJ, Kalin M, Rudmann D, Tiwari AN, Progress in Photovoltaics Research and Applications 12 (2004) 93.

Rousseau JJ, Basic Crystallography, Wiley, (1998).

Sang B, Nagoya Y, Kushiya K, Yamase O, Solar Energy Material & Solar Cells 75 (2003) 179.

Saraby-Reintjies A, Peter LM, Ozsan ME, Dennison S, Webster S, Journal of the Electrochemical Society 140 (10) (1993) 2880.

Savadogo O, Solar Energy Materials & Solar Cells 52 (1998) 361.

Schock HW, Noufi R, Progress in Photovoltaics: Research and Applications 8 (2000) 151.

Schorr S, Geandier G, Crystal Research & Technology 41 (2006) 450, http://cds.dl.ac.uk/ accessed 07/08.

Schubert EF, Physical Foundations of Solid State Devices, (Rensselaer Polytechnic Institute, Troy NY, USA) (2007), available online http://www.rpi.edu/~schubert/ last accessed 04/08.

Sene C, Calixto ME, Dobson KD, Birkmire RW, Thin Solid Films 516 (8) (2008) 2188.

Siebentritt S, Thin Solid Films 403 (2002) 1.

Silver GL, Martin SF, Ammonia release method for deposited metal oxides, U.S. Patent 5,372,847 (1994).

Sittinger V, Ruske F, Werner W, Szyszka B, Menner R, Powalla M, Dimmler B, 21st European Photovoltaic Solar Energy Conference, 4-8th September (2006), Dresden Germany

Skomorokhov AN, Trot DM, Knapp M, Bickulova NN, Fuess H, Journal of Alloys and Compounds 421 (2006) 64, http://cds.dl.ac.uk/ accessed 07/08.

Sobiesierski Z, Dharmadasa IM, Williams RH, Applied Physics Letters 53 (26) (1988) 2623.

Sowa H, Ahsbahs H, Journal of Applied Crystallography 39 (2006) 169 http://cds.dl.ac.uk/ accessed 10/08.

Stuart RV, Vacuum Technology, Thin Films and Sputtering: An Introduction, Academic Press, (1983).

Sugimoto Y, Peter LM, Journal of Electroanalytical Chemistry 386 (1995) 183.

Sundaram KB, Bhagavat GK, Journal of Physics D: Applied Physics 14 (1981) 921.

Sze SM, Ng KK, Physics of Semiconductor Devices, 3rd Edition, Wiley, (2007).

Taunier S, Sicx-Kurdi J, Grand PP, Chomont A, Ramdani O, Parissi L, Panheleux P, Naghavi N, Hubert C, Ben-Farah M, Fauvarque JP, Connolly J, Roussel O, Mogensen P, Mahe E, Guillemoles JF, Lincot D, Kerrec O, Thin Solid Films 480–481 (2005) 526.

Mullan CA, Kiely CJ, Casey SM, Imanieh M, Yakushev MV, Tomlinson RD, Journal of Crystal Grwoth 171 (3) (1997) 415.

Titus J, Birkmire RW, Hack C, Miller G, McKeown P, Journal of Applied Physics 99 (2006) 043502-1.

Turner AK, Woodcock JM, Ozsan ME, Cunningham DW, Johnson DR, Marshall RJ, McCandless BE, Moulton LV, Birkmire RW, Progress in Photovoltaics: Research and Applications 5 (1994) 249.

Tuttle JR, Contreras MA, Ramanathan KR, Asher SE, Bhattacharya RN, Berens TA, Keane J, Noufi R, American Institute of Physics Conference Proceedings 394 83, Lakewood CO (1996).

Tyagi MS, Introduction to Semiconductor Materials and Devices, Wiley, (1991).

Wagner S, Shay JL, Migliorato P, Kasper HM, Applied Physics Letters 25 (8) (1974) 434.

Wang Q, Wang G, Jie J, Han X, Xu B, Hou JG, Thin Solid Films 492 (2005) 61.

Wang X, Li SS, Kim WK, Yoon S, Craciun V, Howard JM, Easwaran S, Manasreh O, Crisalle OD, Anderson TJ, Solar Energy Materials & Solar Cells 90 (2006) 2855.

Wei SH, Zhang B, Zunger A, Applied Physics Letters 72 (24) (1998) 3199.

Wei SH, Zhang B, Zunger A, Journal of Applied Physics 85 (10) (1999) 7214.

Wu X, Keane JC, Dhere RG, Dehart C, Albin DS, Duda A, Gessert TA, Asher S, Levi DH, Sheldon P, 17th European Photovoltaic Solar Energy Conference 22-26th October (2001), Munich Germany.

Yoshida T, Tochimoto M, Schlettwein D, Wohrle D, Sugiura T, Minoura H, Chemistry of Materials 11 (1999) 2657.

Yoshida T, Pauporte T, Lincot D, Oekermann T, Minoura H, Journal of the Electrochemical Society 150 (9) (2003) C608.

Yoshida T, Komatsu D, Shimokawa N, Minoura H, Thin Solid Films 451-452 (2004) 166.

Zein El Abedin S, Saad AY, Farag HK, Borisenko N, Liu QX, Endres F, Electrochimica Acta 52 (2007) 2746.